energies

Special Issue Reprint

# Advances in Stability Analysis and Control of Power Systems

Edited by
Yong Li, Weiyu Wang and Junjie Ma

mdpi.com/journal/energies

MDPI

# Advances in Stability Analysis and Control of Power Systems

# Advances in Stability Analysis and Control of Power Systems

Guest Editors

**Yong Li**
**Weiyu Wang**
**Junjie Ma**

MDPI

Basel • Beijing • Wuhan • Barcelona • Belgrade • Novi Sad • Cluj • Manchester

*Guest Editors*
Yong Li
College of Electrical and Information Engineering
Hunan University
Changsha
China

Weiyu Wang
School of Electrical and Information Engineering
Changsha University of Science and Technology
Changsha
China

Junjie Ma
School of Intelligent Manufacturing
Hunan First Normal University
Changsha
China

*Editorial Office*
MDPI AG
Grossepeteranlage 5
4052 Basel, Switzerland

This is a reprint of the Special Issue, published open access by the journal *Energies* (ISSN 1996-1073), freely accessible at: https://www.mdpi.com/journal/energies/special_issues/RE28P1V2H0.

For citation purposes, cite each article independently as indicated on the article page online and as indicated below:

| |
|---|
| Lastname, A.A.; Lastname, B.B. Article Title. *Journal Name* **Year**, *Volume Number*, Page Range. |

**ISBN 978-3-7258-3325-2 (Hbk)**
**ISBN 978-3-7258-3326-9 (PDF)**
**https://doi.org/10.3390/books978-3-7258-3326-9**

# Contents

# About the Editors

**Yong Li**

Yong Li received his B.Sc. and Ph.D. degrees in 2004 and 2011, respectively, from the College of Electrical and Information Engineering, Hunan University (HNU), Changsha, China. From 2009, he worked as a Research Associate at the Institute of Energy Systems, Energy Efficiency, and Energy Economics, TU Dortmund University, Germany, where he received his second Ph.D. degree in June 2012. After that, he worked as a Research Fellow at the University of Queensland, Brisbane, Australia. Since 2014, he has been a Full Professor of electrical engineering at HNU. His current research interests include AC/DC energy conversion systems, analysis and control of power quality, and HVDC and FACTS technologies.

**Weiyu Wang**

Weiyu Wang received his B.S. and Ph.D. degrees from the College of Electrical and Information Engineering, Hunan University, Changsha, China, in 2014 and 2020, respectively. He was also a visiting researcher at the University of Liverpool, Liverpool, UK, from 2018 to 2019. From 2020, he worked as a lecturer at the School of Electrical and Information Engineering, Changsha University of Science and Technology, China. Since 2025, he has been an Associate Professor of electrical engineering at CSUST. He is one of the outstanding reviewers for *IEEE Transactions on Power Systems* in 2022 and 2023. His research interests include the inertia analysis and frequency control of power systems, wind-band oscillation analysis and damping control, grid-forming converter technology, and other topics related to the stability analysis and control of hybrid AC/DC power systems.

**Junjie Ma**

Junjie Ma received his B.S. and Ph.D. degrees from the College of Automation, Center South University, Changsha, China, in 2011 and 2019, respectively. He worked as a postdoctoral fellow at the College of Electrical and Information Engineering, Hunan University, Changsha, China from 2019 to 2022. Since 2023, he has been an Associate Professor at the School of Intelligent Manufacturing, Hunan First Normal University, Changsha, China. His current research interests include stability analysis and control for power electronic-based power systems, signal analysis, and wide-area measurement systems.

# Preface

The integration of power electronics-interfaced devices (PEDs), e.g., renewable energy sources (RES), high-voltage direct current (HVDC) technologies, energy storage systems (ESS), and electric vehicles (EVs), into modern power systems has brought both unprecedented opportunities and challenges to power systems. These PEDs have significantly enhanced the flexibility, efficiency, and sustainability of modern power systems, but also pose critical challenges to the stability, reliability, and resilience of modern power systems, characterized by reduced inertia, nonlinear interactions, and stochastic behavior.

This Reprint collects a selection of groundbreaking studies addressing key aspects of power system stability, control, fault management, and optimization in the context of high PED penetration. The articles span a wide range of topics, from advanced control strategies and stability analysis to data-driven methodologies and fault recovery mechanisms. The scope of this Reprint reflects a commitment to tackling real-world challenges faced by modern power systems, combining theoretical innovation with practical application.

The motivation for this Reprint stems from the increasing urgency to address the complex and multi-faceted stability issues associated with modern power systems. With the ongoing transformation of global energy systems and the growing emphasis on renewable energy integration, researchers must navigate a rapidly changing landscape. This Reprint aims to serve as a valuable resource for engineers, scientists, and policymakers seeking innovative solutions to ensure the secure and sustainable operation of modern power systems.

The contributions presented in this Reprint reflect the collective efforts of an outstanding group of authors, each bringing unique expertise and perspectives to their respective fields. Topics explored include advanced control methodologies, fault detection and localization, grid resilience enhancement, and machine learning applications for stability assessment. Notable studies, such as the inertia analysis in high PED-penetrated systems, transient stability evaluation through interpretable machine learning, and robust decentralized stabilization techniques, demonstrate the depth and breadth of research within this collection.

This Reprint is intended for a diverse audience, including academics, industry professionals, and graduate students, who are actively engaged in the study and development of modern power systems. By providing insights into the latest advancements and practical applications, this Reprint could foster collaboration, inspire new research directions, and contribute to the ongoing evolution of the field.

We would like to express our deepest gratitude to the authors, reviewers, and editors whose efforts have made this Reprint possible. Their dedication and expertise have ensured the high quality and relevance of the included works. Additionally, we acknowledge the support and guidance provided by our academic and industrial collaborators, whose contributions have enriched the perspectives presented in this collection.

In conclusion, this Reprint represents a milestone in the pursuit of stable, resilient and efficient power systems. We hope it inspires readers to explore innovative solutions and address the pressing challenges of modern power grids.

**Yong Li, Weiyu Wang, and Junjie Ma**

*Guest Editors*

*energies*

*Article*

# A Novel Classification of the 330 kV Nigerian Power Network Using a New Voltage Stability Pointer

**Tayo Uthman Badrudeen [1,2,*], Funso Kehinde Ariyo [2], Saheed Lekan Gbadamosi [3] and Nnamdi I. Nwulu [3]**

1 Department of Electrical and Electronics Engineering, Oduduwa University, Ile-Ife 5533, Nigeria
2 Department of Electronic and Electrical Engineering, Obafemi Awolowo University, Ile-Ife 220282, Nigeria
3 Center for Cyber Physical Food, Energy and Water Systems, University of Johannesburg, Johannesburg 2006, South Africa
* Correspondence: tiyoh4energie@gmail.com

**Abstract:** The incessant power outages that characterize the Nigerian power network (NGP), as in all developing countries, are not limited to the shortage of fuel for power generation. However, differential power shortages between the generated power and the load demand are alarming. In this study, we propose a new voltage stability pointer (NVSP) based on a reduced one-line power network to act as a classifier. The NVSP was trained with a support vector machine (SVM) using a medium Gaussian kernel classification toolbox (mGkCT) in the MATLAB environment. This classification is based on the power network susceptibility to voltage instability. NGP 28-bus 330 kV data were extracted and modeled in the MATLAB environment and tested with the NVSP-mGkCT classifier. The NVSP-mGkCT was able to classify the lines viz. stable and unstable lines for the base and contingency cases. Similarly, the linear load dynamics and non-linear load dynamics were evaluated on the basis of critical buses using the NVSP. The aim of this work was to help the Transmission Company of Nigeria (TCN) and the National Control Centre (NCC) to be pre-emptive with respect to possible voltage collapse due to voltage instability. The simulation results show that NVSP was able to flag vulnerable lines in the NGP.

**Keywords:** voltage stability; new voltage stability pointer (NVSP); contingency; support vector machine; Nigerian power network (NGP); critical lines

**Citation:** Badrudeen, T.U.; Ariyo, F.K.; Gbadamosi, S.L.; Nwulu, N.I. A Novel Classification of the 330 kV Nigerian Power Network Using a New Voltage Stability Pointer. *Energies* **2022**, *15*, 7247. https://doi.org/10.3390/en15197247

Academic Editor: Djaffar Ould-Abdeslam

Received: 28 August 2022
Accepted: 27 September 2022
Published: 2 October 2022



## 1. Introduction

Power system planning in most developing countries is associated with several challenges due to the non-linear relationship between the increasing population and power generation, low reliability on capital investment, dispersed utilities, etc. [1]. Gross deficiency in power generation has driven many developing countries to forced load shedding to ensure that the meager generated power reaches the considerable population. In such a context, power system operators are concerned about active power control, which is invariably associated with the frequency stability [2], and rarely consider reactive power control, which is associated with voltage stability [3]. Furthermore, the rotor, frequency and voltage stability control are essential components of a reliable power system [4].

The Nigerian power network (NGP) comprised approximately twenty-six power plants with a combined optimal power generation of slightly more than seven thousand megawatts (7000 MW) [5], which are provided hydro and thermal power plants [6]. This generated power serves a population of more than two hundred million (200,000,000) people [7]. The NGP is faced several crises, including insufficient generation of electric power to match the demand [8,9], overstretched transmission lines and support, [10] and the inability to withstand transient conditions [11]. The average number of the recorded power outages, both partial and total, in the NGP every year is alarming [12], and there seems to be no end in sight with respect to addressing this increasing figure. The high rate of blackouts in Nigeria has driven many small-scale businesses out of operation [13], and the few remaining companies operate at a high cost of production due to the increase in prices of alternative sources of fuel, for example, diesel, gas, etc. Hence, there is a need to develop a tool to identify the weak buses and lines that are vulnerable to voltage collapse, which could lead to a national blackout.

The framework of this research is to (1) develop a new voltage stability pointer (NVSP) for evaluation of voltage stability, (2) train the NVSP with the support vector machine using a medium Gaussian kernel classification toolbox in a MATLAB environment and (3) adapt it to the Nigerian power network to classify it into two classes, i.e., stable and unstable. The lines and buses under the unstable classification will be flagged as vulnerable.

## 2. Related Work

The effort of the Nigerian government to increase the power generation capacity of the country has not yielded satisfactory results despite the considerable capital investment in the power sector over the years. According to the World Bank Energy Progress Report, only 55.4 percent of the Nigerian population had access to electricity in the year 2020 [7]. The geographical structure of the transmission lines in Nigeria is shown in Figure 1.


**Figure 1.** Geographical structure of the NGP transmission lines [6].

The load demand is predicted to reach 50,000 MW by the year 2035 [6]. However, there little effort has been made to date to scale up the generation capacity to meet this future demand. The recorded cases of power outages in the NGP between January and June 2022 are estimated to be five [14]. This number is high compared to other developed nations [7]. The variation in load demand is among the factors that affect the power network stability [15]. Ramirez-Gonzalez M. et al. [16] studied contingencies in a power network and their effects on security. A convolutional neural network was used to allocate power injection stations in the power network, with the result proving the effectiveness of the proposed method.

Similarly, Abdulkareem A. et al. [10] suggested that the NGP topology be changed from a radial to ring structure to minimize losses and voltage instability. The TCN annual technical report also set a goal to achieve this transition before the year 2030 [6]. However, such a transition will be time-consuming and cost-intensive, and a solution is urgently required before it can be implemented. In addition, Obi P. I. et al. [17] presented a technique to improve the NGP with static Var compensators to fulfill the voltage quality requirements. However, this technique is regarded as a short-term solution to the lingering problem faced by the Nigerian power grid. Moreover, Adebayo et al. [18] proposed two methods to identify vulnerable buses in a power network. The first method was achieved through the maximum loading limit technique, and the other was based on the configuration of the power network. The NGP 24-bus and IEEE 30-bus systems were used to evaluate the proposed method. The critical buses were strengthened with FACTS components. Simulation results showed that optimal placement of a compensating device could improve the voltage profile. In [19], a stability concept for power systems based on the frequency control of synchronous machines was presented. The system was tested with various loading patterns, and the results were compared with conventional synchro-converter models.

In a research paper presented by Kasis A. et al. [20], a technique was evaluated to solve the problem associated with fluctuations of renewable energy sources and the effects on power stability. Multiple possibilities for frequency dynamics were modeled, considering the variability of the inherent power supply. The results showed the immunity of the power stability to a high-frequency cycle. A surge in renewable power penetration in power distribution networks might result in overvoltage at network buses in the absence of an effective control mechanism. Heidari Yazdi et al. [21] proposed a method to regulate voltage magnitude based on the load demand. Power demand usually varies; therefore, means to compensate for the peak consumption period is necessary. An overvoltage resulting from excessive reactive power injection was considered and addressed for a stable power system.

In an effort to solve problems associated with power network configuration, Narimani et al. [22] proposed a novel method of analyzing several contingency problems associated with the architecture of the network. This was achieved through a graph theory approach that identifies different power components responsible for contingency, especially between two successive contingencies. The results showed that the proposed method could rapidly identify multiple contingencies. In the same vein, Randey A et al. [23] proposed a network reconfiguration technique for NGP to secure the network from a possible grid collapse and thereby improve the voltage profile. Contingency analysis resulted suggested that the redistribution of notable generators to defined voltage set-points would reduce power outages.

In a paper presented by Nkan et al. [24], several compensative devices were investigated with the aim of combining two similar controllers. The method was tested on NGP in the power system analysis toolbox (PSAT) in MATLAB. Analysis results showed that the combination of similar compensating devices could reduce power losses to a considerable extent. Some NGP buses are currently operating below their standard rated voltage [25] as a result of overload and congestion, with no adequate plan for contingency. Moreover, Liu S. et al. [26] presented a study on the dynamism of a stability point in a power network through the injection of noise and time delay. The aim of this method is to improve the integrity of the power network in a smart grid. The authors assessed the effect of noise on power system stability.

The power stability problem has recently received attention from many researchers, and efforts are being made to address the problems associated with power stability. Alnasseir et al. [27] addressed the power stability problem by introducing a static synchronous compensator (STATCOM) and a thyristor-controlled series capacitor (TCSC). The two compensators were assessed independently, and their results were compared. The results showed that the TCSC is relatively effective in securing power stability. Similarly, Calma E. and Pacis M. [28] studied voltage stability indices for different states of operation in a power system. The proposed approach involved an artificial neural network, and the Newton–Raphson power flow was employed in the MATLAB environment. The results demonstrated the feasibility of the proposed approach, especially compared with other machine learning techniques in terms of assessing the voltage stability of a power network. In addition, Collados-Rodriguez et al. [29] analyzed the effect of power electronics components on power system stability. Several cases of stability were evaluated to assess the minimum power generation expected to ensure power network security with the installation of compensative components. The stability indices considered for the evaluation were frequency and voltage, which were sufficient to identify the vulnerable lines in the network [2,3].

The effect of harmonics on power stability cannot be overemphasized [30]. Abirami and Ravi [31] recommended a technique to reduce harmonic distortion, especially with the advent of electric car charging stations in the distribution network. They suggested that a shunt capacitive filter be connected in parallel with dynamic loads in a radial distribution network. Simulation results revealed that adequate control of harmonic could enhance the power quality delivery to end consumers. Similarly, Zaheb H. et al. [32] investigated the effect of inductive load dynamics on various voltage stability indices. The researchers emphasized the suitability of these indices for online application. The obtained results were used to classify the indices in terms of their ability to assess, formulate and analyze the voltage stability.

The NVSP proposed in this study was developed to (a) verify the voltage stability status of the Nigerian power network, (b) assess the vulnerability of each transmission line to voltage instability, (c) flag unstable lines and buses and (d) suggest a reactive power injection station. With this approach, it is expected that the outcome of this research will help to tame the frequent power outages in the NGP, and thus, improves the economic viability of the country.

## 3. Proposed Methodology

The proposed method is based on successive dependence of three approaches viz. power flow solution, development of a new voltage stability pointer for voltage stability evaluation from the power flow data and training of the NVSP through a support vector machine.

### 3.1. Power Flow Solution

In this research, the Newton–Raphson method was adopted, owing to its fast convergence time. Saadat [33] considered an n-bus network (Figure 2) for as a power flow solution.

$$I_i = \sum_{j=1}^{n} Y_{ij} V_j \tag{1}$$

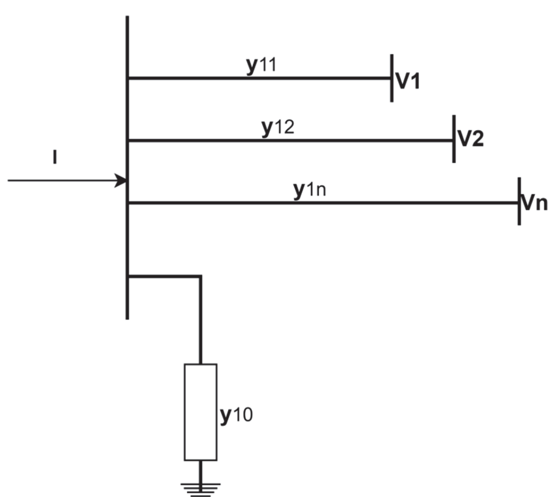


**Figure 2.** n-bus power network [33].

The polar-form representation of the equation is:

$$I_i = \sum_{j=1}^{n} |Y_{ij}|V_j||\angle\theta_{ij} + \delta_j \tag{2}$$

The power at bus 1 is expressed as:

$$P_i - jQ_i = V_i^* I_i \tag{3}$$

Substituting Equation (2) into Equation (3) yields:

$$P_i - jQ_i = |V_i|\angle - \delta_i \sum_{j=1}^{n} |Y_{ij}||V_j|\angle\theta_{ij} + \delta_j \tag{4}$$

Separating the real from the imaginary part yields:

$$P_i = \sum_{j=1}^{n} |V_i||V_j||Y_{ij}| \cos\left(\theta_{ij} - \delta_j + \delta_j\right) \tag{5}$$

$$Q_i = -\sum_{j=1}^{n} |V_i||V_j||Y_{ij}| \sin\left(\theta_{ij} - \delta_j + \delta_j\right) \tag{6}$$

Expanding Equations (5) and (6) using Taylor's series yields:

$$\begin{bmatrix} \Delta P_2^{(k)} \\ \vdots \\ \Delta P_n^{(k)} \\ - \\ \Delta Q_2^{(k)} \\ \vdots \\ \Delta Q_n^{(k)} \end{bmatrix} = \left[\begin{array}{cccccc} \frac{\partial P_2^{(k)}}{\partial \delta_2} & \cdots & \frac{\partial P_2^{(k)}}{\partial \delta_n} & \frac{\partial P_2^{(k)}}{\partial \delta_2} & \cdots & \frac{\partial P_2^{(k)}}{\partial \delta_n} \\ \vdots & \ddots & \vdots & \vdots & \ddots & \vdots \\ \frac{\partial P_n^{(k)}}{\partial \delta_2} & \cdots & \frac{\partial P_n^{(k)}}{\partial \delta_n} & \frac{\partial P_n^{(k)}}{\partial \delta_2} & \cdots & \frac{\partial P_n^{(k)}}{\partial \delta_n} \\ \hline \frac{\partial P_2^{(k)}}{\partial \delta_2} & \cdots & \frac{\partial P_2^{(k)}}{\partial \delta_n} & \frac{\partial P_2^{(k)}}{\partial \delta_2} & \cdots & \frac{\partial P_2^{(k)}}{\partial \delta_n} \\ \vdots & \ddots & \vdots & \vdots & \ddots & \vdots \\ \frac{\partial P_n^{(k)}}{\partial \delta_2} & \cdots & \frac{\partial P_n^{(k)}}{\partial \delta_n} & \frac{\partial P_n^{(k)}}{\partial \delta_2} & \cdots & \frac{\partial P_{n_k}^{(k)}}{\partial \delta_n} \end{array}\right] \begin{bmatrix} \Delta \delta_2^{(k)} \\ \vdots \\ \Delta \delta_n^{(k)} \\ - \\ \Delta \left| V_2^{(k)} \right| \\ \vdots \\ \Delta \left| V_n^{(k)} \right| \end{bmatrix} \tag{7}$$

Equation (7) can be expressed in short form as:

$$\begin{bmatrix} \Delta P \\ \Delta Q \end{bmatrix} = \begin{bmatrix} J_1 & J_2 \\ J_3 & J_4 \end{bmatrix} \begin{bmatrix} \Delta\delta \\ \Delta|V| \end{bmatrix} \tag{8}$$

The diagonal and off-diagonal components of $J_1$, $J_2$, $J_3$ and $J_4$ are estimated to obtain the differential residual power and bus voltages:

$$\Delta P_i^{(k)} = P_i^{sch} - P_i^{(k)} \tag{9}$$

$$\Delta Q_i^{(k)} = Q_i^{sch} - Q_i^{(k)} \tag{10}$$

$$\delta_i^{(k+1)} = \delta_2^{(k)} + \Delta\delta_i^{(k)} \tag{11}$$

$$\left|V_n^{(k+1)}\right| = \left|V_i^{(k)}\right| + \Delta\left|V_i^{(k)}\right| \tag{12}$$

### *3.2. Derivation of the Proposed New Voltage Stability Pointer*

The proposed NVSP is derived from a reduced one-line diagram as shown in Figure 3.

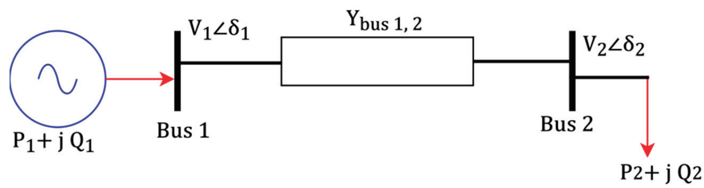


**Figure 3.** A reduced one-line diagram.

The line current (I) from the generator bus is expressed as:

$$I = (V_1 - V_2).Y_{bus} \tag{13}$$

The current at the load bus can also be calculated as:

$$I = \left(\frac{S_2}{V_2}\right) = \frac{P_2 - jQ_2}{V_2\angle - \delta_2} \tag{14}$$

Assuming the line loss due to the load current is neglected, then Equation (13) will equate to Equation (14):

$$P_2 - jQ_2 = (V_1 - V_2).Y_{bus} \,.\, V_2\angle - \delta_2 \tag{15}$$

$$P_2 - jQ_2 = |V_1V_2Y_{bus}|\angle(\theta - \delta_2) - |V_2|^2.|Y_{bus}|\angle\theta \tag{16}$$

Dividing Equation (16) by $|Y_{bus}|\angle\theta$ yields:

$$\frac{P_2 - jQ_2}{|Y_{bus}|\angle\theta} = |V_1V_2|\angle - \delta_2 - |V_2|^2 \tag{17}$$

Equation (17) can be rewritten as:

$$|V_2|^2 - |V_1V_2|\angle - \delta_2 + \frac{P_2 - jQ_2}{|Y_{bus}|\angle\theta} = 0 \tag{18}$$

From Equation (18):

$$a = 1; b = |V_1|\angle - \delta_2 \;\; and \; c = \frac{P_2 - jQ_2}{|Y_{bus}|\angle\theta}$$

$$V_2 = |V_1|\angle - \delta_2 \pm \frac{\sqrt{|V_1|\angle - \delta_2\Big|2 - 4\frac{P_2 - jQ_2}{|Y_{bus}|\angle\theta}}}{2} \tag{19}$$

If $\left(|V_1|\angle - \delta_2\;\Big|2 - 4\frac{P_2 - jQ_2}{|Y_{bus}|\angle\theta}\right)$ is discriminated to zero, the real roots of $V_2$ can be expressed as $|V_1|\angle - \delta_2\Big|2 - 4\frac{P_2 - jQ_2}{|Y_{bus}|\angle\theta} \;\leq\; 0$; then:

$$\frac{4(P_2 - jQ_2)}{|G - jB|\angle\theta|V_1|\angle - \delta_2\;|^2} \leq 1 \tag{20}$$

If Equation (20) is rearranged into real and imaginary parts, then the real part is $\frac{4P_2}{G\;cos\theta\;.\;|V_1|^2\;cos^2\;(-\delta_2\;)} \leq 1$, and if the voltage angle ($\delta_2$ ) is very small, then it is reduced to$\approx$ $\frac{4P_2|Z|}{|V_1|^2} \leq 1$.

Likewise, the imaginary part is $\frac{4Q_2}{B\;sin\;\theta\;.\;|V_1|^2\;sin^2\;(-\delta_2\;)} \leq 1$; if the voltage angle ($\delta_2$ ) is assumed to be negligible, then it is reduced to$\approx$ $\frac{4Q_2|Z|}{|V_1|^2} \leq 1$.

Therefore, the new voltage stability pointer (NVSP) is:

$$\text{NVSP} = \frac{4Q_2|Z|}{|V_1|^2} \leq 1 \tag{21}$$

where $V_1$ is the voltage at the sending end bus, $Q_2$ is the reactive power at the load bus and $Z$ is the line impedance. The index Equation (21) depends on the extracted data from the power flow solution of Equations (8), (10) and (12). The NGP 28-bus line diagram is shown in Figure 4.

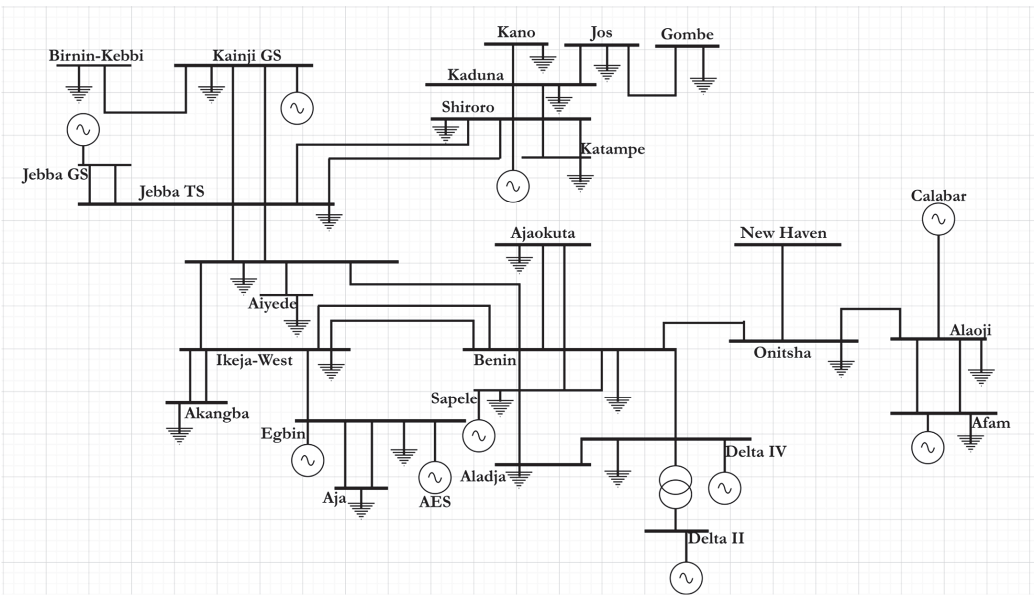


**Figure 4.** Single-line diagram of the 28-bus, 330 kV NGP.

### 3.3. *Classification through Support Vector Machine Algorithm*

The support vector machine (SVM) algorithm has been widely used to classify data of different sets that are separable into classes [34]. Squires [35] defined the Gaussian elimination with a function $f(x) = \exp(-x)$ with parametric extension:

$$f(x) = a \exp\left(-\frac{(x-b)^2}{2c^2}\right) \tag{22}$$

where $a$ and $b$ are real constants, and $c$ is a non-zero variable. However, the Gaussian function is usually expressed as:

$$g(x) = \frac{1}{\sigma\sqrt{2\pi}} \exp\left(-\frac{1}{2}\frac{(x-\mu)^2}{\sigma^2}\right) \tag{23}$$

where $\sigma$ is the expected value and $\mu$ is the variance.

Assuming [36] that the training data $(x_i, y_i)$ for $i = 1 \ldots\ldots N \; with \; X_i \in \mathbb{R}^d \; and \; y_i \in \{-1, 1\}$, the classifier $f(x)$ is:

$$f(x_i) = \begin{cases} \geq 0 & y_i = +1 \\ < 0 & y_i = -1 \end{cases} \tag{24}$$

and

$$f(x) = W^T X + b \tag{25}$$

where $X$ is the input vector, $W$ is the vector weight and $b$ is the bias. The NVSP was trained by the support vector machine algorithm in MATLAB using the medium Gaussian kernel classification tool according to the function $k(x_{ij})$ in Equation (26):

$$k_{ij} = \begin{cases} +1 & if\ 0.00 < \text{NVSP} < 0.80\ (Stable) \\ -1 & if\ 0.80 < \text{NVSP} < 1.00\ (Unstable) \end{cases} \tag{26}$$

where $k_{ij}$ is the NVSP-mGkCT trained index value between the two buses.

## 4. Results and Discussion

### *4.1. Assessment of the NGP 28-Bus, 330 kV Base Case*

The simulation results obtained from the voltage stability assessment of the NGP using the NVSP are presented in Table 1, and the training results from the support vector machine in the MATLAB environment are shown in Figure 5. The NGP 28-bus voltage magnitude in the base case is depicted in Figure 6.

**Table 1.** Voltage stability assessment of 28-bus 330 kV NGP transmission line using NVSP in the base case.

| From | Bus Name | To | Bus Name | NVSP |
|---|---|---|---|---|
| 3 | Aja | 1 | Egbin | 0.0087 |
| 4 | Akangba | 5 | Ikeja-west | 0.1033 |
| 1 | Egbin | 5 | Ikeja-west | 0.0777 |
| 5 | Ikeja-west | 8 | Benin | 0.9673 |
| 5 | Ikeja-west | 9 | Ayede | 0.3404 |
| 5 | Ikeja-west | 10 | Osogbo | 0.4711 |
| 6 | Ajaokuta | 8 | Benin | 0.5410 |
| 2 | Delta | 8 | Benin | 0.3432 |
| 2 | Delta | 7 | Aladja | 0.0242 |
| 7 | Aladja | 24 | Sapele | 0.0109 |
| 8 | Benin | 14 | Onitsha | 0.2159 |
| 8 | Benin | 10 | Osogbo | 0.4213 |
| 8 | Benin | 24 | Sapele | 0.0080 |
| 9 | Aiyede | 10 | Osogbo | 0.2290 |
| 15 | Birnin | 21 | Kanji | 0.0171 |
| 10 | Osogbo | 14 | Jebba TS | 0.0153 |
| 11 | AFAM | 12 | Alaoji | 0.0818 |
| 12 | Alaoji | 14 | Onitsha | 0.2210 |
| 13 | New Haven | 14 | Onitsha | 0.1656 |
| 16 | Gombe | 19 | Jos | 0.1335 |
| 17 | Jebba TS | 18 | Jebba GS | 0.0000 |
| 17 | Jebba TS | 23 | Shiroro | 0.0986 |
| 17 | Jebba TS | 21 | Kanji | 0.0041 |
| 19 | Jos | 20 | Kaduna | 0.0275 |
| 20 | Kaduna | 22 | Kano | 0.3689 |
| 20 | Kaduna | 23 | Shiroro | 0.0389 |
| 23 | Shiroro | 26 | Katempe | 0.2223 |
| 12 | Alaoji | 25 | Calabar | 0.1797 |
| 14 | Onitsha | 27 | Okpai | 0.0000 |
| 25 | Calabar | 27 | Okpai | 0.0000 |
| 5 | Ikeja-west | 28 | AES GS | 0.0000 |

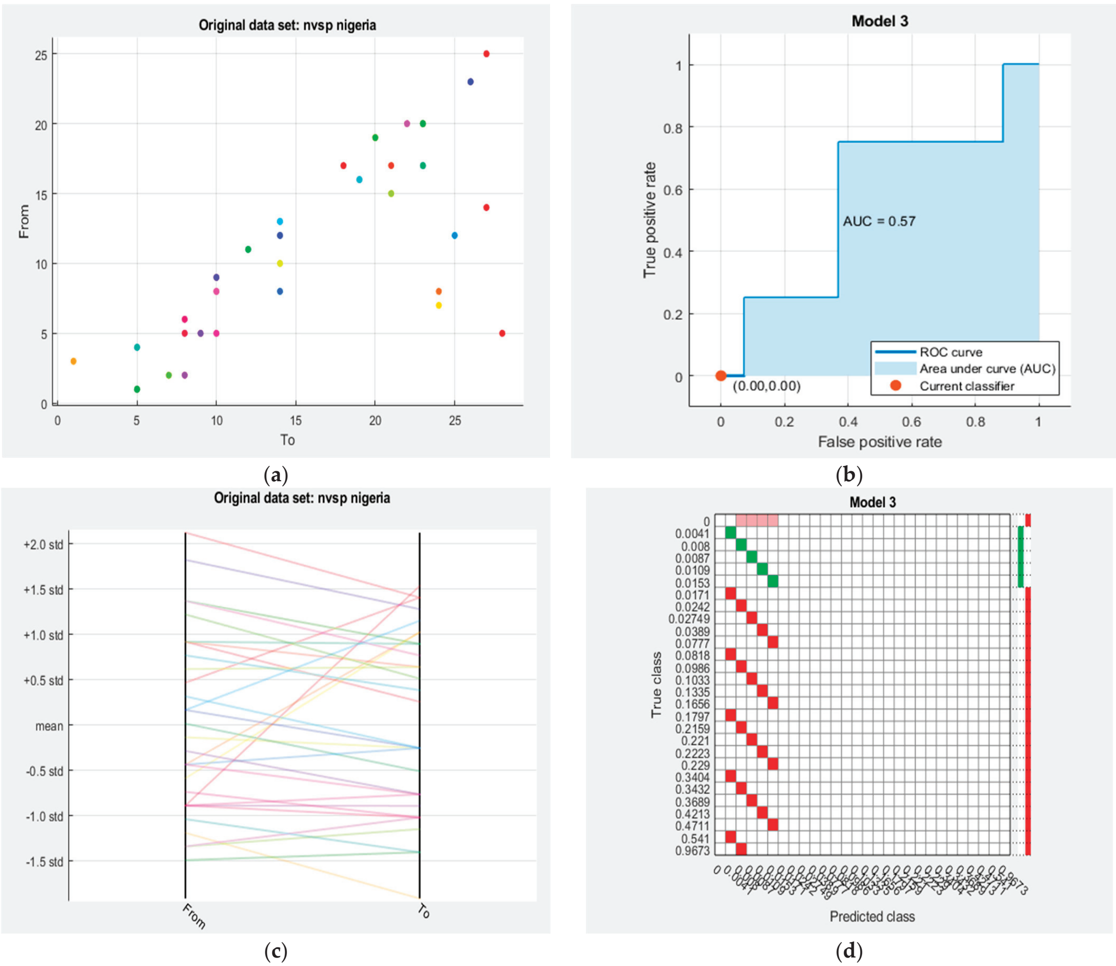


**Figure 5.** Training results of NVSP using support vector machine in the MATLAB environment. (**a**) Scatter plot of the NGP. (**b**) Receiver operating characteristic (ROC) curve. (**c**) Parallel coordinate plot. (**d**) Confusion matrix.

### *4.2. Analysis of the 28-Bus, NGP 330 kV Base Case*

The overall percentage accuracy of the predicted class of NVSP, 28-bus NGP 330 kV line to the true class is 72.48, with a training time of about 2.02 s. The area under the curve from the receiver operating characteristic (ROC) is 0.57. All lines and buses are stable in the base case, except the Ikeja-west bus and the Ikeja-west–Benin line. The NVSP index value is 0.9673, and the voltage magnitude is 0.997 (p.u), indicating the vulnerability of the line to voltage instability. In the base case, the Ikeja-west load bus has 474. 5 MVar, as shown in Table A1, as a result of heavy industrial presence in the region. The NVSP index values for all other lines are far less than unity, indicating their immunity to voltage instability in the base case, as shown in Figure 7.

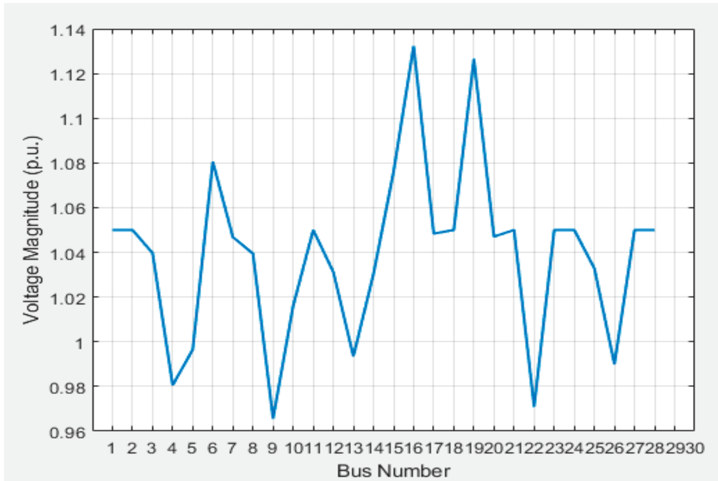


**Figure 6.** The NGP 28-bus voltage per unit in the base case.

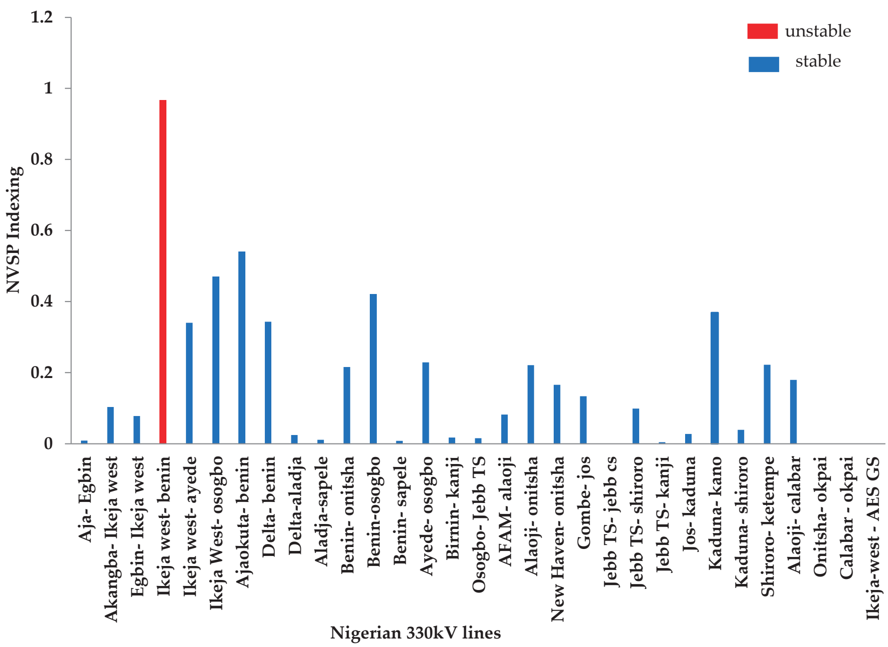


**Figure 7.** Classification of the NGP transmission lines using NVSP in the base case.

The placement of the static synchronous compensator (STATCOM) at the Ikeja-west bus provides stability at the bus, as the NVSP index value from the Ikeja-west–Benin line changes from 0.9673 to 0.7621. The voltage magnitude of the Ikeja-west bus also changes from 0.997 (p.u) to 1.023 (p.u). This effect yielded a positive result with respect to the overall performance of the NGP, as none of the lines are near the unity NVSP index value, and the voltage profile is also improved, as shown in Figure 8.

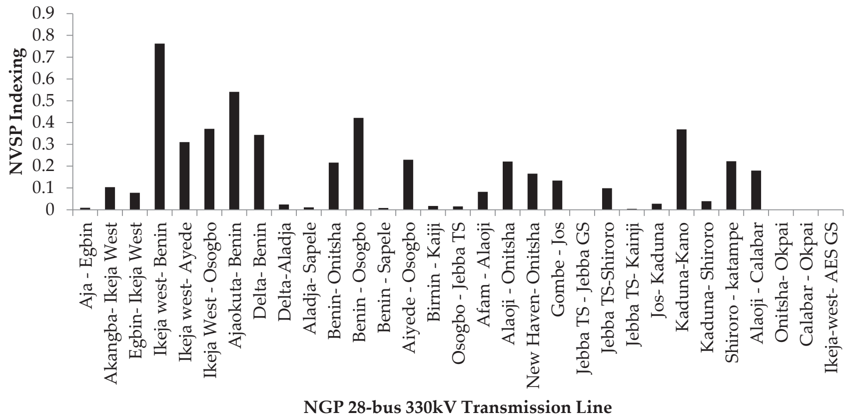


**Figure 8.** The NGP 28-bus 330 kV transmission lines after STATCOM compensation in the base case.

### 4.3. Contingency Assessment of the NGP 28-Bus Using NVSP

The contingency analysis is among the performance indices used to evaluate the power network stability, especially with respect to its loading capacity limit [15]. Contingency analysis can assist the system operator in identifying the most critical and vulnerable lines and buses to voltage instability. The contingency analysis of the NGP, 28-bus using NVSP is presented in Table 2. The NVSP index and the power flow convergence methods were used to evaluate the loadability of all the NGP P-Q buses. The power flow solution is programmed to return non-convergence after 100 iterations without convergence.

**Table 2.** Realization of the NGP critical lines and the maximum reactive power loading points.

| P-Q Bus | From | To | NVSP | Voltage Mag. (p.u) | Qmax (MVar) | Remark |
|---|---|---|---|---|---|---|
| Aja | Aja | Egbin | 0.0260 | 0.600 | 6005.58 | Non-convergence |
| Akangba | Akangba | Ikeja-west | 0.2527 | 0.6270 | 2050.8 | Non-convergence |
| Ikeja-west | Ikeja-west | AES-GS | 0.0000 | 0.9760 | 774.9 | NVSP indexing |
| | Egbin | Ikeja-west | 0.1268 | | | |
| | Ikeja-west | Benin | 1.0077 | | | |
| | Ikeja-west | Osogbo | 0.4908 | | | |
| | Akangba | Ikeja-west | 0.1758 | | | |
| | Ikeja-west | Ayede | 0.3546 | | | |
| Ajaokuta | Ajaokuta | Benin | 0.9980 | 0.7960 | 355.3 | NVSP-indexing |
| Aladja | Aladja | Sapele | 0.0174 | 0.8280 | 2972.4 | NVSP-indexing |
| | Delta | Alajda | 0.9946 | | | |
| Benin | Benin | Sapele | 0.0080 | 1.0390 | 295.5 | NVSP-indexing |
| | Delta | Benin | 0.3528 | | | |
| | Benin | Osogbo | 0.4318 | | | |
| | Ikeja-west | Benin | 0.9944 | | | |
| | Benin | Onitsha | 0.2161 | | | |
| | Akaokuta | Benin | 0.5566 | | | |
| Aiyede | Aiyede | Osogbo | 0.6678 | 0.5650 | 906.8 | NVSP-indexing |
| | Osogbo | Jebba TS | 0.0171 | | | |
| Osogbo | Benin | Osogbo | 0.8660 | 0.9840 | 300.9 | NVSP indexing |
| | Ikeja-west | Osogbo | 0.9501 | | | |
| | Ayede | Osogbo | 0.4776 | | | |
| Alaoji | Afam | Alaoji | 0.9763 | 0.7450 | 3820.2 | NVSP-indexing |
| | Alaoji | Onitsha | 0.4231 | | | |
| | Alaoji | Calabar | 0.3440 | | | |
| New Haven | New Haven | Onitsha | 0.3602 | 0.6740 | 633.4 | NVSP-indexing |

**Table 2.** *Cont.*

| P-Q Bus | From | To | NVSP | Voltage Mag. (p.u) | Qmax (MVar) | Remark |
|---|---|---|---|---|---|---|
| Onitsha | Benin | Onitsha | 0.9591 | 0.9840 | 605.4 | NVSP-indexing |
| | Alaoji | Onitsha | 0.9787 | | | |
| | New Haven | Onitsha | 0.8013 | | | |
| Birni-Kebbi | Birni-Kebbi | Kainji | 0.3560 | 0.7470 | 285.9 | NVSP-indexing |
| Gombe | Gombe | Jos | 0.1358 | 1.1230 | 100.9 | Non-convergence |
| Jebba TS | Jebba Ts | Shiroro | 0.1004 | 1.0390 | 500.2 | NVSP-indexing |
| | Jebba TS | Kainji | 0.0048 | | | |
| | Jebba TS | Jebba GS | 0.0000 | | | |
| | Osogbo | Jebba TS | 0.9436 | | | |
| Jos | Gombe | Jos | 0.6662 | 0.8860 | 142.7 | Non-convergence |
| | Jos | Kaduna | 0.4442 | | | |
| Kaduna | Kaduna | Shiroro | 0.0512 | 0.9120 | 332.7 | NVSP indexing |
| | Kaduna | Kano | 0.4858 | | | |
| | Jos | Kaduna | 0.9508 | | | |
| Calabar | Alaoji | Calabar | 0.9517 | 0.9050 | 459 | NVSP indexing |
| | Calabar | Okapi | 0.0000 | | | |
| Katampe | Shiroro | Katampe | 0.7128 | 0.7980 | 465 | Non-convergence |
| Kano | Kaduna | Kano | 0.6185 | 0.8080 | 210.9 | Non-convergence |

The maximum reactive power at all the P-Q buses of the NGP 28-bus is presented in Table 3. The results show the peak loading limit of all the load buses, and a step above this threshold results in voltage instability. The contingency ranking was obtained based on the increment of reactive power at the load buses. The maximum reactive power that drives the NVSP index value to unity or the power flow solution to non-convergence is regarded as maximum loadability. In other words, the safe operating limit of reactive power at the load buses was attained by considering the power flow convergence and the NVSP indexing value. The NVSP of every line should be maintained well below unity in order to ensure voltage stability.

**Table 3.** Contingency analysis of the NGP buses and lines.

| Ranking | Bus Name | From | To | NVSP | Voltage Mag. (p.u) | Qmax (MVar) |
|---|---|---|---|---|---|---|
| 1 | Gombe | Gombe | Jos | 0.1358 | 1.1230 | 100.9 |
| 2 | Jos | Gombe | Jos | 0.6662 | 0.8860 | 142.7 |
| 3 | Kano | Kaduna | Kano | 0.6185 | 0.8080 | 210.9 |
| 4 | Birni-Kebbi | Birni-Kebbi | Kainji | 0.3560 | 0.7470 | 285.9 |
| 5 | Benin | Ikeja-west | Benin | 0.9944 | 1.0390 | 295.5 |
| 6 | Osogbo | Ikeja-west | Osogbo | 0.9501 | 0.9840 | 300.9 |
| 7 | Kaduna | Jos | Kaduna | 0.9508 | 0.9120 | 332.7 |
| 8 | Ajaokuta | Ajaokuta | Benin | 0.9980 | 0.7960 | 355.3 |
| 9 | Calabar | Alaoji | Calabar | 0.9517 | 0.9050 | 459 |
| 10 | Katampe | Shiroro | Katampe | 0.7128 | 0.7980 | 465 |
| 11 | Jebba TS | Osogbo | Jebba TS | 0.9436 | 1.0390 | 500.2 |
| 12 | Onitsha | Alaoji | Onitsha | 0.9787 | 0.9840 | 605.4 |
| 13 | New Haven | New Haven | Onitsha | 0.3602 | 0.6740 | 633.4 |
| 14 | Ikeja-west | Ikeja-west | Benin | 1.0077 | 0.9760 | 774.9 |
| 15 | Ayede | Ayede | Osogbo | 0.6678 | 0.5650 | 906.8 |
| 16 | Akangba | Akangba | Ikeja-west | 0.2527 | 0.6270 | 2050.8 |
| 17 | Aladja | Delta | Alajda | 0.9946 | 0.8280 | 2972.4 |
| 18 | Alaoji | Afam | Alaoji | 0.9763 | 0.7450 | 3820.2 |
| 19 | Aja | Aja | Egbin | 0.0260 | 0.6000 | 6005.58 |

The results presented in Table 3 show that the most critical bus and line under contingency rankings are Gombe and Gombe-Jos, with a maximum operating limit of 100.9 MVar and an NVSP index value of 0.1358, respectively. The Jos, Kano, Birni-Kebbi and Benin buses, which are ranked second, third, fourth and fifth, with maximum reactive power limits of 142.7 MVar, 210.9 MVar, 285.9 MVar and 295.5 MVar, respectively, are also vulnerable to perturbation or transient conditions. The voltage magnitude and maximum reactive power limit of the NGP P-Q bus are presented in Figures 9 and 10, respectively.

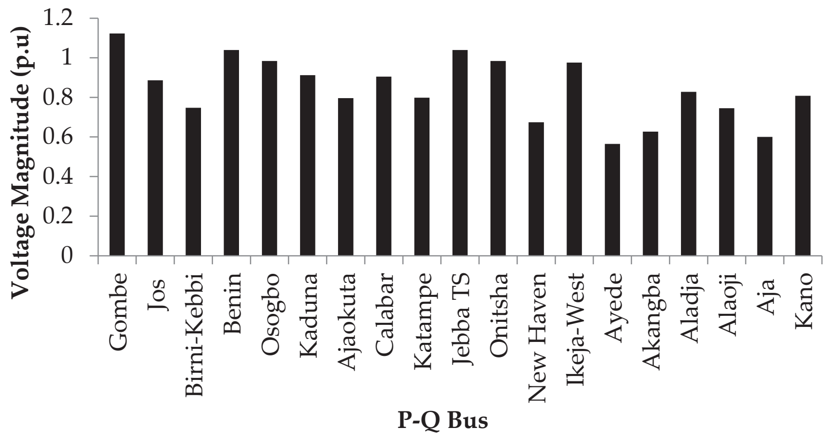


**Figure 9.** Voltage magnitude of the NGP P-Q bus under contingency conditions.

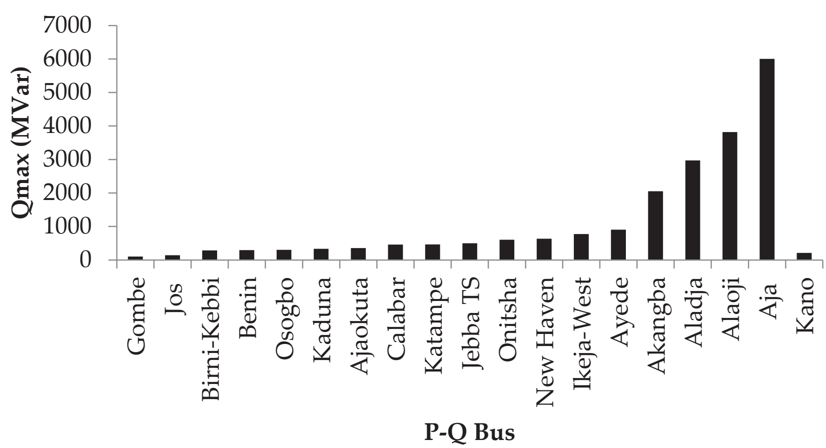


**Figure 10.** Maximum loading limit of the NGP P-Q bus.

The results presented in Table 3 show that the order of stable buses of the NGP under contingency conditions is: Aja, Alaoji, Aladja, Akangba, Ayede, Ikeja-west and New Haven. Conversely, the order of unstable P-Q buses under contingency conditions is: Gombe, Jos, Kano, Birni-Kebbi, Osogbo, Kaduna, Calabar, Katampe, Jebba TS and Onitsha. Based on the results presented in Figures 9 and 10 and a stamp to ensure a safe margin of operation at the vulnerable buses in the NGP, we recommended that the loads at the critical P-Q buses be optimally shed, especially during peak load hours. However, this approach is regarded as a short-term solution to power system stability [37].

### *4.4. Assessment of Dynamic Load on 28-Bus NGP Critical Lines and Vulnerable Buses*

The effect of the dynamic load on the vulnerable P-Q buses in the NGP 28-bus system were considered for this analysis, including the first, second and third rankings in Table 3, i.e., Gombe, Jos and Kano, respectively. In addition, we evaluated both linear load dynamics and non-linear load dynamics to assess the power stability of the NGP.

#### 4.4.1. Linear Load Dynamics

The linear increment in both P and Q at Gombe, Jos and Kano buses of the 28-bus NGP are presented in Tables 4–6, respectively. The results presented in Table 4 show that the lowest power consumption at Gombe bus is 60.0 MW and 70.0 MVar. The power flow solution using the Newton–Raphson method did not converge at this loading point after 100 iterations, implying that any further drop in the load-active power and reactive power would lead to voltage instability. However, maximum dynamic loads of 145.0 MW and 150.0 MVar were recorded at Gombe bus, as shown in Table 4.

**Table 4.** Linear load dynamics at Gombe bus in the 28-bus NGP.

| Bus Name | Critical Line | | Load Dynamics | | NVSP | Voltage Mag. (p.u) |
|---|---|---|---|---|---|---|
| | From | To | Active Power, P, (MW) | Reactive Power, Q, (MVar) | | |
| Gombe | Gombe | Jos | 60.0 | 70.0 | Non-convergence | - |
| | | | 90.6 | 50.9 | 0.1242 | 1.174 |
| | | | 95.0 | 105.0 | 0.1284 | 1.155 |
| | | | 100.0 | 110.0 | 0.1331 | 1.134 |
| | | | 105.0 | 115.0 | 0.1385 | 1.112 |
| | | | 125.0 | 135.0 | 0.1711 | 1.000 |
| | | | 145.0 | 150.0 | Non-convergence | - |

**Table 5.** Linear load dynamics at Jos bus in the 28-bus NGP.

| Bus Name | Critical line | | Load Dynamics | | NVSP | Voltage Mag. (p.u) |
|---|---|---|---|---|---|---|
| | From | To | Active Power, P, (MW) | Reactive Power, Q, (MVar) | | |
| Jos | Gombe | Jos | 40.3 | 55.7 | 0.1372 | 1.140 |
| | | | 30.3 | 45.7 | 0.1079 | 1.161 |
| | | | 20.0 | 25.7 | 0.0567 | 1.195 |
| | | | 10.0 | 10.0 | 0.0210 | 1.221 |
| | | | 100.0 | 85.0 | 0.2604 | 1.042 |
| | | | 120.0 | 105.0 | 0.3936 | 0.962 |
| | | | 140.0 | 125.0 | Non-convergence | - |

**Table 6.** Linear load dynamics at Kano bus in the 28-bus NGP.

| Bus Name | Critical Line | | Load Dynamics | | NVSP | Voltage Mag. (p.u) |
|---|---|---|---|---|---|---|
| | From | To | Active Power, P, (MW) | Reactive Power, Q, (MVar) | | |
| Kano | Kaduna | Kano | 50.6 | 40.0 | Non-convergence | - |
| | | | 80.6 | 90.9 | 0.2091 | 1.112 |
| | | | 100.0 | 120.0 | 0.2848 | 1.068 |
| | | | 150.0 | 120.0 | 0.3206 | 1.033 |
| | | | 250.0 | 150.0 | 0.4006 | 0.933 |
| | | | 350.0 | 250.0 | Non-convergence | - |

According to the results presented in Table 5, the Jos bus is relatively stable, even at the lowest load consumption. However, a shunt reactor should be installed at the Jos bus to prevent cases of overvoltage, especially during the lowest power consumption period. In the same vein, the maximum active power and reactive power at the Jos bus are 140 MW and 125 MVar, respectively.

As shown in Table 6, the lowest stable power consumptions at Kano bus are 50.6 MW and 40.9 MVar for active power and reactive power, respectively. The maximum linear load dynamics before instability are 350 MW and 250 MVar for active and reactive power, respectively.

#### 4.4.2. Non-Linear Dynamic Load

An evident load disagreement pattern often occurs when a surge in reactive power load occurs as a result of a massive drop in active power load and vice-versa. The results obtained from the non-linear load dynamic on the critical P-Q buses of the 28-bus NGP are presented in Tables 7–9. The Gombe bus was subjected to various incoherent loading patterns of active and reactive power, and the stability of the NGP was evaluated accordingly. The results presented in Table 7 depict voltage instability at Gombe bus during an uneven loading pattern of 40.0 MW and 200 MVar.

**Table 7.** Non-linear load dynamics at Gombe bus in the 28-bus NGP.

| Bus Name | Critical Line | | Load Dynamics | | NVSP | Voltage Mag. (p.u) |
|---|---|---|---|---|---|---|
| | From | To | Active Power, P, (MW) | Reactive Power, Q, (MVar) | | |
| Gombe | Gombe | Jos | 50.6 | 120.9 | 0.1291 | 1.152 |
| | | | 170.6 | 40.9 | 0.1119 | 1.237 |
| | | | 250.6 | 20.9 | 0.1278 | 1.157 |
| | | | 40.0 | 200.0 | Non-convergence | - |

**Table 8.** Non-linear load dynamics at Jos bus in the 28-bus NGP.

| Bus Name | Critical Line | | Load Dynamics | | NVSP | Voltage Mag. (p.u) |
|---|---|---|---|---|---|---|
| | From | To | Active Power, P, (MW) | Reactive Power, Q, (MVar) | | |
| Jos | Gombe | Jos | 30.0 | 90.7 | 0.2511 | 1.086 |
| | | | 20.0 | 100.7 | 0.2868 | 1.073 |
| | | | 10.0 | 250.7 | Non-convergence | - |
| | | | 150.0 | 30.7 | 0.0815 | 1.050 |
| | | | 350.0 | 20.0 | Non-convergence | - |

**Table 9.** The non-linear load dynamics at Kano bus in the 28-bus NGP.

| Bus Name | Critical Line | | Load Dynamics | | NVSP | Voltage Mag. (p.u) |
|---|---|---|---|---|---|---|
| | From | To | Active Power, P, (MW) | Reactive Power, Q, (MVar) | | |
| Kano | Kaduna | Kano | 90.6 | 182.9 | 0.4664 | 0.977 |
| | | | 70.6 | 200.0 | 0.5124 | 0.955 |
| | | | 50.6 | 220.0 | 0.5752 | 0.925 |
| | | | 30.0 | 280.0 | 0.8250 | 0.768 |
| | | | 10.0 | 300.0 | Non-convergence | - |
| | | | 350.0 | 50.0 | 0.1272 | 1.019 |
| | | | 450 | 30.0 | 0.0865 | 0.914 |
| | | | 650 | 20.0 | Non-convergence | - |

After several load permutations at the Jos bus, it was deduced that the nonlinear load pattern combinations that may lead to voltage instability at the Jos bus are 10.0 MW-250.7 MVar and 350.0 MW-20 MVar for the P-Q, as presented in Table 8.

Similarly, Kano bus appeared to be stable under a nonlinear load combination of 450 MW and 30.0 MVar. However, as voltage instability set in, a step in an almost inverse progression of P and Q occurred. As shown in Table 9, load combinations of

650 MW-20.0 MVar and 10.0 MW-300.0 MVar for the P-Q are the unstable load set points for the Kano bus.

### 4.5. Comparison of Past Research Work

Many researchers have assessed the NGP in the last couple of years and suggested ways to improve the stability of the network. However, there is a need to improve on this existing knowledge, which was the motivation for the present study. Oluseyi et al. [11] suggested that Ikeja-west be supported by increasing the injection capacity of the Egbin power plant. However, the issue was addressed through the NVSP by placing the STATCOM device close to the Ikeja-west bus, as shown in Figure 8; this approach was also corroborated by Obi et al. [17]. The NGP contingency ranking results obtained in [18] for the first to fourth rankings were consistent with the NVSP analysis; however, the contingency ranking by the NVSP were more accurate, with a relatively faster computing time. In addition, this research assessed the load dynamics of the NGP. The authors of [10,23,38] recommended that the Gombe bus and Kano bus be changed from radial to ring structures. However, such a transition would be cost-intensive and time-consuming. Similarly, renewable energy incorporation at the weak buses was suggested to improve the stability of power network [39–41]. However, there are some notable problems associated with the injection of renewable energy sources into a power network, such as intermittency, fluctuations, etc. [20].

## 5. Conclusions

In this paper, we presented a novel voltage stability index, the NVSP, for the classification of the 28-bus NGP, 330 kV transmission lines and buses. The classification was based on the vulnerability of each line to voltage collapse for the base and contingency cases. The results presented in Table 1 show that the Ikeja-west–Benin line was the only unstable line in the base case, with an NVSP index value of 0.9672 and a voltage magnitude of 0.997 (p.u). However, the problem was remedied by the installation of a STATCOM at the Ikeja-west bus, which improved the voltage stability of the line to an NVSP index value of 0.7621, as presented in Figure 8, with the voltage magnitude enhanced to 1.023 (p.u). A contingency analysis was carried out to evaluate the loadability of the P-Q buses of the 28-bus, 330 kV NGP. The Gombe, Jos and Kano P-Q buses were ranked as the most critical buses, with a maximum reactive power limit of 100.9 MVar, 142.9 MVar and 210.9 MVar, respectively. The most stable P-Q buses are Aja, Alaoji, Aladja and Akangba, with a maximum reactive power limit of 6005.58 MVar, 3820.2 MVar, 2972.4 MVar and 2,0508 MVar, respectively. Furthermore, the results obtained in this research show that (1) the installation of injection substations close to the flagged points will reduce the number possible blackouts, especially at Gombe, Jos and Kano buses; (2) increasing the power generation capacity from the Shiroro plant will also help to prevent the P-Q buses at these critical buses from operating close to their maximum capacity limit; and (3) the load at the P-Q buses for the critical buses—Gombe, Jos and Kano—could be optimally shed, especially during peak load hours, to maintain the stability of the NGP.

**Author Contributions:** Formal analysis, N.I.N.; Software, T.U.B., S.L.G. and N.I.N.; Validation, S.L.G.; Writing—original draft, T.U.B. and F.K.A.; Writing—review & editing, S.L.G. All authors have read and agreed to the published version of the manuscript.

**Funding:** This research received no external funding.

**Data Availability Statement:** All data used in this research have been adequately declared.

**Conflicts of Interest:** The authors declare no conflict of interest.

## Appendix A

The NGP 28-bus, 330-kV bus and line data are presented in Tables A1 and A2, respectively, as declared in [42]. The Table A3 presents the results of the 28-bus NGP transmission line flow and losses using Newton-Raphson power flow solution technique in 2018a MATLAB environment.

**Table A1.** Bus data of the 330-kV, 28-bus Nigerian power network [42].

| Bus No. | Bus Name | Bus Code | Voltage Mag. PU | Angle Degree | Load | | Generation | |
|---|---|---|---|---|---|---|---|---|
| | | | | | MW | MVAr | MW | MVAr |
| 1 | Egbin | 1 | 1.05 | 0 | 68.9 | 51.7 | 251.538 | 641.299 |
| 2 | Delta | 2 | 1.05 | 15.424 | 0 | 0 | 670 | 82.628 |
| 3 | Aja | 0 | 1.04 | −0.57 | 274.4 | 205.8 | 0 | 0 |
| 4 | Akangba | 0 | 0.94 | 0.482 | 344.7 | 258.5 | 0 | 0 |
| 5 | Ikeja-west | 0 | 0.986 | 1.408 | 633.2 | 474.9 | 0 | 0 |
| 6 | Ajaokuta | 0 | 1.026 | 8.739 | 13.8 | 10.3 | 0 | 0 |
| 7 | Aladja | 0 | 1.046 | 14.04 | 96.5 | 72.4 | 0 | 0 |
| 8 | Benin | 0 | 1.011 | 9.306 | 383.4 | 287.5 | 0 | 0 |
| 9 | Ayede | 0 | 0.932 | 2.335 | 275.8 | 206.8 | 0 | 0 |
| 10 | Osogbo | 0 | 0.966 | 8.642 | 201.2 | 150.9 | 0 | 0 |
| 11 | Afam | 2 | 1.05 | 13.273 | 52.5 | 39.4 | 431 | 0 |
| 12 | Alaoji | 0 | 1.007 | 12.057 | 427 | 320.2 | 0 | 0 |
| 13 | New Haven | 0 | 0.905 | 3.322 | 177.9 | 133.4 | 0 | 0 |
| 14 | Onitsha | 0 | 0.949 | 6.268 | 184.6 | 138.4 | 0 | 0 |
| 15 | Birnin-Kebbi | 0 | 1.01 | 26.299 | 114.5 | 85.9 | 0 | 0 |
| 16 | Gombe | 0 | 0.844 | 4.905 | 130.6 | 97.9 | 0 | 0 |
| 17 | Jebba | 0 | 1.046 | 25.523 | 11 | 8.2 | 0 | 0 |
| 18 | Jebba GS | 2 | 1.05 | 26.022 | 0 | 0 | 495 | 159.231 |
| 19 | Jos | 0 | 0.93 | 12.901 | 70.3 | 52.7 | 0 | 0 |
| 20 | Kaduna | 0 | 0.951 | 8.791 | 193 | 144.7 | 0 | 0 |
| 21 | Kainji | 2 | 1.05 | 31.819 | 7.5 | 5.2 | 624.7 | −65.319 |
| 22 | Kano | 0 | 0.818 | −1.562 | 220.6 | 142.9 | 0 | 0 |
| 23 | Shiroro | 2 | 1.05 | 13.47 | 70.3 | 36.1 | 388.9 | 508.034 |
| 24 | Sapele | 2 | 1.05 | 12.015 | 20.6 | 15.4 | 190.3 | 283.405 |
| 25 | Calabar | 0 | 0.951 | 21.703 | 110 | 89 | 0 | 0 |
| 26 | Katampe | 0 | 1 | 9.242 | 290.1 | 145 | 0 | 0 |
| 27 | Okapi | 2 | 1.05 | 46.869 | 0 | 0 | 750 | 193.093 |
| 28 | AES-GS | 2 | 1.05 | 5.871 | 0 | 0 | 750 | 488.128 |

**Table A2.** Line data of the 330-kV, 28-bus NGP [42].

| Line No | From Bus | Bus Name | To Bus | Bus Name | R (pu) | X (pu) | Susceptance B (pu) |
|---|---|---|---|---|---|---|---|
| 1 | 3 | Aja | 1 | Egbin | 0.00066 | 0.00446 | 0.06627 |
| 2 | 4 | Akangba | 5 | Ikeja-west | 0.0007 | 0.00518 | 0.06494 |
| 3 | 1 | Egbin | 5 | Ikeja-west | 0.00254 | 0.01728 | 0.25680 |
| 4 | 5 | Ikeja-west | 8 | Benin | 0.01100 | 0.08280 | 0.40572 |
| 5 | 5 | Ikeja-west | 9 | Ayede | 0.00540 | 0.04050 | 0.00000 |
| 6 | 5 | Ikeja-west | 10 | Osogbo | 0.01033 | 0.07682 | 0.96261 |
| 7 | 6 | Ajaokuta | 8 | Benin | 0.00799 | 0.05434 | 0.80769 |
| 8 | 2 | Delta | 8 | Benin | 0.00438 | 0.03261 | 0.40572 |
| 9 | 2 | Delta | 7 | Aladja | 0.00123 | 0.00914 | 0.1146 |
| 10 | 7 | Aladja | 24 | Sapele | 0.00258 | 0.01920 | 0.24065 |
| 11 | 8 | Benin | 14 | Onitsha | 0.00561 | 0.04176 | 0.52332 |
| 12 | 8 | Benin | 10 | Osogbo | 0.01029 | 0.07651 | 0.95879 |
| 13 | 8 | Benin | 24 | Sapele | 0.00205 | 0.01393 | 0.2071 |

**Table A2.** *Cont.*

| Line No | From Bus | Bus Name | To Bus | Bus Name | R (pu) | X (pu) | Susceptance B (pu) |
|---|---|---|---|---|---|---|---|
| 14 | 9 | Ayede | 10 | Osogbo | 0.00471 | 0.03506 | 0.43928 |
| 15 | 15 | Birnin | 21 | Kanji | 0.01271 | 0.09450 | 1.18416 |
| 16 | 10 | Osogbo | 17 | Jebb TS | 0.00643 | 0.04786 | 0.59972 |
| 17 | 11 | AFAM | 12 | Alaoji | 0.00102 | 0.00697 | 0.10355 |
| 18 | 12 | Alaoji | 14 | Onitsha | 0.00566 | 0.04207 | 0.52714 |
| 19 | 13 | New Haven | 14 | Onitsha | 0.00393 | 0.02926 | 0.36671 |
| 20 | 16 | Gombe | 19 | Jos | 0.01082 | 0.08048 | 1.00844 |
| 21 | 17 | Jebb TS | 18 | Jebb CS | 0.00033 | 0.00223 | 0.03314 |
| 22 | 17 | Jebb TS | 23 | Shiroro | 0.01000 | 0.07438 | 0.93205 |
| 23 | 17 | Jebb TS | 21 | Kanji | 0.00332 | 0.02469 | 0.30941 |
| 24 | 19 | Jos | 20 | Kaduna | 0.00803 | 0.05975 | 0.74869 |
| 25 | 20 | Kaduna | 22 | Kano | 0.00943 | 0.07011 | 0.87857 |
| 26 | 20 | Kaduna | 23 | Shiroro | 0.00393 | 0.02926 | 0.36671 |
| 27 | 23 | Shiroro | 26 | Katempe | 0.00614 | 0.04180 | 0.6213 |
| 28 | 12 | Alaoji | 25 | Calabar | 0.0071 | 0.0532 | 0.38 |
| 29 | 14 | Onitsha | 27 | Okpai | 0.00213 | 0.01449 | 0.21538 |
| 30 | 25 | Calabar | 27 | Okpai | 0.0079 | 0.0591 | 0.39000 |
| 31 | 5 | Ikeja-west | 28 | AES GS | 0.00160 | 0.01180 | 0.09320 |

**Table A3.** The 28-bus NGP transmission line flow and losses determined by the Newton–Raphson method in the MATLAB environment.

| Line | | Power at Bus and Line Flow | | | Line Loss | |
|---|---|---|---|---|---|---|
| From | To | MW | MVar | MVA | MW | MVar |
| 3 | 1 | −274.40 | −298.70 | 405.60 | | |
| 1 | 3 | 275.41 | 305.54 | 411.35 | 1.01 | 6.85 |
| 4 | 5 | −344.70 | −352.55 | 493.06 | | |
| 5 | 4 | 346.56 | 366.29 | 504.25 | 1.86 | 13.74 |
| 1 | 5 | −113.49 | 450.74 | 464.81 | | |
| 5 | 1 | 118.47 | −416.88 | 433.39 | 4.98 | 33.86 |
| 5 | 8 | −303.38 | 23.23 | 304.27 | | |
| 8 | 5 | 314.00 | 56.74 | 319.09 | 10.62 | 79.98 |
| 5 | 9 | 38.70 | 161.33 | 165.91 | | |
| 9 | 5 | −37.15 | −149.70 | 154.24 | 1.55 | 11.63 |
| 5 | 10 | −96.20 | 24.86 | 99.36 | | |
| 10 | 5 | 97.26 | −16.95 | 98.73 | 1.06 | 7.91 |
| 6 | 8 | −13.80 | 81.69 | 82.84 | | |
| 8 | 6 | 14.28 | −78.41 | 79.70 | 0.48 | 3.27 |
| 2 | 8 | 346.98 | 45.52 | 367.81 | | |
| 8 | 2 | −359.61 | −5.50 | 359.65 | 5.37 | 40.01 |
| 2 | 7 | 305.02 | −0.25 | 305.02 | | |
| 7 | 2 | −303.98 | 7.97 | 304.8 | 1.04 | 7.71 |
| 7 | 24 | 207.48 | −41.44 | 211.58 | | |
| 24 | 7 | −206.43 | 49.28 | 212.23 | 1.05 | 7.84 |
| 8 | 14 | −214.11 | 36.33 | 217.17 | | |
| 14 | 8 | 216.62 | −17.64 | 217.34 | 2.51 | 18.68 |
| 8 | 10 | 235.22 | 60.61 | 242.90 | | |
| 10 | 8 | −229.46 | −17.78 | 230.15 | 5.76 | 42.82 |
| 8 | 24 | −373.19 | −108.52 | 388.65 | | |
| 24 | 8 | 376.13 | 128.48 | 397.47 | 2.94 | 19.96 |
| 9 | 10 | −238.65 | −120.71 | 267.44 | | |
| 10 | 9 | 242.72 | 150.98 | 285.84 | 4.07 | 30.27 |

**Table A3.** *Cont.*

| Line | | Power at Bus and Line Flow | | | Line Loss | |
|---|---|---|---|---|---|---|
| **From** | **To** | **MW** | **MVar** | **MVA** | **MW** | **MVar** |
| 15 | 21 | −114.50 | 51.20 | 125.43 | | |
| 21 | 15 | 116.23 | −38.36 | 122.39 | 1.73 | 12.84 |
| 10 | 17 | −311.72 | −87.00 | 323.63 | | |
| 17 | 10 | 318.84 | 139.97 | 348.20 | 7.12 | 52.92 |
| 11 | 12 | 378.50 | 237.22 | 446.69 | | |
| 12 | 11 | −376.65 | −224.60 | 438.54 | 1.85 | 12.61 |
| 12 | 14 | −21.86 | 11.22 | 24.57 | | |
| 14 | 12 | 21.89 | −10.98 | 24.49 | 0.03 | 0.24 |
| 13 | 14 | −177.90 | −97.42 | 202.83 | | |
| 14 | 13 | 179.55 | 109.69 | 210.40 | 1.65 | 12.27 |
| 16 | 19 | −130.60 | 31.39 | 134.32 | | |
| 19 | 16 | 132.12 | −20.07 | 133.64 | 1.52 | 11.33 |
| 17 | 18 | −494.24 | −81.23 | 500.88 | | |
| 18 | 17 | 495.00 | 86.34 | 502.47 | 0.76 | 5.11 |
| 17 | 23 | 657.81 | 57.55 | 660.32 | | |
| 23 | 17 | −618.00 | 238.49 | 662.43 | 39.80 | 296.04 |
| 17 | 21 | −493.40 | 80.85 | 499.98 | | |
| 21 | 17 | 500.97 | −24.51 | 501.57 | 7.58 | 56.34 |
| 19 | 20 | −202.42 | 190.37 | 277.88 | | |
| 20 | 19 | 207.31 | −154.02 | 258.26 | 4.89 | 36.35 |
| 20 | 22 | 225.83 | 98.96 | 246.56 | | |
| 20 | 23 | −6.26.14 | 128.94 | 639.28 | | |
| 23 | 20 | 640.79 | −19.86 | 641.10 | 14.65 | 109.08 |
| 23 | 26 | 295.82 | 123.03 | 320.38 | | |
| 26 | 23 | −290.10 | −84.12 | 302.05 | 5.72 | 38.92 |
| 12 | 25 | −28.49 | 0.58 | 28.50 | | |
| 25 | 12 | 28.54 | −0.18 | 28.54 | 0.05 | 0.41 |
| 14 | 27 | −602.66 | −47.11 | 604.50 | | |
| 27 | 14 | 610.03 | 97.27 | 617.74 | 7.34 | 50.15 |
| 25 | 27 | −138.54 | −6.72 | 138.71 | | |
| 27 | 25 | 139.97 | 17.38 | 141.04 | 1.43 | 10.66 |
| 5 | 28 | −737.35 | −462.82 | 870.57 | | |
| 28 | 5 | 750 | 556.13 | 933.69 | 12.65 | 93.31 |
| | | TOTAL LOSS | | | 158.32 | 1162.06 |

## References


1. Al-Shaalan, A.M. Essential aspects of power system planning in developing countries. *J. King Saud Univ.-Eng. Sci.* **2011**, *23*, 27–32. [CrossRef]
2. Saccomanno, F. Frequency and active power control. In *Electric Power Systems: Analysis and Control*; IEEE: Piscataway, NJ, USA, 2003; Chapter 3; pp. 173–288. [CrossRef]
3. Eremia, M.; Shahidehpour, M. Voltage and reactive power control. In *Handbook of Electrical Power System Dynamics: Modeling, Stability and Control*; IEEE: Piscataway, NJ, USA, 2013; pp. 340–450. [CrossRef]
4. Hatziargyriou, N.; Rahmann, C.; Canizares, C.; Hisken, I.; Pourbeik, P.; Cutsem, T. Definition and Classification of Power System Stability—Revisited & Extended. *IEEE Trans. Power Syst.* **2021**, *36*, 3271–3281. [CrossRef]
5. National Electricity Regulation Commission. Peak Daily Electricity Generation. Available online: http://nerc.gov.ng/index.php/library/industry-statistics/generation/379-peak#graph (accessed on 15 July 2022).
6. Transmission Company of Nigeria. *Annual Technical Report*; Transmission Company of Nigeria: Abuja, Nigeria, December 2017.
7. The World Bank. Global Electrification Database, SDG 7: The Energy Report. (Access to electricity (% of population)—Nigeria). Available online: https://data.worldbank.org/indicator/EG.ELC.ACCS.Zs?locations=NG (accessed on 27 August 2022).
8. Akwukwaegbu, I.O.; Izuegbunam, F.I.; Ndinechi, M.C. Voltage stability analysis of 86-bus 330kV Nigeria power grid based on reserved energy potential via continuation power flow technique. *Int. J. Res. Technol. IJERT* **2021**, *10*. [CrossRef]
9. Adebanji, B.; Ojo, A.; Fasina, T.; Adeleye, S.; Abere, J. Integration of renewable energy with smart grid application into the Nigeria's power network: Issues, challenges and Opportunities. *Eur. J. Eng. Technol. Res.* **2022**, *7*, 18–24. [CrossRef]
10. Abdulkareem, A.; Somefun, T.E.; Awosope, C.O.A.; Olabenjo, O. Power system analysis and integration of the proposed Nigerian 750-kV power line to the grid reliability. *SN Appl. Sci.* **2021**, *3*, 846. [CrossRef]

11. Oluseyi, P.O.; Adelaja, T.S.; Akinbulire, T.O. Analysis of the transient stability limit of Nigeria's 330 kV transmission sub-network. *Niger. J. Technol. NIJOTECH* **2017**, *36*, 213–226. [CrossRef]
12. Ayamolowo, O.; Elutunji, B.; Salau, A.; Dada, J. Nigeria Electricity Power Supply System: The Past, Present and the Future. In Proceedings of the IEEE PES/IAS PowerAfrica Project, Abuja, Nigeria, 20–23 August 2019. [CrossRef]
13. Akuru, U.B.; Okoro, O.I. Economic implication of constant power outages on SMEs in Nigeria. *J. Energy S. Afr.* **2022**, *25*, 61–66. [CrossRef]
14. Blackout as National Grid Suffers Collapse—Fifth Time in 2022. The Cable Newspaper. Available online: https://www.thecable.ng/blackout-as-national-grid-suffers-collapse-second-in-less-than-three-months/amp (accessed on 15 June 2022).
15. Pani, S.R.; Samal, R.K. Vulnerability Assessment of Power System Under N-1 Contingency Conditions. In Proceedings of the 2022 Second International Conference on Power, Control and Computing Technologies (ICPC2T), Raipur, India, 1–3 March 2022; pp. 1–4. [CrossRef]
16. Ramirez-Gonzalez, M.; Sevilla, S.F.R.; Korba, P. Convolutional neural network based approach for static security assessment of power systems. In Proceedings of the 2021 World Automation Congress (WAC), Taipei, Taiwan, 1–5 August 2021; pp. 106–110. [CrossRef]
17. Obi, P.I.; Ulas, J.A.; Offor, K.J.; Chidolue, G.C. Improving electric power quality in Nigerian existing 330kV 28 bus electric power systems using static var compensator system. *Int. J. Eng. Res. Technol.* **2013**, *2*, 1–7.
18. Adebayo, I.; Jimoh, A.; Yusuff, A. Techniques for the Identification of Critical Nodes Leading to Voltage Collapse in a Power System. *Int. J. Emerg. Electr. Power Syst.* **2018**, *19*, 20170129. [CrossRef]
19. Reissner, F.; Yin, H.; Weiss, G. A Stability Result for Network Reduced Power Systems Using Virtual Friction and Inertia. *IEEE Trans. Smart Grid* **2022**, *13*, 1668–1678. [CrossRef]
20. Kasis, A.; Timotheou, S.; Polycarpou, M. Stability of power networks with time-varying inertia. In Proceedings of the 2021 60th IEEE Conference on Decision and Control (CDC), Austin, TX, USA, 14–17 December 2021; pp. 2788–2793. [CrossRef]
21. Heidari Yazdi, S.S.; Rahimi, T.; Khadem Haghighian, S.; Bagheri, M.; Gharehpetian, G.B. Over-Voltage Regulation of Distribution Networks by Coordinated Operation of PV Inverters and Demand Side Management Program. *Front. Energy Res.* **2022**, *10*, 738. [CrossRef]
22. Narimani, M.R.; Huang, H.; Ummunakwe, A.; Mao, Z.; Sahu, A.; Zonouz, S.; Davis, K. Generalized contingency analysis based on graph theory and line outage distribution factor. *IEEE Syst. J.* **2022**, *16*, 626–636. [CrossRef]
23. Randey, A.; Agarwal, A.; Jereminov, M.; Nwachuku, T.; Rawn, B.; Pileggi, L. Improving voltage profile of the Nigerian Power Grid. IEEE PowerAfrica 2019. *arXiv* **2019**, arXiv:1905.13090.
24. Nkan, I.E.; Okpo, E.E.; Okoro, O.I. Multi-type FACTS controllers for power system compensation: A case study of the Nigerian 48-Bus, 330kV System. *Niger. J. Technol. Dev.* **2021**, *18*, 63–69. [CrossRef]
25. Airoboman, E.; James, P.; Araga, I.A.; Wamdeo, C.L.; Okakwu, I.K. Contingency Analysis on the Nigerian Power Systems Network. In Proceedings of the 2019 IEEE PES/IAS PowerAfrica, Abuja, Nigeria, 20–23 August 2019; pp. 70–75. [CrossRef]
26. Liu, S.; Zhao, D.; Fan, W.; Li, T.; Cui, D. The Stability Analysis of a Class of Electric Power Network Model. In Proceedings of the 2021 China International Conference on Electricity Distribution (CICED), Shanghai, China, 7–9 April 2021; pp. 589–593. [CrossRef]
27. Alnasseir, J.; Alcharea, R.; Almaghout, F. Improving the Stability of Smart Grids by Using Flexible AlternatingCurrent Transmission Systems (FACTS). In Proceedings of the 2021 12th International Renewable Engineering Conference (IREC), Amman, Jordan, 14–15 April 2021; pp. 1–3. [CrossRef]
28. Calma, E.R.B.; Pacis, M.C. Artificial Neural Network-based Voltage Stability Analysis of Power Transmission Networks with Distributed Generation using Phasor Measurement Unit Synthetic Data. In Proceedings of the 2021 IEEE 12th Control and System Graduate Research Colloquium (ICSGRC), Shah Alam, Malaysia, 7 August 2021; pp. 1–6. [CrossRef]
29. Collados-Rodriguez, C.; Cheah-Mane, M.; Prieto-Araujo, E.; Gomis-Bellmunt, O. Stability and operation limits of power systems with high penetration of power electronics. *Int. J. Electr. Power Energy Syst.* **2022**, *138*, 107728. [CrossRef]
30. Gbadamosi, S.L.; Nwulu, N.I.; Siano, P. Harmonics constrained Approach to Composite Power System Expansion Planning with Large-Scale Renewable Energy Sources. *Energies* **2020**, *15*, 4070. [CrossRef]
31. Abirami, P.; Ravi, C.N. Enhancing grid stability by maintaining power quality in distribution network using FOPID and ANN controlled shunt active filter. *Environ. Dev. Sustain.* **2022**, *24*, 7551–7578. [CrossRef]
32. Zaheb, H.; Danish, M.S.S.; Senjyu, T.; Ahmadi, M.; Nazari, A.M.; Wali, M.; Khosravy, M.; Mandal, P. A contemporary novel classification of voltage stability indices. *Appl. Sci.* **2020**, *10*, 1639. [CrossRef]
33. Saadat, H. *Power System Analysis*, 4th ed.; McGraw-Hill Series in Electrical and Computer Engineering; McGraw-Hill: New York, NY, USA, 1999; pp. 232–238.
34. Savas, C.; Dovis, F. The impact of different kernel functions on the performance of scintillation detection based on support vector machines. *Sensors* **2019**, *19*, 5219. [CrossRef]
35. Squires, G.L. *Practical Physics*, 4th ed.; Cambridge University Press: Cambridge, UK, 2001; ISBN 978-0-521-77940-1. [CrossRef]
36. Zisserman, A. Lecture 2: The SVM Classifier. C19 Machine Learning, 2015. 2021. Available online: http://www.robots.ox.ac.uk/~{}az/lectures/ml (accessed on 24 August 2022).
37. Amusan, T.O.; Nwulu, N.I.; Gbadamosi, S.L. Identification of Weak Buses for Optimal Load Sheddingusing Differential Evolution. *Sustainability* **2022**, *14*, 3146. [CrossRef]

38. Abdulkareem, A.; Adesanya, A.; Agbetuyi, A.F.; Alayande, A.S. Novel approach to determine unbalanced current circuit on Nigerian 330kV transmission grid for reliability and security enhancement. *Heliyon* **2021**, *7*, e07563. [CrossRef] [PubMed]
39. Gbadamosi, S.L.; Nwulu, N.I. A multi-period composite generation and transmission expansion planning model incorporating renewable energy sources and demand response. *Sustain. Energy Technol. Assess.* **2020**, *26*, 100726. [CrossRef]
40. Gbadamosi, S.L.; Nwulu, N.I. A comparative analysis of generation and transmission expansion planning models for power loss minimization. *Sustain. Energy Grids Netw.* **2022**, *26*, 100456. [CrossRef]
41. Gbadamosi, S.L.; Nwulu, N.I. Reliability assessment of composite generation and transmission expansion planning incorporating renewable energy sources. *J. Renew. Sustain. Energy* **2020**, *12*, 026301. [CrossRef]
42. Samuel, I.A. A New Voltage Stability Index for Predicting Voltage Collapse in Electrical Power System Networks. Ph.D. Thesis, Covenant University, Ota, Ogun State, Nigeria, January 2017.

*energies*

*Article*

# Voltage Stability Control Based on Angular Indexes from Stationary Analysis

**Gabriel J. Lopez *, Jorge W. González, Idi A. Isaac, Hugo A. Cardona and Oscar H. Vasco**

Research Group on Transmission and Distribution of Electric Power, Universidad Pontificia Bolivariana, Medellin 050031, Colombia
* Correspondence: gabriel.lopez@upb.edu.co

**Abstract:** This paper presents a novel methodology for the calculation of angular indexes of an electrical system from stationary analysis, using load flow and nose curves (P–V) in each of the buses of the system to perform control actions and preserve or improve voltage stability. The control actions are proposed considering a novel method based on the concepts of the cutset angle (CA) and center of angle (COA). The target is a fast estimation of voltage-stability margins through an appropriate angular characterization of the whole system and for each load bus with a complete network and N-1 contingency criteria. The most significant enhancement is that the angular characterization is based on the COA, which is related to the angular dynamics of the system, and indirectly reflects the inertia and the respective angles of the generator rotor, as well as the impact on the angular equivalent-system model. Simulations showed that the COA is an important index to determine the location of occurrence of the events. The COA can also help aim where control actions, like the amount of load shedding, should be carried out to remedy the voltage problems. The proposed method is assessed and tested in the benchmark IEEE 39-bus system.

**Keywords:** cutset angle; center of angle; angular index; load flow; voltage stability; angular characterization; IEEE 39-bus system; PMU; synchrophasor; power-system stability

**Citation:** Lopez, G.J.; González, J.W.; Isaac, I.A.; Cardona, H.A.; Vasco, O.H. Voltage Stability Control Based on Angular Indexes from Stationary Analysis. *Energies* **2022**, *15*, 7255. https://doi.org/10.3390/en15197255

Academic Editor: Abu-Siada Ahmed

Received: 6 September 2022
Accepted: 27 September 2022
Published: 2 October 2022



## 1. Introduction

In general, the stability of the power system has been classified from the causes that lead to instability [1,2]. However, any type of instability cannot be caused solely by an angular, voltage, or frequency problem. In highly stressed power systems, one form of instability can give rise to another, even generating cascading events that result in power-system collapses [3].

Although the classification of the stability of the electrical system is effective [1], and the means to face the complexities of the problem are convenient, the global stability of the system must always be the basis for the solution of any category of stability challenges (angle, voltage, or frequency), but not at the expense of affecting another stability category. It is essential to look at all aspects of the stability phenomenon from more than one point of view, inclusively, integrating the bus voltage angles more effectively.

In this article, a methodology is proposed to carry out stability analyses with the criterion of maintaining a safe voltage by applying classical methods of long-term voltage stability [1,2]. By using angular indexes calculated from synchrophasor measurements [3–7], this study aims to develop a wide-area control system as other references have initiated [5,8].

In many cases, static analysis can be used to estimate stability margins, which can be done even more so using Thevenin equivalents alongside loadability curves or control methods [9,10], identify factors that influence stability, and analyze a wide range of system conditions and a large number of scenarios [5,11–13]. When the time of the control actions is important, the analyses must be complemented by quasi-static, dynamic, or transient simulations [14,15].

The contributions of this paper are as follows:

We propose a novel method based on the cutset angle (CA) and center of angle (COA) [16–19] in the field of voltage stability for real-time operations, including bus voltage magnitudes and phase angles as obtained from PMUs. The system framework is simple to implement.

The study proposes a global voltage-stability margin to be estimated for the whole system and for each load bus with a complete network and N-1 contingency criteria. It was observed that the calculation of the indexes, especially the COA, yields the characterization of an electrical power system. It is even possible to determine if a contingency is critical once a detailed prior characterization of the system is available. In addition, the COA proved to be an important index in determining the location of occurrence of events, and where control actions should be carried out to alleviate the voltage problem in this case.

Compared with previous work [20], the most significant enhancement is that our angular characterization is based on the COA, which is related to the angular dynamics of the system, and indirectly reflects the inertia and the respective angles of the generator rotor, as well as the impact on the angular equivalent-system model [21,22]; this helps to carry out control actions based on load shedding and COA characterization to avoid voltage instabilities. This method can be applied to systems with a high penetration of renewables because a wide variety of controls that emulate inertia are currently being proposed [23–26].

The proposed methodology is promissory for the multiplicity of wide-area applications. Reference [20] does not include equivalent angles that allow for the characterization of the system to take control actions and keep voltage stability; the general proposal in [20] is to evaluate angle severity and thresholds that are obtained by considering the bulk transfer of power throughout the area, as limited by overloads of lines inside the area [20].

The proposed method here is assessed in the benchmark IEEE 39-bus system. The simulation results demonstrate an accurate evaluation with a significantly reduced system-response time.

Section 2 introduces some basic concepts of voltage-stability theory, P–V curves, recommended actions to improve voltage profiles in an electrical system, and the calculation of angular indexes. Sections 3 and 4 present a methodology and its application for the calculation of indexes with stationary analysis. Section 5 proposes a methodology for applying control actions based on angular indexes, Section 6 shows the simulations, and Section 7 shows the results obtained using the proposed methodology. The last section includes the conclusions.

## 2. Voltage Stability, Controls, and Indexes

Voltage stability can be classified as a short-term or long-term phenomenon. The study-time horizon for this type of problem can vary from a few seconds to tens of minutes [1].

Long-term voltage stability involves slow-acting equipment, such as transformers with load tap changers (LTCs), thermostatically controlled loads, and generator current limiters (OXLs or Overexcitation Limiters). The study time can extend to several or many minutes, and long-term simulations are required for the analysis of the dynamic performance of the system.

### *2.1. Power-System Voltage Stability*

It should be noted that the action time varies for different control measures. In general, in order to achieve a long-term balance in voltage, the load can be restored to a constant power type by the voltage controlling action of LTCs. The amount of power recovery, which in turn satisfies an allowable voltage band, depends on the voltage setpoint on the LTC. Sometimes, the load amount will even have to be reduced.

The pre- and post-contingency PV curves are presented in Figure 1 with solid lines. The pre-contingency operating point is A and the demand corresponding to that point is PA. Long-term (constant power type) curves or characteristics are shown as vertical dashed lines and the short-term equivalent are shown as quadratic dashed lines. P–V curves play a prominent role in understanding and explaining voltage instability; it could be said that they are the most used worldwide for these analyses [4,12,14,27–29].

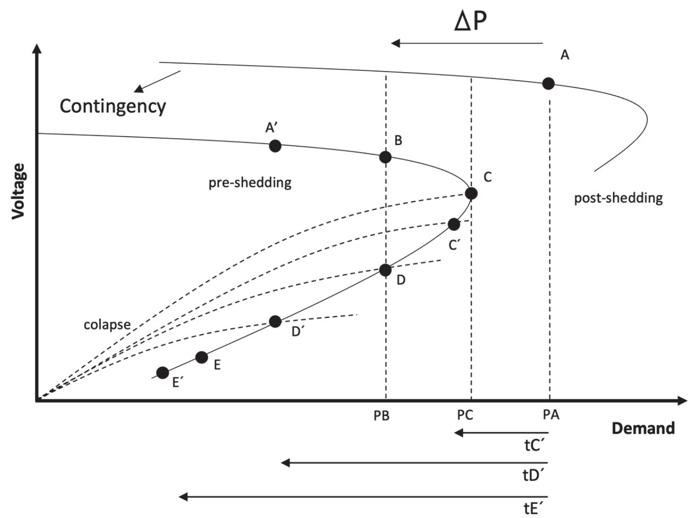


**Figure 1.** Load shedding effect after a contingency [4].

In the event of a contingency, there will be long-term instability at operating point A, because the demand PA is greater than the maximum power PC. By varying the LTC setpoint and shedding a load amount, it is possible to consolidate the new operating point B.

Load shedding is a case similar to load reduction through LTC with an extra complexity, as load is shed to improve the long-term characteristic, while the short-term characteristic also changes. This allows a little more time to perform control actions. The analysis is limited to the goal of restoring stable equilibrium, but the results also apply to the goal of stopping system degradation.

The load-shedding effect can be seen in Figure 1, where a restoration is assumed, by the action of the power system to the type of constant power load. When the amount of load shed is the minimum, PA–PC, the time limit for the restoration of an equilibrium is tC′, which is the time required for the short-term characteristic to reach point C′, so that the short-term load characteristic after shedding moves through point C. After time tC′, the value of the load to be shed increases. This is also true for the difference between the short-term characteristics for pre- and post-shedding. Therefore, load is shed at PA–PB, the time limit to restore stability at B is tD′ where point D′ corresponds to the short-term pre-shedding characteristic, so that the post-shedding feature moves toward point D.

Finally, it has to be noticed that the time tE, which is the last limit for control actions, remains unchanged because at E, the system is unstable.

Short-term voltage instability lasts a few seconds, whereas long-term voltage instability can last some minutes. Both are generally considered to be relatively quick for control actions to be undertaken. However, the time it takes for long-term instability, while it is short for an operator action, is long enough for an efficient code to run and scan the problem, warn the operator, and propose or apply corrective actions.

## 2.2. *Angular Indexes*

The cutset angle and the central angle are special angular indexes proposed and discussed in [16–19,30–32].

Cutset angles/areas conjugate plenty of angular measurements in a grid. This method yields weighted angles and the susceptance among two areas [16]. A Krön reduction has to be applied [33] to yield an effective relation between two areas as a function of the power flows and transmission line susceptance/angles in the boundary nodes of the system.

Figure 2 shows a basic diagram in which the equations of the cutset angle are explained.

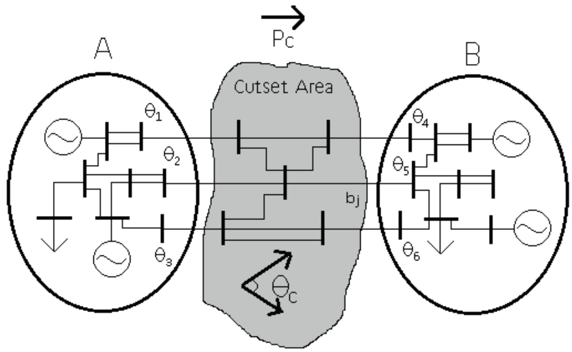


**Figure 2.** Cutset angle between two areas.

Figure 2 shows two areas named A and B, divided by lines denominated "cutset lines" in the cutset area [16] This cutset area is spread out all over the network. Equations (1)–(3) are obtained by dc load flow [17]. An AC load-flow solution was used for this study.

$$b_c = \sum\nolimits_{j \in C} b_j, \tag{1}$$

$$\hat{\theta}_c = \sum_{j \in C} \frac{b_j}{b_c} \widehat{\theta}_j, \tag{2}$$

$$P_c = b_c \widehat{\theta}_c, \tag{3}$$

The COA algorithm is based on the calculation of angular differences between busbars of a network, considering a reference angle [16,17,34]. A main objective is to determine transient angular instability. This analysis is related to angular dynamics, which reflects the inertia and the angles of generator rotors, as well as the influence on the angular equivalent-system model. The COA can be interpreted as the center of mass of a body, being a universal reference, with dynamic phenomena. Disturbance could lead the system far from the center of mass, destabilizing the system.

For the proper use of COA concepts, reduction methods are required to relate several areas of a power system based on power flows, transmission line susceptance, and voltage angles in the boundary busbars, as shown in Figure 2.

As mentioned before, the COA is a real-time reference. The variation from the center of inertia of the phase angle can be calculated using the COA as defined in (4) and (5) [35].

$$\delta_{COA} = \frac{\sum_{i=1}^{N} \delta_i H_i}{\sum_{i=1}^{N} H_i}, \tag{4}$$

$$\delta_{COA} = \frac{\sum_{i=1}^{N} \delta_i P_i}{\sum_{i=1}^{N} P_i}, \tag{5}$$

where in the case of generator *i*:
$\delta_i$ is the rotor angle
$H_i$ is the inertia time constant
$N$ is the total number of generators in the areas of the system

$\delta_{COA}$ is the central angle (or "Center of Angle").

As (4) could be complicated for a real-time calculation, it may be useful, for each plant, to estimate the generation units' dispatching power. It should be performed as a function of time to obtain an equivalent H in the areas of the network.

The angle in (4) can be replaced by power injection measurements due to the direct relationship of weighting factor H to the real power injected [6]. As a consequence of the difficulty in measuring the internal angle of the rotor in real time, it is supposed that it has the same tendency as the voltage angle measured in the busbar (if the rotor angle increases or decreases, then the angle bus also increases or decreases, respectively).

It is possible to obtain the angular difference between the rotor and busbar using the internal voltage behind the machine synchronous reactance and produce a replica of the machine angular displacement. Phasor diagrams in Figure 3 provide the latter explanation. The COA calculation is therefore expressed in terms of variables measurable by PMUs.

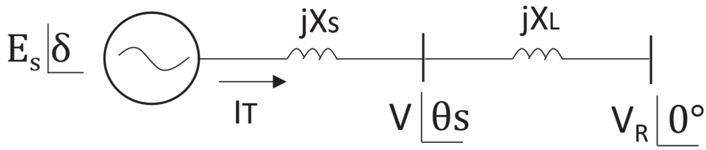


**Figure 3.** Equivalent system diagram (generator and infinite bus).

This system diagram model neglects saliency effects and stator resistance. Therefore, if the saliency is neglected [36]:

$$X_S = X_d = X_q, \tag{6}$$

A voltage law equation must be written around each of the meshes, as follows (see Figure 4):

$$E_s\lfloor\delta = I_T j(X_S + X_L) + V_R\lfloor 0^\circ, \tag{7}$$

$$V\lfloor\theta_s = I_T j(X_L) + V_R\lfloor 0^\circ, \tag{8}$$

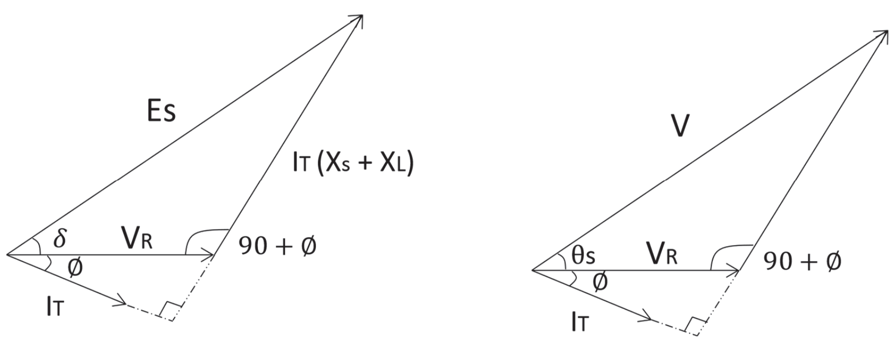


**Figure 4.** Steady-state phasor diagrams for Equations (7) (**left**) and (8) (**right**).

Applying the law of sines and cosines, it is possible to find the relationship between $\delta$ and $\theta g$ (9).

$$\sin\delta = \frac{|V|}{|E_s|}\frac{(X_S + X_L)}{X_L}\sin\theta_s, \tag{9}$$

where

$X_S$ is the synchronous reactance

$X_L$ is the transmission line reactance

$|V|$ is the magnitude of the voltage angle bus

$|E_s|$ is the magnitude of the internal voltage of the synchronous machine

$\delta$ is the internal rotor angle
$\theta_s$ angle bus is measured by PMUs:
where

$$\frac{|V|}{|E_s|}\frac{(X_S + X_L)}{X_L} = K_g, \tag{10}$$

Hence,

$$\sin\delta = k_g \sin\theta_s, \tag{11}$$

And Equation (11) is applicable for small angles:

$$\delta = k_g \theta_s, \tag{12}$$

Finally, Equation (12) clearly shows the relationship between the rotor angle and the bus angle [37]. The tendency of the angle at the terminal machine is proportional to the rotor angle; however, it depends on the relationship between the voltages and reactance of the system (kg factor). Figure 5 shows the tendency of two load conditions.

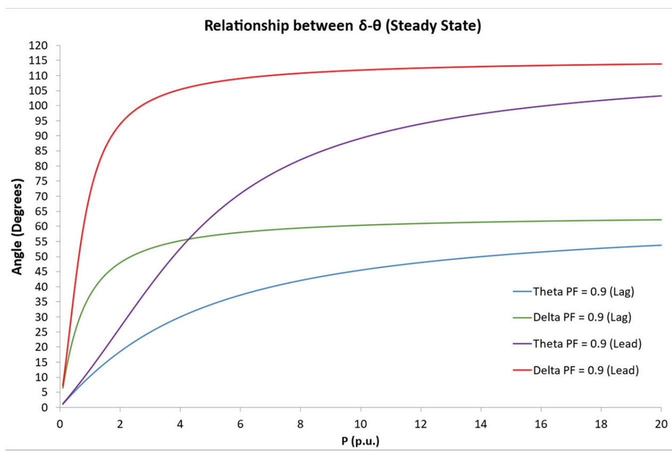


**Figure 5.** Relationship between δ and θ for different load conditions.

For any specific area i of the power system, the center angle is defined in Equation (13). Where $\delta^i_{COA}$ is the central angle for the area $i$, $\delta^i_j$ is the rotor angle of each generator, $P^i_j$ the power injected by the generator, and $N^i$ is the total number of generators in the area $i$.

The global center of inertia can be calculated solving (5).

$$\delta_C = \frac{\sum_{i=1}^{N} \delta^i_{COA} P^i}{\sum_{i=1}^{N} P^i}, \tag{13}$$

where N corresponds to all the areas and $P^i$ belongs to the total power generated in area i.

According to the COA of the system, a heuristic criterion to detect transient instability in real time is addressed. In case that the COA of an area is increased beyond a predetermined value from the center of inertia, it can be interpreted that the area has been separated from the rest of the system. An appropriate corrective action could be to either shed generation or load in this area [18].

It is advisable to develop a detailed characterization of the system in order to appropriate define thresholds for each area of the operation. In the same manner, it is important to clarify that the proposed method is compatible with any network in which inertia is obtained, either from synchronous generator data or from inertia constants emulated by generation integrated by power inverters. Inertia emulation is a feasible function which is even required by some national operators nowadays [23].

## 3. Angular Characterization Methodology with Stationary Analysis

An angular characterization methodology is proposed from load flows (steady state) as mechanisms for taking control actions in the system.

It is proposed to generate safe operation thresholds (V $\geq$ 0.9 p.u.), considering contingencies N-1 for each of the proposed indexes, the central angle (COA) and the cutset angle (AngC).

The proposed methodology has the following stages:

### *3.1. Stage 1*

The load flows and the voltage and load characteristics in each busbar of the electrical power system (P–V or nose curves) are calculated. These curves are obtained for different scenarios and for all possible N-1 contingencies. After that, the known angular indexes are calculated: the cutset angle and the central angle.

### *3.2. Stage 2*

Demand scenarios are established at each intersection of the P–V curve with the safe voltage limit, see Figure 6.

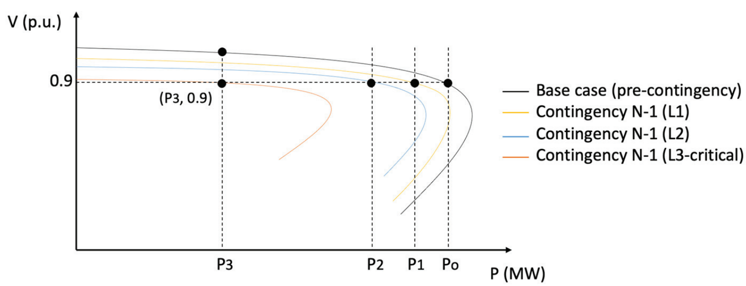


**Figure 6.** Determination of demand scenarios for the voltage limit (0.9 p.u.).

The worst contingency is sought, which is determined by the curve that reaches the lowest demand value: it is assumed that this is the one that exhibits the greatest stress for that particular condition because it represents the scenario that has the least possibility to stress the system in a greater proportion (close to the collapse point). Once the worst contingency has been determined, a vertical line is drawn that intersects the curve at 0.9 p.u., and the demand point (P3 in Figure 6) that ensures the operation limit is found.

Subsequently, using a relationship [P-theta (angular index)], the angles that maintain the voltage within the proposed limits (0.9 p.u.) are calculated, both for the curve of the base scenario and for the scenario of the worst contingency. The intersection of curves with point P3 in Figure 7 can be observed. Subsequently, the delta of the COA index is found. The above procedure is performed for different operating scenarios.

With these angular values, it is suggested to build maximum and minimum limit curves for the operating areas and for each scenario, in which voltages above 0.9 p.u. are ensured and the deltas of the COA are related, see Figure 8. In this way, it is ensured that any contingency N-1 is within the band limited by the maximum and minimum angular values for a specific load demand.

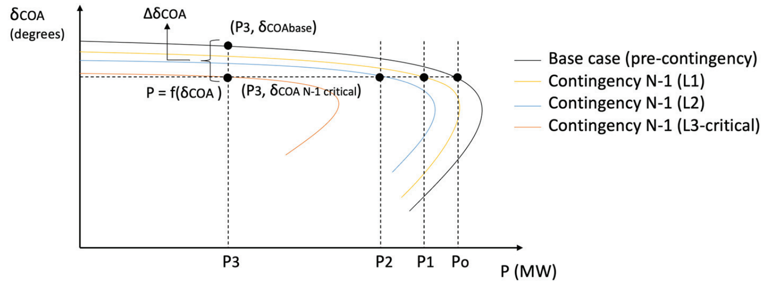


**Figure 7.** Determination of the angular index for different demand scenarios with voltage limit (0.9 p.u.).

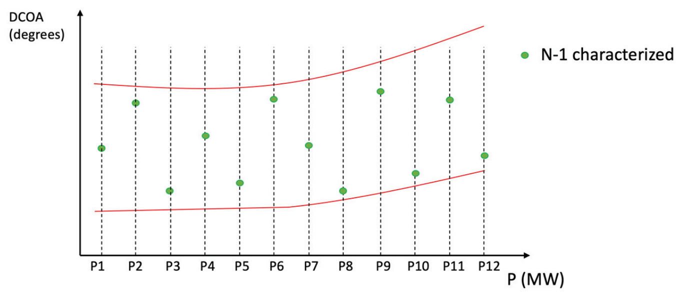


**Figure 8.** Determination of angular thresholds for a demand scenario with contingencies N-1.

### *3.3. Stage 3*

This stage is for angular data collection, with which it is sought to carry out off-line training that allows for a complete characterization of the electrical power system, regardless of its operating or topological conditions.

## **4. Application of Angular Characterization Methodology to the IEEE 39-Bus System**

### *4.1. IEEE 39-Bus System*

The proposed methodology is validated in the IEEE 39-bus System [6]. This system is composed of 10 generators, 19 loads, and 34 lines. The system parameters are taken from the book *Energy Function Analysis for Power System Stability* [36]. In a stable-steady and pre-contingency state with all its elements in normal operation, the system presents a generation of 6140.81 MW and a demand of 6097.10 MW.

This system can be divided into four operational areas in order to perform COA and AngC analyses, as shown in Figure 9.

Table 1 shows the data in normal operation and the pre-contingency for each operative area.

**Table 1.** Data of the operational areas in IEEE 39-bus system.

| Area | Busbars | Generation [MW] | Load [MW] |
|---|---|---|---|
| Area 1 | 1, 2, 3, 18, 25, 30, 37 | 790 | 704 |
| Area 2 | 17, 26, 27, 28, 29, 38 | 830 | 909.5 |
| Area 3 | 4, 5, 6, 7, 8, 9, 10, 11, 12, 13, 31, 32, 39 | 2170.8 | 2376.5 |
| Area 4 | 14, 15, 16, 19, 20, 21, 22, 23, 24, 33, 34, 35, 36 | 2350 | 2107 |

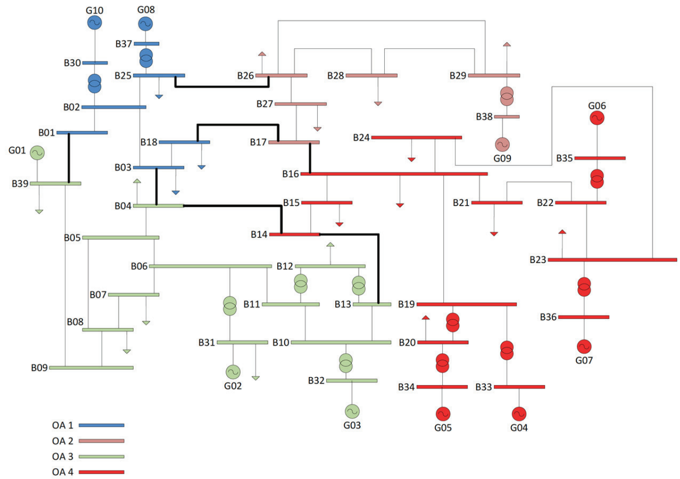


**Figure 9.** IEEE 39-Bus System.

### *4.2. Angular Characterization in IEEE 39-Bus System*

With the help of DIgSILENT PowerFactory software, the P–V curves are calculated for the IEEE 39-bus System, and the indexes are calculated with different scenarios of demand increase in a certain area of the system (area 1, area 2 and area 3, the entire system, etc.). Reactive power limits of generators were considered for P–V curve tracing. This same process is carried out for contingency scenarios N-1; that is, scenarios of increased demand and the unavailability of one element of the system at a time.

It is important to mention that this paper presents the characterization for the central angle COA as little variability was observed for the cutset angle AngC.

Subsequently, for each scenario, the contingency that leads the voltage in any bus of the system to a lower demand is identified (graphically, it would be the P–V curve that first crosses the value of 0.9, see Figure 6). Once the event has been identified, the values of the indexes are captured, in this case the delta of the COA (DCOA, see Figure 7), and the demand and the angular value are obtained, up to which it is ensured that no contingency N-1 causes sub-voltages in the system (see Table 2).

**Table 2.** Parameters of the operational areas in IEEE 39-bus system.

| Area | Load [MW] | DCOA1 [°] | DCOA3 [°] | DCOA4 [°] | DCOA3 [°] |
|---|---|---|---|---|---|
| 1 | 1048.19 | −3.70 | 3.82 | −2.38 | 2.44 |
| 2 | 1008.86 | −1.63 | 4.60 | −4.70 | 3.46 |
| 3 | 2606.78 | −1.86 | 6.11 | −4.88 | 3.47 |
| 4 | 2157.88 | −1.38 | 6.37 | −5.43 | 3.36 |

Finally, the maximum and minimum values of the DCOA indexes are calculated, thus obtaining two final curves depending on the demand for each index, which represent the maximum and minimum values of the DCOA that can be given for different demands of each area of the system (a safe operating band, see Figure 8), which finally represents the operating ranges between which each index would move for the different contingencies N-1 of the system.

In Figures 10–13, the characterization carried out according to the described procedure is shown; that is, the variation for areas 1, 2, 3, and 4 of the DCOA central angle delta index.

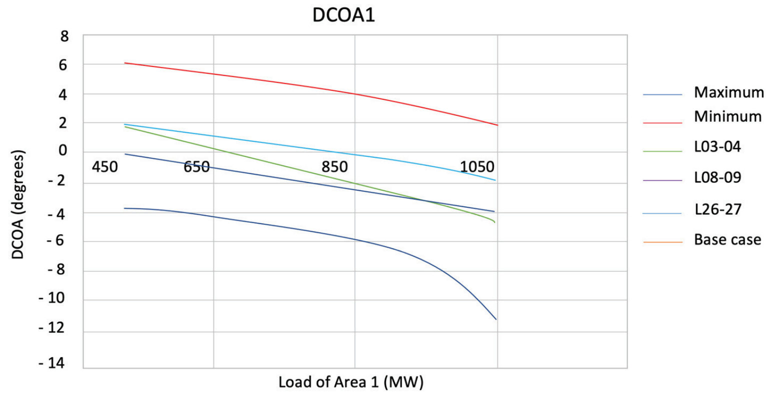


**Figure 10.** Angular characterization for contingencies N-1 in operational area 1.

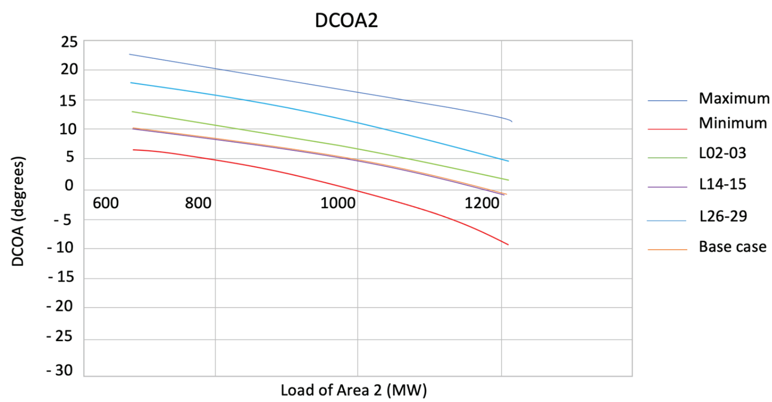


**Figure 11.** Angular characterization for contingencies N-1 in operational area 2.

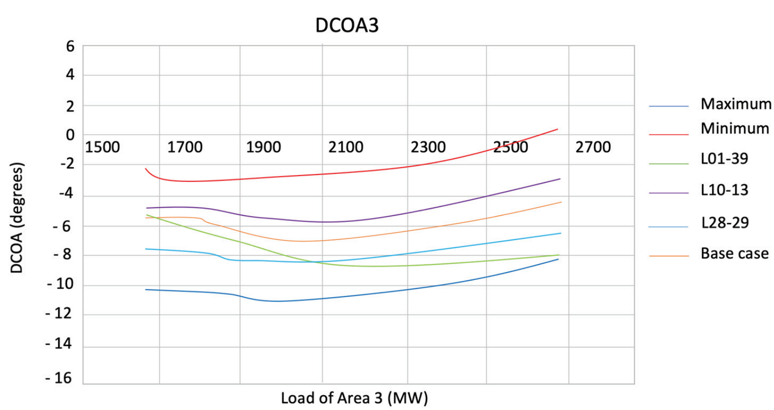


**Figure 12.** Angular characterization for contingencies N-1 in operational area 3.

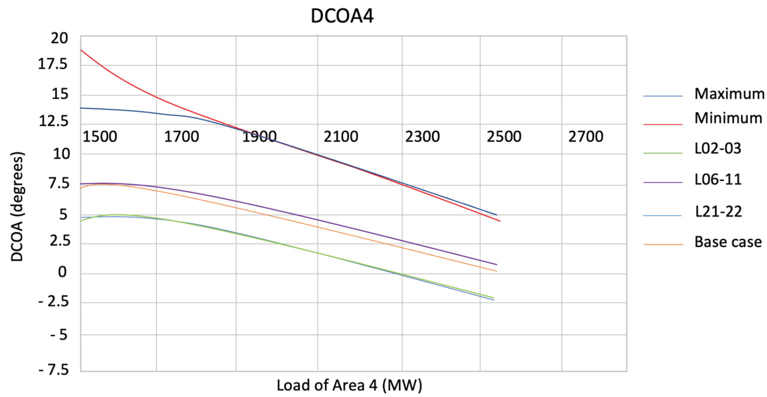


**Figure 13.** Angular characterization for contingencies N-1 in operational area 4.

## 5. Angular Characterization Methodology with Stationary Analysis

To evaluate the possibility of taking control actions through a stationary analysis, a methodology composed of the following stages is proposed:

### *5.1. Stage 1*

This stage intends to carry out a stationary and dynamic analysis of the performance of the indexes for contingencies that were considered critical in the previous angular characterization. Where contingencies such as outages of transmission lines, generators, transformers, and busbars were carried out, the values of the indexes are taken in a stable and dynamic state in order to observe their behavior.

### *5.2. Stage 2*

Once these critical contingencies are found, a load-flow analysis is carried out, and the P–V "nose curve" is plotted for each of them. The load flow shows a non-convergence for the evaluated scenario (because it is a critical contingency scenario). At this point, a dynamic simulation is performed, analyzing the behavior of the voltages and frequencies in the system, and its criticality is verified. It should be clarified that the behavior of the frequency is outside the scope of this methodology because only the voltage stability is being studied. However, it has been verified that, by taking the optimized load shedding and additional generation rejection actions, it is possible to stabilize the behavior of the frequency.

### *5.3. Stage 3*

Subsequently, a load-shedding scheme based on the stationary load-flow analysis is carried out. The methodology to identify the place and percentage of the load to shed is based on the angular characterization, as explained above.

Once the criticality of the event is validated, the most affected operational area is identified by calculating the delta of the COA. This identification is made with the calculation of the deltas that are located outside the limit bands found in the characterization carried out.

In the next stage, the P–V "nose curves" are generated for all of the busbars of the affected area, and the weakest bars are identified due to the contingency performed (the weakest bar is identified with the P–V "nose curve" that reaches a bifurcation or a lower value of voltage). The load-shedding actions in this case are taken as shown in Figure 14, where:

a: Point of maximum power in bus i before non-convergence for the base case.
a′: Safe operating point for the base case.
a″: Safe operating point for the base case. It is the initial condition.
b: Minimum voltage point found for bus i after carrying out the critical contingency from point a″.
b′: Safe operating point for critical contingency.

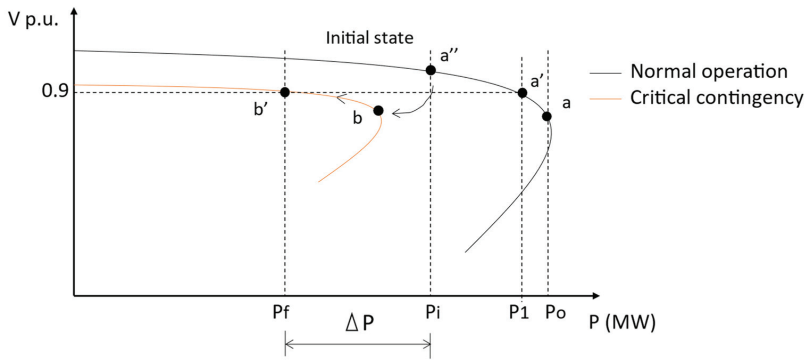


**Figure 14.** P–V curve for normal and contingency operation (determination of load shedding).

The load-shedding action is performed by finding the power delta from point a″ to point b′, and the percentage of load to be shed is calculated using Equation (14):

$$\%\text{load shedding } OA_i = \frac{\Delta P}{P_{area\_i}}, \quad (14)$$

This percentage of load shedding is carried out for all loads in the affected area.

## 6. Simulation

The outage of transmission lines 5–8 and 6–7 was simulated, separating bus 7, 8, and 9 from the rest of the system, connected only by line 9–39, which caused a voltage drop in the busbars and the loads connected to them: 230 MW (bus 7) and 522 MW (bus 8).

The most affected area was identified according to the angular indexes (see Figure 17). It can be seen in Figure 17 that the contingency of lines 5–8 and 6–7 was outside the thresholds defined in the angular characterization for contingencies N-1 in operational area 3 (DCOA3). For the other areas, this event did not represent any problem in the bus voltages of the system (see Figures 15–18).

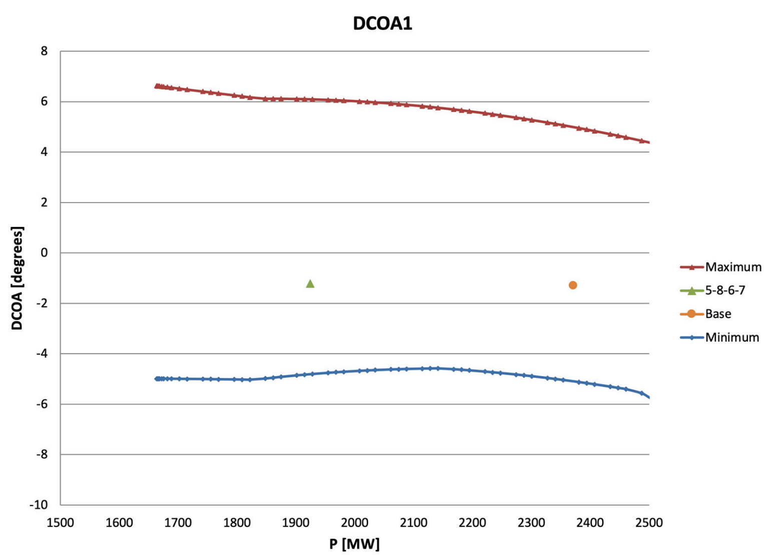


**Figure 15.** Angular threshold characterization for contingencies N-1 in operational area 1 (outages of lines 5–8 and 6–7).

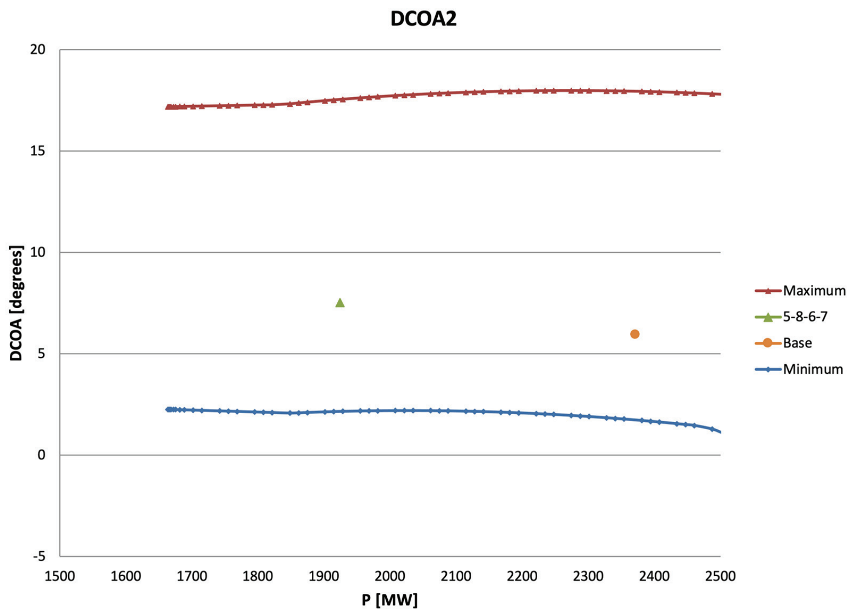


**Figure 16.** Angular thresholds characterization for contingencies N-1 in operational area 2 (outages of lines 5–8 and 6–7).

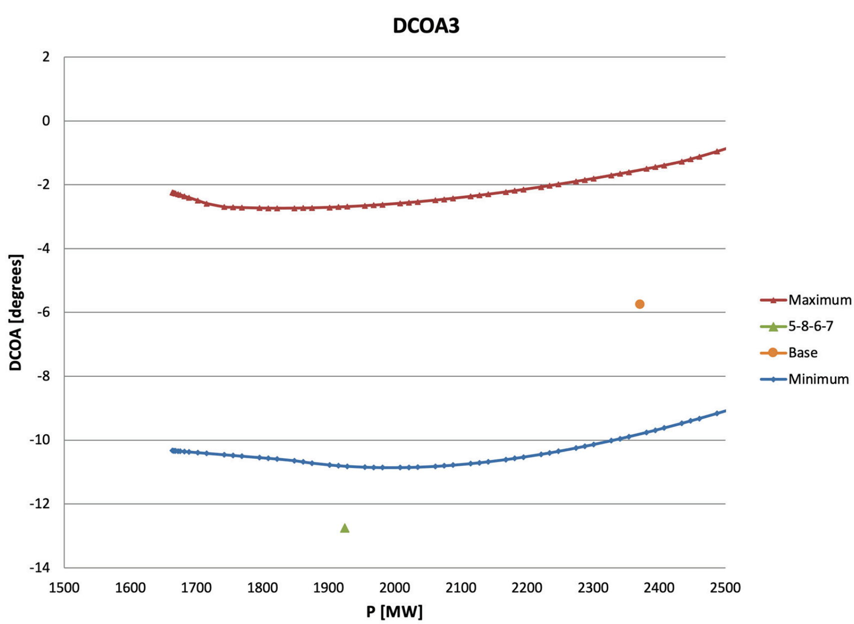


**Figure 17.** Angular thresholds characterization for contingencies N-1 in operational area 3 (outages of lines 5–8 and 6–7).

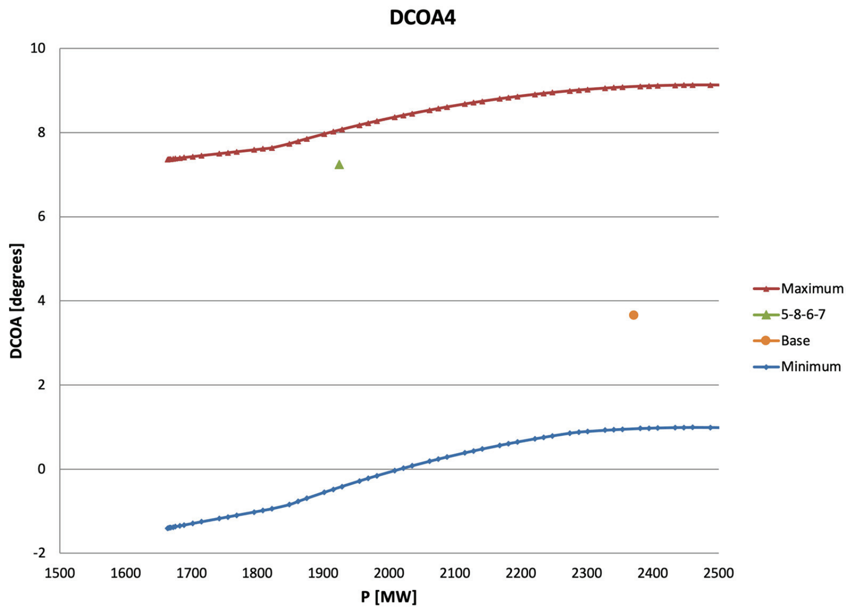


**Figure 18.** Angular thresholds characterization for contingencies N-1 in operational area 4 (outages of lines 5–8 and 6–7).

After identifying the most affected operational area (area 3), the amount of load to be shed was found.

From Figure 19, the control action was performed based on the ΔP and the total load of operational area 3:

$$\Delta P \approx 1000 \text{ MW}, \tag{15}$$

$$\text{P area } 3 = 2400 \text{ MW}, \tag{16}$$

$$\% \text{ Load shedding OA3} = (1000 \text{ MW})/(2400 \text{ MW}) = 42\%, \tag{17}$$

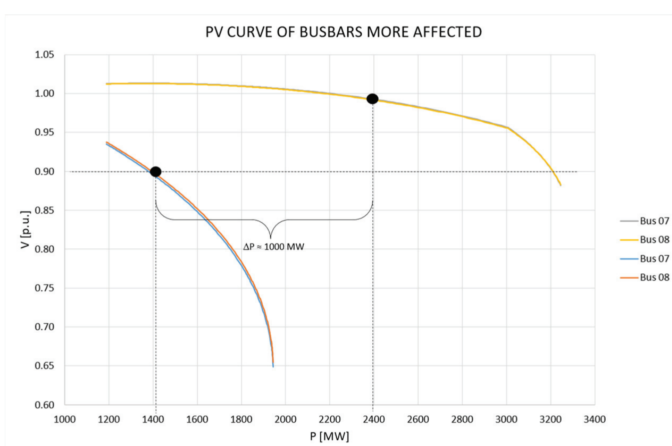


**Figure 19.** P–V curves for normal and contingency operation in operational area 3 (load shedding calculation).

## 7. Results

This section shows the behavior of the voltages in all busbars for different OAs of the IEEE 39-bus system. The results were carried out taking into account the angular characterization using the COA and DCOA for each load bus and the N-1 contingency criteria. In this case, the control actions were conducted using the classical P–V curves and their relationship with the COA and DCOA indexes. Then, the simulations results and figures were addressed and explained in detail.

Figure 20 shows the voltage results. It can be seen that, when performing the simulation with respect to time without control actions, there was a clear loss of stability, with oscillations and voltages below 0.9 in almost all the busbars of the system by operational area; voltages around 0.7 p.u. were particularly appreciated in area 3. When performing control actions in operational area 3 (OA3), a notable improvement in the voltage profiles was observed, damping the oscillation that appears in the system.

Comparative results are presented for our method against the classical literature P–V curve construction as it is a conventional methodology frequently used in the industry (see Table 3). It can be seen that the COA method is promissory for voltage-stability requirements in a power system.

**Table 3.** Voltage deviation comparison for the classical literature method and proposed COA method. Outages of transmission lines 5–8 and 6–7.

| Most Affected Voltage Bus in OA | Maximum Voltage Deviation w/o COA Method | Maximum Voltage Deviation with COA Method | Minimum Voltage Deviation w/o COA Method | Minimum Voltage Deviation with COA Method | Voltage Stabilization Time w/o COA Method [s] | Voltage Stabilization Time w/o COA Method [s] |
|---|---|---|---|---|---|---|
| 1 | 1.150 | 1.098 | 0.787 | 0.951 | 17 | - |
| 2 | 1.157 | 1.096 | 0.883 | 0.992 | 16 | - |
| 3 | 1.111 | 1.092 | 0.686 | 0.897 | >20 | 4 |
| 4 | 1.130 | 1.095 | 0.911 | 0.971 | 16 | - |

Without control actions

With control actions

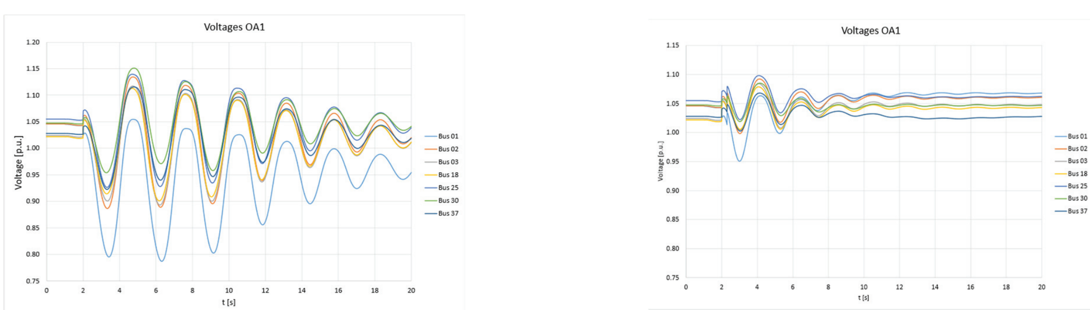


(**a**)

**Figure 20.** *Cont.*

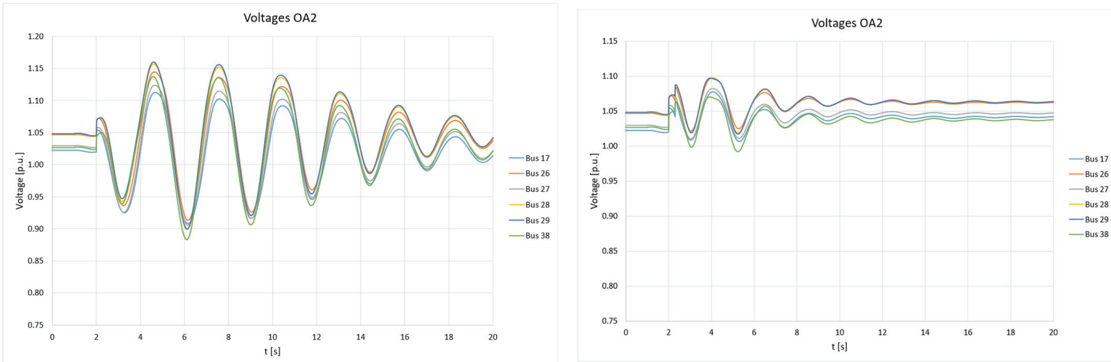


(**b**)

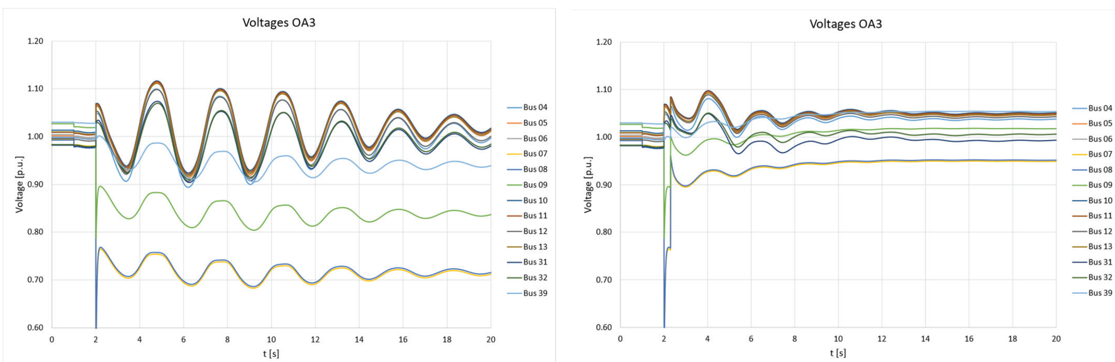


(**c**)

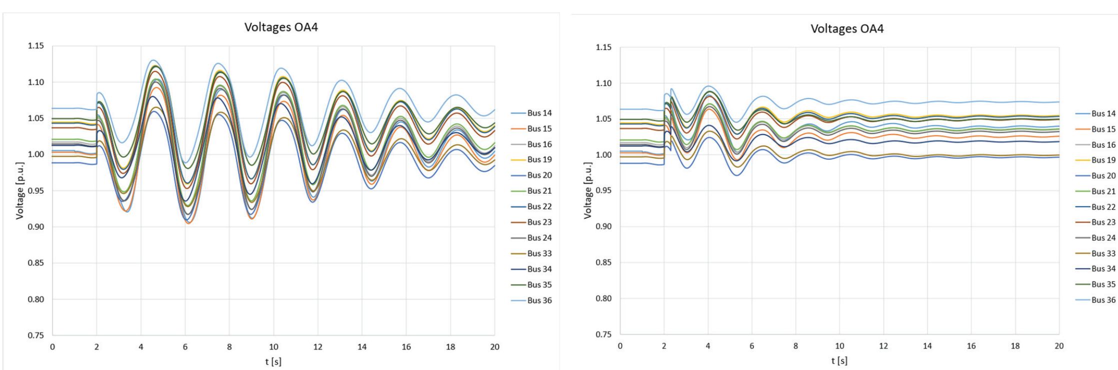


(**d**)

**Figure 20.** Voltage results without and with control actions (outages of lines 5–8 and 6–7). (**a**) Voltages OA1. (**b**) Voltages OA2. (**c**) Voltages OA3. (**d**) Voltages OA4.

## 8. Conclusions

In this paper, a novel method for voltage stability based on P–V curves and analysis of angular indexes calculated by synchrophasors was addressed.

It was observed that the center of angle (COA) and delta of center of angle (DCOA) yield the characterization of an electrical power system. It was even possible to determine if a contingency is critical when a detailed prior characterization of the system is available. In addition, the COA proved to be an important index to determine the location of the occurrence of the events, and where control actions should be carried out to remedy the stress problem in this case.

A limitation of the stationary analysis is the non-convergence against critical events, which would not yield the characterization of the angular index. Based on this limitation, the stationary analysis does not provide the necessary information for the contingencies of rare occurrences and the high impact in which convergence is not achieved.

**Author Contributions:** The authors contributed to the paper in the following capacities: conceptualization, G.J.L.; methodology, J.W.G.; analysis, I.A.I. and O.H.V.; simulation, H.A.C. All authors have read and agreed to the published version of the manuscript.

**Funding:** This research was funded by the program: "Estrategia de transformación del sector energético colombiano en el horizonte de 2030" funded by the research call 778 of MinCiencias Ecosistema Científico. Contract FP44842-210-2018.

**Data Availability Statement:** The data presented in this study are available on request from the corresponding author. The data are not publicly available due to the data use agreement.

**Acknowledgments:** The authors would like to thank the support to Carlos Eduardo Restrepo, Andrés Felipe Eusse and Camilo Andrés Villarreal Rueda.

**Conflicts of Interest:** The authors declare no conflict of interest.

## References

1. Hatziargyriou, N.; Milanovic, J.; Rahmann, C.; Ajjarapu, V.; Canizares, C.; Erlich, I.; Hill, D.; Hiskens, I.; Kamwa, I.; Pal, B.; et al. Definition and Classification of Power System Stability—Revisited & Extended. In *IEEE Transactions on Power Systems*; IEEE: Piscataway, NJ, USA, 2021; Volume 36, pp. 3271–3281. [CrossRef]
2. Eremia, M.; Shahidehpour, M. *Background of Power System Stability, the Handbook of Electrical Power System Dynamics: Modeling, Stability, and Control*; Wiley-IEEE Press: Hoboken, NJ, USA, 2013.
3. Eremia, M.; Shahidehpour, M. *Major Grid Blackouts: Analysis, Classification, and Prevention, the Handbook of Electrical Power System Dynamics: Modeling, Stability, and Control*; Wiley-IEEE Press: Hoboken, NJ, USA, 2013.
4. Van Cutsem, T.; Vournas, C. *Voltage Stability of Electric Power Systems*; Springer: Berlin/Heidelberg, Germany, 2008.
5. Taylor, C.W.; Erickson, D.C.; Martin, K.E.; Wilson, R.E.; Venkatasubramanian, V. WACS—Wide-area stability and voltage control system: R&D and online demonstration. In Proceedings of the IEEE; IEEE: Piscataway, NJ, USA, 2005; Volume 93, pp. 892–906. [CrossRef]
6. Sherwood, M.; Ajjarapu, V.; Leonardi, P.B. Real-Time Security Assessment of Angle Stability and Voltage Stability Using Synchrophasors Final Project Report Project Team Vaithianathan 'Mani' Venkatasubramanian (project leader). 2010. Available online: http://www.pserc.org (accessed on 1 July 2022).
7. Su, H.-Y.; Liu, C.-W. Estimating the Voltage Stability Margin Using PMU Measurements. *IEEE Trans. Power Syst.* **2015**, *31*, 1–9. [CrossRef]
8. Phadke, A.G.; Thorp, J.S. *Synchronized Phasor Measurements and Their Applications*; Springer: Berlin/Heidelberg, Germany, 2008.
9. Pourbagher, R.; Derakhshandeh, S.Y.; Golshan, M.E.H. A novel method for online voltage stability assessment based on PMU measurements and Thevenin equivalent. *IET Gener. Transm. Distrib.* **2022**, *16*, 1780–1794. [CrossRef]
10. Peng, L.; Li, Y.; Mili, L.; Tang, Y.; Xu, Y.; Zhao, B.; Li, J. A Real-Time Enhanced Thevenin Equivalent Parameter Estimation Method for PLL Synchronization Stability Control in VSC. *IEEE Trans. Power Deliv.* **2022**, *37*, 2650–2660. [CrossRef]
11. O'Brien, J.; Deronja, A.; Apostolov, A.; Arana, A.; Begovic, M.; Brahma, S.; Brunello, G.; Calero, F.; Faulk, H.; Hu, Y.; et al. Use of synchrophasor measurements in protective relaying applications. In Proceedings of the 2014 67th Annual Conference for Protective Relay Engineers, College Station, TX, USA, 31 March–3 April 2014.
12. Sahu, P.; Verma, M.K. Online monitoring of voltage stability margin using PMU measurements. *Int. J. Electr. Comput. Eng.* **2020**, *10*, 1156–1168. [CrossRef]
13. Paramo, G.; Bretas, A.; Meyn, S. Research Trends and Applications of PMUs. *Energies* **2022**, *15*, 5329. [CrossRef]
14. Ashwin, N.; Sreedevi, J.; Dixit, P.; Meera, K.S. Voltage stability of power system using pv curve and pmu data. *Int. J. Recent Technol. Eng.* **2019**, *8*, 7654–7659. [CrossRef]
15. Wang, X.; Chiang, H. Analytical Studies of Quasi Steady-State Model in Power System Long-Term Stability Analysis. *IEEE Trans. Circuits Syst. I Regul. Pap.* **2014**, *61*, 943–956. [CrossRef]
16. Dobson, I.; Parashar, M. A cutset area concept for phasor monitoring. In Proceedings of the IEEE PES General Meeting, Minneapolis, MN, USA, 25–29 July 2010.

17. Dobson, I.; Parashar, M.; Carter, C. Combining Phasor Measurements to Monitor Cutset Angles. In Proceedings of the 2010 43rd Hawaii International Conference on System Sciences, Honolulu, HI, USA, 5–8 January 2010; IEEE: Piscataway, NJ, USA, 2010.
18. Lopez, G.J.; Gonzalez, J.W.; Leon, R.A.; Sanchez, H.M.; Isaac, I.A.; Cardona, H.A. Proposals based on cutset area and cutset angles and possibilities for PMU deployment. In Proceedings of the 2012 IEEE Power and Energy Society General Meeting, San Diego, CA, USA, 22–26 July 2012; pp. 1–6. [CrossRef]
19. López, G.; González, J.; Díez, A.; Isaac, I.; Cardona, H.A.; Leon, R.A. Contingency Analysis Model of Electrical Power Systems Based on Central Angles from PMUs. *Adv. Mat. Res.* **2013**, *772*, 664–672. [CrossRef]
20. Darvishi, A.; Dobson, I. Threshold-Based Monitoring of Multiple Outages with PMU Measurements of Area Angle. *IEEE Trans. Power Syst.* **2016**, *31*, 2116–2124. [CrossRef]
21. Sherwood, M.; Hu, D.; Venkatasubramanian, V.M. Real-time detection of angle instability using synchrophasors and action principle. In Proceedings of the 2007 iREP Symposium-Bulk Power System Dynamics and Control-VII. Revitalizing Operational Reliability, Charleston, SC, USA, 19–24 August 2007; IEEE: Piscataway, NJ, USA, 2007. [CrossRef]
22. Feng, K.; Zhang, Y.; Liu, Z.; Li, T.; Ma, H. A wide area information based online recognition of coherent generators in power system. *Dianwang Jishu/Power Syst. Technol.* **2014**, *38*, 2082–2086. [CrossRef]
23. Matevosyan, J.; Badrzadeh, B.; Prevost, T.; Quitmann, E.; Ramasubramanian, D.; Urdal, H.; Achilles, S.; MacDowell, J.; Huang, S.H.; Vital, V.; et al. Grid-forming inverters: Are they the key for high renewable penetration? In *IEEE Power and Energy Magazine*; IEEE: Piscataway, NJ, USA, 2019; Volume 17, pp. 89–98. [CrossRef]
24. Denis, G.; Prevost, T. MIGRATE D3.6: Requirement guidelines for operating a grid with 100% power electronic devices. *Migrate Proj.* **2019**, *10*. [CrossRef]
25. Haldar, A.; Khatua, R.; Malkhandi, A.; Senroy, N.; Mishra, S. Delay Based Virtual Inertia Emulation for a Grid Forming System. In *2022 IEEE Power and Energy Conference at Illinois (PECI)*; IEEE: Piscataway, NJ, USA, 2022; pp. 1–6. [CrossRef]
26. Qi, Y.; Deng, H.; Liu, X.; Tang, Y. Synthetic Inertia Control of Grid-Connected Inverter Considering the Synchronization Dynamics. *IEEE Trans. Power Electron.* **2022**, *37*, 1411–1421. [CrossRef]
27. Thilakarathne, C.; Meegahapola, L.; Fernando, N. Real-time voltage stability assessment using phasor measurement units: Influence of synchrophasor estimation algorithms. *Int. J. Electr. Power Energy Syst.* **2020**, *119*, 105933. [CrossRef]
28. Lee, Y.; Han, S. Real-time voltage stability assessment method for the Korean power system based on estimation of Thévenin equivalent impedance. *Appl. Sci.* **2019**, *9*, 1671. [CrossRef]
29. Kiseng, S.M.; Muriithi, C.M.; Nyakoe, G.N. Under voltage load shedding using hybrid ABC-PSO algorithm for voltage stability enhancement. *Heliyon* **2021**, *7*, e08138. [CrossRef] [PubMed]
30. Ajjarapu, V.; Christy, C. The continuation power flow: A tool for steady state voltage stability analysis. In *IEEE Transactions on Power Systems*; IEEE: Piscataway, NJ, USA, 1992; Volume 7, pp. 416–423. [CrossRef]
31. Lopez, G.J.; Gonzalez, J.W.; Escobar, D.A.; Leon, R.A.; Isaac, I.A.; Cardona, H.A. Network characterization based on central angles and PMU deployment. In Proceedings of the 2012 IEEE Power and Energy Society General Meeting, San Diego, CA, USA, 22–26 July 2012; IEEE: Piscataway, NJ, USA, 2012; pp. 1–6. [CrossRef]
32. Darvishi, A.; Dobson, I. Area angle can monitor cascading outages with synchrophasors. In Proceedings of the 2015 IEEE Power & Energy Society Innovative Smart Grid Technologies Conference, Washington, DC, USA, 18–20 February 2015; IEEE: Piscataway, NJ, USA, 2015. [CrossRef]
33. Dobson, I. Voltages Across an Area of a Network. In *IEEE Transactions on Power Systems—IEEE TRANS POWER SYST*; IEEE: Piscataway, NJ, USA, 2012; Volume 27, pp. 993–1002. [CrossRef]
34. Aljarrai, K.; Sherwali, H. Using WACS Algorithm based on Center of Angle (COA) Technique in Assessing the Stability of the Libyan Grid. In Proceedings of the 2021 IEEE 1st International Maghreb Meeting of the Conference on Sciences and Techniques of Automatic Control and Computer Engineering MI-STA, Tripoli, Libya, 25–27 May 2021; IEEE: Piscataway, NJ, USA, 2021. [CrossRef]
35. Real-Time Security Assessment of Angle Stability Using Synchrophasors Final Project Report PSERC. 2010. Available online: http://www.pserc.org (accessed on 1 July 2022).
36. Lauby, M.G.; Kundur, P.; Balu, N.J. *Power System Stability and Control*; McGraw-Hill: New York, NY, USA, 1994.
37. Chow, J.; Chakrabortty, A.; Arcak, M.; Bhargava, B.; Salazar, A. Synchronized Phasor Data Based Energy Function Analysis of Dominant Power Transfer Paths in Large Power Systems. In *IEEE Transactions on Power Systems*; IEEE: Piscataway, NJ, USA, 2007; Volume 22, pp. 727–734. [CrossRef]

*energies*

*Article*

# Local Evolution Model of the Communication Network for Reducing Outage Risk of Power Cyber-Physical System

**Yuchen Fang, Xiafei Tang *, Li Tang, Yang Chen and Weiyu Wang**

School of Electrical and Information Engineering, Changsha University of Science & Technology, Changsha 410205, China
* Correspondence: xiafeitang@csust.edu.cn

**Abstract:** The deep integration of power grids and communication networks is the basis for realizing the complete observability and controllability of power grids. The communication node or link is always built according to the physical nodes. This step is alternatively known as "designing with the same power tower". However, the communication networks do not form a "one-to-one correspondence" relationship with the power physical network. The existing theory cannot be applied to guide the practical power grid planning. In this paper, a local evolution model of a communication network based on the physical power grid topology is proposed in terms of reconnection probabilities. Firstly, the construction and upgrading of information nodes and links are modeled by the reconnection probabilities. Then, the power flow entropy is employed to identify whether the power cyber-physical system (CPS) is at the self-organized state, indicating the high probability of cascading failures. In addition, on the basis of the cascading failure propagation model of the partially dependent power CPS, operation reliabilities of the power CPS are compared with different reconnection probabilities using the cumulative probability of load loss as the reliable index. In the end, a practical provincial power grid is analyzed as an example. It is shown that the ability of the power CPS to resist cascading failures can be improved by the local growth evolution model of the communication networks. The ability is greater when the probability of reconnection is $p = 0.06$. By updating or constructing new links, the change in power flow entropy can be effectively reduced.

**Keywords:** power cyber-physical system (power CPS); topology evolution model; cascading failures; interdependent networks; self-organized state

**Citation:** Fang, Y.; Tang, X.; Tang, L.; Chen, Y.; Wang, W. Local Evolution Model of the Communication Network for Reducing Outage Risk of Power Cyber-Physical System. *Energies* **2022**, *15*, 7876. https://doi.org/10.3390/en15217876

Academic Editor: Saeed Golestan

Received: 18 September 2022
Accepted: 12 October 2022
Published: 24 October 2022



## 1. Introduction

In the modern smart grid, the deep interactions between power grids and communication networks are emerging. Their couplings bring new challenges to the safety and reliability of the power system. Power grids become more intelligent with the extensive operation of the information system, realizing more complete functions. However, the interdependency between power system and communication network results in some hidden risks [1]. For example, in 2015, hackers attacked the Ukraine power grid and embedded malicious software, which led to power failure [2]. Another remarkable accident occurred in Venezuela. From the 7th to 9th March 2019, the local power system of 18 states in Venezuela were subjected to two continuous network attacks, resulting in the collapse of power systems directly [3]. These examples demonstrate that even though the power grid can operate normally, the damage to communication networks has grievous effects on entire power grids. Since the traditional modeling of cascading failures in the power grid does not consider the influence of the communication network, the reliability and accuracy of the power grid model cannot be guaranteed. Evaluating communication networks should become an essential part of the power CPS evaluation.

In power CPS, the blackout is always in the form of cascading failures, and multiple regions are affected. Basically, the large-scale transfer of power flow is still the intrinsic reason for cascading failures in power grids [4]. Thus, the interaction between the power and information networks should be considered in cascading failure modeling. In 2010, a model for cascading failure in the interdependent network was put forward first in [5]. Based on this model, the static and dynamic analysis methods are proposed for the cascading failure spreading theory in interdependent networks. By extracting the network topological eigenvector, the static analytical method in [6] calculates the topological feature parameters and presents the structure characteristic index set. The topological characteristic parameters of the two-layer coupling network are generated to describe the effect of the interdependent relation to cascading failures. The dynamic analytical method analyzes the spreading process of cascading failures based on the static topological model. The dynamic approach suggested in [7,8] is employed to study the robustness of the interdependent networks to resist cascading failures and assists to establish the real-world networks [9]. In addition, a CPS model for the hierarchical and distributed control system (HDCS) is also examined in [10]. The information flow in the control process of the active distribution network (ADN) is analyzed and the information and physical performance of the ADN control process is integrated successfully.

In particular, the above research on interdependent relations needs to satisfy an important assumption that both the nodes and the line scales of power grids and communication networks are the same [11]. Based on this assumption, the spreading process of cascading failures under the interaction of two networks can be better discussed.

However, research and actual operation cases indicate that the scale of the real communication network is smaller than the power grid. In other words, the scale of the power grid and communication network is not exactly a "one-to-one correspondence" relationship [12] but a kind of partial interdependency [13]. Under this relationship, the observability and controllability of the power grid cannot be realized fully. Therefore, the practical power grid cannot satisfy the communication requirement of the interdependent network. It makes the research stay in the theoretic stage rather than put it into practice. In [14], the future control center is designed. It intends to build and operate perfect communication networks for optimizing the information networks. Unfortunately, this plan needs huge investment and a long time for construction. Thus, most of the current research still focuses on how to avoid the influence originated by the partial interdependency. The real networks have similar characteristics with the small-world network [15,16]. The employment of the small-world network adds numerous nodes and general links, and then, the dimension of the complex networks rises. This means the theoretical probability of cascading failure occurrence is increased and the analyzing accuracy is affected. In addition, the random small-world network generated with the same "degree" has multiple possibilities which introduces uncertainty to the model. In practical engineering, it is discovered that the topology of existing power grids is obviously different from the random small-world networks. The theoretical model of partial interdependent networks cannot explain the communication process of cascading failure propagation under the interaction of the power and communication networks. Consequently, power grid companies cannot construct and improve the existing communication networks with regards to the suggested topological structure. Therefore, regarding the practical engineering project, the partial interdependency in the power CPS should be deeply studied to improve the perception of the power grid and decrease the probability of cascading failures. It has a remarkable practical significance in engineering.

In this paper, a local evolution model of the communication network is proposed to reduce the outage risk of the power cyber-physical system. The actual communication network is considered as the base, and the natural growth law of the small-world networks is selected as the principle for adding a few important nodes and essence links into the communication networks in order to achieve the "one-to-one correspondence" relationship. Then, the observability and controllability of the power grid can be realized. In addition, the power flow entropy is utilized as a sensitivity index to set the smallest number of communication links of the power CPS to prevent the power grid from entering the self-organized critical state. This model can minimize the probability of blackout brought by cascading failures. It has a guiding significance for the construction of the communication networks.

The outline of the paper is organized as follows. Section 2 lays out the method of analyzing partial interdependency of power CPS and the CPS evolving process. The case studies are included for verification in Section 3. Finally, a conclusion is presented in Section 4.

## 2. Method of Analyzing Partial Interdependency of Power CPS and Evolution of CPS

### *2.1. Partial Interdependent Characteristics of Power CPS*

In power CPS, the interaction between the power grids and communication networks can be summarized as the energy interdependent relationship and the information interdependent relationship. The energy interdependent relationship means that the nodes in the energy interdependent power grid provide the power required for the operation of the nodes in the communication network. The information interdependent relationship means that the nodes in the information interdependent communication network process the monitoring and scheduling of information from the power grid nodes.

Generally, the power nodes provide energy to the information nodes. The information nodes collect measurement information. The dispatching center obtains the operation state information through the situational awareness, and then, gives optimal scheduling instructions to the power grid to realize the closed-loop control, as shown in Figure 1. Abbreviated as physical-information node pairs, physical nodes and information nodes form the interdependent relationship.

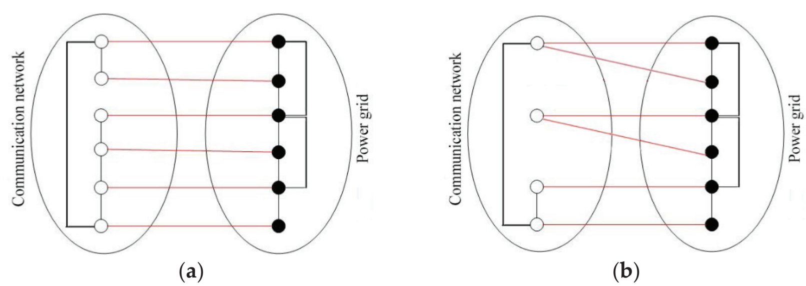


**Figure 1.** Two types of interdependent networks. (**a**) One-to-one correspondent interdependent network; (**b**) Partial interdependent network.

In the physical layer, the power plant and the transformer substation in the actual physical grid are abstracted as the topological node, whereas transmission lines are abstracted as power edges amongst nodes. This structure realizes the power flow transmission between generation nodes and load nodes. In the communication network structure, the information flow realizes the bidirectional transmission with the shortest route through information edges. Information nodes are also dispatching centers and communication plants and stations, whereas the information edges are communication links [17]. However, in different developing stages, upgrading or newly building the information nodes and links is limited by resource allocation. The scale of the communication network gradually increases after updating the corresponding power grids. Therefore, there is a scale difference between power grids and communication networks. The difference can be defined as the partial interdependency.

### *2.2. The Evolution Model of New Node Connections*

To realize closed-loop control, communication links locally evolve according to the topology of power grids [18]. As the rule of designing with the same power tower is widely used, the optical fiber should be erected on power towers. Therefore, the local evolutionary model of the power communication network is constructed via the following steps:

1. Number all the nodes in the power communication network. The unbalance of nodes in the existing power and communication network is considered. Some nodes are added to ensure that the number of nodes in the communication network equals that in power grids.
2. Number the new nodes in sequence and connect them with the nearest four nodes to construct the nearest coupling network, as shown in Figure 2a.
3. Select the nodes to be added (Node *i*) and reconnect them. Node *i* is disconnected with the first two nodes at first, and then is reconnected with a probability from 0 to 1. Node *i* is reconnected to other nodes randomly following the rule of no self-loop or no repeat connection, as shown in Figure 3a.
4. Repeat step 3. It is necessary to ensure the chosen nodes are not selected again until all the added nodes have been chosen, as shown in Figure 2b.
5. After reconnection, inspect whether the network is connected. If not, repeat steps 3–4 until the network is connected. The sketch map of disconnection is shown in Figure 3b.

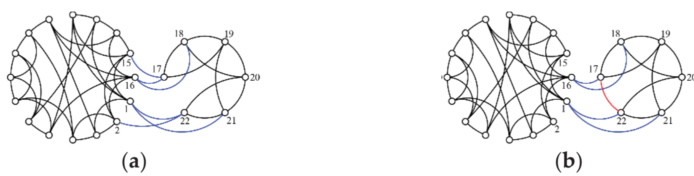


**Figure 2.** Schematic diagram of coupling network and correct reconnection. (**a**) The nearest-neighbor coupling network; (**b**) correct reconnection.


**Figure 3.** Schematic diagram of repeated edges and disconnection. (**a**) Schematic diagram of repeated edges; (**b**) schematic diagram of disconnection.

Different power communication networks can be obtained by changing the reconnection probability $p$. If the reconnection probability $p = 0$, the communication network is the regular network. If the reconnection probability $p = 1$, it is the random network [19].

### *2.3. The Evolution Model of New Links and Reconnections*

Research shows that power flow entropy is an important index to identify whether the power system enters the self-organized state. The power flow entropy is shown in Equation (1). If the power flow entropy is larger, the unbalanced distribution of power flow is as well, thus, the power system faces a higher risk of blackout [20].

$$H = -C\sum_{k=1}^{n-1} P(k)lnP(k) \tag{1}$$

where $H$ is the power flow entropy, $P(k)$ is the proportion of the lines of the load rates $\mu_i$ between $U_k$ and $U_{k+1}$ to the total lines, $U$ is a constant sequence ($U = \{0, 0.02, \ldots, 2.0\}$), and C is ln 10.

According to the process of Figure 3, a communication network which has the same number of nodes as the power grid can be obtained. However, the number of communication links is less than the number of transmission lines. Therefore, to realize the "one to one correspondence", the communication links should be added.

The corresponding communication links of important transmission lines should be added first. The research points out that, if the system power flow entropy changes greatly after communication links fail, these transmission lines are important lines [21]. It is not conducive to the realization of closed-loop control if the corresponding acquisition and information control units are not configured for these important lines.

Therefore, when the economy is considered, the following methods are designed to realize the evolution of communication links, which reach the lowest load loss. The simulation flow chart is shown in Figure 4.

1. Find the transmission lines without corresponding communication links. Form a Set $s$ of the physical lines which do not have the acquisition and information control units (the lines are $i_k j_k$ if the nodes at both ends of each line are $i_k j_k$).
2. Trigger the cascading failures in these transmissions. Calculate the variation of the power flow entropy with Equation (1) when any line in the Set $s$ fails.
3. List the power flow entropy in descending order; thus, important transmission lines can be obtained. Then, update Set $s$.
4. Add the communication links which correspond to the transmission lines in Set $s$, in turn, to form the different CPS models. Judge whether the power CPS enters a self-organized critical state and calculate the load loss.
5. Compare different CPS models' load losses after experiencing the cascading failure.
6. Find out the optimal plan of adding communication links.

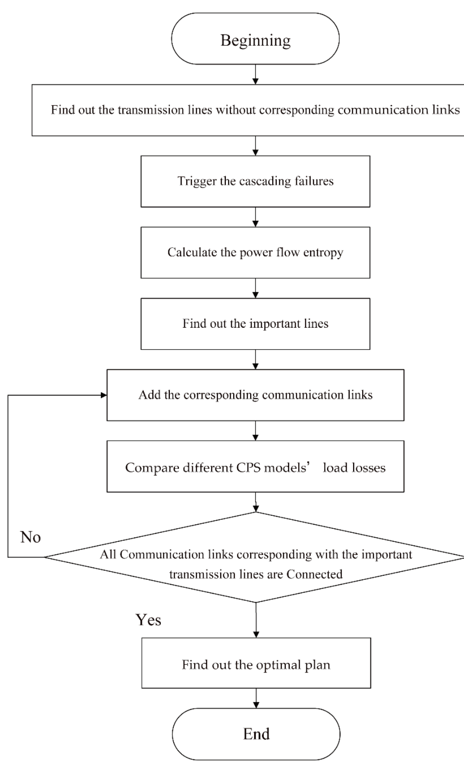


**Figure 4.** The simulation flow chart of cascading failure.

### 2.4. Cascading Failure Mechanism through the Partial Interdependency

The dispatching center takes the charge of the complete closed-loop control. Once the physical nodes fail, links fail, or the function is invalid, the corresponding information nodes acquire the status and then upload the information to the dispatching center through the communication network. If the dispatching center received the failure information, the control instruction will be made based on the minimum cut-off load and the control signals will be sent to the corresponding physical elements. If the physical elements work normally, it is considered that the closed-loop control is successful; otherwise, it fails.

In the power communication network, the failure of the power grid optimization will cause the power flow transfer. There might be some wrong actions caused by the improper software configuration or hardware damage of the relay protection device. These actions will cause not only the faulty links, but also other links to be cut [22]. As a result, the topological structure of the power grid will be changed and the corresponding communication network nodes will break down at the same time. The route selection of information packs is then affected, as it will cause a significant increase in information packs to be brought to the information layer. Once information transfer is beyond the bandwidth limitation of the communication link, or the physical equipment fails, the communication links will be blocked.

Then, the corresponding information cannot reach the dispatching center. The closed-loop control of the dispatching center will be invalid, and will cause the cascading failure. Packs will be lost and a pack delivering error will appear. The network might be attacked maliciously because of the packs' abnormal delivering in the communication network, such as by the defense of service attack [23] and false data attack [24]. The correct optimization and control information from the dispatching center cannot be sent to the corresponding nodes in time because of the transmission delay or loss, which leads to the failure of the power grid optimization. Eventually, this causes the vicious cycle of the cascading failures.

The mechanism of cascading failure propagation under the interaction of two networks is shown in Figure 5. In the CPS, the failure of the power grid optimization will cause the power flow transfer. There are some wrong actions produced by the improper software configuration or hardware damage of the relay protection device. These actions will cause not only the failed lines, but also other lines to be cut. Therefore, the topological structure of the power grid will be changed and the corresponding communication network nodes will fail at the same time. Moreover, it will affect the routing of information packs. When the increase in the information packs outnumbers the bandwidth limitation of the transmission lines, or the physical equipment fails, it will cause the blockage of communication links. Then, the corresponding information cannot reach the dispatching center. The closed-loop control of the dispatching center will be invalid, and will cause cascading failures. Packs will be lost and a transmission error will appear. The network might receive malicious attacks because of the abnormal transmission of the communication network (for example, the defense of service attack and false data attack). The correct optimization information of the network cannot be sent to the corresponding nodes in time because of the transmission delay, which leads to the failure of the power grid optimization. Eventually, this causes the vicious cycle of cascading failures.

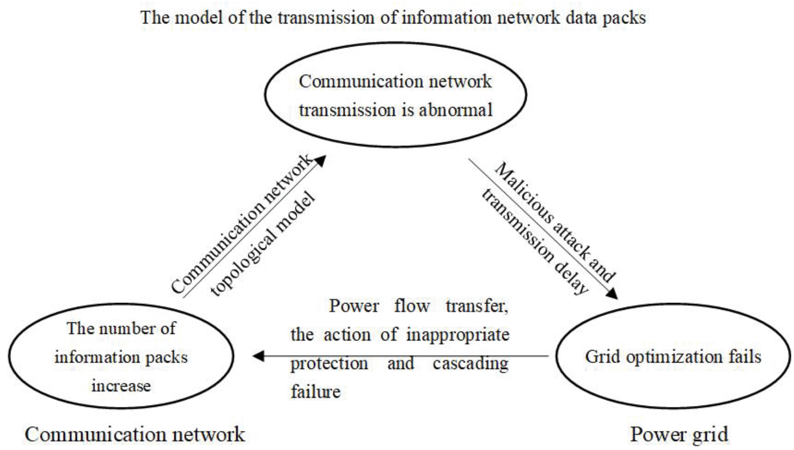


**Figure 5.** Mechanism diagram of cascading failure propagation under the interaction of two networks [25].

*2.5. Cascading Failure Model Based on the Partial Interdependency*

**In the physical layer:** when the dispatching center obtains the abnormal information, the minimum load loss of the partial interdependent power CPS is calculated based on the DC power flow calculation.

**In the cyber layer:** the improved routing strategy for information transmission is applied in the communication network to deliver the information pack [26,27], in which the distance from Node $i$ to the target node is $H_i$.

$$H_i = h_d\, d_i + (1 - h_d)\, c_i \tag{2}$$

where $d_i$ is the length between Node $i$ and the target node (which is the shortest path length), $c_i$ is the length of the information packs' queue, and $h_d$ is the routing control strategy.

In the next stage, the probability $P_j$ is given by:

$$P_j = \frac{\mathrm{e}^{-\beta \mathrm{H_j}}}{\sum_{\mathrm{m} \in \mathrm{L_i}} \mathrm{e}^{-\beta \mathrm{H_j}}} \tag{3}$$

where $P_j$ is the probability that the neighbor node j of Node $i$ is selected to receive information packs produced by the source node, $\beta$ is the routing probability control coefficient, and $L_i$ is the neighbor node set of Node $i$.

The basic simulation process is shown as follows:

1. Initialize the power grid, and the grid evolves with the probability $p$ in Equation (3) to obtain the corresponding power communication network.
2. Choose an initial line or lines from the power grid randomly, then remove it/them and trigger the cascading failure.
3. When the initial transmission line or lines are cut, calculate the DC power flow according to the parameters of the power grid.
4. Overloaded lines will appear in the power grid due to the power flow transferring from the initial transmission line to others. The corresponding information nodes will produce abnormal information packs.
5. Judge whether the power flow of overloaded lines is beyond the thermal stability limit. If the power flow of overloaded lines exceeds the thermal stability limit, it will be cut off, and the corresponding information node will produce the outage information packs.
6. Send all information from steps 3, 4, and 5 to the dispatching center.

7. The dispatching center makes decisions to balance the generation and load with the purpose of minimizing the cut-off load. Then, the control information is sent to the corresponding physical devices.
8. Judge whether the power grid is disconnected. If it is disconnected, that will be the end of the cascading failure simulation. Otherwise, go back to step 3.

## 3. Case Studies

### 3.1. The Partial Interdependency of the Provincial Grids

A provincial power grid is shown as an example. The corresponding power grid and communication network topological model is established in Figure 6a, and 6c. There are 258 nodes and 414 edges in the province's power grid, and 220 nodes and 294 edges in the communication network. The scale of the nodes and links of the power grid and the communication network is different. It is obvious that the topology interdependency of the power grid and the communication networks is not exactly "one to one correspondence" relationship. The number of nodes and edges in the power grid is more than that in the communication networks.

The structure characteristic parameters of the provincial power grid and the communication network are shown in Table 1. $N$ is the number of the network's nodes. $M$ is the number of the network's edges. $<k>$ is the average degree of the network. $L$ is the shortest path length of the network. $C$ is the network convergence factor. $L_{random}$ is the shortest path length of the random network, which has the same number of nodes and edges as that network. $C_{random}$ is the convergence factor of the random network which has the same number of nodes and edges as that network.

**Table 1.** The structure characteristic parameters of a complex network between the power grid and the communication network in the province.

| Network | $N$ | $M$ | $<k>$ | $L$ | $C$ | $L_{random}$ | $C_{random}$ |
|---|---|---|---|---|---|---|---|
| Power grid | 258 | 414 | 3.260 | 5.705 | 0.209 | 4.774 | 0.013 |
| Communication network | 220 | 294 | 2.673 | 6.110 | 0.102 | 5.486 | 0.012 |

The small-world network is between the regular network and random network. Its characteristic is that very few remote connections are introduced with probability $p$. According to the small-world network criteria $L \geq L_{random}$ and $C >> C_{random}$, it is found that the average shortest distance between the power grid and the communication network is longer than that of their corresponding random network, whereas the clustering coefficient is 10 times to 20 times bigger than the clustering coefficient of the corresponding random network. Thus, it is assumed that the provincial power grid and the communication network are basically consistent with the small-world characteristic.

This illustrates that the characteristic of strong interdependence and interaction exists between the physical network and the communication network in the provincial power grid. Even a local change in the communication network might cause a global chain reaction in the physical network. Therefore, it is essential to reveal the failure propagation mechanism in the interaction between the communication network and the physical network.

(**a**)

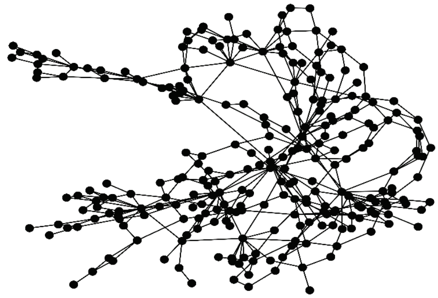

(**b**)

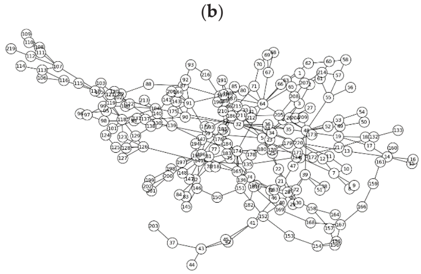

(**c**)

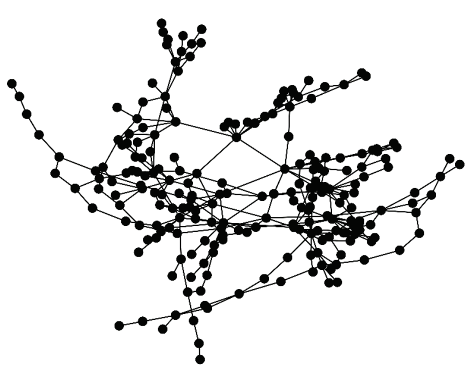

(**d**)

**Figure 6.** The power grid and the communication network of the province. (**a**) The power grid of the province; (**b**) the power grid of the province without numbers; (**c**) the communication network of the province; (**d**) the communication network of the province without numbers.

### 3.2. Evolution Results of Communication Network in the Provincial Power CPS

The relationship of "one-to-one correspondence" between power grids and information networks can be realized by applying the evolution method proposed in Section 2. In the simulation, each topological structure of the power grid with a reconnection probability of $p$ = 0.00, $p$ = 0.02, $p$ = 0.04, $p$ = 0.06, $p$ = 0.08, and $p$ = 0.10 is established separately. Table 2 shows the structure characteristic parameters of the power communication network with different reconnection probabilities.

**Table 2.** The communication network of the province and the complex network structure's characteristic parameters of the communication networks with different reconnection probability evolutions.

| Communication Network | $N$ | $M$ | $<k>$ | $L$ | $C$ |
|---|---|---|---|---|---|
| Original communication network | 220 | 294 | 2.6727 | 6.2896 | 0.1019 |
| $p$ = 0.00 | 258 | 372 | 2.8837 | 7.4462 | 0.1625 |
| $p$ = 0.02 | 258 | 372 | 2.8837 | 6.6970 | 0.1527 |
| $p$ = 0.04 | 258 | 372 | 2.8837 | 6.5981 | 0.1484 |
| $p$ = 0.06 | 258 | 372 | 2.8837 | 6.5220 | 0.1496 |
| $p$ = 0.08 | 258 | 372 | 2.8837 | 6.4122 | 0.1344 |
| $p$ = 0.10 | 258 | 372 | 2.8837 | 6.2422 | 0.1326 |

From Table 2, it is clear that the communication network, which evolves with different reconnection probabilities, has the same number of nodes and edges. This means the average degrees of the networks are equivalent. The average shortest path length $L$ of the power communication network with a reconnection probability of $p$ = 0.00 is 7.4462, and the clustering coefficient $C$ is 0.1625. The average shortest path length $L$ of the power communication network with a reconnection probability of $p$ = 0.10 is 6.2422, and the clustering coefficient $C$ is 0.1326.

With the increase in the reconnection probability, the average shortest length $L$ and the clustering coefficient $C$ decrease consistently. With the decrease in the average shortest path length $L$, the transmission efficiency increases as well. Thus, if the information can be transmitted to the dispatching center more rapidly while the links break down, a cascading failure can be avoided efficiently.

### 3.3. Cascading Failure of Partial Interdependent Power CPS

Figure 7 shows the complementary cumulative probability of the load loss by employing a cascading failure simulation. The x-axis is the whole system load loss. The y-axis is the complementary cumulative probabilities which correspond to different load losses.

$$\lambda = 1 - \frac{C \sum_{i=1}^{N_1} P_{load}(i)}{P_s} \tag{4}$$

Equation (4) is the power grid's load loss after the cascading failure. $P_{load}$ ($i$) is the load of Node $i$. $P_s$ is the total load. $N_1$ is the number of the power grid nodes.

It is noticed that the load loss is less than 0.8 at the beginning of the cascading failure. In this stage, considering the same load loss, the possibility of a big blackout occurrence is the smallest when the reconnection probability $p$ = 0.06.

In the later stage, while the load loss is greater than 0.8, the cumulative probability of occurrence decreases rapidly, and the probability of the power CPS, which evolves with the reconnection probability $p$ = 0.06, having a big blackout occur is still the smallest. Thus, for this provincial power CPS, it is shown that when the reconnection probability of the communication network is around $p$ = 0.06, there might be the best reconnection probability which can make the load loss probability the lowest.

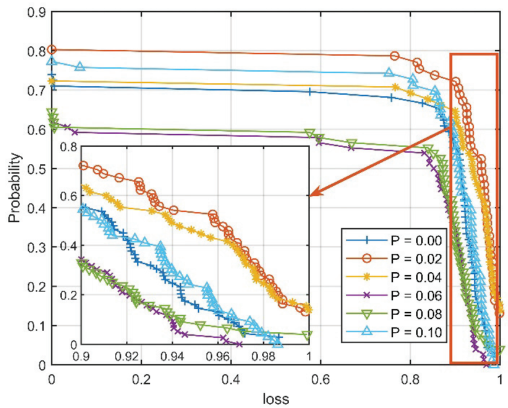


**Figure 7.** Complementary cumulative probability distribution diagram of load loss in power CPS with different reconnection probabilities.

### *3.4. Resistance to Cascading Failure Based on the Power Flow Entropy*

After the evolution of the communication network, it is clear that the nodes in communication networks form a "one-to-one correspondence" with the nodes in power physical networks. However, the number of power grid transmission lines is 44 more than the number of communication links. In Table 2, with the reconnection probability $p = 0.06$, the number of communication links is 372, whereas the number of power grid transmission lines is 414.

Thus, when the transmission lines without communication links fail, the power flow entropy is bigger, which means the original transmission line would lead to a bigger load loss. Table 3 shows the results of the power flow entropy after triggering the transmission lines without communication links. That is, the system power flow entropy reaches a maximum of 3.26 when the transmission lines (18, 20) fail. It can be noted that these lines do not correspond with any communication link. The next are (12, 8) and (67, 211), in which the power flow entropy of these is greater than 2.0 as well. These transmission lines' failures have the biggest effects on the power grid reliability.

**Table 3.** The power flow entropy after the cascading failure.

| Number | Transmission Lines without Communication Links | Power Flow Entropy |
|---|---|---|
| 1 | (18, 20) | 3.267269469 |
| 2 | (12, 8) | 3.262736109 |
| 3 | (67, 211) | 2.521364395 |
| 4 | (128, 196) | 1.7862966 |
| 5 | (9, 25) | 1.590954952 |

Thus, based on the results of power flow entropy, a plan of adding the smallest number of communication links can be concluded to resist cascading failure.

- Plan A: add the communication link (18, 20);
- Plan B: based on Plan A, then add the communication link (12, 8);
- Plan C: based on Plan B, then add the communication link (67, 211).

The results of load loss in the power CPS are shown in Figure 8.

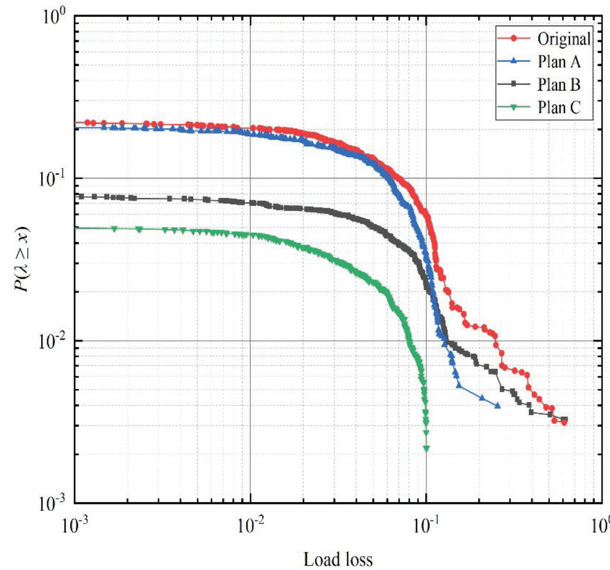


**Figure 8.** The result after adding the communication links.

In Figure 8, it is clear that the power CPS of the original system and the systems of Plan A and Plan C enter the self-organized critical state. This means the power CPS is facing the risk of cascading failures and a big blackout under three such kinds of situations. Plan B has the smallest probability of a big blackout.

Although adding two communication links can improve the ability of the power CPS against the cascading failure, in the case of Plan C, the power CPS does not enter a self-organized critical state. It is found that the power CPS will not face the risk of cascading failure when at least three communication links are added. Thus, the reliability of the power CPS is the highest in this case.

## 4. Conclusions

Regarding the situation where the power grid and the communication network are not exactly in a relationship of "one to one correspondence", but rather, partial interdependency in the power CPS, an evolution model is proposed in this paper. It adds new nodes and communication links into the communication network to achieve the relationship of "one to one correspondence". Then, the comprehensive observability and controllability of power systems is realized, and the risk of cascading failures is decreased. The relevant results are concluded as follows:

1. In the practical power system, there exists an optimal reconnection probability $p = 0.06$ of adding new communication nodes to the power CPS to realize the "one to one correspondence", but also to minimize the cumulative probability of the load loss.
2. In the case of "one-to-one correspondence", by comparing the power entropy of different power CPSs, the best plan that adds the smallest number of communication links can be made, so that the power CPS will not enter the self-organized critical state.

Through the continuation of this research, the optimal model to obtain the best evolution results will be studied in the coming work.

**Author Contributions:** Conceptualization, Y.C.; methodology, X.T.; Software, Y.C. and X.T.; validation, Y.C., W.W., Y.F. and L.T.; formal analysis, X.T.; writing—original draft, Y.F.; writing—review and editing, X.T. and W.W.; project administration, X.T. All authors have read and agreed to the published version of the manuscript.

**Funding:** This research was funded by the National Natural Science Foundation of China, No. 52277076, by the Joint Funds of the National Natural Science Foundation of China, No. U1966207, and by the Natural Science Foundation of Hunan Province under grant number 2020JJ5585.

**Institutional Review Board Statement:** Not applicable.

**Informed Consent Statement:** Not applicable.

**Data Availability Statement:** The data that support the findings of this study are available from the State Grid. Restrictions apply to the availability of these data, which were used under license for this study. Data are available with the permission of the State Grid.

**Conflicts of Interest:** The authors declare no conflict of interest.

## References

1. Zografopoulos, I.; Ospina, J.; Liu, X.; Konstantinou, C. Cyber-Physical Energy Systems Security: Threat Modeling, Risk Assessment, Resources, Metrics, and Case Studies. *IEEE Access* **2021**, *9*, 29775–29818. [CrossRef]
2. Liang, G.; Weller, S.R.; Zhao, J.; Luo, F.; Zhao, Y. The 2015 Ukraine Blackout: Implications for False Data Injection Attacks. *IEEE Trans. Power Syst.* **2017**, *32*, 3317–3318. [CrossRef]
3. Sun, Y.; Wang, Z.; Long, C.; Li, G.; Xia, D.; Li, Y. Method for Power Flow Controller Location-Allocation and Optimized Flow Control method of Meshed DC Grid. In Proceedings of the 2019 4th IEEE Workshop on the Electronic Grid (eGRID), Xiamen, China, 11–14 November 2019.
4. Li, F.; Yan, X.; Xie, Y.; Sang, Z.; Yuan, X. A Review of Cyber-Attack Methods in Cyber-Physical Power System. In Proceedings of the 2019 IEEE 8th International Conference on Advanced Power System Automation and Protection (APAP), Xi'an, China, 21–24 October 2019.
5. Johansson, J.; Hassel, H. An approach for modelling interdependent infrastructures in the context of vulnerability analysis. *Reliab. Eng. Syst. Saf.* **2010**, *95*, 1335–1344. [CrossRef]
6. Hu, J.; Yu, J.; Cao, J.; Ni, M.; Yu, W. Topological interactive analysis of power system and its communication module: A complex network approach. *Phys. A Stat. Mech. Its Appl.* **2014**, *416*, 99–111. [CrossRef]
7. Cheng, Z.; Cao, J.; Hayat, T. Cascade of failures in interdependent networks with different average degree. *Int. J. Mod. Phys. C* **2014**, *25*, 1440006. [CrossRef]
8. Wang, W.; Chen, J.; Lin, L.; Liu, X.; Nie, Q. Vulnerability Assessment Method of Electrical Cyber–Physical Interdependent Network Considering Node Heterogeneity. In Proceedings of the 2020 IEEE 4th Conference on Energy Internet and Energy System Integration (EI2), Wuhan, China, 30 October–1 November 2020.
9. Chen, Z.; Du, W.; Cao, X.; Zhou, X. Cascading failure of interdependent networks with different coupling preference under targeted attack. *Chaos Solitons Fractals* **2015**, *80*, 7–12. [CrossRef]
10. Yin, M.; Wang, L.; Yao, C.; Wu, X.; Song, Y.; Zhang, Y. Research on an Cascade Failure Model of Improved Scale-Free Network. In Proceedings of the 2021 7th International Conference on Computer and Communications (ICCC), Chengdu, China, 10–13 December 2021.
11. Wang, C.; Guo, J.; Shen, A.; Zhang, D. Research on Robustness Simulation of Interdependent Networks. In Proceedings of the 2020 International Conference on Computer Science and Management Technology (ICCSMT), Shanghai, China, 20–22 November 2020.
12. Wang, Y.; Liu, D.; Xu, X.; Dai, H. Cyber-physical Power System Modeling for Timing-driven Control of Active Distribution Network. *J. Mod. Power Syst. Clean Energy* **2020**, *8*, 549–556. [CrossRef]
13. Liu, S.; Yin, C.; Chen, D.; Lv, H.; Zhang, Q. Cascading Failure in Multiple Critical Infrastructure Interdependent Networks of Syncretic Railway System. *IEEE Trans. Intell. Transp. Syst.* **2021**, *99*, 5740–5753. [CrossRef]
14. Sturaro, A.; Silvestri, S.; Conti, M.; Das, S.K. A Realistic Model for Failure Propagation in Interdependent Cyber-Physical Systems. *IEEE Trans. Netw. Sci. Eng.* **2018**, *7*, 817–831. [CrossRef]
15. Wang, Y.; Yu, J.; Baroud, H. Generating Synthetic Systems of Interdependent Critical Infrastructure Networks. *IEEE Syst. J.* **2022**, *16*, 3191–3202. [CrossRef]
16. Marot, A.; Kelly, A.; Naglic, M.; Barbesant, V.; Cremer, J.; Stefanov, A.; Viebahn, J. Perspectives on Future Power System Control Centers for Energy Transition. *J. Mod. Power Syst. Clean Energy* **2022**, *10*, 328–344. [CrossRef]
17. Zhu, W.; Milanovic, J. Cyber-physical system failure analysis based on Complex Network theory. In Proceedings of the 17th IEEE International Conference on Smart Technologies, Ohrid, Macedonia, 6–8 July 2017.
18. Wang, J.; Peng, Y. Distributed Optimal Dispatching of Multi-Entity Distribution Network with Demand Response and Edge Computing. *IEEE Access* **2020**, *8*, 141923–141931. [CrossRef]
19. Watts, D.J.; Strogatz, S.H. Collective dynamics of 'small-world' networks. *Nature* **1998**, *393*, 440–442. [CrossRef] [PubMed]
20. Cao, N.; Cao, S.; Yu, Q.; He, Q. Risk measurement and forewarning of power blackouts based on the entropy theory. In Proceedings of the 2016 International Conference on Probabilistic Methods Applied to Power Systems (PMAPS), Beijing, China, 16–20 October 2016.

21. Zhang, S.; Li, Y.; Jin, T.; Yu, H.; Yang, G.; Liu, Z. Analysis and Research on Power Flow Entropy Index of Power System. In Proceedings of the 2018 IEEE 3rd Advanced Information Technology, Electronic and Automation Control Conference (IAEAC), Chongqing, China, 12–14 October 2018.
22. Zhao, L.; Li, X.; Ni, M.; Li, T.; Cheng, Y. Review and prospect of hidden failure: Protection system and security and stability control system. *J. Mod. Power Syst. Clean Energy* **2019**, *7*, 1735–1743. [CrossRef]
23. Mukherjee, D.; Chakraborty, S. Real-time Identification of False Data Injection Attack in Smart Grid. In Proceedings of the 2021 IEEE Region 10 Symposium (TENSYMP), Jeju, Korea, 23–25 August 2021.
24. Fu, J.; Wang, L.; Hu, B.; Xie, K.; Chao, H.; Zhou, P. A Sequential Coordinated Attack Model for Cyber-Physical System Considering Cascading Failure and Load Redistribution. In Proceedings of the 2018 2nd IEEE Conference on Energy Internet and Energy System In-tegration (EI2), Beijing, China, 20–22 October 2018.
25. Zhao, T.; Wang, D.; Lu, D.; Zeng, Y.; Liu, Y. A risk assessment method for cascading failure caused by electric cyber-physical system (ECPS). In Proceedings of the 2015 5th International Conference on Electric Utility Deregulation and Restructuring and Power Technologies (DRPT), Changsha, China, 26–29 November 2015.
26. Jia, W.; Jiang, T. Information-defined networks: A communication network approach for network studies. *China Commun.* **2021**, *18*, 197–210. [CrossRef]
27. Li, X.; Cheng, T. Cascading Failure Analysis of Cyber-Physical Power Systems under Communication Congestion. In Proceedings of the 2021 International Conference on Cyber-Physical Social Intelligence (ICCSI), Beijing, China, 18–20 December 2021.

energies

MDPI

Article

# The Semi-Scheduling Mode of Multi-Energy System Considering Risk–Utility in Day-Ahead Market

**Xian Yang [1,2], Ye Cai [1,*], Yijia Cao [1], Shaowei Duan [1], Liang Tang [1] and Zhijian Jia [3]**

1 School of Electrical and Information Engineering, Changsha University of Science and Technology, Changsha 410004, China
2 Hunan Key Laboratory of Energy Perception and Edge Computing, Hunan City University, Yiyang 413002, China
3 State Grid Yiyang Power Supply Company, State Grid, Yiyang 413000, China
* Correspondence: caiye@csust.edu.cn; Tel.: +86-137-3905-1201

**Abstract:** The large-scale development of renewable energy has an urgent demand for an adjustable power supply. For a multi-energy system with multiple types of heterogeneous power sources, including wind power, photovoltaic (PV) power, hydropower, thermal power and pumped storage, a novel semi-scheduling mode and a solution method were proposed in this paper. Firstly, based on the load and the reserve demand during the peak load period, the semi-scheduling mode was adopted to determine the start-up combination of thermal power units. Furthermore, by predicting the generating/pumping power, the working state of pumped storage units was determined to realize the independent solution of discrete integer variables. Secondly, the risk–utility function was constructed to quantify the attitude of pumped storage towards the uncertainty of renewable energy output, which completed the quotation and clearing of the pumped storage in the ancillary service market. Finally, by taking the minimum total quotation cost as the objective, the wind–solar–hydro-thermal-pumped storage coordinated (WSHTPC) model was built in the day-ahead market. The feasibility and effectiveness of the proposed model were verified through the simulation of a typical day with different renewable energy penetration rates.

**Keywords:** multi-energy system; semi-scheduling mode; pumped storage; ancillary service market; risk–utility

**Citation:** Yang, X.; Cai, Y.; Cao, Y.; Duan, S.; Tang, L.; Jia, Z. The Semi-Scheduling Mode of Multi-Energy System Considering Risk–Utility in Day-Ahead Market. *Energies* **2022**, *15*, 8147. https://doi.org/10.3390/en15218147

Academic Editor: Abdelali El Aroudi

Received: 14 September 2022
Accepted: 27 October 2022
Published: 1 November 2022



## 1. Introduction

At present, China is in a critical period of low-carbon energy transformation. With the large-scale development of renewable energy, the anti-peak shaving characteristics of wind power and the strong randomness of PV power lead to the frequent deep peak shaving of thermal power units [1–3]. Furthermore, the thermal power units may even be forced to shut down in the low net load period. However, once the thermal power unit is shut down, it takes 8–10 h to restart. In a power system dominated by thermal power, the quick-adjusting capacity of the system is obviously insufficient, resulting in a serious energy abandonment problem [4–6]. Therefore, in order to enhance the consumption of renewable energy and improve energy utilization efficiency, it is an effective measure to fully exploit the system reserve space [7,8]. In existing studies, pumped storage is often used as an independent peak-shaving resource [9]. However, pumped storage also has excellent frequency regulation ability and rotating reserve ability [10–12]. Thus, the allocation of pumped storage's reserve capacity is a problem worthy of discussion. On the one hand, if the reserve capacity is too small to stabilize the fluctuation of renewable energy, the purpose of promoting the consumption of renewable energy cannot be achieved [13]. On the other hand, too much reserve capacity decreases the opportunity cost for pumped storage to make profits in the real-time market [14].

With the diversified development of power source structure, the joint scheduling of multiple heterogeneous power sources becomes the focus to promote the healthy and sustainable development of power systems [15,16]. In order to increase the amount of clean energy consumption and avoid deep peak shaving of thermal power units, the pumped storage is usually bundled with wind power, PV power or thermal power. Generally, the economy and stability operation of thermal power [17,18], the minimum energy abandonment of clean energy [19,20] and the minimum load fluctuation [21] are often taken as objectives, and a large number of scheduling models have been built [22], which ignore the benefits of pumped storage. However, if considered an independent market entity [23], pumped storage operators have the right to determine the scheduling mode by themselves to safeguard their own benefits.

The outline of the paper is described as follows. Section 2 includes ancillary service and semi-scheduling mechanism of pumped storage units. Section 3 outlines the semi-scheduling model. Section 4 highlights the risk–utility function used in the ancillary service market decision-making model. WSHTPC's mathematical model of the day-ahead market is built in Section 5. The case study and the results are discussed in Section 6. To conclude the work, a conclusion in Section 7 was given.

## 2. Ancillary Service and Semi-Scheduling Mechanism of Pumped Storage Units

### *2.1. Demand Analysis of Reserve Capacity*

In order to prompt the low-carbon development of the multi-energy system, the proportion of renewable energy access has been greatly improved, resulting in insufficient system adequacy. Thus, the difficulties of scheduling have become prominent. As shown in Figure 1, when renewable energy accesses the system, the demand for peak shaving, frequency regulation and rotating reserve of the net load curve increase significantly. In September 2021, the state issued the medium- and long-term development plan for pumped storage (2021–2035), which stated that as a low-carbon and adjustable power supply, pumped storage could quickly respond to market signals and has a good cooperation effect with wind power, PV power and thermal power [24]. When combined with China's energy resource conditions, pumped storage is the key way to meet the regulation demand of power systems at present and in the future. It plays an important role in ensuring the security of power systems and promoting the large-scale development and consumption of renewable energy [25].

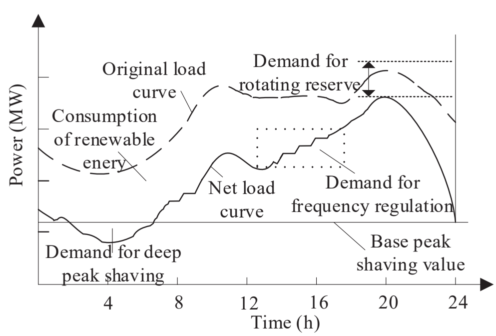


**Figure 1.** Schematic diagram of regulating demand of power systems.

### *2.2. Scheduling Mode of Pumped Storage*

Affected by power market reform and policy factors, it will be a new normal for pumped storage to participate in power market transactions as an independent market entity and obtain corresponding benefits. In the current power market environment in the United States, there are mainly three kinds of scheduling modes for pumped storage [26]. The characteristics of the three scheduling modes are shown in Table 1 [27].

**Table 1.** Comparison of Pumped Storage Scheduling Mode.

| Scheduling Mode | Declared Data | Optimized Objective | Joint [1]? | Technical Difficulty | Advantage | Disadvantage |
|---|---|---|---|---|---|---|
| Self-scheduling | Day-ahead output curve | Maximum operators benefit | No | Lower | Rapid clearing speed | High demand for electricity price forecast |
| Full-scheduling | Operating parameters | Maximum social benefit | Yes | Higher | Less system cost | Long simulation time |
| Semi-scheduling | Generating/pumping window and quotation | Minimum total quoted cost | Yes | Medium | Not considering the working state | Unable to reflect the real cost |

[1] Joint is whether the pumped storage units are jointly scheduled with conventional units.

In the self-scheduling mode, the output curve of pumped storage units, as the boundary condition of day-ahead market clearing, could be determined by the operators in advance. Thus, its obvious advantage is rapid clearing speed. However, it requires high accuracy of electricity price forecast. Pumped storage operators could make a profit with an accurate electricity price forecast. On the contrary, they may suffer great economic loss.

In the full-scheduling mode, pumped storage operators only need to provide the operating parameters. Additionally, pumped storage units are jointly scheduled with other units to maximize the social benefit. Thus, the pumped storage plays an important role in regulating the effect under this mode. However, it needs a long simulation time. The simulation time, in particular, is multiplied if there are a number of pumped storage units.

The semi-scheduling mode, being widely used in all independent system operators (ISO) except PJM, is a compromise between the self-scheduling mode and the full-scheduling mode. In the semi-scheduling mode, the pumped storage operators declared the generating/pumping window and quotation according to the price signals. Generally, the generating/pumping quotation, including electric energy quotation, frequency regulation quotation and rotating reserve quotation, reflects the unit generating/pumping cost value. Then, the pumped storage units and conventional units are jointly scheduled to achieve the goal of minimizing the total quotation cost [28,29].

Compared with the self-scheduling mode, the semi-scheduling mode can correct the unreasonable output results caused by the operator's prediction error of the electricity price, which brings greater benefits to the operator and the whole system. Compared with the full-scheduling mode, under the semi-scheduling mode, the pumped storage operators are profitable, and the working state of pumped storage units could be determined in advance, which could speed up the clearing process. Thus, considering the pumped storage operator's benefits and the whole system's benefits comprehensively, as well as the clearing process, the pumped storage semi-scheduling mode is a more appropriate choice for the initial power market.

As China's power market is still in its infancy, the market mechanism is imperfect, and the regulation pressure of the power system is huge, so we can not completely copy the semi-scheduling mode abroad. In order to achieve the win–win goal of pumped storage and power system, a novel semi-scheduling mode of pumped storage needs to be built on the basis of a stable power supply in China.

## 3. Semi-Scheduling Mode

### 3.1. Semi-Scheduling Flow

Based on the energy complementation, the process of semi-scheduling mode is shown in Figure 2. Firstly, based on the predicted information, including the curve of wind power, PV power, load and external electricity the next day, considering the system demand of frequency regulation and rotating reserve, the start-up combination of thermal power units was determined. Furthermore, considering that the pumped storage units generate electricity at the peak load period and pump water at the low load period, the working state of the pumped storage units is determined by predicting its generating/pumping power. Finally, the start-up combination of thermal power units, the working state of the pumped storage units, and the quotation of pumped storage operators are transmitted into the WSHTPC mathematical model as inputs.

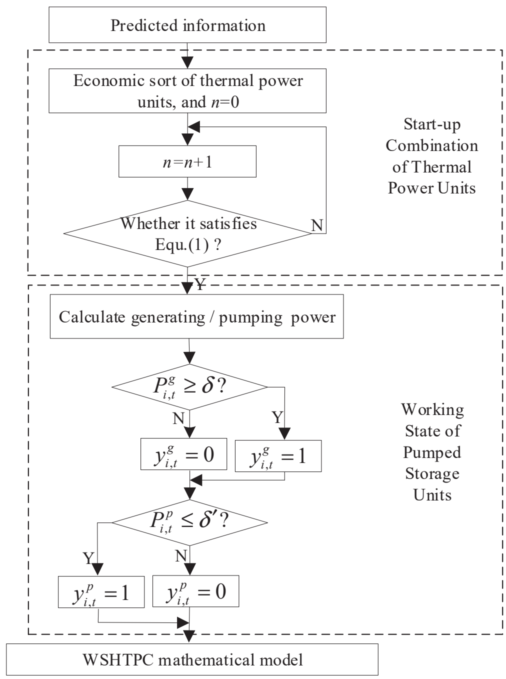


**Figure 2.** Semi-scheduling Flow Chart.

### 3.2. Start-Up Combination of Thermal Power Units

The large-scale access to renewable energy will lead to the redundancy of thermal power installed capacity in the power system. In order to avoid the imbalance between the power supply and the load demand, it is necessary to determine the start-up combination of thermal power units in advance. The specific steps are as follows:

S1: Economic sort of thermal power units according to the minimum specific consumption;

S2: On the premise that all wind power and PV power are consumed, and the hydropower and pumped storage units are fully generated, the maximum start-up combination of thermal power units is determined at the moment of maximum load. The start-up combination of thermal power units meets the following requirement:

$$\sum_{i=1}^{n-1} P_{i,\max}^{Th} < D_{e,\max} - P_{\max}^{E} - \sum_{i \in W} P_{i,\max}^{W} - \sum_{i \in S} P_{i,\max}^{S} - \sum_{i \in H} P_{i,\max}^{H} - C_p \cdot N_P + D_r + D_s \leq \sum_{i=1}^{n} P_{i,\max}^{Th} \tag{1}$$

where $n$ is the number of start-up combinations of the thermal power units; $W$, $S$ and $H$ are the set of wind power units, PV power units and hydropower units, respectively; the superscript of $Th$, $W$, $S$, $H$ and $E$ represent thermal power, wind power, PV power, hydropower and external electricity, respectively; $P_{i,\max}$ is the maximum output of unit $i$; $D_{e,\max}$ is the maximum load; $P_{\max}^{E}$ is the external electricity at the moment of maximum load; $C_p$ and $N_P$ are the installed capacity and the number of pumped storage units; $D_r$ and $D_s$ are the demand of frequency regulation and rotating reserve in the power system.

Generally speaking, the more thermal power units are started, the more frequency regulation and rotating reserve are provided. However, it should be noted that if the minimum technical output of thermal power units cannot be met during the low load period, the dispatcher should choose to shut down one thermal power unit or abandon some renewable energy according to the actual situation.

### *3.3. Working State of Pumped Storage Units*

The application of pumped storage can effectively lighten the peaking shaving task of thermal power units, and the thermal power units can undertake more base load and waist load of the power system to reduce their coal consumption. Thus, based on the determined start-up combination of thermal power units, considering that the pumped storage units generate electricity at the peak load period and pump water at the low load period, the working state of the pumped storage units is determined by predicting the generating/pumping power.

At the peak load period, the thermal power units generally operate at 100% installed capacity. By assuming that wind power, PV power and hydropower are consumed completely, the generating power of the pumped storage unit can be calculated according to Equation (2). If the generating power is greater than the threshold value, it indicates that the power supply is insufficient, and the pumped storage unit should be in the generating window to shave the load, as shown in Equation (4).

At the low load period, the thermal power unit generally operates at low load or is shut down directly. Considering that the basic peak shaving benchmark of the thermal power unit is 50% installed capacity when the basic peak shaving cannot meet the peak shaving demand, the pumped storage unit is usually in the pumping state. By assuming that wind power, PV power and hydropower are consumed completely and all thermal power units operate at 50% installed capacity, the pumping power of the pumped storage unit can be calculated according to Equation (3). If the pumping power is less than the threshold value, it indicates that the power supply is redundant, and the pumped storage unit should be in the pumping window to fill the load, as shown in Equation (5).

$$P_{i,t}^{g} = D_{e,t} - P_t^E - \sum_{i \in G} P_{i,\max}^{Th} - \sum_{i \in W} P_{i,t}^{W} - \sum_{i \in S} P_{i,t}^{S} \tag{2}$$

$$P_{i,t}^{p} = D_{e,t} - P_t^E - 0.5 \times \sum_{i \in G} P_{i,\max}^{Th} - \sum_{i \in W} P_{i,t}^{W} - \sum_{i \in S} P_{i,t}^{S} \tag{3}$$

$$y_{i,t}^{g} = \begin{cases} 1, & P_{i,t}^{g} \geq \delta \\ 0, & P_{i,t}^{g} < \delta \end{cases} \tag{4}$$

$$y_{i,t}^{p} = \begin{cases} 1, & P_{i,t}^{p} \leq \delta' \\ 0, & P_{i,t}^{p} > \delta' \end{cases} \tag{5}$$

where $G$ is the set of thermal power units; the superscript of $g$ and $p$ represent generating window and pumping window of pumped storage; $P_{i,t}^{g}$ and $P_{i,t}^{p}$ are the generating power and pumping power at time $t$; $D_{e,t}$ and $P_t^E$ are the load and the external electricity at time $t$; $P_{i,t}^{W}$ and $P_{i,t}^{S}$ are the output of wind power and PV power at time $t$; $y_{i,t}$ is the state variable of unit $i$ at time $t$; $\delta$ and $\delta'$ are power threshold values, which are set according to the system conditions and the installed capacity of pumped storage units.

## 4. Ancillary Service Market Decision-Making Model

Generally speaking, it is the obligation for pumped storage to stabilize the uncertainty of renewable energy output. The greater the uncertainty of renewable energy output, the more reserve capacity the pumped storage units need to provide, pumped storage units could make profits in the ancillary service market by providing reserve capacity, if pumped storage units sell too much reserve capacity, their opportunity cost of making profits in the real-time market will be affected. Thus, the allocation of reserve capacity for pumped storage units is a decision-making problem that needs to consider risks.

### 4.1. Risk–Utility Model of Pumped Storage Units

The risk attitudes of pumped storage units were divided into risk aversion and risk preference in this paper. Additionally, the risk attitude closely connects to the form of a utility function. Furthermore, the exponential function is a typical convex function, indicating that $y$ is sensitive to the increase in $x$, and the logarithmic function is a typical concave function, indicating that $y$ is slow to the increase in $x$. The two are the common analytic expression to express the utility curve by computing. Thus, the corresponding risk–utility functions can also be divided into the concave utility function and the convex utility function.

For risk-averse pumped storage units, with the increase in renewable energy output, the willingness of pumped storage units to provide reserve capacity decreases, which means the proportion of pumped storage units providing reserve capacity decreases. Then, the pumped storage unit is regarded as risk-averse, and its risk–utility function is constructed as the concave, the general form of logarithmic function [30], as shown in Equation (6).

$$U(x_t) = c_1 + a_1 \log(c_3 x_t + c_2) \tag{6}$$

where $x_t$ is the predicted output value of renewable energy at time $t$; $U(x_t)$ is the utility value of the pumped storage unit providing reserve capacity, called utility capacity; and $a_1$, $a_2$, $c_1$, $c_2$ and $c_3$ are parameters of the function.

For risk-preference pumped storage units, with the increase in renewable energy output, the willingness of the pumped storage unit to provide reserve capacity increases, which means the proportion of the pumped storage unit providing reserve capacity increases. Then, the pumped storage unit is regarded as a risk preference, and its risk–utility function is constructed as the convex, the general form of the exponential function, as shown in Equation (7).

$$U(x_t) = c_1 + a_1 \cdot e^{a_2 x_t + c_2} \tag{7}$$

### 4.2. Clearing Calculation

The clearing calculation process is shown in Figure 3. In the ancillary service market decision-making model, based on the predicted output values of renewable energy, including wind power and PV power the next day, assuming that the error of the actual output values of the renewable energy follows the normal distribution, a large number of actual output data are generated by Monte Carlo sampling method. Then, the output deviation is calculated between the actual value and the predicted value according to Equation (8), and generate the "output-deviation" scatter diagram. Furthermore, the risk attitude of the pumped storage unit is constructed according to Equations (6) and (7), and call *curve_fit* function on the Python platform to fit the risk–utility function. Finally, the declared capacity of reserve capacity is decided as shown in Equations (9)–(11).

$$\Delta P_{t,i} = |P_{t,i} - x_t| \tag{8}$$

where $\Delta P_{t,i}$ is the renewable energy output deviation $i$ at time $t$.

$$\overline{P}_{i,t}^{g} = \lambda \frac{U(x_t)}{N_P} \tag{9}$$

$$\overline{P}_{r,i,t}^{g} = \lambda_1 \cdot \overline{P}_{i,t}^{g} \tag{10}$$

$$\overline{P}_{s,i,t}^{g} = \lambda_2 \cdot \overline{P}_{i,t}^{g} \tag{11}$$

where $\overline{P}_{i,t}^{g}$ is the declared capacity of reserve capacity for the pumped storage unit $i$ at time $t$; $\overline{P}_{r,i,t}^{g}$ and $\overline{P}_{s,i,t}^{g}$ are declared capacity of frequency regulation and rotating reserve, respectively; $\lambda$, $\lambda_1$ and $\lambda_2$ are the capacity coefficients, which are set according to the output deviation of renewable energy and the installed capacity of pumped storage units.

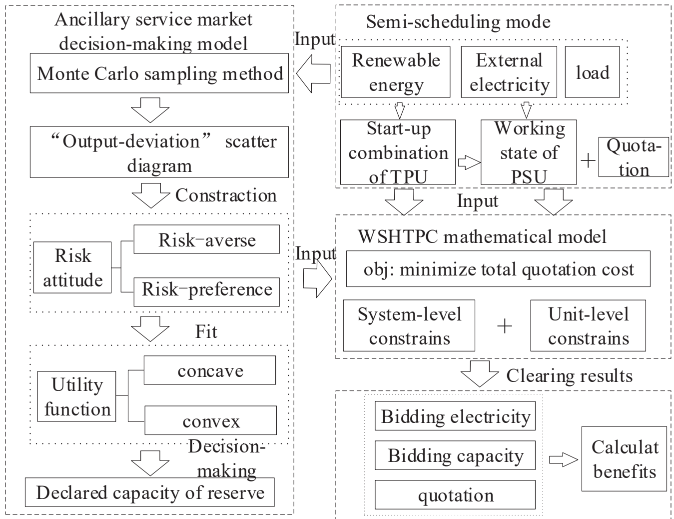


**Figure 3.** Framework of WSHTPC Model.

## 5. WSHTPC Mathematical Model of Day-Ahead Market

The overall framework of the WSHTPC model in the day-ahead market is shown in Figure 3, including the semi-scheduling mode, ancillary service market decision-making model and WSHTPC mathematical model. Firstly, the inputs were transmitted, including the start-up combination of thermal power units $n$, the working state of pumped storage units $y^g_{i,t}$ and $y^p_{i,t}$ in the semi-scheduling model, and the declared reserve capacity of pumped storage $\overline{P}^g_{r,i,t}$ and $\overline{P}^g_{s,i,t}$ in the ancillary service market decision-making model, into the WSHTPC mathematical model. Then, by taking the minimum total quotation cost as the objective, the clearing results of units were optimized by calling Gurobi Optimizer in the Python platform. Finally, the benefits in combination with the unit quotation were calculated.

### 5.1. Objective Function

Based on the quotation data and operating parameters of the units, according to Equations (13), (15) and (17), the quotation cost of the thermal power units, hydropower units and pumped storage units were calculated, respectively; Equation (14) represents the electricity generation cost function of thermal power units; Equation (16) represents the dynamic characteristic of hydropower units. Then, by taking the minimum total quotation cost as the objective as Equation (12), the clearing results in the day-ahead market were optimized, as shown below.

$$\min CTP + CHP + CPS \tag{12}$$

where $CTP$, $CHP$ and $CPS$ are quotation costs of thermal power units, hydropower units and pumped storage units, respectively.

$$CTP = \sum_{i \in G} \sum_{t \in T} \left( f_i(P^{Th}_{i,t}) \cdot y^{Th}_{i,t} + C^{Th}_{r,i,t} \cdot P^{Th}_{r,i,t} + C^{Th}_{s,i,t} \cdot P^{Th}_{s,i,t} \right) \tag{13}$$

$$f_i\left(P^{Th}_{i,t}\right) = a_i \cdot \left(P^{Th}_{i,t}\right)^2 + b_i \cdot P^{Th}_{i,t} + c_i \tag{14}$$

$$CHP = \sum_{i \in H} \sum_{t \in T} \left( C^g_{i,t} \cdot P^H_{i,t} \cdot y^H_{i,t} + C^g_{r,i,t} \cdot P^H_{r,i,t} + C^g_{s,i,t} \cdot P^H_{s,i,t} \right) \tag{15}$$

$$P^H_{i,t} = 9.81 y^H_{i,t} \eta^H_i q_{i,t} h_{i,t} \tag{16}$$

$$CPS = \sum_{i \in P} \sum_{t \in T_{g,i}} \left( C^g_{i,t} \cdot P^g_{i,t} \cdot y^g_{i,t} + C^g_{r,i,t} \cdot P^g_{r,i,t} + C^g_{s,i,t} \cdot P^g_{s,i,t} \right) + \sum_{i \in P} \sum_{t \in T_{p,i}} \left( -C^p_{i,t} \cdot P^p_{i,t} \cdot y^p_{i,t} + C^p_{r,i,t} \cdot P^p_{r,i,t} + C^p_{s,i,t} \cdot P^p_{s,i,t} \right) \quad (17)$$

where $P$ is the set of pumped storage units; $T$ is the scheduling time set; $P_{i,t}$ is the bidding electricity of unit $i$ at time $t$; $f_i(\cdot)$ is the electricity generation cost function of unit $i$, and $a_i$, $b_i$ and $c_i$ are power generation cost coefficient; $C_{r,i,t}$ and $P_{r,i,t}$ are quotation and bidding capacity of frequency regulation of unit $i$ at time $t$; $C_{s,i,t}$ and $P_{s,i,t}$ are quotation and bidding capacity of rotating reserve of unit $i$ at time $t$; $C_{i,t}$ is the quotation of electricity generation cost of unit $i$ at time $t$; $\eta_i^H$ is the efficiency of hydropower unit $i$.

### *5.2. Constraint Condition*

#### 5.2.1. System-Level Constraints

Equation (18) represents the load balance constraint; Equation (19) represents the constraint of system demand of frequency regulation; Equation (20) represents the constraint of system demand of reserve capacity.

$$\sum_{i \in G} P^{Th}_{i,t} + \sum_{i \in H} P^H_{i,t} + \sum_{i \in P} P^g_{i,t} + \sum_{i \in W} P^W_{i,t} + \sum_{i \in S} P^S_{i,t} + P^E_t = D_{e,t} + \sum_{i \in P} P^p_{i,t} + \sum_{i \in W} W^W_{i.t} + \sum_{i \in S} W^S_{i.t} \quad (18)$$

$$\sum_{i \in G} P^{Th}_{r,i,t} + \sum_{i \in H} P^H_{r,i,t} + \sum_{i \in P} \left( P^g_{r,i,t} + P^p_{r,i,t} \right) \geq D_r \quad (19)$$

$$\sum_{i \in G} (P^{Th}_{r,i,t} + P^{Th}_{s,i,t}) + \sum_{i \in H} (P^H_{r,i,t} + P^H_{s,i,t}) + \sum_{i \in P} (P^g_{r,i,t} + P^p_{r,i,t} + P^g_{s,i,t} + P^p_{s,i,t}) \geq D_r + D_s \quad (20)$$

where $W_{i,t}$ is the energy curtailment of unit $i$ at time $t$.

#### 5.2.2. Unit-Level Constraints

(1) Constraints of thermal power units, hydropower units and pumped storage units

Equations (21)–(24) represent the upper and lower limits constraints of bidding capacity of reserve capacity for thermal power units, hydropower units and pumped storage units. Equations (25) and (26) represent the climbing constraint of the above units.

$$0 \leq P_{r,i,t} \leq \overline{P}_{r,i,t} \quad (21)$$

$$0 \leq P_{s,i,t} \leq \overline{P}_{s,i,t} \quad (22)$$

$$P_{i,t} - P_{r,i,t} \geq y_{i,t} \cdot P_{i,\min} \quad (23)$$

$$P_{i,t} + P_{r,i,t} + P_{s,i,t} \leq y_{i,t} \cdot P_{i,\max} \quad (24)$$

$$P_{i,t} - P_{i,t-1} \leq r_{u,i} \quad (25)$$

$$P_{i,t-1} - P_{i,t} \leq r_{d,i} \quad (26)$$

where $\overline{P}_{r,i,t}$ and $\overline{P}_{s,i,t}$ are declared capacity of frequency regulation and rotating reserve of unit $i$; $P_{i,\max}$ and $P_{i,\min}$ are the maximum and minimum output of unit $i$; and $r_{u,i}$ and $r_{d,i}$ are climbing and landslide rate of unit $i$.

(2) Constraints of wind power units and PV power units

Equations (27) and (28) represent restriction constraints of wind curtailment and PV curtailment.

$$0 \leq W^W_{i,t} \leq P^W_{i,t} \quad (27)$$

$$0 \leq W^S_{i,t} \leq P^S_{i,t} \quad (28)$$

#### 5.2.3. Station-Level Constraints

Equation (29) represents the upper and lower limits constraint of upper reservoir capacity for the pumped storage station; Equation (30) represents the changing relationship of upper reservoir capacity for the pumped storage station; Equation (31) represents the upper reservoir capacity balance constraint for the pumped storage station.

$$V_{\min} \le V_t \le V_{\max} \tag{29}$$

$$V_t = V_{t-1} + \sum_{i \in P} P_{i,t}^{p} \eta_i^{p} \cdot \Delta t - \sum_{i \in P} P_{i,t}^{g} / \eta_i^{g} \cdot \Delta t \tag{30}$$

$$V_0 = V_T \tag{31}$$

where $\eta_i^g$ and $\eta_i^p$ are generating and pumping efficiency of pumped storage unit $i$.

## 6. Case Study

### *6.1. Basic Information*

In order to verify the effectiveness of the model, taking regional scheduling as an example, the scheduling cycle was set as 24 h, and the time scale was set as 1 h. The region includes 34 thermal power units; 4 pumped storage units; and multiple wind farms, PV power stations and hydropower stations. The total installed capacity of thermal power, pumped storage, wind power, PV power and hydropower are 17,160 MW, 1200 MW, 5000 MW, 3000 MW and 15,000 MW, respectively. This paper assumed that the maximum generating/pumping power of pumped storage units is 300 MW, the minimum generating/pumping power is 30 MW, and the generating/pumping efficiency is 0.85. The system demand for frequency regulation and the rotating reserve were taken as 3% and 5% of the maximum load, respectively. In terms of quotation, in order to simplify the calculation, for hydropower units and pumped storage units, it was assumed that the generating quotation and pumping quotation are CNY 210/MWh and CNY 138/MWh, respectively, and the frequency regulation quotation and the rotating reserve quotation are CNY 25/MW and CNY 13/MW, respectively. For thermal power units, it was assumed that the frequency regulation quotation and the rotating reserve quotation are CNY 64/MW and CNY 20/MW, respectively. In addition, the simulation model was optimized by calling Gurobi Optimizer in the Python platform.

The predicted curve of the wind power (WP), the PV power (PP), the external electricity (EE), the original load and the net load of a typical day are shown in Figure 4.

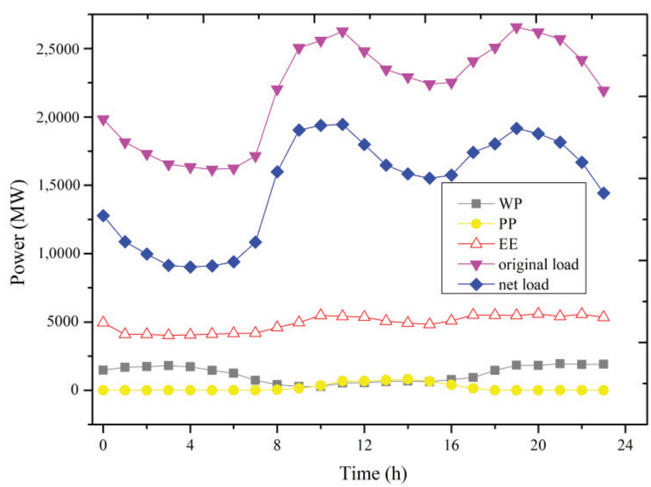


**Figure 4.** Input Data of Typical Day.

### *6.2. Benefit Analysis of Pumped Storage in Ancillary Service Market*

By taking the typical day as an example to analyze the benefits of pumped storage in the ancillary service market, assuming that the output error of renewable energy is 10%, the risk–utility functions of concave and convex were fitted. Three scenarios, low, medium and high penetration of renewable energy, were defined to simulate the uncertainty of renewable energy output.

The installed capacity of wind power units and PV power units of the basic information were set as the medium penetration of renewable energy.

The installed capacity of wind power units was set 0.5 times, and the installed capacity of PV power units as the low penetration of renewable energy was set 0.5 times.

The installed capacity of wind power units was set 1.2 times, and the installed capacity of PV power units as the high penetration of renewable energy was set 1.2 times.

According to the clearing calculation mentioned in 4.2, the fitting functions of risk–utility are shown in Figure 5. The green and yellow lines represent the concave and convex utility functions, respectively.

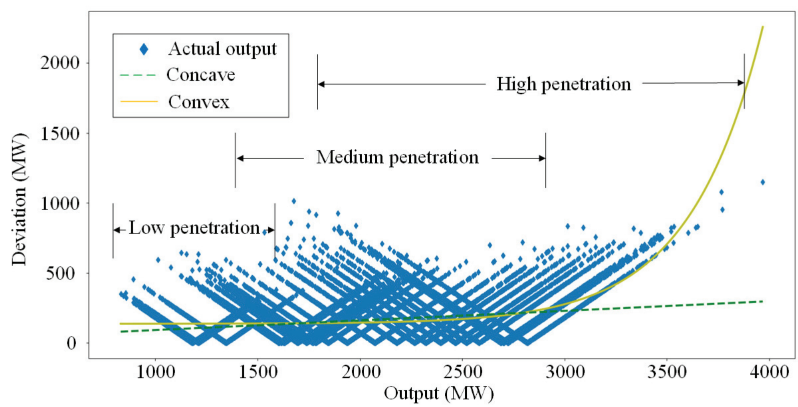


**Figure 5.** Fitting functions of risk–utility.

Table 2 shows the comparison of unit quotation costs under different penetration scenarios. Under the low, medium and high penetration of renewable energy, the number of start-up thermal power units is 32, 29 and 27, respectively, indicating that the higher the penetration of renewable energy, the lower the electricity cost of thermal power. Furthermore, pumped storage plays a more important role in capacity cost change, which reflects the reserve capacity, rather than electricity cost change, which reflects peak shaving. For example, in the low penetration of renewable energy, the electricity cost of pumped storage increased by 2.19% from CNY 47.89 million to CNY 48.94 million, and the capacity cost of pumped storage increased by 47.8% from CNY 11.61 million to CNY 17.16 million.

The relationship between risk–utility and pumped storage reserve capacity is analyzed. As shown in Figure 6a, in the low penetration of renewable energy, the convex function image is above the concave function image, indicating that as the risk-preference pumped storage units, the utility value of reserve capacity is large, with an average value of 141 MW, accounting for 11.75% of the installed capacity. Compared with the risk-averse, as the risk-preference pumped storage units, the electricity cost of peak shaving increases by CNY 1.05 million, and the capacity cost of reserve capacity increases by CNY 5.55 million, indicating the market performance is more active. However, the total quotation cost increased by CNY 1.16 million. Therefore, in the low penetration of renewable energy, if the purpose is to increase the benefits of the multi-energy system, it is suggested that the pumped storage units should be risk-averse to deal with the uncertainty of renewable energy output. However, if the purpose is to make full use of the ancillary service of pumped storage units, it is suggested that the pumped storage units should be a risk preference to deal with the uncertainty of renewable energy output.

**Table 2.** Comparison of units quotation cost under different penetration scenarios.

| Penetration Scenarios | Risk–Utility Function | Thermal Power | | Hydropower | | Pumped Storage | | |
|---|---|---|---|---|---|---|---|---|
| | | Electricity Cost /Million Yuan | Capacity Cost /Million Yuan | Electricity Cost /Million Yuan | Capacity Cost /Million Yuan | Electricity Cost /Million Yuan | Capacity Cost /Million Yuan | Total Cost /Million Yuan |
| Low | Concave | 7638.33 | 56.08 | 1765.23 | 43.68 | 47.89 | 11.61 | 9562.84 |
| | Convex | 7595.87 | 52.26 | 1809.85 | 39.88 | 48.94 | 17.16 | 9564.00 |
| Medium | Concave | 7217.36 | 47.62 | 1748.83 | 43.20 | 48.87 | 17.25 | 9123.16 |
| | Convex | 7208.83 | 47.51 | 1756.88 | 42.42 | 49.04 | 17.94 | 9122.63 |
| High | Concave | 6966.48 | 44.74 | 1739.63 | 43.44 | 49.15 | 18.97 | 8862.43 |
| | Convex | 6962.28 | 41.78 | 1742.93 | 43.00 | 49.16 | 21.23 | 8860.40 |

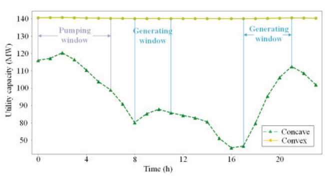


(**a**) low penetration

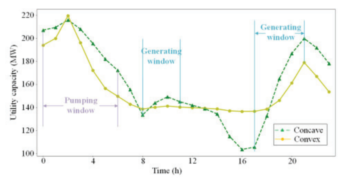


(**b**) medium penetration

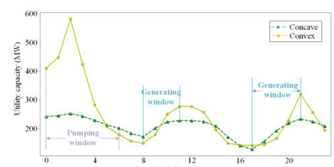


(**c**) high penetration

**Figure 6.** Utility Capacity of Pumped Storage.

As shown in Figure 6b, in the medium penetration of renewable energy, the pumped storage units are in the pumping state at times 0–6 and in the generating state at times 8–11 and 17–21. It can be seen from Figure 6b that during the above-mentioned period, there is little difference between the concave and convex function images enclosed by the coordinate axis. Compared with the risk-averse, as the risk-preference pumped storage units, the electricity cost of peak shaving increases by CNY 0.17 million, and the capacity cost of reserve capacity increases by CNY 0.69 million, indicating the market performance is slightly more active. Additionally, the total quotation cost decreases by CNY 0.53 million. Therefore, in the medium penetration of renewable energy, it is suggested that the pumped storage units should be a risk preference to deal with the uncertainty of renewable energy output.

As shown in Figure 6c, in the high penetration of renewable energy, similar to the medium penetration of renewable energy, compared with the risk-averse, as the risk-preference pumped storage units, the electricity cost of peak shaving increases by CNY 0.01 million, and the capacity cost of reserve capacity increases by CNY 2.26 million, indicating the market performance is slightly more active. Additionally, the total quotation cost decreased by CNY 2.03 million. Therefore, in the high penetration of renewable energy, it is suggested that the pumped storage units should be a risk preference to deal with the uncertainty of renewable energy output.

### 6.3. Benefit Analysis of Day-Ahead Scheduling

As shown in Table 3, in terms of simulation time, it is obvious that the simulation time of full-scheduling mode is longer, nearly double that of semi-scheduling mode. Moreover, in the semi-scheduling mode and the full-scheduling mode, the number of start-up thermal power units is the same, but the total cost is lower in the full-scheduling mode. The reasons may be as follows: On the one hand, the closer the thermal power output is to the rated value, the lower the marginal cost. In the full-scheduling mode, the increase in electricity cost of thermal power units indicates that their output is relatively large, which can correspondingly reduce the output of hydropower units and pumped storage units so that hydropower and pumped storage have room to play a regulating role. On the other hand, because the quotation of reserve capacity of hydropower units and pumped storage units are lower than that of thermal power units, the reserve capacity is provided by hydropower units and pumped storage units as far as possible, which results in less capacity cost of thermal power units in the full-scheduling mode.

**Table 3.** Comparison of 0ptimization results under different scheduling mode.

| | | Semi-Scheduling Mode | Full-Scheduling Mode | Without Pumped Storage |
|---|---|---|---|---|
| Simulation time | | 0.71 s | 1.36 s | 0.66 s |
| Number of thermal power units | | 29 | 29 | 32 |
| Thermal power units | Electricity cost/million yuan | 7217.36 | 7299.36 | 7396.34 |
| | Capacity cost/million yuan | 47.62 | 18.90 | 57.65 |
| Hydropower units | Electricity cost/million yuan | 1748.83 | 1683.24 | 1646.67 |
| | Capacity cost/million yuan | 43.20 | 52.94 | 54.19 |
| Pumped storage units | Electricity cost/million yuan | 48.87 | 21.60 | / |
| | Capacity cost/million yuan | 17.25 | 26.09 | / |
| | Total cost/million yuan | 9123.16 | 9102.16 | 9154.85 |

Compared with the semi-scheduling mode, in the scheduling mode without pumped storage, for thermal power units, the electricity cost increased from CNY 7217.36 million to CNY 7396.34 million, increasing by 2.48%, and the capacity cost increased from CNY 47.62 million to CNY 57.65 million, increasing by 21.06%. For hydropower units, the electricity cost decreased from CNY 1748.83 million to CNY 1646.67 million, decreasing by 5.84%, and the capacity cost increased from CNY 43.20 million to CNY 54.19 million, increasing by 25.44%. The increase or decrease in the electricity power cost of thermal power and hydropower is slight. It can be inferred that the three more thermal power units, replacing the pumped storage, are mainly to meet the reserve capacity in the scheduling mode without pumped storage.

As shown in Figure 7a, pumped storage units are in a pumping state at times 0–6 and in generating state at times 8–11 and 17–21. When comparing the scheduling result of wind power at time 0–6 in Figure 7a with that in Figure 7b, it is obvious that in the scheduling mode without pumped storage, the wind power consumption decreases. Generally, the wind power output is large at times 0–6. If there is not enough load consumption, it is bound to result in wind curtailment. However, in the semi-scheduling mode, the pumped storage units could be transformed to load to consume wind power.

Specifically, as shown in Figure 7c, there is no wind power curtailment at time 0–6 in the semi-scheduling mode, but the wind power curtailment is as high as 691.54 MW at time 4 in the scheduling mode without pumped storage. As shown in Figure 7d, the reserve capacity of pumped storage units is 648.89 MW at time 4. In this case, if the pumped storage is bundled with wind power, 93.83% of the wind power curtailment can be consumed in the scheduling mode without pumped storage.

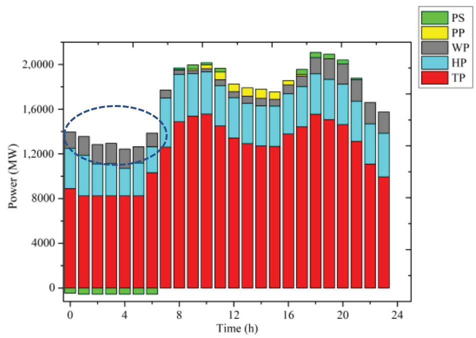


(**a**) semi-scheduling mode

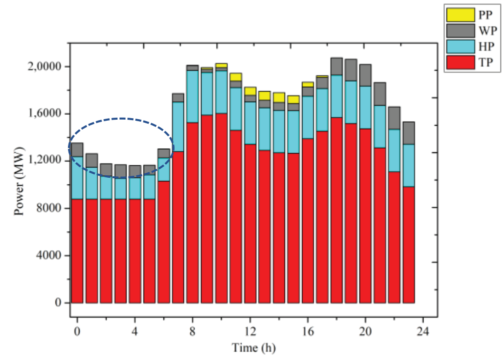


(**b**) without pumped storage

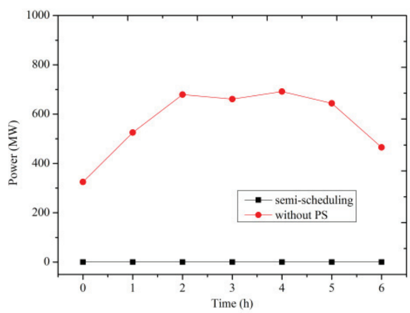


(**c**) wind curtailment

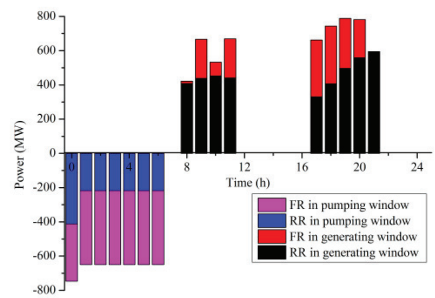


(**d**) reserve capacity of pumped storage

**Figure 7.** Scheduling results under semi-scheduling mode and scheduling mode without PS (PS means pumped storage, PP means PV power, WP means wind power, TP means thermal power, HP means hydropower, FR means frequency regulation and RR means rotating reserve).

## 7. Conclusions

As a low-carbon and adjustable power supply, pumped storage has great advantages in coping with the fluctuations and uncertainty of renewable energy. In this paper, a novel semi-scheduling mode and its solution method for the WSHTPC model were established. Additionally, the risk–utility was introduced to provide reserve capacity of pumped storage to promote the consumption of renewable energy. Then, aiming at minimizing the total quotation cost of thermal power, hydropower and pumped storage, the WSHTPC mathematical model was built to optimize scheduling in the day-ahead market.

Through the case study on the typical daily, the risk attitude of pumped storage responding to the uncertainty of renewable energy output in the ancillary service market can be determined: in the low penetration of renewable energy, considering the market performance of pumped storage and the benefit of the multi-energy system comprehensively, the risk attitude of pumped storage participating in the ancillary service market depends on the specific objectives; in the medium and high penetration of renewable energy, it is suggested that the pumped storage units should be a risk preference to deal with the uncertainty of renewable energy output. In addition, by taking a typical day as an example, through jointly scheduling with thermal power units and hydropower units, the regulating ability of pumped storage can be exploited to improve the benefit of the multi-energy system.

It should also be pointed out that under the background of the spot market, the optimal scheduling of the multi-energy system should comprehensively consider the influence of market factors such as bidding strategy, and the establishment of a complete spot market joint optimization model will be the next content in future research.

**Author Contributions:** X.Y. and Y.C. (Ye Cai) contributed to the experiment, measurement, manuscript concept, methodology, original draft writing, visualization and editing. Y.C. (Yijia Cao), S.D., L.T. and Z.J. contributed to the writing of sections, reviewing, visualization and editing. All authors have read and agreed to the published version of the manuscript.

**Funding:** This research was funded by the National Natural Science Foundation of China, grant number 52277076.

**Data Availability Statement:** The data presented in this study are available on request from the corresponding author.

**Conflicts of Interest:** The authors declare no conflict of interest.

## References

1. Mousumi, B. Dynamic economic dispatch with demand-side management incorporating renewable energy sources and pumped hydroelectric energy storage. *Electr. Eng.* **2019**, *101*, 877–893.
2. Vasilev, Y.S.; Elistratov, V.V.; Kudryasheva, I.G. Use of the flexibility characteristics of hydroelectric power plants and pumped-storage power plants in a power system with renewable energy sources. *Power Technol. Eng.* **2019**, *53*, 294–299. [CrossRef]
3. Zhou, X.; Chen, S.; Lu, Z.; Huang, Y.; Ma, S.; Zhao, Q. Technology features of the new generation power system in China. *Proc. CSEE* **2018**, *38*, 14–18. (In Chinese)
4. Wang, K.; Luo, X.; Li, Z.; Jia, R.; Zhou, C. Short-term coordinated scheduling of wind-pumped-hydro-thermal power system with multi-energy complementarities. *Power Syst. Technol.* **2020**, *44*, 3631–3640. (In Chinese)
5. Wang, X.; Chang, J.; Meng, X.; Wang, Y. Short-term hydro-thermal-wind-photovoltaic complementary operation of interconnected power systems. *Appl. Energy* **2018**, *229*, 945–962. [CrossRef]
6. Basu, M. Economic environmental dispatch of solar-wind-hydrothermal power system. *Renew. Energy Focus* **2019**, *30*, 107–122. [CrossRef]
7. Yang, L.; Zhang, Z.; Lu, X.; Wang, M.; Liang, J. Economic dispatch on power systems with wind power and pumped-storage station considering prohibited zones under influence of reserve capacity. *Power Syst. Technol.* **2017**, *41*, 1548–1553. (In Chinese)
8. Cui, D.; Xu, F.; Ge, W.; Huang, P.; Zhou, Y. A coordinated dispatching model considering generation and operation reserve in wind power-photovoltaic-pumped storage system. *Energies* **2020**, *13*, 4834. [CrossRef]
9. Cheng, C.; Su, C.; Wang, P.; Shen, J.; Lu, J.; Wu, X. An MILP-based model for short-term peak shaving operation of pumped-storage hydropower plants serving multiple power grids. *Energy* **2018**, *163*, 722–733. [CrossRef]
10. Blakers, A.; Stocks, M.; Lu, B.; Cheng, C. A review of pumped hydro energy storage. *Prog. Energy* **2021**, *3*, 22003. [CrossRef]
11. Liu, Y.; Wu, L.; Yang, Y.; Chen, Y.; Baldick, R.; Bo, R. Secured reserve scheduling of pumped-storage hydropower plants in ISO day-ahead market. *IEEE Trans. Power Syst.* **2021**, *36*, 5722–5733. [CrossRef]
12. Barbour, E.; Wilson, I.G.; Radcliffe, J.; Ding, Y.; Li, Y. A review of pumped hydro energy storage development in significant international electricity markets. *Renew. Sustain. Energy Rev.* **2016**, *61*, 421–432. [CrossRef]
13. Bafrani, A.A.; Rezazade, A.; Sedighizadeh, M. Robust electrical reserve and energy scheduling of power system considering hydro pumped storage units and renewable energy resources. *J. Energ. Storage* **2022**, *54*, 105310. [CrossRef]
14. Chazarra, M.; Pérez-Díaz, J.I.; García-González, J.; Helseth, A. Modeling the Real-Time Use of Reserves in the Joint Energy and Reserve Hourly Scheduling of a Pumped Storage Plant. In Proceedings of the 5th International Workshop on Hydro Scheduling in Competitive Electricity Markets, Trondheim, Norway, 17–18 September 2015.
15. Chazarra, M.; Perez-Diaz, J.I.; Garcia-Gonzalez, J. Optimal joint energy and secondary regulation reserve hourly scheduling of variable speed pumped storage hydropower plants. *IEEE Trans. Power Syst.* **2018**, *33*, 103–115. [CrossRef]
16. Xia, S.; Ding, Z.; Du, T.; Zhang, D.; Shahidehpour, M.; Ding, T. Multitime scale coordinated scheduling for the combined system of wind power, photovoltaic, thermal generator, hydro pumped storage, and batteries. *IEEE Trans. Ind. Appl.* **2020**, *56*, 2227–2237. [CrossRef]
17. Gao, R.; Wu, F.; Zou, Q.; Chen, J. Optimal dispatching of wind-PV-mine pumped storage power station: A case study in Lingxin Coal Mine in Ningxia Province, China. *Energy* **2022**, *243*, 123061. [CrossRef]
18. Karimi, A.; Heydari, S.L.; Kouchakmohseni, F.; Naghiloo, M. Scheduling and value of pumped storage hydropower plant in Iran power grid based on fuel-saving in thermal units. *J. Energ. Storage* **2019**, *24*, 100753. [CrossRef]
19. Liu, R.; Bao, Z.; Zheng, J.; Lu, L.; Yu, M. Two-stage robust and economic scheduling for electricity-heat integrated energy system under wind power uncertainty. *Energies* **2021**, *14*, 8434. [CrossRef]
20. Bitaraf, H.; Rahman, S. Reducing curtailed wind energy through energy storage and demand response. *IEEE Trans. Sustain. Energy* **2018**, *9*, 228–236. [CrossRef]

21. Kong, X.; Quan, S.; Sun, F.; Chen, Z.; Wang, X.; Zhou, Z. Two-stage optimal scheduling of large-scale renewable energy system considering the uncertainty of generation and load. *Appl. Sci.* **2020**, *10*, 971. [CrossRef]
22. Zhao, J.; He, Y.; Fang, Y.; Weng, Y.; Ma, W.; Xiao, S.; Liang, Y. Multi-source optimal dispatch considering ancillary service cost of pumped storage power station based on cooperative game. *Energy Rep.* **2021**, *7*, 173–186. [CrossRef]
23. Khani, H.; Zadeh, M.R.; Varma, R.K. Optimal scheduling of independently operated, locally controlled energy storage systems as dispatchable assets in a competitive electricity market. *IET Gener. Transm. Distrib.* **2017**, *11*, 1360–1369. [CrossRef]
24. National Energy Administration. The Medium and Long Term Development Plan for Pumped Storage (2021–2035). Available online: http://www.nea.gov.cn/2021-09/17/c_1310193456.htm (accessed on 17 September 2021).
25. Pronob, D.; Barun, D.; Nirendra, M.; Sakir, T. A review on pump-hydro storage for renewable and hybrid energy systems applications. *Energ. Storage* **2021**, *3*, 1–24.
26. Borenstein, S.; Bushnell, J. The US electricity industry after 20 years of restructuring. *Annu. Rev. Econ.* **2015**, *7*, 437–463. [CrossRef]
27. Liu, Y.H.; Zhang, X.; Sun, H.Y.; Feng, H. Analysis and enlightenment of pumped storage dispatch modes under American electricity market. *Autom. Electr. Power Syst.* **2021**, *45*, 1–11. (In Chinese)
28. A Configuration Based Pumped-Storage Hydro Unit Model in MISO Day-Ahead Market. Available online: https://www.ferc.gov/CalendarFiles/20190626080917-3-SessionW1BAConfigurationBasedPumped-storageHydroModel.pdf (accessed on 18 May 2022).
29. Reliable, Efficient and Incentive-Compatible Solutions for Operating Energy Storage in ISO/RTO Markets. Available online: https://www.ferc.gov/CalendarFiles/20170627124612-T3-B1,Ela,EPRI.pdf (accessed on 22 May 2020).
30. Qian, S.; Gan, Y.; Tian, F. *Operational Research*; Tsinghua University Press: Beijing, China, 2014; p. 494.

*energies*

*Article*

# The Definition of Power Grid Strength and Its Calculation Methods for Power Systems with High Proportion Nonsynchronous-Machine Sources

**Zheng Xu *, Nan Zhang, Zheren Zhang and Ying Huang**

Department of Electrical Engineering, Zhejiang University, Hangzhou 310027, China
* Correspondence: xuzheng007@zju.edu.cn

**Abstract:** This paper studies the definition and calculation method of power grid strength in the environment of high-proportion nonsynchronous-machine sources, focusing on the effect of nonsynchronous-machine sources on voltage support strength and frequency support strength. By dividing the nonsynchronous-machine sources into four types, the equivalent circuits of each type under normal state and fault state are derived, respectively. Based on the Thevenin equivalent impedance of the power grid and the equivalent impedance of the connected device, the definition and calculation method of voltage support strength is given, and the new meaning of single-infeed short-circuit ratio and multi-infeed short-circuit ratio in the context of high proportion nonsynchronous-machine sources is presented. Based on the initial frequency change rate and the steady-state frequency deviation of any node in the power grid under the maximum expected active power disturbance, the equivalent inertia lifting factor and steady-state frequency deviation decreasing factor are defined, respectively, to describe the contribution of nonsynchronous-machine sources to the power grid frequency support strength, and the calculation methods of the equivalent inertia lifting factor and the steady-state frequency deviation decreasing factor are given.

**Keywords:** power grid strength; voltage stiffness; short-circuit ratio; inertia; frequency change rate; frequency deviation factor

**Citation:** Xu, Z.; Zhang, N.; Zhang, Z.; Huang, Y. The Definition of Power Grid Strength and Its Calculation Methods for Power Systems with High Proportion Nonsynchronous-Machine Sources. *Energies* **2023**, *16*, 1842. https://doi.org/10.3390/en16041842

Academic Editors: Yong Li, Weiyu Wang and Junjie Ma

Received: 14 January 2023
Revised: 5 February 2023
Accepted: 10 February 2023
Published: 13 February 2023



## 1. Introduction

Power grid strength is one of the fundamental concepts of the power system. It is typically used to quantify the effect of interaction between the grid and the connected device, and the above-mentioned connected device can be a power source, a load, or a station of various types. The most straightforward explanation of power grid strength is the classic concept of an infinite power source. If a bus in the power system is referred to as an infinite power source, it has two connotations [1–3]: The first connotation is that the voltage amplitude of the bus will remain constant regardless of the type and capacity of the connected device, and the second connotation is that the voltage frequency of the bus will remain constant regardless of the type and capacity of the connected device. It can be seen that for the infinite power source, its voltage amplitude and frequency are not affected by the type and capacity of the connected device. For the actual power grid, the voltage amplitude and frequency of any bus must be affected by the type and capacity of the connected device, and the corresponding index describing the degree of effect is the power grid strength. Corresponding to the first connotation of an infinite power source, we use the voltage support strength to describe the degree of voltage amplitude change by the connection of the device, and corresponding to the second connotation of an infinite power source, we use the frequency support strength to describe the degree of voltage frequency change by the connection of the device. Thus, the so-called infinite power source can be understood as the power source with infinite grid strength.

In the traditional power system dominated by synchronous generators, the voltage support strength is usually represented by the short circuit ratio (SCR) [4–6]. The SCR is defined as the ratio of the three-phase short-circuit capacity of the connecting bus (the interface bus between the connected device and the grid, denoted as the point of common coupling (PCC) in the following) to the capacity of the connected device. The three-phase short-circuit capacity here refers to the short-circuit capacity provided by the synchronous generators. In traditional power systems, the typical application of SCR is to describe the power grid strength when the high voltage direct current (HVDC) transmission converter station is connected. It is generally believed that the HVDC transmission converter station can operate stably when SCR is greater than 3 [4–6].

With the transition from a traditional power system to a new type of power system with a high proportion of nonsynchronous-machine sources, it is unreasonable to continue using the conventional SCR definition to describe the voltage support strength. This is because the conventional SCR definition considers only the short-circuit current supplied by the synchronous generators, ignoring the contribution of nonsynchronous-machine sources. Then, a question naturally arises: if the short-circuit current of the nonsynchronous-machine source is considered in the calculation of the SCR, is it still possible to utilize the conventional SCR definition to characterize the voltage support strength? The answer is no, and the reasons for this statement will be presented in later sections of this paper. For the new type of power system, the voltage support strength indexes extended from the conventional SCR definition have been extensively studied. Reference [7] proposes a generalized short circuit ratio (GSCR) based on a modal method to decouple the multi-infeed system. However, the modal method is difficult to calculate, so its engineering applicability is limited. Reference [8] presents a multiple renewable energy station short circuit ratio (MRSCR) based on the ratio of system short circuit capacity to grid-connected capacity of new energy, which has engineering applicability. However, the precision of its calculations is insufficient because only the external properties of new energy as current sources are considered. Therefore, how to define the voltage support strength in the new type of power system considering both accuracy and engineering applicability is a pressing issue that must be tackled [9,10].

In the actual power system, frequency support strength usually exhibits its meaning in two dimensions. The first is the inertia support capability [1–3], which describes the initial frequency change rate after an active power disturbance to the power grid. The second is the primary frequency regulation capability [1–3], which describes the amount of active power that the power grid can absorb or release during the frequency deviation.

In the traditional power system dominated by synchronous generators, the inertia support capability can be expressed by the kinetic energy stored in the rotors of the synchronous generators in the entire grid, and its unit is MWs. It can also be described by the equivalent inertia time constant of the whole grid $H$. In other words, $H$ is the time required for the kinetic energy stored in the rotors of grid-wide synchronous generators to be released to zero at the constant active power equaling the total capacity of the grid-wide synchronous generators in the unit of second. For the calculation of inertia and the minimum inertia demand, there have been numerous pertinent discussions in the literature [11–22] from the generating unit and system perspectives. In contrast to the synchronous generator, where the inertia is constant, the inertia of the nonsynchronous-machine source is dependent on its control system, and the amount of the inertia varies with the change of the operating point of the nonsynchronous-machine source. Therefore, the total inertia of the system changes with the operation state from the system's perspective. However, how to calculate the inertia support capability in the power system where synchronous generators and nonsynchronous-machine sources coexist is an issue to be solved.

In the traditional power system dominated by synchronous generators, the primary frequency regulation capability is typically described by the frequency deviation factor $\beta$ [1–3], which is related to the droops of the synchronous generator governors and the frequency sensitivity coefficient of the active load of the whole grid. The unit of $\beta$ is MW/(0.1 Hz). However, in the power system where synchronous generators and nonsynchronous-machine sources coexist, how to account for the primary frequency regulation capability of the nonsynchronous-machine sources is an urgent problem to be solved.

In this paper, the expressions and the calculation methods of the power grid strength for the power system with high proportion nonsynchronous-machine sources are examined, including the voltage support strength, the inertia support capability, and the primary frequency regulation capability. The rest of the paper is organized as follows. Section 2 discusses the classification and description of the external characteristics of the nonsynchronous-machine sources; Section 3 describes the operating states and their corresponding equivalent circuits for the nonsynchronous-machine sources. Section 4 addresses the definition and calculation method of the voltage support strength at any point in the power grid. Section 5 explores the new meaning of the single-infeed SCR and the multi-infeed SCR. Section 6 addresses the definition and calculation method of the frequency support strength in the power system where synchronous generators and nonsynchronous-machine sources coexist. Finally, Section 7 draws on the conclusion.

## 2. Classification and Description of the External Characteristics of Nonsynchronous-Machine Sources

The typical structure of nonsynchronous-machine sources is shown in Figure 1 [23]. In Figure 1, $U_{dc}$ and $i_{dc}$ represent the DC voltage and DC current of the voltage source converter (VSC), respectively; $u_v$ and $u_s$ represent the valve-side voltage and the grid-side AC bus voltage of the VSC respectively; $P_s$ and $Q_s$ represent the active power and the reactive power input to the AC grid respectively. On the whole, nonsynchronous-machine sources can be categorized as either grid-forming or grid-following sources [24–31]. The external characteristic of the grid-forming source is an adjustable voltage source, and when its active power is adjustable in a wide range, it can serve as a support source of a passive grid. The external characteristic of the grid-following source is an adjustable current source, and the grid-following source must be connected to the active power grid.

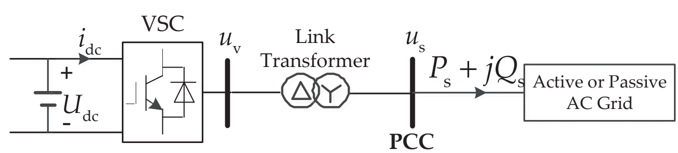


**Figure 1.** Typical structure of nonsynchronous-machine sources.

### 2.1. Classification and Controller Structure of Grid-Forming Nonsynchronous-Machine Sources

The grid-forming nonsynchronous-machine sources can be further subdivided into two types according to their active power adjustable capability. The first type is referred to as the Vθ type grid-forming nonsynchronous-machine source, and the second type is referred to as the PV-type grid-forming nonsynchronous-machine source.

#### 2.1.1. Vθ Type Grid-Forming Nonsynchronous-Machine Source

The Vθ type grid-forming nonsynchronous-machine source is characterized by maintaining the amplitude $U_{sm}$ and frequency $f$ of the AC bus voltage at the reference values. For the typical structure of the nonsynchronous-machine sources depicted in Figure 1, the prerequisite for becoming a Vθ type grid-forming nonsynchronous-machine source is that $U_{dc}$ remains essentially constant when the active power output by the VSC to the AC grid varies substantially. Moreover, maintaining a constant $U_{dc}$ is the duty of the external circuit connecting to the DC side of the VSC, not the VSC itself. If the external characteristic of the

Vθ type grid-forming nonsynchronous-machine source is seen from the PCC of the AC grid, it is just analogous to the slack bus in the power flow calculation. In other words, it plays a role in voltage support and power balance in the AC grid. As depicted in Figure 2, the general structure of the controller of the Vθ type grid-forming nonsynchronous-machine source is a three-loop controller. The outermost controller loop is the V/f generator, which determines the reference values of the voltage amplitude $U_{\mathrm{sm}}^{*}$ and frequency $f^{*}$ of the AC bus voltage us, based on the operating conditions of the DC side of VSC, VSC itself, and the AC grid. The rest dual-loop controller consists of the typical inner and outer loop controllers, where the control principles are mature [32–34] and will not be described here. The inner and outer loop controllers in Figure 2 operate according to $U_{\mathrm{sm}}^{*}$ and the phase angle reference value $\theta^{*}$; and both the $d$-axis and $q$-axis current reference values $i_{\mathrm{vd}}^{*}$ and $i_{\mathrm{vq}}^{*}$ are subjected to the current limiters to prevent the VSC from overcurrent. Besides, $u_{\mathrm{vd}}^{*}$ and $u_{\mathrm{vq}}^{*}$ represent the $d$-axis and $q$-axis voltage reference values output by the inner loop current controller, respectively.

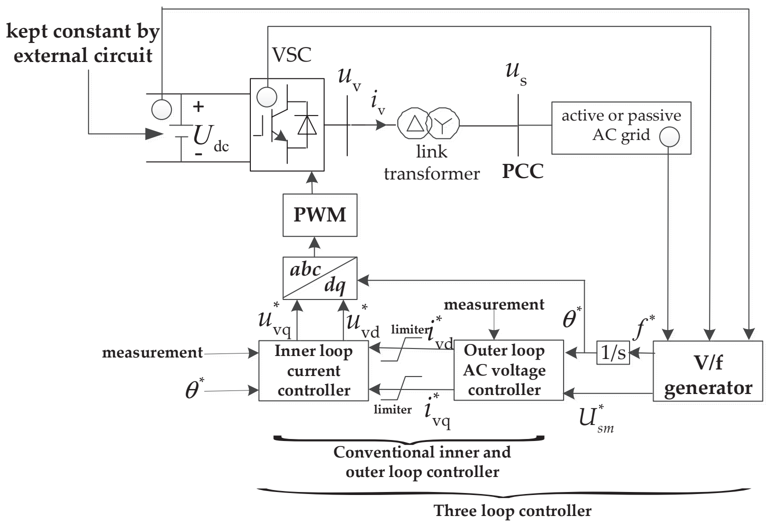


**Figure 2.** Three-loop controller diagram of the Vθ type grid-forming nonsynchronous-machine source.

### 2.1.2. PV Type Grid-Forming Nonsynchronous-Machine Sources

The PV-type grid-forming nonsynchronous-machine source is characterized by maintaining $U_{\mathrm{sm}}$ at $U_{\mathrm{sm}}^{*}$ and adjusting the phase angle $\theta$ to maintain $U_{\mathrm{dc}}$ at its reference value $U_{\mathrm{dc}}^{*}$. The PV-type grid-forming nonsynchronous-machine source corresponds to the photovoltaic units or wind turbines. The following contents use the photovoltaic unit as an illustration of the characteristics of the PV-type grid-forming nonsynchronous-machine source. Assume that the nonsynchronous-machine source shown in Figure 1 is a photovoltaic unit. Under the Maximum Power Point Tracking (MPPT) control condition [35], the reference value $U_{\mathrm{dc}}^{*}$ of $U_{\mathrm{dc}}$ is determined by the requirement of the MPPT control; and if the condition of $U_{\mathrm{dc}}$ equaling $U_{\mathrm{dc}}^{*}$ is reached, the phase angle $\theta$ is set down, and the output active power $P_{\mathrm{s}}$ of VSC is equal to the maximum generating power of the photovoltaic unit. That is, the PV-type grid-forming nonsynchronous-machine source can maintain its AC bus voltage amplitude at its reference value and set down its AC bus voltage phase angle $\theta$ according to the value of $P_{\mathrm{s}}$. However, $P_{\mathrm{s}}$ is changing continuously and equaling the maximum generating power of the photovoltaic unit. Note that the fundamental difference between the PV-type grid-forming nonsynchronous-machine source and Vθ type grid-forming nonsynchronous-machine source is whether it can be used as an independent support source for the passive power grid. The PV-type grid-forming nonsynchronous-machine source can only operate when connected to the active power grid. If the external characteristic of the PV-type grid-forming nonsynchronous-machine source is seen from the PCC of the AC grid, it is analogous to the PV bus in the power flow calculation. In other words, it supports voltage and outputting determinate active power in the grid. As depicted in Figure 3, the general structure of the controller of the PV-type grid-forming nonsynchronous-machine source is also a three-loop controller. The outermost controller loop is the V/θ generator, which determines $\theta^*$ by maintaining $U_{dc}$ at $U_{dc}^*$, and determines $U_{sm}^*$ based on the operating conditions of the AC grid. The rest dual-loop controller is the same as that in Figure 2.

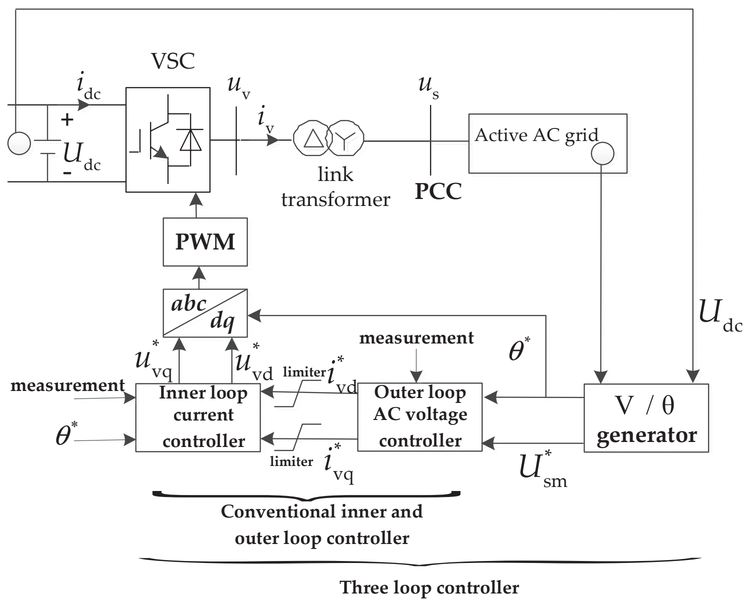


**Figure 3.** Three-loop controller diagram of the PV type grid-forming nonsynchronous-machine source.

### 2.2. *Classification and Controller Structure of Grid-Following Nonsynchronous-Machine Sources*

According to whether the grid-following nonsynchronous-machine sources are capable of supporting the AC bus voltage, they can be further subdivided into two types: the PV type grid-following nonsynchronous-machine source and the PQ type grid-following nonsynchronous-machine source. The fundamental difference between the grid-following nonsynchronous-machine sources and the grid-forming nonsynchronous-machine sources is whether the phase-locked loop (PLL) is adopted to keep synchronization with the grid [36–41]. Therefore, the grid-following nonsynchronous-machine sources can only operate when connected to the active power grid.

#### 2.2.1. PV Type Grid-Following Nonsynchronous-Machine Sources

The first type of grid-following nonsynchronous-machine source is referred to as the PV type grid-following nonsynchronous-machine source, where the grid synchronization $\theta$ is obtained by PLL. The purpose of reactive power control is to maintain $U_{sm}$ at $U_{sm}^*$, while the objective of active power control is to maintain $U_{dc}$ and $P_s$ at their respective reference values $U_{dc}^*$ and $P_s^*$. If the external characteristic of the PV-type grid-following nonsynchronous-machine source is seen from the PCC of the AC grid, it is analogous to the PV bus in the power flow calculation. In other words, it plays the role of supporting voltage and outputting determinate active power in the grid. The difference between the PV-type grid-following nonsynchronous-machine source and the PV-type grid-forming nonsynchronous-machine source is only the control strategy, so the same photovoltaic unit or wind turbine can be constructed as either a PV-type grid-following nonsynchronous-machine source or a PV type grid-forming nonsynchronous-machine source. As depicted in Figure 4, the general structure of the controller of the PV-type grid-following nonsynchronous-machine source is also a three-loop controller. The outermost controller loop is the P/V generator, which determines $P_s^*$ and $U_{sm}^*$ based on the operating conditions of the DC side of the VSC and the AC grid. The rest dual-loop controller consists of the typical inner and outer loop controllers, which are very mature and widely accepted.

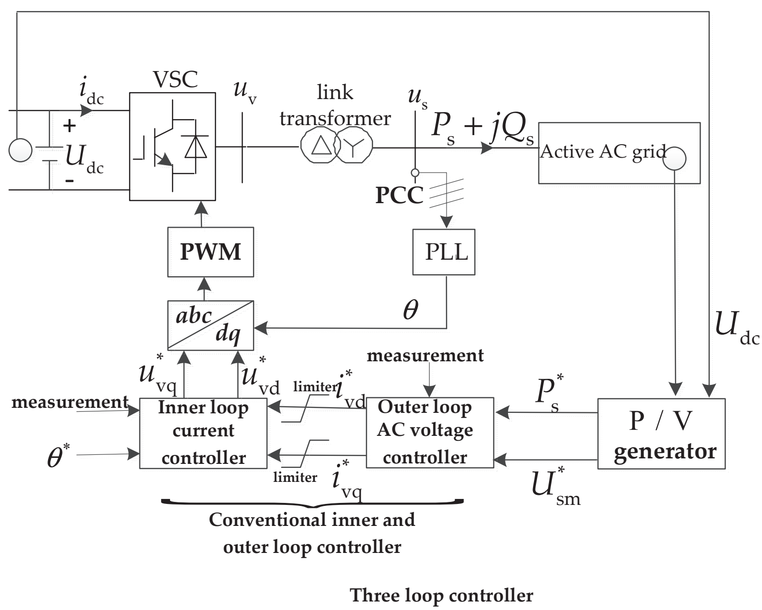


**Figure 4.** Three-loop controller diagram of the PV type grid-following nonsynchronous-machine source.

### 2.2.2. PQ Type Grid-Following Nonsynchronous-Machine Sources

The second type of grid-following nonsynchronous-machine source is referred to as the PQ-type grid-following nonsynchronous-machine source, where the control strategy is the same as that of the PV-type grid-following nonsynchronous-machine source. The difference is only in the purpose of the reactive power control. The purpose of the reactive power control of the PQ-type grid-following nonsynchronous-machine source is to maintain the VSC output reactive power $Q_s$ at its reference value $Q_s^*$. If the external characteristic of the PQ-type grid-following nonsynchronous-machine source is seen from the PCC of the AC grid, it is analogous to the PQ bus in the power flow calculation and injects active and reactive power to the grid. As depicted in Figure 5, the general structure of the controller of the PQ-type grid-following nonsynchronous-machine source is also a three-loop controller. The outermost controller loop is the P/Q generator, which determines $P_s^*$ and $Q_s^*$ based on the operating conditions of the DC side of VSC and the AC grid. The rest dual-loop controller is similar to that in Figure 4.

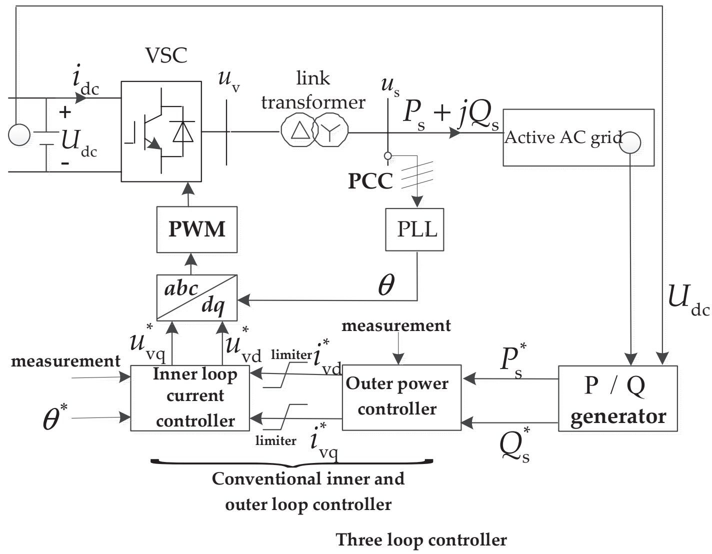


**Figure 5.** Three loop controller diagram of the PQ type grid-following nonsynchronous-machine source.

## 3. Operating State and External Characteristic Equivalent Circuits of Nonsynchronous-Machine Sources

For the four types of nonsynchronous-machine sources described in Section 2, if the three-loop controller shown in Figures 2–5 is used, the outermost loop controller determines the synchronization signal $\theta^*$ or the active power reference value ($P_s^*$ or $U_{dc}^*$) and the reactive power reference value ($Q_s^*$ or $U_{sm}^*$). The actual control objective is then accomplished by the conventional inner and outer loop controllers, and the final control block adopts the inner loop current controller with direct current control [32–34]. Because of the limiters of $i_{vd}^*$ and $i_{vq}^*$ in the inner loop current controller, once the limiter is activated, the nonsynchronous-machine source enters the current saturation state; and the output of the inner loop current controller can no longer achieve the outer loop controller's predetermined control target. Thus, the external characteristic of the nonsynchronous-machine source depends on whether the inner loop current controller operates in the limiter state. Clearly, the voltage amplitude at the PCC is the primary cause for the inner loop current controller entering the limiter state. Based on the voltage drop range of the PCC, the operating states of the nonsynchronous-machine sources can be classified into two types: the normal state and the fault state. Under the normal state, the voltage of the PCC is close to the rated value, and $i_{vd}^*$ and $i_{vq}^*$ will not exceed the limit values, allowing the nonsynchronous-machine sources to reach the predetermined control target. Under the fault state, the voltage drop of the PCC is relatively large, forcing $i_{vd}^*$ and $i_{vq}^*$ equalling the current limit values. That is, the nonsynchronous-machine source enters the current saturation state and is unable to attain the predetermined control target. The following describes the external characteristic equivalent circuits of the aforementioned four nonsynchronous-machine source types under their normal and fault states.

### *3.1. External Characteristic Equivalent Circuits of Nonsynchronous-Machine Sources under the Normal State*

Under the normal state, a Vθ type grid-forming nonsynchronous-machine source can be equivalent to a voltage source with the constant voltage amplitude and frequency connected to the PCC as viewed from the AC grid.

Under the normal state, a PV-type grid-forming or grid-following nonsynchronous-machine source can be equivalent to a voltage source with the constant voltage amplitude and phase angle connected to the PCC.

Under the normal state, a PQ-type grid-following nonsynchronous-machine source can be equivalent to a current source with a constant current amplitude and phase angle.

### *3.2. External Characteristic Equivalent Circuits of Nonsynchronous-Machine Sources under the Fault State*

Under the fault state, $i_{\mathrm{vd}}^{*}$ and $i_{\mathrm{vq}}^{*}$ equal to the current limit values, the nonsynchronous-machine source enters the current saturation state. Therefore, the nonsynchronous-machine source can be equivalent to a current source with a constant current amplitude and phase angle.

## **4. Definition and Calculation of Voltage Support Strength at Any Point in the Grid**

### *4.1. Relationship between Thevenin Equivalent Impedance and SCR at Any Bus in the Grid*

When exploring the voltage support strength of the power grid, the positive-sequence AC power grid operating at the fundamental frequency is the objective of the investigation. Then, based on the Thevenin equivalence theorem [42,43], when viewed from any bus SYS in the grid, the entire grid can be represented by a Thevenin equivalent circuit, as illustrated in Figure 6. The Thevenin equivalent circuit is composed of the Thevenin equivalent electromotive force $\underline{E}_{\mathrm{th}} = E_{\mathrm{th}}\angle\theta_{\mathrm{th}}$ and the Thevenin equivalent impedance $\underline{Z}_{\mathrm{th}} = Z_{\mathrm{th}}\angle\varphi_{\mathrm{th}}$ connected in series. (Note that this paper represents the complex number with a line at the bottom of the variable). When the device is not connected to the grid, $\underline{E}_{\mathrm{th}}$ equals the no-load voltage at SYS $\underline{U}_{\mathrm{sys0}} = U_{\mathrm{sys0}}\angle\theta_{\mathrm{sys0}}$. $\underline{Z}_{\mathrm{th}}$ equals the equivalent impedance when all the independent sources in the fundamental-frequency positive-sequence grid are set to zero, as seen from SYS to the grid.

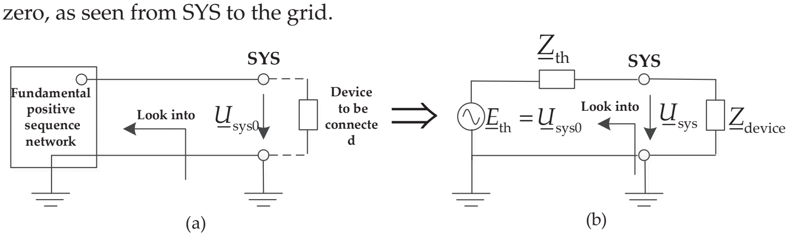


**Figure 6.** Thevenin equivalence principle of a power grid: (**a**) before the device is connected to the grid; (**b**) after the device is connected to the grid.

The following discussion assumes that when the device is not connected to the grid, the magnitude of the no-load voltage at SYS $U_{\mathrm{sys0}}$ is equal to the rated voltage $U_{\mathrm{N}}$.

Thus, according to Figure 6b, the short-circuit capacity $S_{\mathrm{sc}}$ at SYS can be calculated as follows:

$$S_{\mathrm{sc}} = \frac{E_{\mathrm{th}}^2}{Z_{\mathrm{th}}} = \frac{U_{\mathrm{sys0}}^2}{Z_{\mathrm{th}}} = \frac{U_{\mathrm{N}}^2}{Z_{\mathrm{th}}} \tag{1}$$

If the impedance of the connected device is $\underline{Z}_{\mathrm{device}} = Z_{\mathrm{device}}\angle\varphi_{\mathrm{device}}$, the capacity of the connected device at the rated voltage $S_{\mathrm{device}}$ is calculated as (2).

$$S_{\mathrm{device}} = \frac{U_{\mathrm{N}}^2}{Z_{\mathrm{device}}} \tag{2}$$

Then, the short circuit ratio $\lambda_{\mathrm{SCR}}$ of bus SYS corresponding to $\underline{Z}_{\mathrm{device}}$ is:

$$\lambda_{\mathrm{SCR}} = \frac{S_{\mathrm{sc}}}{S_{\mathrm{device}}} = \frac{U_{\mathrm{N}}^2}{Z_{\mathrm{th}}} \cdot \frac{Z_{\mathrm{device}}}{U_{\mathrm{N}}^2} = \frac{Z_{\mathrm{device}}}{Z_{\mathrm{th}}} \tag{3}$$

Next, we investigate how the device voltage, namely the voltage of bus SYS $\underline{U}_{\text{sys}} = U_{\text{sys}}\angle\theta_{\text{sys}}$, changes after the device is connected to the grid.

According to Figure 6b,

$$\begin{aligned}\underline{U}_{\text{sys}} &= \frac{\underline{Z}_{\text{device}}}{\underline{Z}_{\text{device}}+\underline{Z}_{\text{th}}}\underline{U}_{\text{sys0}} \\ &= \frac{\lambda_{\text{SCR}}\angle(\varphi_{\text{device}}-\varphi_{\text{th}})}{1+\lambda_{\text{SCR}}\angle(\varphi_{\text{device}}-\varphi_{\text{th}})}U_{\text{sys0}}\angle\theta_{\text{sys0}}\end{aligned} \tag{4}$$

According to (4), after the $\underline{Z}_{\text{device}}$ is connected to the grid, the magnitude of the device voltage $U_{\text{sys}}$ changes with $\lambda_{\text{SCR}}$, $\varphi_{\text{device}}$, and $\varphi_{\text{th}}$. Considering a typical case, the Thevenin equivalent impedance of the grid is purely inductive, while the equivalent impedance of the connected device is purely resistive, namely, $\varphi_{\text{th}} = 90°$ and $\varphi_{\text{device}} = 0°$, respectively. Under such circumstances, the expression of $U_{\text{sys}}$ can be simplified to (5).

$$U_{\text{sys}} = \frac{\lambda_{\text{SCR}}}{\sqrt{1+\lambda_{\text{SCR}}^2}}U_{\text{sys0}} = \frac{\lambda_{\text{SCR}}}{\sqrt{1+\lambda_{\text{SCR}}^2}}U_{\text{N}} \tag{5}$$

Based on (5), if $\lambda_{\text{SCR}} >> 1$, $U_{\text{sys}} \approx U_{\text{N}}$. Otherwise, $U_{\text{sys}}$ is always less than $U_{\text{N}}$. The variation characteristic of $U_{\text{sys}}$ with $\lambda_{\text{SCR}}$ is shown in Figure 7. When $\lambda_{\text{SCR}} = 5$, $U_{\text{sys}} = 0.98U_{\text{N}}$; when $\lambda_{\text{SCR}} = 3$, $U_{\text{sys}} = 0.95U_{\text{N}}$; and when $\lambda_{\text{SCR}} = 1$, $U_{\text{sys}} = 0.71U_{\text{N}}$. Consequently, it is commonly believed that when SCR is larger than 3, then SYS is a strong bus, as the voltage drop after being loaded is less than 5% of the rated voltage.

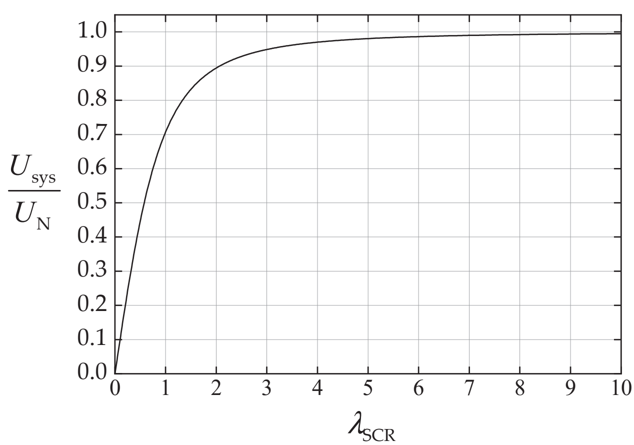


**Figure 7.** Variation of device voltage with the short-circuit ratio.

### *4.2. Definition of Voltage Support Strength of Any Bus in the Grid*

Inspired by the concept of infinite power source, the voltage support strength of any bus in the grid is defined as the ability to maintain the voltage magnitude close to the no-load voltage. It is described by $U_{\text{sys}}/U_{\text{sys0}}$, which is called the voltage stiffness $K_{\text{vtg}}$. Then according to (4),

$$\begin{aligned}K_{\text{vtg}} &= \frac{U_{\text{sys}}}{U_{\text{sys0}}} = \left|\frac{\underline{Z}_{\text{device}}}{\underline{Z}_{\text{th}}+\underline{Z}_{\text{device}}}\right| \\ &= \left|\frac{\lambda_{\text{SCR}}\angle(\varphi_{\text{device}}-\varphi_{\text{th}})}{1+\lambda_{\text{SCR}}\angle(\varphi_{\text{device}}-\varphi_{\text{th}})}\right|\end{aligned} \tag{6}$$

Obviously, the range of $K_{\text{vtg}}$ is [0, 1]. When $Z_{\text{th}}$ is zero, $K_{\text{vtg}}$ is equal to 1; and when $Z_{\text{th}}$ is infinity, $K_{\text{vtg}}$ equals zero.

Comparing $K_{\text{vtg}}$ to $\lambda_{\text{SCR}}$, $K_{\text{vtg}}$ provides more grid information than $\lambda_{\text{SCR}}$. $\lambda_{\text{SCR}}$ reflects only the magnitude of $\underline{Z}_{\text{th}}$ and $\underline{Z}_{\text{device}}$, but not their phase angles. In addition, the range of $\lambda_{SCR}$ is [0, ∞], while the range of $K_{vtg}$ is [0, 1]. Figure 7 can also be regarded as the relationship between short circuit ratio and voltage stiffness under a specific condition.

### *4.3. Definition of Voltage Support Strength of Any Bus in the Grid*

According to (6), $K_{vtg}$ is uniquely determined by $\underline{Z}_{th}$ and $\underline{Z}_{device}$. Due to the known impedance of the connected device $\underline{Z}_{device}$, the calculation of $K_{vtg}$ is equivalent to the calculation of $\underline{Z}_{th}$.

The external characteristic equivalent circuit of a nonsynchronous-machine source is closely related to its operating states, as determined by the analysis in Section 2. Consequently, the calculation of $\underline{Z}_{th}$ at any bus in the grid is closely related to the operating states of the nonsynchronous-machine source. Therefore, each nonsynchronous-machine source must be calculated by the equivalent circuit under the corresponding state.

In accordance with the calculation principle of the Thevenin equivalence impedance $\underline{Z}_{th}$, each independent source in the fundamental-frequency positive-sequence grid is set to zero. This indicates that a branch represents the voltage source is replaced with a short circuit to the ground, and the current source is represented by a branch with an open circuit to the ground. Thus, when calculating $\underline{Z}_{th}$, the synchronous generator is represented by the impedance branch to ground, and the impedance value is typically set to the transient reactance. However, the branch adopted by the nonsynchronous-machine source depends on its operating states.

When the nonsynchronous-machine sources are under the normal states, the Vθ type grid-forming nonsynchronous-machine source, the PV type grid-forming nonsynchronous-machine source, and the PV type grid-following nonsynchronous-machine source can be represented by branches with short circuits to the ground at their PCCs. In contrast, the PQ-type grid-following nonsynchronous-machine source is represented by the branch with an open circuit to ground at the PCC. When the nonsynchronous-machine sources are under the fault states, all four types are represented by branches with open circuits to ground at their PCCs.

During the actual calculation, due to different fault locations, the voltage drop degree of each bus in the power grid is different. This indicates that for the same fault, the operating state of the different nonsynchronous-machine sources may be different, with some under the fault states and others under the normal states. Therefore, $\underline{Z}_{th}$ changes with different fault locations in principle. To simplify the analysis, two types of equivalent impedance are defined for any bus in the grid, which is of great significance. The first is called the normal-state Thevenin equivalent impedance $\underline{Z}_{th,nom}$, and the second is called the fault-state Thevenin equivalent impedance $\underline{Z}_{th,flt}$. Thus, when calculating $\underline{Z}_{th,nom}$, it is assumed that all the nonsynchronous-machine sources are under normal states. When calculating $\underline{Z}_{th,flt}$, it is considered that all the nonsynchronous-machine sources are under the fault states.

In addition, it must be pointed out that when the grid-forming nonsynchronous-machine source does not adopt the conventional inner and outer loop controllers as shown in Figures 2 and 3 but instead adopts the amplitude-phase angle controller without the current inner loop control [44–46], the equivalent circuit of the nonsynchronous-machine source under the fault state is roughly equivalent to the internal electromotive force in series with the total current limiting impedance. The total current limiting impedance is composed of the connected reactance and the virtual impedance, where the value is determined by the controller structure of the nonsynchronous-machine source. The objective of current limiting impedance is to prevent the output current of the nonsynchronous-machine source from exceeding its overload current level under the fault state, which is typically 1.1 times the rated current. Under such circumstances, the fault-state equivalent impedance of the nonsynchronous-machine source is equal to the total current limiting impedance.

### 4.4. Examples of Calculation of Voltage Stiffness and Short-Circuit Ratio

For the system with renewable energy and static synchronous compensator (STATCOM), as shown in Figure 8 [47], it is assumed that both wind turbines and photovoltaic units adopt grid-following control. The impedance of the transmission line $x_{\mathrm{Line}}$ is 40 Ω, and its length is 100 km. The leakage reactance of the transformer $u_k$ is 10%, its ratio is 220 kV/500 kV, and its capacity is 300 MVA. $x_T$ represents the reactance of the transformer. The transient reactance of the synchronous generator $x'_d$ is 10 Ω. The whole output active power of renewable energy is 200 MW. Next, the voltage stiffness and short-circuit ratios are calculated in the following when STATCOM is controlled by the constant AC voltage amplitude control and the constant reactive power control, respectively.

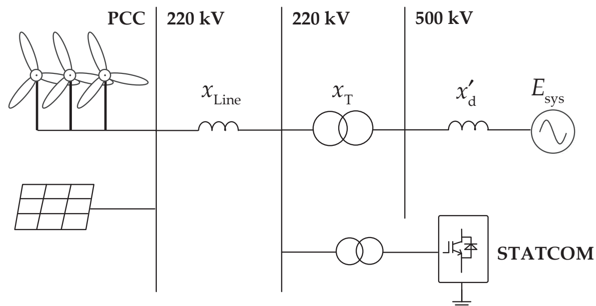


**Figure 8.** Schematic diagram of the system with new energy sources and STATCOM.

When the STATCOM adopts the constant AC voltage amplitude control and the constant active power control, it is a PV-type grid-following nonsynchronous-machine source. According to the rules stated in Section 3.1, the system's Thevenin equivalent circuits are depicted in Figure 9. For the PCC, the wind turbines and the photovoltaic units are collectively regarded as connected devices. Firstly, the voltage stiffness and short circuit ratio of the PCC are calculated when the STATCOM is in the normal state. The equivalent circuit of the STATCOM is a constant voltage source. The independent voltage source is represented by the branch with a short circuit to the ground when calculating the Thevenin equivalent impedance. Therefore, as shown in Figure 9a, $Z_{\mathrm{th,nom}} = x_{\mathrm{Line}}$ when seen from the PCC to the AC system. Thus, $K_{\mathrm{vtg}}$ at the PCC is 0.858, whereas $\lambda_{\mathrm{SCR}}$ at the PCC is 6.05.

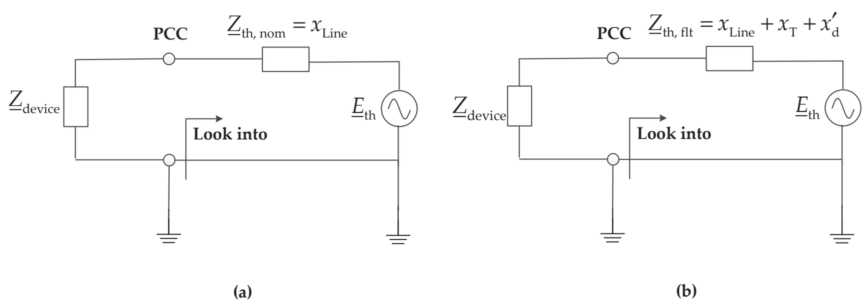


**Figure 9.** Thevenin equivalent circuit of the system when STATCOM adopts the constant AC voltage amplitude control and the constant active power control: (**a**) STATCOM is under the normal state; (**b**) STATCOM is under the fault state.

Then, the voltage stiffness and short-circuit ratio of the PCC are calculated when an AC fault occurs at the 500 kV network, which leads to a large drop in the $E_{\mathrm{sys}}$, and we assume that the AC fault does not change $x'_d$. At this time, due to the AC voltage drop, the STATCOM is under the fault state and operates under the current saturation state. The equivalent circuit of the STATCOM is a constant current source. When calculating the Thevenin equivalent impedance, the independent current source is represented by the branch with an open circuit to the ground. Therefore, as shown in Figure 9b, $\underline{Z}_{\text{th, flt}} = x_{\text{Line}} + x_{\text{T}} + x'_{\text{d}}$. Therefore, $K_{\text{vtg}}$ at the PCC is 0.806, whereas $\lambda_{\text{SCR}}$ at the PCC is 4.167.

When the STATCOM adopts the constant reactive power control and the constant active power control, the system's Thevenin equivalent circuits are depicted in Figure 10. In both scenarios, the equivalent circuit of the STATCOM is a constant current source. When calculating the Thevenin equivalent impedance, the independent current source is represented by the branch with an open circuit to the ground. Therefore, as shown in Figure 10a,b, $Z_{\text{th,nom}} = \underline{Z}_{\text{th, flt}} = x_{\text{Line}} + x_{\text{T}} + x'_{\text{d}}$. Therefore, $K_{\text{vtg}}$ at the PCC is 0.806, whereas $\lambda_{\text{SCR}}$ at the PCC is 4.167.

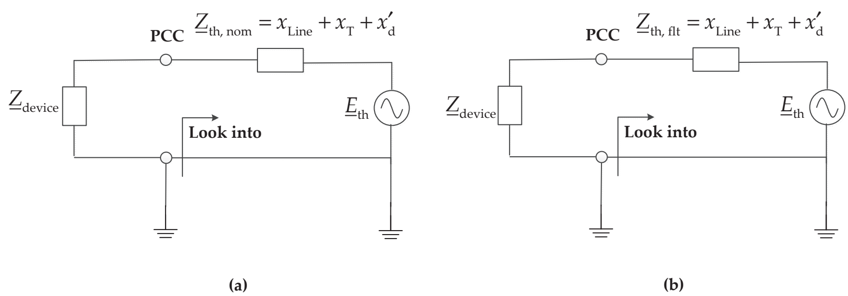


**Figure 10.** Thevenin equivalent circuit of the system when STATCOM adopts the constant reactive power control and the constant active power control: (**a**) STATCOM is under the normal state; (**b**) STATCOM is under the fault state.

## 5. New Exploration of Single infeed SCR and Multi-Infeed SCR

The concept of short circuit ratio has been used in the early development stage of HVDC transmission. In 1992 and 1997, the CIGRE working group on AC/DC interaction and the IEEE working group on the interaction between DC transmission systems and AC systems with low SCR jointly published research reports [4–6] and provided a comprehensive and in-depth description of SCR, which has led to its widespread recognition and application in the field of HVDC transmission [48–52].

The concept of single-infeed SCR proposed by CIGRE and IEEE joint Working Group in 1992 was defined based on the short circuit capacity [4]. When there are only synchronous generators in the power grid, the SCR defined based on short circuit capacity is completely consistent with the SCR defined by the Thevenin equivalent impedance, as the short circuit current of the synchronous generator is entirely determined by its impedance, without any current limiters. However, the SCR based on the short circuit capacity definition and the SCR based on the Thevenin equivalent impedance definition is fundamentally different for the nonsynchronous-machine source. Due to overcurrent limiters, it is useless to describe SCR with the short circuit capacity for nonsynchronous-machine sources. In other words, for nonsynchronous-machine sources, the short circuit capacity cannot characterize the ability of a bus to maintain its loaded voltage close to its no-load voltage. When nonsynchronous-machine sources exist, it is more appropriate to define the SCR by the following expression.

$$\lambda_{\text{SCR}} = \frac{Z_{\text{device}}}{Z_{\text{th}}} \tag{7}$$

Due to the uniform treatment of the synchronous generators and the nonsynchronous-machine sources in this definition, the application of the SCR can be extended to the power grid where synchronous generators and nonsynchronous-machine sources coexist.

In 2007, the CIGRE multiple DC infeed working group [53,54] introduced the notion of effective short circuit ratio (ESCR) to describe the voltage support strength of multiple DC infeed systems. Here we will give a new exploration of the voltage support strength of multiple DC infeed AC systems. The following example of the double DC infeed AC system demonstrates the new exploration.

The investigated double DC infeed AC system is shown in Figure 11a. In accordance with the Thevenin equivalence concept of the two-port network [55], Figure 11b depicts the equivalent circuit of the double DC infeed AC system. In Figure 9, the infeed bus of the double DC lines is represented by *i* and *j*, respectively, and $\underline{U}_{io}$ and $\underline{U}_{jo}$ represent the voltage phasors (i.e., no-load voltages) when the double DC lines are not connected to the power grid. $\underline{Z}_{ii}$, $\underline{Z}_{jj}$, and $\underline{Z}_{ij}$ are the equivalent impedances of the two-port Thevenin equivalent circuit for the fundamental-frequency positive-sequence AC grid. $\underline{Z}_{\mathrm{DC}i}$ and $\underline{Z}_{\mathrm{DC}j}$ are the equivalent impedances of the double DC lines in their rated operating states.

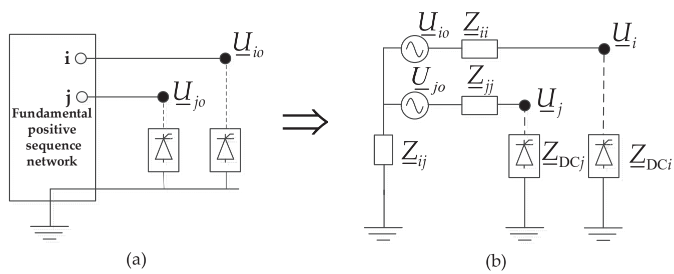


**Figure 11.** Schematic diagram of a double DC infeed system: (**a**) the original structure of the double DC infeed system; (**b**) the Thevenin equivalent circuit of the double DC infeed system.

Consider the DC line *i* as an example. Firstly, the Thevenin equivalent electromotive force $\underline{E}_{\mathrm{th}}$ and the Thevenin equivalent impedance $\underline{Z}_{\mathrm{th}}$, seen from bus *i* to the grid when DC line *j* is not connected, are studied. Then the Thevenin equivalent electromotive force $\underline{E}_{\mathrm{th}}^{\mathrm{m}}$ and the Thevenin equivalent impedance $\underline{Z}_{\mathrm{th}}^{\mathrm{m}}$ are examined when the DC line *j* is connected to the grid. The superscript "m" here represents the multiple DC infeed.

In the single DC infeed condition, that is, when the DC line *j* is not connected, the $\underline{Z}_{\mathrm{DC}j}$ branch in Figure 9b is an open circuit, and $\underline{E}_{\mathrm{th}}$ and $\underline{Z}_{\mathrm{th}}$ are calculated as (8).

$$\begin{cases} \underline{E}_{\mathrm{th}} = \underline{U}_{io} \\ \underline{Z}_{\mathrm{th}} = \underline{Z}_{ij} + \underline{Z}_{ii} \end{cases} \tag{8}$$

In the multiple DC infeed condition, that is, when DC line *j* is connected, $\underline{E}_{\mathrm{th}}^{\mathrm{m}}$ and $\underline{Z}_{\mathrm{th}}^{\mathrm{m}}$ are calculated as (9).

$$\begin{cases} \underline{E}_{\mathrm{th}}^{m} = \underline{U}_{io}^{m} = \underline{U}_{io} + \frac{\underline{Z}_{ij}}{\underline{Z}_{ij}+\underline{Z}_{jj}+\underline{Z}_{\mathrm{DC}j}}\underline{U}_{jo} \\ \underline{Z}_{\mathrm{th}}^{m} = \underline{Z}_{ii} + \frac{\underline{Z}_{ij}(\underline{Z}_{jj}+\underline{Z}_{\mathrm{DC}j})}{\underline{Z}_{ij}+\underline{Z}_{jj}+\underline{Z}_{\mathrm{DC}j}} \end{cases} \tag{9}$$

The ratios of the Thevenin equivalent electromotive forces and the Thevenin equivalent impedances in the two conditions are shown in (10).

$$\begin{cases} \frac{\underline{E}_{\mathrm{th}}^{m}}{\underline{E}_{\mathrm{th}}} = \frac{\underline{U}_{io}^{m}}{\underline{U}_{io}} = 1 + \frac{\underline{Z}_{ij}}{\underline{Z}_{ij}+\underline{Z}_{jj}+\underline{Z}_{\mathrm{DC}j}} \cdot \frac{\underline{U}_{jo}}{\underline{U}_{io}} \\ \frac{\underline{Z}_{\mathrm{th}}^{m}}{\underline{Z}_{\mathrm{th}}} = \frac{\underline{Z}_{ii}}{\underline{Z}_{ij}+\underline{Z}_{ii}} + \frac{\underline{Z}_{ij}}{\underline{Z}_{ij}+\underline{Z}_{ii}} \cdot \frac{\underline{Z}_{jj}+\underline{Z}_{\mathrm{DC}j}}{\underline{Z}_{ij}+\underline{Z}_{jj}+\underline{Z}_{\mathrm{DC}j}} \end{cases} \tag{10}$$

For the actual power grid parameters and operating states, the Thevenin equivalent electromotive force changes greatly in the two conditions, while the Thevenin equivalent impedance changes only slightly. Usually,

$$R_{\mathrm{eth}}^{\mathrm{m}} = \frac{E_{\mathrm{th}}^{\mathrm{m}}}{E_{\mathrm{th}}} = \frac{U_{io}^{\mathrm{m}}}{U_{io}} = \left| 1 + \frac{\underline{Z}_{ij}}{\underline{Z}_{ij}+\underline{Z}_{jj}+\underline{Z}_{\mathrm{DC}j}} \cdot \frac{\underline{U}_{jo}}{\underline{U}_{io}} \right| \leq 1 \tag{11}$$

$$\underline{R}_{\text{zth}}^{\text{m}} = \frac{\underline{Z}_{\text{th}}^{\text{m}}}{\underline{Z}_{\text{th}}} = \frac{\underline{Z}_{ii}}{\underline{Z}_{ij} + \underline{Z}_{ii}} + \frac{\underline{Z}_{ij}}{\underline{Z}_{ij} + \underline{Z}_{ii}} \cdot \frac{\underline{Z}_{jj} + \underline{Z}_{\text{DC}j}}{\underline{Z}_{ij} + \underline{Z}_{jj} + \underline{Z}_{\text{DC}j}} \approx 1 \tag{12}$$

$$\lambda_{\text{SCR}}^{\text{m}} = \frac{Z_{\text{DC}i}}{Z_{\text{th}}^{\text{m}}} \approx \frac{Z_{\text{DC}i}}{Z_{\text{th}}} = \lambda_{\text{SCR}} \tag{13}$$

$$K_{\text{vtg}}^{\text{m}} = \frac{U_i^{\text{m}}}{U_{io}} = \frac{1}{U_{io}} \left| \frac{\underline{E}_{\text{th}}^{\text{m}} \cdot \underline{Z}_{\text{DC}i}}{\underline{Z}_{\text{th}}^{\text{m}} + \underline{Z}_{\text{DC}i}} \right| \approx \frac{E_{\text{th}}^{\text{m}}}{U_{io}} \cdot \left| \frac{\underline{Z}_{\text{DC}i}}{\underline{Z}_{\text{th}} + \underline{Z}_{\text{DC}i}} \right| = R_{\text{eth}}^{\text{m}} K_{\text{vtg}} \tag{14}$$

in (11)–(14), $R_{\text{eth}}^{\text{m}}$ is the ratio of the Thevenin equivalent electromotive forces seen from bus $i$ to the AC grid in the multiple DC infeed condition and in the single DC infeed condition, which is called the multiple DC infeed no-load voltage drop factor. $\underline{U}_{io}$ is the no-load voltage phasor of bus $i$ in the single DC infeed condition and $\underline{U}_{io}^{\text{m}}$ is the no-load voltage phasor of bus $i$ in the multiple DC infeed condition. $R_{\text{zth}}^{\text{m}}$ is the ratio of the Thevenin equivalent impedances seen from bus $i$ to the AC grid in the multiple DC infeed condition and the single DC infeed condition. $\lambda_{\text{SCR}}$ is the SCR of DC line $i$ in the single DC infeed condition and $\lambda_{\text{SCR}}^{\text{m}}$ is the SCR of DC line $i$ in the multiple DC infeed condition. $K_{\text{vtg}}$ is the voltage stiffness of DC line $i$ in the single DC infeed condition and $K_{\text{vtg}}^{\text{m}}$ is the voltage stiffness of DC line $i$ in the multiple DC infeed condition.

As shown in (13), it is insufficient to use the SCR index to characterize the voltage support strength in the multiple DC infeed condition because the values of SCR in single and multiple DC infeed conditions change slightly. However, it is of greater index significance to use voltage stiffness to characterize the voltage support strength in the multiple DC infeed condition because $K_{\text{vtg}}^{\text{m}}$ can reflect the change in the Thevenin equivalent electromotive force in the multiple DC infeed condition and $K_{\text{vtg}}^{\text{m}}$ is equal to $K_{\text{vtg}}$ multiplied by $R_{\text{eth}}^{\text{m}}$ in the multiple DC infeed condition.

It is meaningful to compare $K_{\text{vtg}}^{\text{m}}$ with the multiple DC infeed ESCR proposed by the CIGRE working group [53,54]. It can be found that the multiple DC infeed ESCR cannot directly reflect the drop in the no-load voltage due to multiple DC infeed and does not convey the physical substance of the reduction in voltage support strength in the multiple DC infeed scenario. ESCR, as a voltage support strength index, is difficult to create a unified numerical criterion in practice.

If the DC infeed shown in Figure 9 is generalized by a PQ-type grid-following nonsynchronous-machine source, such as a conventional PQ-type grid-following wind farm or photovoltaic station, the voltage support strength of the AC power grid can also use $K_{\text{vtg}}^{\text{m}}$ as an index.

## 6. Definition and Calculation Method of Frequency Support Strength in the New Type Power System

The frequency support strength has two manifestations: the inertia support capability and the primary frequency regulation capability. The synchronous generator has both inertia support capability and primary frequency regulation capability. The inertia of the synchronous generator is independent of its operating point and is a constant value [1–3]. The primary frequency regulation capability of the synchronous generator is closely related to its operating point and the droop of its governor. The load possesses a small amount of inertia support and frequency regulation effect. Different from the synchronous generator, the inertia support capability and primary frequency regulation capability of the nonsynchronous-machine source are entirely determined by its control modes and output power margin. The nonsynchronous-machine source in the early stage is usually controlled by MPPT, and its output power is decoupled from the frequency of the power grid. Under such circumstances, the nonsynchronous-machine source has no support for the frequency stability of the power grid. With the increasing proportion of the nonsynchronous-machine source, the control strategy of the nonsynchronous-machine source must be changed to couple its output power with the grid frequency so as to have inertia support capability and primary frequency regulation capability.

The inertia support and primary frequency regulation capabilities of the power grid can be characterized by the dynamic response curve after a large disturbance [56,57], as shown in Figure 12, in which the actual frequency dynamic response curve is represented by segmented polylines. Line Section 1 represents the inertia response period, while line Sections 2 and 3 represent the inertia response and primary frequency regulation joint action period. Line Section 4 represents the primary frequency regulation period. Based on the frequency dynamic response curve, three parameters are usually used to describe the inertia support and the primary frequency regulation capability of the power grid. The first parameter is the initial rate of change of frequency (RoCoF) of a disturbance, namely the slope of the line Section 1. The second parameter is the highest or lowest frequency, denoted by $f_{\text{zenith}}$ or $f_{\text{nadir}}$, respectively. The third parameter is the steady-state frequency deviation, denoted by $\Delta f_{\infty}$.

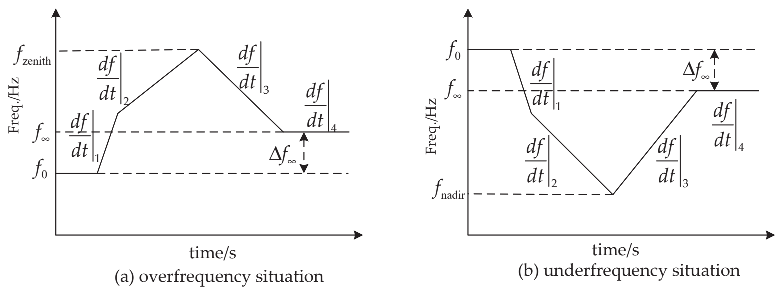


**Figure 12.** Frequency dynamic response curve describing inertia support and primary frequency regulation capability: (**a**) in the overfrequency situation; (**b**) in the underfrequency situation.

### *6.1. Implementation of Inertia and Primary Frequency Regulation of Nonsynchronous-Machine Sources*

For the Vθ type grid-forming nonsynchronous-machine source shown in Figure 2, it is the support source of the connected grid. Within the range of its current capacity, the grid frequency is entirely determined by it and is unaffected by various grid disturbances. Therefore, in the range of its current capacity, the inertia support provided by the Vθ type grid-forming nonsynchronous-machine source is infinite. However, once it hits the current limit as a result of the fault, the inertia support and primary frequency regulation capabilities are no longer available.

For the PV-type grid-forming nonsynchronous-machine source shown in Figure 3, the inertia support capability is determined by the outermost loop controller, namely the V/θ generator, which usually adopts power synchronization control [57,58] or virtual synchronous machine control [59–66]. It has been proved that power synchronization control and virtual synchronous machine control are essentially consistent [67–69]; hence, the distinction between the two is ignored in this article. After adopting the power synchronization control, the V/θ generator is implemented in accordance with the Vθ decoupling mode. The θ generator is the so-called power synchronization loop (PSL) [57,58], which imitates the swing equation of the synchronous generator. The V generator is usually implemented by a reactive power-voltage droop controller [34].

The principle of PSL is to mimic the nonsynchronous-machine source as a synchronous generator, and the output of PSL is the rotor angle $\theta$ [34]. The swing equations of a synchronous generator are:

$$2H\frac{\mathrm{d}\Delta\omega}{\mathrm{d}t} = P_{\mathrm{m}} - P_{\mathrm{e}} - D\Delta\omega \tag{15}$$

$$\frac{\mathrm{d}\theta}{\mathrm{d}t} = \omega \cdot \omega_0 \tag{16}$$

where $H$ is the inertia time constant of the generator (unit: s), which determines the inertia support capability of the nonsynchronous-machine source. $\Delta\omega = \omega_0 - \omega$ is the generator speed deviation. $\omega$ is the actual speed (per unit value), and $\omega_0$ is the rated speed (per unit value). $t$ represents the time, where the unit is s. $P_m$ and $P_e$ are the mechanical power and electromagnetic power (in per unit value); $D$ is the damping coefficient (in per unit value); $\theta$ is the generator's electrical rotor angle, where the unit is rad. By substituting the $P_m$ of the generator for the active power reference value $P_s^*$ of the nonsynchronous-machine source and $P_e$ of the generator for the actual active power, $P_s$, of the nonsynchronous-machine source, the control block diagram of PSL is illustrated in Figure 13 [34].

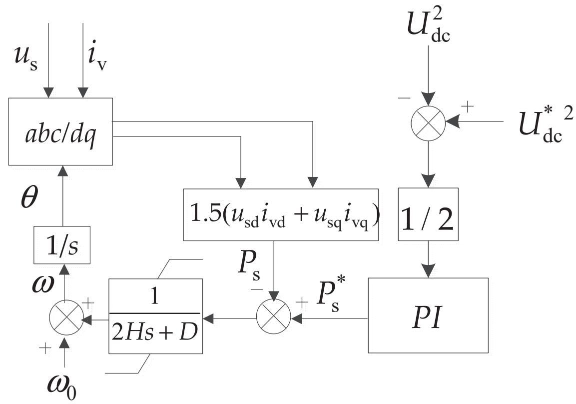


**Figure 13.** Power synchronization loop diagram of the PV-type grid-forming nonsynchronous-machine source.

Notably, the PV-type grid-forming nonsynchronous-machine source achieves its primary frequency regulation by changing the reference value of the DC voltage $U_{dc}^*$. It must have the ability to reduce power for frequency regulation but not necessarily have the ability to increase power for frequency regulation. For example, the initial value of $U_{dc}^*$ corresponds to the maximum power output, but the frequency of the grid is too high, so the active power output must be decreased. Consequently, the primary frequency regulation is to make the nonsynchronous-machine source run away from the maximum power point by changing the value of the $U_{dc}^*$ so as to reduce the active output. Conversely, power increase frequency regulation depends on whether the nonsynchronous-machine source has sufficient power support.

The V generator usually adopts the reactive power-voltage droop control [34], and its typical control strategy is shown as (17).

$$U_{sm}^* = U_{sm0}^* + k_p(Q_s^* - Q_s) \tag{17}$$

where $U_{sm}^*$ is the reference value of the output voltage; $U_{sm0}^*$ is the base voltage; $Q_s^*$ is the reference value of the reactive power; $Q_s$ is the actual reactive power. Then, the diagram of the V generator can be obtained in Figure 14.

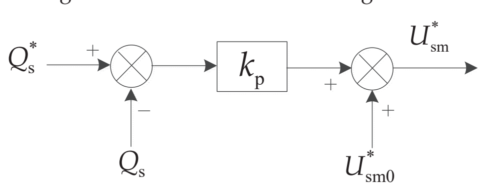


**Figure 14.** The V generator block diagram of the PV-type grid-forming nonsynchronous-machine source.

For the PV-type grid-following nonsynchronous-machine source in Figure 4, its inertia support and primary frequency regulation capabilities are determined by the outermost loop P/V generator. Still, the premise is that the nonsynchronous-machine source provides adequate power reserve. The P/V generator is usually implemented in PV decoupling mode, where the V generator is exactly the same as the V generator of the PV-type grid-forming nonsynchronous-machine source. When the output power reference value $P_s^*$ of the P generator in the outermost loop in Figure 4 is decoupled from the grid frequency, the nonsynchronous-machine source lacks inertia support and primary frequency regulation capabilities. When $P_s^*$ is proportional to the derivative of the power grid frequency, the nonsynchronous-machine source has the inertia support capability. When $P_s^*$ is related to the frequency deviation of the power grid, the nonsynchronous-machine source has the ability of primary frequency regulation.

When the nonsynchronous-machine source possesses both inertia support and primary frequency regulation capabilities, the active power reference value generated by the P generator is typically expressed as (18), where $P_{s0}$ is the constant power component; $f_0$ is the rated frequency of the power grid; $f$ is the actual frequency of the power grid; $M_{\text{non}}$ is the equivalent inertial time constant of the nonsynchronous-machine source; and $k_{\text{non}}$ is the proportional coefficient of the primary frequency regulation of the nonsynchronous-machine source.

$$P_s^* = P_{s0} + M_{\text{non}} \frac{\mathrm{d}f}{\mathrm{d}t} + k_{\text{non}}(f_0 - f) \tag{18}$$

For the PQ-type grid-following nonsynchronous-machine source in Figure 5, its inertia support and primary frequency regulation capabilities are determined by the outermost loop P/Q generator. Still, the premise is that the nonsynchronous-machine source provides adequate power reserve. The P/Q generator is usually implemented separately according to the PQ decoupling method, where the outermost P generator is the same as the PV-type grid-following nonsynchronous-machine source. When the PQ-type grid-following nonsynchronous-machine source has both inertia support and primary frequency regulation capabilities, the active power reference value generated by the P generator is also typically expressed as (18).

### *6.2. Definition and Calculation Method of the Inertia Support Strength of Nonsynchronous-Machine Sources*

The direct manifestation of inertia is the RoCoF. Specifically, the initial RoCoF under a disturbance is exclusively associated with the inertia and the disturbance itself. Thus, the calculation of inertia can be transformed into the calculation of the initial RoCoF.

For a specific power system, there is a maximum limit for RoCoF [56], such as limiting the maximum RoCoF to 1 Hz/s, etc. The minimum inertia requirement is usually calculated from the maximum limit value of the RoCoF and the anticipated maximum active power disturbance. Different power grids have different standards regarding the maximum anticipated active power disturbance. For instance, the maximum active power disturbance specified by the European power grid is the loss of 3000 MW generation power [11], while the maximum active disturbance specified by the Chinese power grid is generally the bipolar blocking of a single maximum UHVDC transmission line [70,71].

In this paper, the Equivalent Inertia Lifting Factor (EILF) is utilized to characterize the inertia support strength of the nonsynchronous-machine source. The derivation process is as follows. Under the specified maximum active power disturbance, the initial RoCoF of a node in the grid is (19) [12,16].

$$\left.\frac{\mathrm{d}f_{\text{node}}}{\mathrm{d}t}\right|_{t=0} = k_{\text{const}} \frac{\Delta P_{\max}}{H_{\text{eq}}} \tag{19}$$

where $k_{\text{const}}$ is a constant related to the operation state of the system; $P_{\max}$ is the unbalanced power under the specified maximum active power disturbance; and $H_{\text{eq}}$ is the equivalent inertial time constant of the system under the investigated operation state.

For the investigated operation state of the system, we define $\left.\frac{\mathrm{d}f_{\mathrm{node}}}{\mathrm{d}t}\right|_{t=0}^{0}$ to represent $\left.\frac{\mathrm{d}f_{\mathrm{node}}}{\mathrm{d}t}\right|_{t=0}$ when all nonsynchronous-machine sources adopt the controllers without inertial support abilities. The controllers without inertial support abilities can be realized by setting $H$ and $M_{\mathrm{non}}$ to zero in Figure 10 and (18). Then we define $\left.\frac{\mathrm{d}f_{\mathrm{node}}}{\mathrm{d}t}\right|_{t=0}^{1}$ to represent $\left.\frac{\mathrm{d}f_{\mathrm{node}}}{\mathrm{d}t}\right|_{t=0}$ when all nonsynchronous-machine sources adopt the controllers with inertial support abilities. Then, the equivalent inertia lifting value contributed by the nonsynchronous-machine sources with the inertial support controllers is defined as the Equivalent Inertia Lifting Factor $H_{\mathrm{amp}}$, as shown in (20).

$$H_{\mathrm{amp}} = \frac{H_{\mathrm{eq}}^{1}}{H_{\mathrm{eq}}^{0}} = \left.\frac{\mathrm{d}f}{\mathrm{d}t}\right|_{t=0}^{0} \Big/ \left.\frac{\mathrm{d}f}{\mathrm{d}t}\right|_{t=0}^{1} \tag{20}$$

In (20), $H_{\mathrm{eq}}^{0}$ represents the equivalent inertia time constant of the whole power system when all the nonsynchronous-machine sources are controlled without inertial support abilities. $H_{\mathrm{eq}}^{1}$ represents the equivalent inertia time constant of the whole power system when all the nonsynchronous-machine sources are controlled with inertial support abilities. Therefore, $H_{\mathrm{amp}}$ can represent the inertia support strength of the nonsynchronous-machine sources. According to (20), $H_{\mathrm{amp}}$ is suitable for digital simulation calculations, and the initial $\left.\frac{\mathrm{d}f_{\mathrm{node}}}{\mathrm{d}t}\right|_{t=0}$ of a disturbance can be obtained by numerical differentiation. In addition, the grid nodes for evaluating the inertia support strength should be chosen based on the actual situation of the grid, and multiple nodes can be chosen simultaneously. Generally, the power grid regions with an insufficient number of synchronous generators are chosen because their RoCoFs are usually the largest; that is, their inertia support strength is the weakest.

### *6.3. Definition and Calculation Method of the Primary Frequency Regulation Capability of Nonsynchronous-Machine Sources*

The primary frequency regulation capability can be represented by the frequency deviation factor [2,72]. In the new type of power system, the frequency deviation factor $\beta$ can be defined as (21).

$$\beta = \frac{1}{R_{\mathrm{gen}}} + D_{\mathrm{load}} + K_{\mathrm{non}} \tag{21}$$

where $R_{\mathrm{gen}}$ is the equivalent droop of all synchronous generator governors, where the unit is Hz/MW; $K_{\mathrm{non}}$ is the equivalent frequency regulation coefficient of all nonsynchronous-machine sources, where the unit is MW/Hz; $D_{\mathrm{load}}$ is the frequency regulation coefficient of the system active power load, and its unit is MW/Hz. The common unit of $\beta$ is MW/0.1 Hz.

$\beta$ represents the relationship between the active power disturbance $\Delta P$ and the steady-state frequency deviation $\Delta f_{\infty}$, as shown in (22).

$$\Delta f_{\infty} = \frac{\Delta P}{\beta} \tag{22}$$

Imitating the definition of inertia support strength, the steady-state frequency deviation decreasing factor $R_{\mathrm{deltf}}$ is adopted to describe the primary frequency regulation capability of the nonsynchronous-machine sources in this paper. $R_{\mathrm{deltf}}$ is defined as (23).

$$R_{\mathrm{deltf}} = \frac{\Delta f_{\infty}^{1}}{\Delta f_{\infty}^{0}} = \frac{\beta^{0}}{\beta^{1}} \tag{23}$$

where $\Delta f_{\infty}^{0}$ and $\beta^{0}$ are the steady-state frequency deviation and the frequency deviation factor when all the nonsynchronous-machine sources are controlled without primary frequency regulation abilities. $\Delta f_{\infty}^{1}$ and $\beta^{1}$ are the steady-state frequency deviation and frequency deviation factors when all the nonsynchronous-machine sources are controlled with primary frequency regulation abilities. Therefore, $R_{\mathrm{deltf}}$ can represent the primary frequency regulation capabilities of the nonsynchronous-machine sources. According to (23), $R_{\mathrm{deltf}}$ can be calculated easily using digital simulation. It is worth noting that the selected frequency monitoring point impacts both $H_{\mathrm{amp}}$ and $R_{\mathrm{deltf}}$ because the frequency of different nodes in the network varies during the transient process.

### 6.4. Simulation Validation

A modified IEEE 39-mode test system, as represented in Figure 15, is built to assess the efficacy of the suggested frequency support strength indices. The installed capacity of the synchronous generator sources is 7600 MW, while the installed capacity of the nonsynchronous-machine sources is 2072 MW. The average inertia of the synchronous generator sources is 4.55, and the rotational reserve rate is 10%. In Figure 15, the nonsynchronous-machine sources are connected to buses 4, 18, and 21 accordingly.

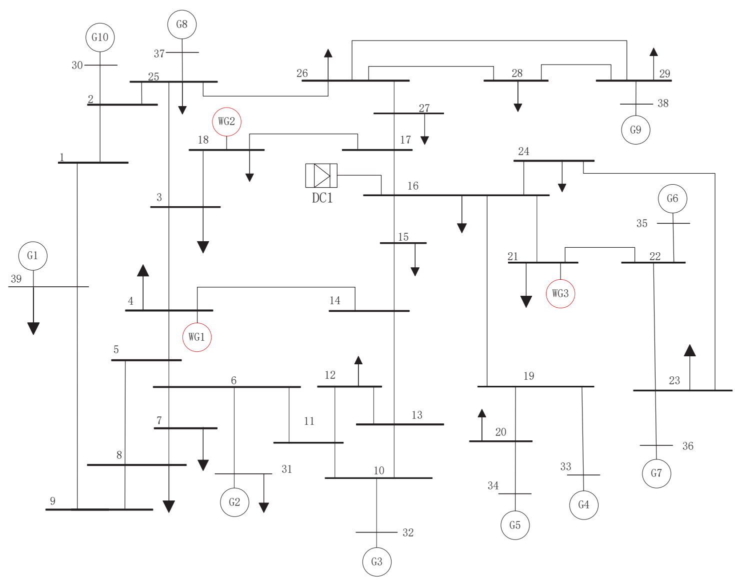


**Figure 15.** Modified IEEE 39-node test system.

The following two scenarios are considered to calculate the equivalent inertia lifting factor and the steady-state frequency deviation decreasing factor. Firstly, when all the nonsynchronous-machine sources adopt the constant active power control and the constant reactive power control, they have no frequency support abilities. The RoCoF and the steady-state frequency deviation can be obtained by the simulation. As shown in Figure 16, $\frac{\mathrm{d}f_{\mathrm{node}}}{\mathrm{d}t}\Big|_{t=0}^{0} = 0.303\ \mathrm{Hz/s}$, and $\Delta f_{\infty}^{0} = -0.136\ \mathrm{Hz}$. Then, when all the nonsynchronous-machine sources adopt the PSL control and the constant reactive power control, they have both inertia support and primary frequency regulation. $M_{\mathrm{non}}$ of all the nonsynchronous-machine sources is set to 6.8, and $k_{\mathrm{non}}$ is set to 30. As shown in Figure 16, $\frac{\mathrm{d}f_{\mathrm{node}}}{\mathrm{d}t}\Big|_{t=0}^{1} = 0.214\ \mathrm{Hz/s}$, and $\Delta f_{\infty}^{1} = -0.096\ \mathrm{Hz}$. Therefore, $H_{\mathrm{amp}}$ is 1.416, and $R_{\mathrm{deltf}}$ is 0.706.

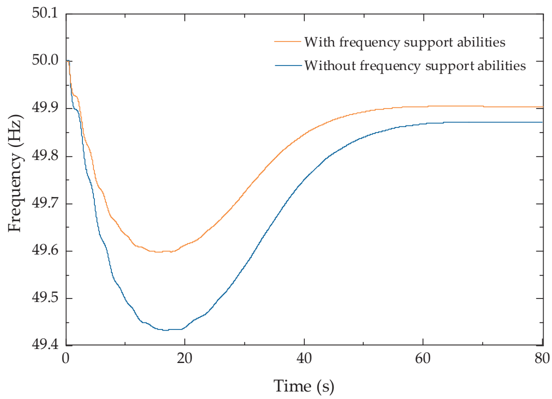


**Figure 16.** Frequency characteristic curves when all the nonsynchronous-machine sources are controlled with and without frequency support abilities, respectively.

## 7. Conclusions

The fundamental characteristic of the new type of power system is that the dominant sources have shifted from traditional synchronous generators to nonsynchronous-machine sources. Accordingly, the definitions and calculation methods of power grid strength must be revised. This paper has investigated these challenges, and the key conclusions are given below.

(1) Nonsynchronous-machine sources can be categorized into four types at the macro level: Vθ type grid-forming, PV-type grid-forming, PV-type grid-following, and PQ-type grid-following.
(2) The external characteristics of nonsynchronous-machine sources are closely related to their operating states. Once they reach the current saturation state, their control objectives cannot be realized.
(3) The classical SCR index can be defined by the Thevenin equivalent impedance of the power grid and the equivalent impedance of the connected device. This definition is more suitable for describing the effect of nonsynchronous-machine sources on the voltage support strength.
(4) The voltage stiffness index $K_{\mathrm{vtg}}$ presented in this paper reflects more comprehensive information than SCR since it considers the respective impedance angles of both the Thevenin equivalent impedance and the equivalent impedance of the connected device.
(5) The physical significance of the multiple DC infeed SCR is further clarified by the multi-port Thevenin equivalent circuit, where the essence is that when multiple nodes in the grid simultaneously connect loads, the voltage drop on each node is larger than when a single node connects a load alone.
(6) The inertia support capability of nonsynchronous-machine sources can be described by the equivalent inertia lifting factor, while the primary frequency regulation capability of nonsynchronous-machine sources can be described by the steady-state frequency deviation decreasing factor.

**Author Contributions:** Conceptualization, Z.X.; methodology, Z.X.; validation, Z.X. and N.Z.; formal analysis, Z.X.; investigation, Z.X., N.Z., Z.Z. and Y.H.; resources, Z.X., Z.Z. and Y.H.; writing—original draft preparation, N.Z.; writing—review and editing, Z.X.; visualization, N.Z. All authors have read and agreed to the published version of the manuscript.

**Funding:** This research received no external funding.

**Data Availability Statement:** Not applicable.

**Conflicts of Interest:** The authors declare no conflict of interest.

## References


1. Anderson, P.; Fouad, A. *Power System Control and Stability*, 2nd ed.; IEEE Press: New York, NY, USA, 2003.
2. Kundur, P.S. *Power System Stability and Control*; McGraw-Hill: New York, NY, USA, 1994.
3. Machowski, J.; Blalek, J.; Bumby, J. *Power System Dynamics-Stability and Control*; John Wiley & Sons Ltd.: New York, NY, USA, 2008.
4. CIGRE Working Group 14.07; IEEE Working Group 15.05.05. *Guide for Planning DC Links Terminating at AC Locations Having Low Short-Circuit Capacities-Part I: AC/DC Interaction Phenomena*; CIGRE Brochure: Paris, France, 1992; p. 68.
5. CIGRE Working Group 14.07; IEEE Working Group 15.05.05. *Guide for Planning DC Links Terminating at AC Locations Having Low Short-Circuit Capacities-Part II: Planning Guidelines*; CIGRE Brochure: Paris, France, 1997; p. 115.
6. IEEE. *IEEE Guide for Planning DC Links Terminating at AC Locations Having Low Short-Circuit Capacities*; IEEE Std 1204-1997: New York, NY, USA, 1997.
7. Xin, H.; Dong, W.; Yuan, X.; Gan, D.; Wu, D. Generalized short circuit ratio for multi power electronic based devices infeed to power systems. *Proc. CSEE* **2016**, *36*, 6013–6027.
8. Sun, H.; Xu, S.; Xu, T.; Guo, Q.; He, J.; Zhao, B.; Zhu, Y. Definition and index of short circuit ratio for multiple renewable energy stations. *Proc. CSEE* **2021**, *41*, 497–505.
9. Sui, T.; Mo, Y.; Marelli, D.; Sun, X.-M.; Fu, M. The Vulnerability of Cyber-Physical System Under Stealthy Attacks. *IEEE Trans. Autom. Control* **2021**, *66*, 637–650. [CrossRef]
10. Sui, T.; Sun, S. The vulnerability of distributed state estimator under stealthy attacks. *Automatica* **2021**, *113*, 109869. [CrossRef]
11. ENTSO-E. *Frequency Stability Evaluation Criteria for the Synchronous Zone of Continental Europe*; ENTSO-E: Brussels, Belgium, 2016.
12. ENTSO-E. *Future System Inertia*; ENTSO-E: Brussels, Belgium, 2016.
13. ENTSO-E. *Parameters Related to Frequency Stability*; ENTSO-E: Brussels, Belgium, 2016.
14. ENTSO-E. *Limited Frequency Sensitive Mode*; ENTSO-E: Brussels, Belgium, 2018.
15. ENTSO-E. *Need for Synthetic Inertia (SI) for Frequency Regulation*; ENTSO-E: Brussels, Belgium, 2018.
16. ENTSO-E. *Inertia and Rate of Change of Frequency (RoCoF)*; ENTSO-E: Brussels, Belgium, 2020.
17. ENTSO-E. *Frequency Ranges*; ENTSO-E: Brussels, Belgium, 2021.
18. ENTSO-E. *System Defense Plan*; ENTSO-E: Brussels, Belgium, 2022.
19. Cao, X.; Stephen, B.; Abdulahadi, I.; Booth, C.D.; Burt, G.M. Switching Markov Gaussian models for dynamic power system inertia estimation. *IEEE Trans. Power Syst.* **2016**, *31*, 3394–3403. [CrossRef]
20. Tuttelberg, K.; Kilter, J.; Wilson, D.; Uhlen, K. Estimation of power system inertia from ambient wide area measurements. *IEEE Trans. Power Syst.* **2018**, *33*, 7249–7257. [CrossRef]
21. Milano, F.; Dörfler, F.; Hug, G.; Hill, D.J.; Verbič, G. Foundations and challenges of low-inertia systems (Invited Paper). In Proceedings of the 2018 Power Systems Computation Conference (PSCC), Dublin, Ireland, 11–15 June 2018; pp. 1–25.
22. Fernández-Guillamóna, A.; Gómez-Lázaro, E.; Muljadi, E.; Molina-García, Á. Power systems with high renewable energy sources: A review of inertia and frequency control strategies over time. *Renew. Sustain. Energy Rev.* **2019**, *115*, 109369. [CrossRef]
23. Xu, Z. Three Technical Challenges Faced by Power Systems in Transition. *Energies* **2022**, *15*, 4473. [CrossRef]
24. Ortjohann, E.; Arias, A.; Morton, D.; Mohd, A.; Hamsic, N.; Omari, O. Grid-forming three-phase inverters for unbalanced loads in hybrid power systems. In Proceedings of the 2006 IEEE 4th World Conference on Photovoltaic Energy Conversion, Waikoloa, HI, USA, 7–12 May 2006; pp. 2396–2399.
25. Ninad, N.; Lopes, L. Per-phase vector (dq) controlled three-phase grid-forming inverter for stand-alone systems. In Proceedings of the 2011 IEEE International Symposium on Industrial Electronics, Gdansk, Poland, 27–30 June 2011; pp. 1626–1631.
26. Pattabiraman, D.; Lasseter, R.; Jahns, T. Comparison of grid following and grid forming control for a high inverter penetration power system. In Proceedings of the 2018 IEEE Power & Energy Society General Meeting (PESGM), Portland, OR, USA, 5–10 August 2018; pp. 1–5.
27. Rosso, R.; Wang, X.; Liserre, M.; Lu, X.; Engelken, S. Grid-forming converters: Control approaches, grid-synchronization, and future trends–A review. *IEEE Open J. Ind. Appl.* **2021**, *2*, 93–109. [CrossRef]
28. ENTSO-E. *High Penetration of Power Electronic Interfaced Power Sources and the Potential Contribution of Grid Forming Converters*; ENTSO-E: Brussels, Belgium, 2021.
29. Shakerighadi, B.; Johansson, N.; Eriksson, R.; Mitra, P.; Bolzoni, A.; Clark, A.; Nee, H. An overview of stability challenges for power-electronic-dominated power systems: The grid-forming approach. *IET Gener. Transm. Distrib.* **2022**, 1–23. [CrossRef]
30. Khan, S.; Wang, M.; Su, W.; Liu, G.; Chaturvedi, S. Grid-forming converters for stability issues in future power grids. *Energies* **2022**, *15*, 4937. [CrossRef]
31. Musca, R.; Gonzalez-Longatt, F.; Gallego Sánchez, C. Power system oscillations with different prevalence of grid-following and grid-forming converters. *Energies* **2022**, *15*, 4273. [CrossRef]
32. Zhang, C.; Zhang, X. *PWM Rectifier and Its Control*; China Machine Press: Beijing, China, 2003.
33. Chen, H.; Xu, Z. Control design for VSC-HVDC supplying passive network. *Proc. CSEE* **2006**, *26*, 42–48.
34. Xu, Z.; Xiao, H.; Zhang, Z.; Xue, Y.; Liu, G.; Tang, G.; Xu, F.; Wang, S.; Tu, Q.; Guan, M.; et al. *Voltage Source Converter Based HVDC Power Transmission Systems*, 2nd ed.; China Machine Press: Beijing, China, 2017; pp. 106–112.

35. Femia, N.; Petrone, G.; Spagnuolo, G.; Vitelli, M. *Power Electronics and Control Techniques for Maximum Energy Harvesting in Photovoltaic Systems*; CRC Press: New York, NY, USA, 2012.
36. Blaabjerg, F.; Teodorescu, R.; Liserre, M.; Timbus, A.V. Overview of control and grid synchronization for distributed power generation systems. *IEEE Trans. Ind. Electron.* **2006**, *53*, 1398–1409. [CrossRef]
37. Zhou, J.; Ding, H.; Fan, S.; Zhang, Y.; Gole, A.M. Impact of short-circuit ratio and phase-locked-loop parameters on the small-signal behavior of a VSC-HVDC converter. *IEEE Trans. Power Deliv.* **2014**, *29*, 2287–2296. [CrossRef]
38. Luna, A.; Rocabert, J.; Candela, I.; Hermoso, J.R.; Teodorescu, R.; Blaabjerg, F.; Rodriguez, P. Grid voltage synchronization for distributed generation systems under grid fault conditions. *IEEE Trans. Ind. Appl.* **2015**, *51*, 3414–3425. [CrossRef]
39. Du, D.; Chen, X.; Wang, H. Parameter tuning of the PLL to consider the effect on power system small-signal angular stability. *IET Renew. Power Gener.* **2018**, *12*, 1–8. [CrossRef]
40. Hu, Q.; Fu, L.; Ma, F.; Ji, F. Large signal synchronizing instability of PLL-based VSC connected to weak AC grid. *IEEE Trans. Power Syst.* **2019**, *34*, 3220–3228. [CrossRef]
41. He, X.; Geng, H.; Ma, S. Transient stability analysis of grid-tied converters considering PLL's nonlinearity. *CPSS Trans. Power Electron. Appl.* **2019**, *4*, 40–49. [CrossRef]
42. Qiu, G.; Luo, X. *Electric Circuits*, 5th ed.; Higher Education Press: Beijing, China, 2006.
43. Anderson, P. *Analysis of Faulted Power Systems*; John Wiley & Sons, INC.: New York, NY, USA, 1995.
44. Guan, M.; Xu, Z. Direct voltage control of MMC-based VSC-HVDC system for passive networks. *Electr. Power Autom. Equip.* **2012**, *32*, 1–5.
45. Lu, X.; Wang, J.; Guerrero, J.; Zhao, D. Virtual-impedance-based fault current limiters for inverter dominated AC microgrids. *IEEE Trans. Smart Grid* **2018**, *9*, 1599–1612. [CrossRef]
46. Liu, H.; Wang, Y.; Liu, Y.; Peng, Y.; Li, M.; Lei, W. The LVRT strategy for VSG based on the quantitatively designed virtual impedance. *High Volt. Eng.* **2022**, *48*, 245–256.
47. Xu, Z.; Zhang, Z.; Xu, W. Research on application of LCC-MMC series hybrid HVDC topology for large scale clean energy base integration. *Power Capacit. React. Power Compens.* **2022**, *43*, 119–126.
48. Xu, Z. Characteristics of HVDC connected to weak AC systems Part I: HVDC transmission capability. *Power Syst. Technol.* **1997**, *21*, 12–16.
49. Xu, Z. The characteristics of HVDC systems to weak ac systems part II: Control modes and voltage stability. *Power Syst. Technol.* **1997**, *21*, 1–4.
50. Xu, Z. *Dynamic Performance Analysis of AC/DC Power Systems*; China Machine Press: Beijing, China, 2004.
51. CIGRE Working Group B4.62. *Connection of Wind Farms to Weak AC Networks*; CIGRE: Paris, France, 2016.
52. Australian Energy Market Operator. *SYSTEM Strength Impact Assessment Guidelines*; AEMO: Melbourne, Australia, 2018.
53. CIGRE Working Group B4.41. Systems with multiple DC infeed. *ELECTRA* **2007**, *15*, 14–18.
54. CIGRE Working Group B4.41. *Systems with Multiple DC Infeed*; CIGRE: Paris, France, 2008.
55. Zhang, H.; Du, Y. Enlarging of the Thevenin's theorem in two-pole network. *J. Binzhou Teach. Coll.* **1999**, *15*, 32–33.
56. ENTSO-E. *Rate of Change of Frequency (RoCoF) Withstand Capability*; ENTSO-E: Brussels, Belgium, 2018.
57. Sun, H.; Wang, B.; Li, W.; Yang, C.; Wei, W.; Zhao, B. Research on inertia system of frequency response for power system with high penetration electronics. *Proceeding CSEE* **2020**, *40*, 5179–5191.
58. Zhang, L.; Harnrfors, L.; Nee, H. Power-synchronization control of grid-connected voltage-source converters. *IEEE Trans. Power Syst.* **2010**, *25*, 809–820. [CrossRef]
59. Zhang, L.; Harnefors, L.; Nee, H. Interconnection of two very weak AC systems by VSC-HVDC links using power-synchronization control. *IEEE Trans. Power Syst.* **2011**, *26*, 344–355. [CrossRef]
60. Beck, H.; Hesse, R. Virtual synchronous machine. In Proceedings of the 2007 9th International Conference on Electrical Power Quality and Utilization, Barcelona, Spain, 9–11 October 2007; pp. 1–5.
61. Driesen, J.; Visscher, K. Virtual synchronous generators. In Proceedings of the 2008 IEEE Power and Energy Society General Meeting-Conversion and Delivery of Electrical Energy in the 21st Century, Pittsburgh, PA, USA, 20–24 July 2008; pp. 1323–1325.
62. Van, T.; Visscher, K.; Diaz, J.; Karapanos, V.; Woyte, A.; Albu, M.; Federenciuc, D. Virtual synchronous generator: An element of future grid. In Proceedings of the 2010 IEEE PES Innovative Smart Grid Technologies Conference Europe, Gothenburg, Sweden, 11–13 October 2010; pp. 1–7.
63. Zhong, Q.; Weiss, G. Synchronverters: Inverters that mimic synchronous generators. *IEEE Trans. Ind. Electron.* **2011**, *58*, 1259–1267. [CrossRef]
64. Zhong, Q.; Nguyen, P.; Ma, Z.; Sheng, W. Self-synchronized synchronverters: Inverters without a dedicated synchronization unit. *IEEE Trans. Power Electron.* **2014**, *29*, 617–630. [CrossRef]
65. Guan, M.; Pan, W.; Zhang, J.; Hao, Q.; Cheng, J.; Zheng, X. Synchronous generator emulation control strategy for voltage source converter (VSC) stations. *IEEE Trans. Power Syst.* **2015**, *30*, 3093–3101. [CrossRef]
66. Zhang, Z.; Xue, Y.; Xu, Z. Versatile static synchronous machine and its reference machine following control strategy. *IET Renew. Power Gener.* **2022**, *16*, 3184–3196. [CrossRef]
67. Wu, H.; Wang, X. Design-oriented transient stability analysis of grid-connected converters with power synchronization control. *IEEE Trans. Ind. Electron.* **2019**, *66*, 6473–6482. [CrossRef]

68. Taul, M.; Wang, X.; Davari, P.; Blaabjerg, F. An overview of assessment methods for synchronization stability of grid-connected converters under severe symmetrical grid faults. *IEEE Trans. Power Electron.* **2019**, *34*, 9655–9670. [CrossRef]
69. Wang, X.; Taul, M.; Wu, H.; Liao, Y.; Blaabjerg, F.; Harnefors, L. Grid-synchronization stability of converter-based resources—An overview. *IEEE Open J. Ind. Appl.* **2020**, *1*, 115–134. [CrossRef]
70. Xu, Z.; Dong, H. Three basic constraints for the reasonable size of synchronous power systems. *Int. J. Electr. Power Energy Syst.* **2017**, *90*, 76–86. [CrossRef]
71. Xu, Z.; Dong, H.; Song, P.; Cheng, B. Three Basic Constraints for Reasonable Size of Synchronous Grids. *Electr. Power Constr.* **2015**, *36*, 77–84.
72. Xu, Z.; Song, P.; Huang, H. Three macroscopic indices for describing the quality of AC/DC power grid structures. *IET Gener. Transm. Distrib.* **2016**, *10*, 175–182. [CrossRef]

energies

MDPI

Article

# An Automated and Interpretable Machine Learning Scheme for Power System Transient Stability Assessment

**Fang Liu [1], Xiaodi Wang [1], Ting Li [1], Mingzeng Huang [2], Tao Hu [2,*], Yunfeng Wen [2] and Yunche Su [1]**

1 State Grid Sichuan Economic Research Institute, Chengdu 610041, China
2 Engineering Research Center of Power Transmission and Transformation Technology of Ministry of Education, Hunan University, Changsha 410082, China
* Correspondence: htao@hnu.edu.cn

**Abstract:** Many repeated manual feature adjustments and much heuristic parameter tuning are required during the debugging of machine learning (ML)-based transient stability assessment (TSA) of power systems. Furthermore, the results produced by ML-based TSA are often not explainable. This paper handles both the automation and interpretability issues of ML-based TSA. An automated machine learning (AutoML) scheme is proposed which consists of auto-feature selection, CatBoost, Bayesian optimization, and performance evaluation. CatBoost, as a new ensemble ML method, is implemented to achieve fast, scalable, and high performance for online TSA. To enable faster deployment and reduce the heavy dependence on human expertise, auto-feature selection and Bayesian optimization, respectively, are introduced to automatically determine the best input features and optimal hyperparameters. Furthermore, to help operators understand the prediction of stable/unstable TSA, an interpretability analysis based on the Shapley additive explanation (SHAP), is embedded into both offline and online phases of the AutoML framework. Test results on IEEE 39-bus system, IEEE 118-bus system, and a practical large-scale power system, demonstrate that the proposed approach achieves more accurate and certain appropriate trust solutions while saving a substantial amount of time in comparison to other methods.

**Keywords:** transient stability; automated machine learning; interpretability; Bayesian optimization; SHAP; CatBoost; PMU

**Citation:** Liu, F.; Wang, X.; Li, T.; Huang, M.; Hu, T.; Wen, Y.; Su, Y. An Automated and Interpretable Machine Learning Scheme for Power System Transient Stability Assessment. *Energies* **2023**, *16*, 1956. https://doi.org/10.3390/en16041956

Academic Editor: J. C. Hernandez

Received: 27 December 2022
Revised: 4 February 2023
Accepted: 10 February 2023
Published: 16 February 2023



## 1. Introduction

With the ever-increasing penetration of uncertain renewable generation and bulk HVDC infeed into power systems, a considerable number of coal-fired synchronous generation units are being displaced [1]. The dynamic characteristics of modern hybrid AC/DC power systems become increasingly complicated, which have imposed unprecedented challenges on transient stability assessment (TSA) in power system planning and operation. A reduction in system inertia and insufficient dynamic grid support are the main factors that could negatively affect the transient response of power systems [2]. The transient stability of power systems is deteriorated by the integration of large amounts of uncertain and intermittent renewable generation [3].

Currently, commonly used TSA tools rely on analytical model-based methods, such as time-domain simulation (TDS) and direct methods [4]. TDS describes the transient response of a power system with a set of high-dimensional nonlinear differential-algebraic equations, and uses numerical integration methods to solve them. TDS is often considered the most accurate method available for TSA. However, the intensively computational burden for massive operation scenarios and credible contingencies make it intractable for online applications. From the energy point of view, direct methods evaluate transient stability via transient energy function (TEF) [5], extended equal area criterion (EEAC) [6,7], trajectory analysis [8,9], etc. However, due to the model simplifications required, direct methods have major drawbacks of poor adaptability and conservative results when employed on practical large-scale power systems.

Nowadays, with widespread deployed phasor measurement units (PMU) in power systems, wide area measurement system (WAMS) and synchronous system measurement data are available. Because the traditional TSA methods cannot meet the needs of real-time TSA, it is urgent to develop a new data-driven scheme to support online TSA, i.e., making fast and accurate evaluation decisions based on the real-time power system operating status accessed from PMU measurements.

Owing to the rapid advancement of artificial intelligence (AI) techniques, it has been identified that machine learning (ML) can be used to implement online TSA. Over the past few years, the use of ML-based methods for TSA has been extensively explored, such as long short-term memory (LSTM) [10], extreme learning machine (ELM) [11], convolutional neural network (CNN) [12,13], decision tree (DT) [14], and hybrid ensemble learning [15]. A support vector machine (SVM)-based imbalanced correction method is proposed to address the problem that unstable samples rarely appear in practical systems giving rise to imbalanced samples [16]. To assess the transient stability of power systems by improving classification accuracy, an artificial intelligence method based on sparse dictionary learning is applied to transient stability assessment [17]. Because of the problem that differentiating between short-term voltage instability and transient rotor angle instability is not an easy task, a method based on graph attention networks (GATs) is proposed to solve it [18]. In [19], effective transient stability prediction in a data-driven manner is achieved by a transient stability assessment method which is based on high expressibility and low-depth quantum circuit.

Compared with conventional methods, ML-based methods do not need to model the power system. Instead, they use predetermined transient stability datasets to derive the relationship between system dynamic response and the corresponding stability conditions. New unlearnt cases can be assessed with a minimum of computational effort with the relationship established [10]. Therefore, ML-based methods are advantageous for real-time fast TSA, lower data requirement, and the enhanced capability of knowledge discovery.

Despite ML-based TSA approaches having achieved certain developments, it is still difficult to directly apply them in operational planning and dispatch of practical power systems. The main reasons are two-fold:

(i) To realize successful application, human experts are heavily involved in the four steps of ML, i.e., feature engineering, model selection, hyperparameter optimization, and performance evaluation, especially hyperparameter optimization [20]. Existing work on ML-based TSA assumes that the predefined input features and parameters of the trained model are always optimal for application. However, this assumption may not be true for power systems due to many practical issues, such as model updating, topology change, and variation of operating conditions. Since human experts are usually limited, to improve the accuracy and adaptability, many repeated manual feature adjustments and much heuristic parameter tuning are required during the debugging of ML-based TSA. This is highly tedious, inefficient, and time-consuming [21].

(ii) On the other hand, the state-of-the-art ML-based TSA approaches have relatively poor transparency, because their models establish the mapping capability through black-box structures, such as deep learning and ensemble learning algorithms [12,13,15]. It is difficult for power system operators to interpret the behaviors of complex ML models and understand how particular decisions are made by these models. Hence, the uninterpretable results produced by ML-based TSA are often not actionable. This lack of interpretability has thus limited the use of ML-based TSA approaches in power industries.

In order to reduce the human effort needed for applying ML, this paper proposes an automated machine learning (AutoML)-based TSA approach. AutoML is naturally the intersection of automation and machine learning, aiming to achieve accurate decisions in a data-driven, automated, and objective manner [22]. In AutoML, feature engineering, model learning, hyperparameter optimization, and performance evaluation can all be realized by computer programs, which makes ML much more accessible for online TSA. Furthermore, to make the AutoML-based method produce interpretable TSA predictions, we introduce Shapley additive explanation (SHAP) [23] into AutoML to explain why a certain prediction is made for a given case. Therefore, the proposed approach can be both automated and explainable for online use.

This work handles both the automation and interpretability issues of ML-based TSA. The main contributions of this paper are summarized as follows:

(i) An AutoML scheme is designed for online TSA, which consists of auto-feature selection, CatBoost, Bayesian optimization, and performance evaluation. To ensure the best performance of the CatBoost-based ensemble learning, auto-feature selection and Bayesian optimization are introduced to automatically determine the best input features and optimal hyperparameters, respectively. By leveraging the adopted techniques, performance improvement is achieved while saving a substantial amount of time for manual feature adjustments and heuristic parameter tuning.

(ii) To address the interpretability issue, this paper introduces SHAP to interpret the outputs of the proposed AutoML-based TSA. The impact of each input feature on AutoML's prediction is represented using SHAP values. The distribution of the SHAP values about the feature with a significant impact on the obtained prediction can provide additional insights into the decision interpretation.

The proposed interpretable AutoML-based TSA is tested on a provincial power system in China, in addition to two IEEE systems. Simulation results compared to other methods demonstrate the effectiveness and superiority of the proposed approach.

## 2. Automated Machine Learning

To enable faster deployment of ML-based TSA and reduce the heavy dependence on human experts, an AutoML scheme is proposed to achieve real-time evaluation. The proposed AutoML (shown in Figure 1) consists of auto-feature selection, CatBoost, Bayesian optimization, and performance evaluation. Firstly, by combining the feature importance and the corresponding threshold, input features with a high impact on the output are automatically selected from raw input characteristics. Then, to mine the mapping relationship between the input characteristics and the postfault transient stability statuses, CatBoost is introduced as a TSA classifier, which avoids the modeling of complex power systems. Meanwhile, Bayesian optimization is applied to determine the hyperparameters of the CatBoost-based learning model automatically. Finally, evaluation indices are built to evaluate the effectiveness of the AutoML model.

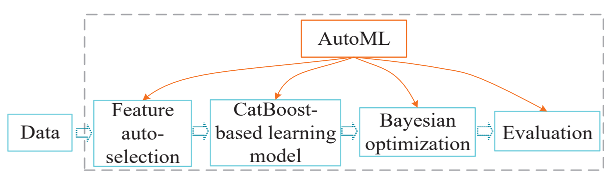


**Figure 1.** The scheme of AutoML in TSA.

### 2.1. Auto-Feature Selection

The dimensionality of the original input dataset increases dramatically with the system scale expansion, which could result in the dimension explosion issue. On the other hand, the use of input features that are effective can enable the ML model to learn faster and perform better in classification. Thus, we utilize an auto-feature selection technique to strengthen the mapping relationship between input features and transient stability statuses. To estimate the importance of each input feature, the split information during the offline training of CatBoost is fully made use of via calculation (1) [24]. To automatically filter useless features, a threshold value $p$ is defined. Only features with impact factor $f_{\mathrm{IF}}$ larger than $p$ are selected as input data [25].

$$f_{\mathrm{IF}} = \sum \left( v_1 - \frac{v_1 \cdot c_1 + v_2 \cdot c_2}{c_1 + c_2} \right)^2 \cdot c_1 + \left( v_2 - \frac{v_1 \cdot c_1 + v_2 \cdot c_2}{c_1 + c_2} \right)^2 \cdot c_2 \tag{1}$$

where $c_1$ and $c_2$ represent the total weight of objects in the left and right leaves, respectively; $v_1$ and $v_2$ represent the formula value in the left and right leaves, respectively.

### 2.2. CatBoost

CatBoost is a new ensemble ML method based on gradient boosting over decision trees [26]. With advantages of improved accuracy, categorical features support, multi-GPU support for training, and reduced overfitting, CatBoost has shown fast, scalable, and high performance for classification, regression, and other machine learning tasks [27].

Given a dataset $D = \{(x_i, y_i)\}_{i=1}^{m}$, where $x_i$ is the input vector of sample $i$, $y_i$ denotes the TSA result of credible contingency $i$, $m$ denotes the number of samples. A series of decision tree models are built up based on $D$, written as [26]:

$$h(x) = \sum_{j=1}^{J} b_j I_{\{x \in R_j\}} \tag{2}$$

where $I(\cdot)$ is an indicator function; $R_j$ is disjoint regions corresponding to leaves of the tree; $J$ is the number of disjoint regions; $b_j$ is the predicted value of $R_j$.

In the gradient boosting procedure, a sequence of approximations ($F^t$) is built iteratively in a greedy manner [26]:

$$F^t = F^{t-1} + \alpha h^t \tag{3}$$

where $h^t$ is a tree in the $t$-th iteration process; $\alpha$ is the step size.

The loss function of CatBoost is given by [26]:

$$h^t = \mathrm{argmin}_{\mathrm{h} \in H} \mathbb{E}\left(-\tau^t(x, y) - h(x)\right)^2 \tag{4}$$

where $\tau$ is the gradient value; The objective of a learning task is to train a series of functions $F^t$ to minimize the loss function. After $T$ iterations, the final model can be obtained:

$$F(x) = \sum_{t=1}^{T} h^t \tag{5}$$

To overcome the residual shift caused by the target leakage issue, ordered boosting [26] is implemented in CatBoost. The principle of the ordered boosting has been described in [28].

### 2.3. Bayesian Optimization

The most fundamental objective in AutoML is to set hyperparameters to optimize the overall performance automatically. This paper introduces Bayesian optimization to realize automatic hyperparameter tuning of the CatBoost-based learning model.

Bayesian optimization is an emerging optimization framework for the global optimization of expensive black-box functions [29]. Acquisition function and probabilistic surrogate model are its two key components [30].

Bayesian optimization is used to obtain the global maximum value X* of function $f(\lambda)$ in candidate hyperparameter set $\chi$, and the corresponding optimal combination of CatBoost's hyperparameters is determined subsequently [31]:

$$\lambda^* = \mathrm{arg}_{\lambda \in \chi} \mathrm{max} f(\lambda) \tag{6}$$

Gaussian process (GP) is employed as the prior function to model the target function due to its closed-form computability and well-calibrated uncertainty estimates [30]. In GP, the combination of finite samples can be represented by [32]:

$$f(\lambda) \sim GP\big(m(\lambda), k\big(\lambda, \lambda'\big)\big) \tag{7}$$

$$k\big(\lambda, \lambda'\big) = \exp\left(-\frac{1}{2\theta}\|\lambda - \lambda'\|^2\right) \tag{8}$$

where $m(\lambda)$ is the mean function of $\lambda$; $k(\lambda, \lambda')$ is the covariance function of $\lambda$; $\theta$ is the length-scale parameter.

Having observed data $\{\lambda_{1:t}, f_{1:t}\}$, the joint distribution of observed data $f_{1:t}$ and prediction $f_{t+1} = f(\lambda_{t+1})$ agrees with the multivariate Gaussian distribution as shown in Equation (9):

$$\begin{bmatrix} f_{1:t} \\ f_{t+1} \end{bmatrix} \sim N\left(0, \begin{bmatrix} K & \mathrm{k} \\ \mathrm{k}^{\mathrm{T}} & k(\lambda_{t+1}, \lambda_{t+1}) \end{bmatrix}\right) \tag{9}$$

where k = $[k(\lambda_{t+1}, \lambda_1)\ k(\lambda_{t+1}, \lambda_2) \ldots\ k(\lambda_{t+1}, \lambda_t)]$; $K$ is a covariance matrix; $N(\cdot)$ denotes the joint Gaussian distribution.

The predictive distribution $P(\cdot)$ at a new sampling point $\lambda_{t+1}$ can be expressed by:

$$P(f_{t+1}|\lambda_{t+1}, \lambda_{1:t}, f_{1:t}) = N\big(\mu_t(\lambda_{t+1}), {\sigma_t}^2(\lambda_{t+1})\big) \tag{10}$$

where $\mu_t(\lambda_{t+1})$ and ${\sigma_t}^2(\lambda_{t+1})$ denote the predictive mean and variance, respectively.

The acquisition function of Bayesian optimization is the probability of improvement (POI):

$$PI(\lambda) = \phi\left(\frac{u(\lambda) - f(\lambda^+) - \varepsilon}{\delta(\lambda)}\right) \tag{11}$$

where $\phi(\cdot)$ is the normal cumulative distribution function; $\varepsilon$ is a trade-off parameter; function $\delta(\lambda)$ is the standard deviation. By maximizing the acquisition function, the most prospective sampling points for the next search are computed.

### *2.4. Evaluation Indices*

To reasonably evaluate the effectiveness of the proposed AutoML, *Accuracy* and *Recall* are used as evaluation indices. *Accuracy* and *Recall* represent the ability of AutoML to accurately identify all and unstable samples, respectively [33].

$$Accuracy = \frac{f_{11} + f_{00}}{f_{11} + f_{00} + f_{01} + f_{10}} \tag{12}$$

$$Recall = \frac{f_{00}}{f_{00} + f_{01}} \tag{13}$$

where $f_{11}$ and $f_{00}$ are the number of stable instances and unstable instances correctly classified, respectively; $f_{10}$ and $f_{01}$ are the number of stable instances and unstable instances falsely classified, respectively.

*AUC*, an important metric for measuring the classification performance under imbalanced conditions [34], is also used for the performance evaluation of the AutoML:

$$AUC = \frac{1}{n^+ n^-} \sum_{i=1}^{n^+} \sum_{j=1}^{n^-} I\left(f\left(x_i^+\right) > f\left(x_j^-\right)\right) \tag{14}$$

where $n^+$ and $n^-$ are the number of instances predicted as stable and unstable, respectively; ${x_i}^+$ and ${x_j}^-$ are, respectively, the instance predicted as stable and unstable; $f(x)$ is the AutoML classifier; $I(\cdot)$ is the indicator function.

## 3. Proposed AutoML-Based TSA with Interpretability Analysis

This paper establishes a nonlinear relationship between the system dynamic response and the transient stability using the proposed AutoML as the assessment model. The offline training stage and the online application stage form the entire framework of the proposed method. To help operators understand why a stable/unstable status prediction is made, interpretability analysis is embedded into both the offline and online stages of the AutoML framework, which helps to engender appropriate trust in the AutoML-based TSA predictions. Figure 2 provides an illustration of the flowchart of the proposed interpretable AutoML-based TSA method.

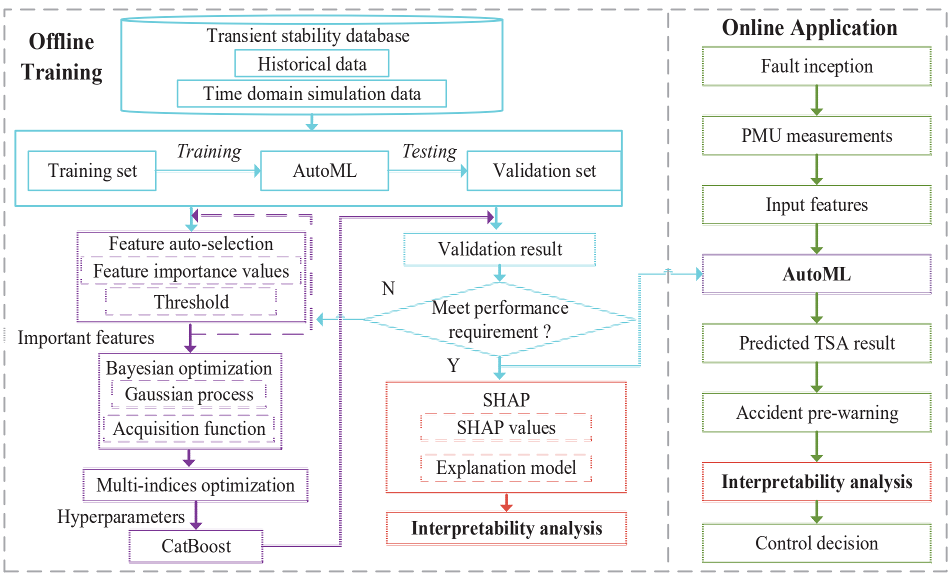


**Figure 2.** Flowchart of the proposed interpretable AutoML-based TSA method.

### 3.1. *Offline Training*

The following are the main steps of the offline training stage:

(1) Historical PMU data and fault recordings are used as the dataset for offline training. When historical data is insufficient, simulation can be conducted to obtain a certain amount of dataset. The postfault system stability can be determined by the transient stability index (TSI) [16]:

$$\eta = (360^\circ - |\Delta\delta|_{\max})/(360^\circ + |\Delta\delta|_{\max}) \tag{15}$$

where $|\Delta\delta|_{\max}$ denotes the absolute value of the maximum angle deviation of any two generators. The system is considered stable only when $\eta > 0$. Combining historical and offline simulation data, a sample dataset with diversity can be obtained.

(2) The comprehensive dataset is divided into a training set and a validation set to test the performance of the AutoML-based TSA.

(3) During the offline training process of CatBoost, the individual impact factor $f_{\mathrm{IF}}$ of each original input feature (i.e., active and reactive power of transmission lines, phase angle, voltage amplitude [11]) is calculated by Equation (1). Then, critical features are automatically selected as input features based on impact factor $f_{\mathrm{IF}}$ and threshold value $p$.

(4) Bayesian optimization is used to automatically search the optimal hyperparameters of the CatBoost learning model. Because TSA is a non-equilibrium classification problem,

i.e., unstable samples rarely appear in practice, the AutoML's capability to recognize transient instability may be greatly affected if only one single indicator (i.e., accuracy) is used as the objective. To obtain better performance of the CatBoost learning model, we introduce multiple indices (i.e., *Accuracy*, *Recall*, *AUC*) into the objective function:

$$Maximize \quad w_1 \cdot Accuracy + w_2 \cdot Recall + w_3 \cdot AUC \tag{16}$$

$$p_{i\min} \leq p_{\mathrm{i}} \leq p_{i\max} \tag{17}$$

where $w_j$ is the weight of the $j$-th evaluation index; $p_1$, $p_2$, $p_3$, and $p_4$ represent the parameters of CatBoost, i.e., learning rate, l2 leaf regularization *(l2_leaf_reg)*, the maximum depth of trees (max_depth), and the number of estimators (n_estimators). As the unstable status judged to be stable will cause cascading failure or even widespread blackout, the capability to accurately identify unstable samples (Recall) needs more attention in the hyperparameter optimization. Hence, the weight of Recall in the objective function (16) should be set larger than those of Accuracy and AUC. Through the GP and POI mechanism, Bayesian optimization iteratively validates hyperparameter combinations to maximize the objective function with multiple indices.

### 3.2. Online Application

When the AutoML-based TSA is well trained, it can be implemented online to predict system transient stability. Once a fault is detected, the critical features acquired from real-time PMU measurements are fed into the learned AutoML to perform TSA. If the system is insecure, operators will receive an early warning, and then they can quickly take emergency control actions to maintain the stability of the system. To improve the adaptability of AutoML, evaluated instances with accurate TSA assessment can be fed back to the offline stage to enrich the training database.

### 3.3. Interpretability Analysis

The increasing tension between the accuracy and interpretability of ML-based predictions has motivated the development of approaches that help users understand the predictions. SHAP [18] is a recently proposed novel unified framework for interpreting model predictions. Leveraging SHAP, the proposed AutoML's prediction can be explained as a sum of SHAP values corresponding to each feature. As shown in Figure 2, the original AutoML-based TSA model is approximated using an explanation model $g$, which is defined as a linear function of binary variables [23]:

$$g(z') = \phi_0 + \textstyle\sum_{i=1}^{M} \phi_i {z_i}' \tag{18}$$

where ${z_i}'$ represents a feature being observed (${z_i}'$ = 1) or unobserved (${z_i}'$ = 0); $M$ is the number of input features; SHAP values $\phi_i$ (feature attribution values), explaining a prediction $f$, can be computed by [23]:

$$\phi_i = \sum_{s \subseteq N \backslash \{i\}} \frac{|S|!(M - |S| - 1)!}{M!} \Delta_i(S) \tag{19}$$

$$\Delta_i(S) = f_x(S \cup \{i\}) - f_x(S) \tag{20}$$

As shown in Equation (19), SHAP values are evaluated by combining the conditional expectation $E[f(x) \mid x_S]$ with the classic Shapley values, where $f_x(x) = E[f(x) \mid x_S]$ corresponds to the desired outcome of the function conditioned on a subset $S$; $S$ is a subset of $N$ with non-zero indices in $z'$; $N$ is the set of all input features; $\Delta_i(S)$ denotes the contribution of feature $i$ to $S$.

Specifically, the attribution values of the explanation model $g$ match the AutoML-based TSA model for a specific input, which can be represented as [23]:

$$f(x) = \phi_0 + \sum_{i=1}^{M} \phi_i \tag{21}$$

where $\phi_0(f,x) = E[f(x)]$ is the desired value of the AutoML-based TSA model over the transient stability dataset.

Aided by the explanation model $g$ and SHAP values, the impacts of each input feature on the transient stability prediction are evaluated. Then, the AutoML-based TSA prediction can be explained based on the summation of SHAP values. Therefore, features with significant impact on the stability prediction can be easily identified by comparing their SHAP values. The process of the interpretability analysis of the AutoML-based TSA is illustrated in Algorithm 1.

**Algorithm 1. The process of interpretability analysis**

**Input:** $f(x)$—Trained AutoML model; *X_train*—Trained data; *X_e*—A stable or unstable instance that needs to be explained.
**Output:** SHAP values for each input system features
Train an explainer through ($f(x)$, *X_train*)
**for** each $i \in$ input features(*X_train*) do
  Use EXPVALUE method to estimate E[$f(x) \mid x_S$]
  **procedure** EXPVALUE($x$, $S$, *tree*)
    **procedure** G($j$, $w$)
      **if** $v_j \neq$ *internal* **then**
        **return** $w \cdot v_j$
      **else**
        **if** $d_j \in S$ **then**
          **return** G($a_j$, $w$) **if** $x_{dj} \leq t_j$ **else** G($b_j$, $w$)
        **else**
          **return** G($a_j$, $wr_{aj}/r_j$) + G($b_j$, $wr_{bj}/r_j$)
    **return** G(1,1)
    **end procedure**
  **end procedure**
  Calculating attribute values $\phi_i$ by (19)
  Establishing an explanation model $g$ by (18)
  **return** $g$
Interpretability for X_e
**for** each $i \in$ input system features(*X_e*) do
  SHAP values [$i$] ← *explainer.shapvalues(X_e, i)*
**return** SHAP values [$i$]
A certain predicted status of the power system can be interpreted based on the sum of SHAP values [$i$].

## 4. Case Study

To demonstrate the effectiveness of the proposed approach, two IEEE test systems (IEEE 39-bus and 118-bus systems) and a large-scale provincial power system (PPG) in China were utilized for simulation. The IEEE 39-bus system has 39 buses, 10 generators, 19 loads, and 46 branches. The IEEE 118-bus system has 118 buses, 54 thermal units, 91 loads, and 186 branches. The practical grid has 1154 buses, 208 generators, and 451 loads in 2020. Furthermore, ten HVDC links are fed out to deliver electric power to other provincial systems. PSD-BPA software is used for data generation. The proposed interpretable AutoML-based TSA was deployed on the Python 3.7 platform. The SHAP values of AutoML models were calculated and visualized with the help of a python-based SHAP library [35]. All testing was performed on a personal computer with Intel Core i5-10400F 2.9 GHz CPU, 16.0 GB RAM.

### 4.1. Database Generation

TDS was implemented on the PSD-BPA software to generate input dataset. As for the IEEE 39-bus and IEEE 118-bus systems, ten load levels (75, 80, 85, 90, 95, 100, 105, 110, 115, 120%) were considered. All three-phase to ground faults at any bus were considered in the contingency set, and the faults were assumed occurring on each transmission line at four locations (at 0, 25, 50, and 70% of the length); Each fault was set to start at 1.0 s and being cleared at two cases: 1.1 s and 1.2 s. The duration of each simulation was 20 s. For the practical grid, four operation modes were considered, all three-phase to ground faults and HVDC blockings were analyzed. The numbers of stable and unstable instances in each dataset of the three test systems are listed in Table 1. For each test system, the dataset was split into a training sample set and a testing sample set in a ratio of 8:2.

**Table 1.** Database of the three test systems.

| System | No. of Instances | Unstable Instances | Stable Instances | Raw Features | Selected Features |
|---|---|---|---|---|---|
| 39-bus | 3668 | 973 | 2695 | 170 | 36 |
| 118-bus | 6781 | 1394 | 5387 | 586 | 37 |
| PPG | 9495 | 2705 | 7920 | 828 | 45 |

### 4.2. The Selection of Important Features

Necessary features were automatically selected by the AutoML using Equation (1), in which the threshold $p$ is set at 0.7. The fifth and sixth columns of Table 1 show the dimensions of raw features and selected important features. One can observe that for the IEEE 39-bus system, the dimensions of raw features were 170, but most of them were useless, which posed great computational burden. By leveraging the auto-feature selection mechanism, only 36-dimensional features were retained. Similarly, dimensions of selected important input features for the IEEE 118-bus system and the practical grid were 37 (6.3% of the raw features) and 45 (5.4% of the raw features), respectively. Consequently, the dimension explosion issue when applying AutoML to large-scale systems could be avoided.

### 4.3. Bayesian Optimization

The effectiveness of utilizing Bayesian optimization (BO) in the AutoML to find optimal hyperparameters was compared with the other two traditional methods, which were grid search (GS) and randomized search (RS). All tests were carried out using the same training and testing dataset. The weights of *Accuracy*, *Recall*, and *AUC* in the objective function of BO were set at 0.25, 0.5 and 0.25, respectively.

The hyperparameter tuning process of RS and BO on the IEEE 39-bus system is shown in Figure 3. To visualize the process of the sequential selection of hyperparameters, the impact of the combination of any two hyperparameters (learning rate, l2_leaf_reg, and n_estimators) on the evaluation indices (*Accuracy*, *Recall*, *AUC*) was analyzed. The background of Figure 3a–d are colored based on the values of *Accuracy*, *Recall*, and *AUC*, respectively. It can be seen that hyperparameters determined by RS were irregularly distributed in Figure 3a–d, which results in the optimal hyperparameters being easily skipped. BO determines hyperparameters through GP and POI, hence it is more persuasive. Compared with RS, there were more hyperparameters determined by BO located in the optimal space. According to Figure 3, the appropriate search space of learning rate, l2_leaf_reg, and n_estimators could be set at [0.01, 0.3], [1, 10], and [40, 120], respectively.

The CPU time and evaluation indices produced by BO, GS, and RS optimized CatBoost are compared and shown in Table 2. For the IEEE 39-bus system, the Bayesian optimized CatBoost had an Accuracy of 98.77%, Recall of 98.44%, and AUC of 98.67%, which was 0.41, 1.57 and 1.04% higher than the RS optimized CatBoost, respectively. GS traverses all parameter combinations to find the best hyperparameters, which makes it easy to encounter the combination explosion issue. Although evaluation indices obtained by GS are closer to those obtained by BO, it is extremely time-consuming to run GS (the total time required is 25 h). The CPU time (93.1 s) of performing BO was only 0.1% of the GS. By mining the rules on transient data, BO can efficiently find optimal hyperparameters, which saves substantial amounts of time and avoids the inefficiency of heuristic parameter tuning.

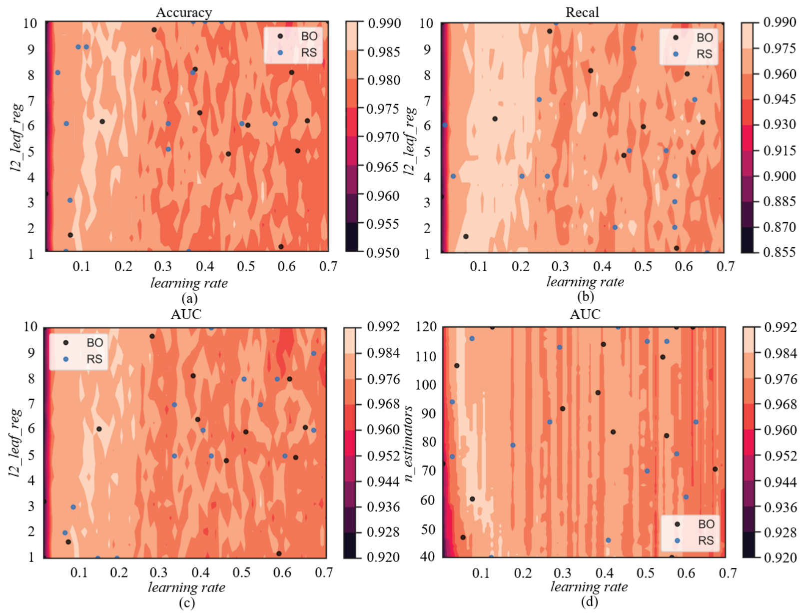


**Figure 3.** (**a**) Distribution of Accuracy impacted by learning rate and l2_leaf_reg; (**b**) distribution of Recall impacted by learning rate and l2_leaf_reg; (**c**) distribution of AUC impacted by learning rate and l2_leaf_reg; (**d**) distribution of AUC impacted by learning rate and n_ estimators.

**Table 2.** Performance comparison of different parameter tuning methods.

| Method | System | Tuning Time | Accuracy/% | Recall/% | AUC/% |
|---|---|---|---|---|---|
| BO | 39-bus | 93.1 s | 98.77 | 98.44 | 98.67 |
| GS | 39-bus | 25 h | 98.36 | 97.39 | 97.86 |
| RS | 39-bus | 214.7 s | 98.36 | 96.87 | 97.63 |
| BO | 118-bus | 102.3 s | 97.19 | 96.80 | 97.08 |
| GS | 118-bus | 25 h | 97.13 | 96.09 | 96.74 |
| RS | 118-bus | 220.3 s | 96.46 | 96.08 | 96.32 |
| BO | PPG | 114.1 s | 97.85 | 96.22 | 97.23 |
| GS | PPG | 26 h | 97.51 | 95.41 | 96.84 |
| RS | PPG | 256.8 s | 97.18 | 94.71 | 96.39 |

Tests concerning the effectiveness of BO were also performed on the IEEE 118-bus system and the practical grid, and the results are provided in Figure 4 and Table 2 (rows 4–9). As shown in Table 2, the CPU time of performing BO was significantly lower than that of GS and BS, while the CatBoost can achieve the best performance based on hyperparameters found by BO. Figure 4 shows that the highest range of the AUC index achieved by BO optimized CatBoost was [96%, 97.5%] for both the 118-bus system and the practical grid. The space of this range produced by BO (drawn with light color) is quite large in Figure 4a,b, revealing that BO-optimized CatBoost can accurately classify TSA statuses when applied to large-scale power systems.

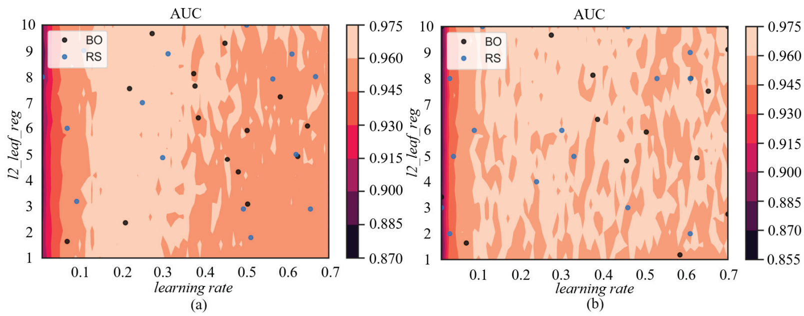


**Figure 4.** (**a**) Distribution of AUC impacted by learning rate and l2_leaf_reg on the 118-bus system; (**b**) distribution of AUC impacted by learning rate and l2_leaf_reg on the practical grid.

### *4.4. Comparison of the Classifiers' Performance*

The proposed AutoML-based TSA has been compared with some other ML methods, such as LSTM, XGBoost, RF, and DT. Table 3 shows the evaluation indices obtained by the five methods in all test systems. For all three test systems, the proposed AutoML-based TSA had the highest Accuracy, Recall, and AUC in comparison with the other four ML-based TSA methods. For example, for the practical power system (Yunan power grid), AutoML achieved an Accuracy of 97.77%, Recall of 96.22%, and AUC of 97.23%. Note that, for the three systems, the Recall of the proposed AutoML-based TSA were all over 96%, demonstrating that AutoML can accurately identify the unstable operating status immediately following a fault. Because of the simple structure, the DT-based TSA method learns restrictedly and had the lowest level of Accuracy, Recall, and AUC for the three systems. XGBoost and LSTM-based TSA approaches have better performance than DT, but evaluation indices obtained by them are all lower than the proposed AutoML-based TSA. As the scale of the system expanded, the Recall index produced by LSTM, XGBoost, RF, and DT-based TSA decreased significantly. Taking the practical grid as an example, the Recall index produced by LSTM and XGBoost were around 93%, while RF and DT both had a Recall lower than 90%. Hence, the ability of these methods to identify unstable samples was not satisfactory when applied to large-scale systems. The proposed AutoML-based TSA still maintained good performance. The averages of the three evaluation indices produced by AutoML on the two large systems exceeded 97%.

**Table 3.** Results obtained by different methods on the three power systems.

| Method | System | Accuracy/% | Recall/% | AUC/% |
|---|---|---|---|---|
| AutoML | 39-bus | 98.77 | 98.44 | 98.67 |
| LSTM | 39-bus | 97.57 | 95.92 | 97.04 |
| XGBoost | 39-bus | 97.68 | 95.83 | 98.09 |
| RF | 39-bus | 96.19 | 94.55 | 95.71 |
| DT | 39-bus | 95.43 | 91.51 | 94.39 |
| AutoML | 118-bus | 97.20 | 96.80 | 97.05 |
| LSTM | 118-bus | 95.58 | 93.23 | 94.71 |
| XGBoost | 118-bus | 95.51 | 95.30 | 95.45 |
| RF | 118-bus | 94.85 | 94.67 | 94.78 |
| DT | 118-bus | 93.37 | 90.75 | 92.40 |
| AutoML | PPG | 97.85 | 96.22 | 97.23 |
| LSTM | PPG | 96.57 | 92.94 | 95.42 |
| XGBoost | PPG | 97.37 | 93.47 | 96.13 |
| RF | PPG | 95.54 | 89.06 | 93.47 |
| DT | PPG | 94.23 | 89.94 | 92.87 |

Figure 5 shows the 2D visualization of the predicted results obtained by AutoML, XGBoost, and RF-based TSA methods on the IEEE 39-bus system. The background of

Figure 5 is colored based on the probabilistic prediction of these methods. In the evaluation results of CatBoost-based AutoML, the pink background of isolated unstable samples is more obvious, indicating that compared with XGBoost and RF, the proposed approach can better distinguish isolated unstable samples, which is helpful to avoid misjudging the unstable operation state of the system after a disturbance accident.

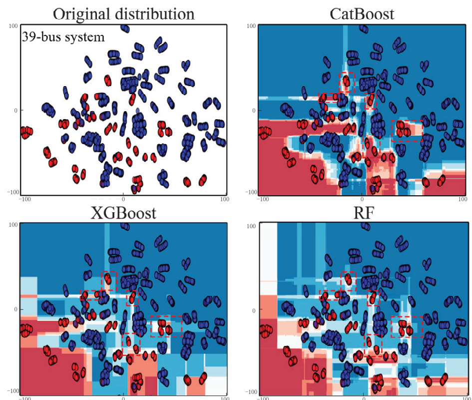


**Figure 5.** Visualization of prediction results. Red square in the figure represents the isolated unstable samples.

In real-time, the training time and testing time of ML-based TSA tools are of great concern. Table 4 compares the CPU time of AutoML and TDS on the three test systems. The proposed AutoML-based TSA is computationally efficient for both offline training and online testing. Furthermore, the effect of system scale on the model training is not significant, because redundant features are eliminated by using the AutoML. As for TDS, the excessive computational time required prevents its online use. Specifically, the CPU time of TDS is 17.7 h on the practical grid. However, the proposed AutoML-based TSA only needs 2.27 s, which is only 0.003% of that required by TDS. Thus, AutoML is more suitable for online TSA for large-scale power systems, which can help to save more time for subsequent control actions.

**Table 4.** Solution time on the three power systems.

| Systems | Training Time of AutoML | Testing Time of AutoML | Time of TDS |
|---|---|---|---|
| 39-bus system | 1.18 s | 0.02 s | 0.69 h |
| 118-bus system | 2.16 s | 0.02 s | 1.13 h |
| PPG | 2.27 s | 0.01 s | 17.71 h |

### *4.5. Interpretability Analysis*

SHAP was embedded into AutoML to interpret the behaviors of the AutoML-based TSA method and understand how a particular decision (the system will be transient stable/unstable) for a given case is made.

For clarity, transient stability prediction following a three-phase short-circuit fault occurring at line 2-30 in the IEEE-39 bus system was taken as an example for interpretability analysis. The fault lasted 0.1 s, and the system became unstable after clearing the fault. Figure 6 explains why the system is classified as instability by the AutoML-based TSA method based on SHAP values. The red-colored features in Figure 6 pushed the risk of transient instability lower, while the blue-colored features pushed the risk higher. Because the influence of the blue-colored features on the output prediction of the contingency was higher, AutoML predicted that the system would lose transient stability after the fault. As shown in Figure 6, input features $\theta_3$, $\theta_2$, $P_{2\text{-}30}$, and $Q_{2\text{-}25}$ had larger SHAP values, hence they had much more impact on the obtained prediction. These features were all directed to bus 2, which was consistent with the fault.

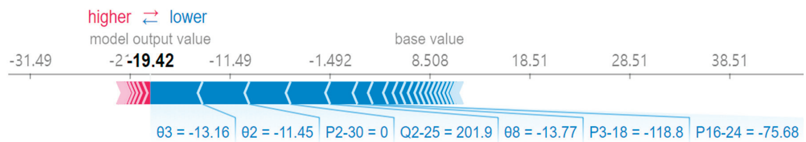


**Figure 6.** Interpretability of a prediction produced by AutoML on the IEEE-39.

To further interpret the effect of these features on the prediction, the SHAP dependence plots were used. Figure 7a–d show how SHAP values varied as a function of features $\theta_3$, $\theta_2$, $P_{2\text{-}30}$, and $Q_{2\text{-}25}$, respectively. The color corresponds to the values of the feature from low (blue) to high (red). The lower the SHAP values were, the higher risk of transient instability. Coloring each dot by $\theta_3$ and $\theta_2$ revealed that transient instability was more alarming when their values were low. When the value of $P_{2\text{-}30}$ belonged to the normal range ([−220, −110]) affected by the active power of generator G32, the risk of transient instability was low. Furthermore, the system will lose stability when the value of $Q_{2\text{-}30}$ is higher than 70. Consequently, the values of $\theta_3$, $\theta_2$, $P_{2\text{-}30}$, and $Q_{2\text{-}25}$ were all in the range where the risk of transient instability was high. Therefore, the unstable result obtained by the AutoML-based TSA was reasonable and credible.

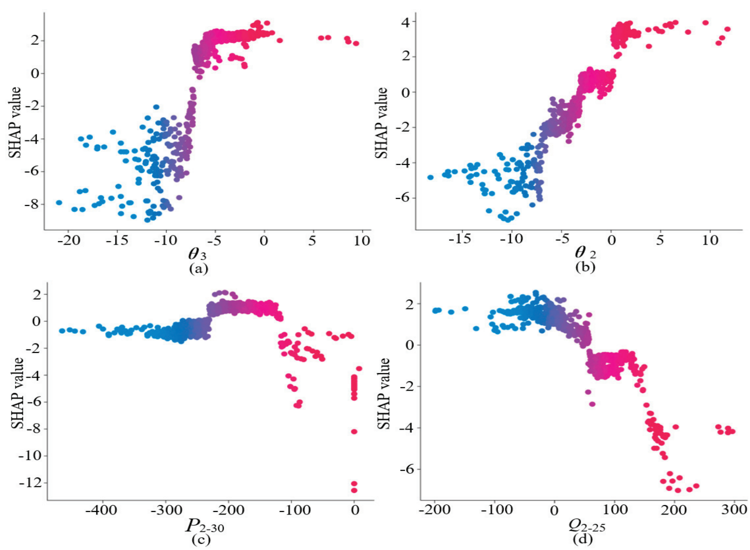


**Figure 7.** (**a**) SHAP dependence of $\theta_3$; (**b**) SHAP dependence of $\theta_2$; (**c**) SHAP dependence of $P_{2\text{-}30}$; (**d**) SHAP dependence of $Q_{2\text{-}35}$.

Figure 8 explains why the practical grid was considered unstable after a specific fault, i.e., lines 37 and 38 were disconnected following the three-phase short-circuit fault (N-2). Since lines 37 and 38 were disconnected after the fault, the power flow values of $P_{37}$ and $P_{38}$ became 0. Figure 8 reveals that $P_{37}$ and $P_{38}$ significantly pushed the risk of instability higher, which reflected the credibility of the explanation model. Prior to the fault, the values of $P_{39}$ and $P_{40}$ were −278.56 and −282.91, respectively, whereas, the values after the fault for $P_{39}$ and $P_{40}$ were −774.1 (277% of the raw value) and −802.4 (283% of the raw value), respectively. The values of $P_{39}$ and $P_{40}$ changed significantly after the fault was removed. It can be inferred that this fault caused an enormous impact on the surrounding lines. Due to the seriousness of the fault, AutoML predicted that the practical grid was unstable after the fault.

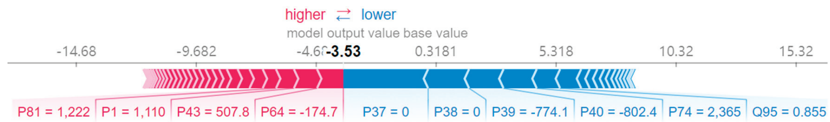


**Figure 8.** Interpretability of a prediction produced by AutoML on the Yunnan.

Figure 9 shows the distribution of SHAP values about $P_{37}$ and $P_{38}$. As we can see from Figure 9, the risk of transient instability is high when the value of $P_{37}$ or $P_{38}$ is 0, reflecting the vulnerability of the corresponding lines.

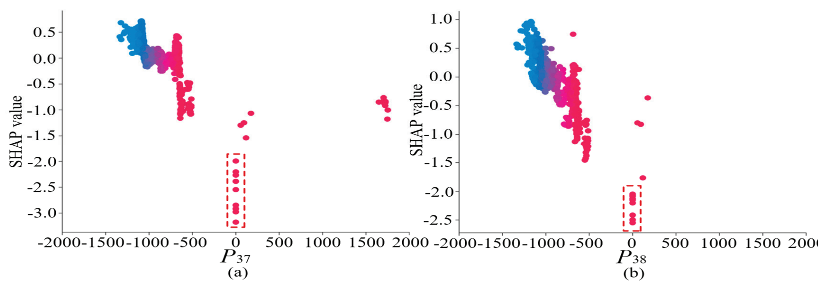


**Figure 9.** (**a**) SHAP dependence of $P_{37}$; (**b**) SHAP dependence of $P_{38}$. The red square means the risk of transient instability is high when the value of P37 or P38 is 0.

## 5. Conclusions

An automated ML scheme (AutoML) was proposed to realize power system online TSA. Under this framework, auto-feature selection and Bayesian optimization were respectively introduced to automatically determine the crucial input features and optimal hyperparameters of the CatBoost-based TSA learning model. Multiple evaluation indices were considered to improve the performance of Bayesian optimization. By leveraging these techniques, faster deployment of the ML-based TSA could be achieved, and the dependence on human expertise is significantly reduced.

To help operators understand why a stable/unstable status prediction is made, interpretability analysis was embedded into both offline and online stages of the AutoML framework. By leveraging the SHAP technique, the proposed AutoML's TSA prediction can be explained as a sum of SHAP values corresponding to each input feature. Furthermore, additional insight into the independent effects of important features can be gained by analyzing the distribution of SHAP values.

Test results showed that the evaluation indices obtained by the proposed AutoML-based TSA in all test systems were the best over the other methods, and appropriate trust in the AutoML-based TSA predictions can be achieved. Furthermore, the proposed AutoML-based TSA saves a great deal of solution time and is applicable to large-scale power systems. In future work, an in-depth analysis of the impact of RES penetration on the transient stability of the power system may be conducted.

**Author Contributions:** Conceptualization, F.L. and T.L.; methodology, X.W.; validation, M.H. and T.H.; formal analysis, X.W.; investigation, M.H.; resources, Y.S.; data curation, F.L.; writing—original draft preparation, M.H. and X.W.; writing—review and editing, Y.W.; supervision, Y.W.; project administration, F.L.; funding acquisition, T.L. All authors have read and agreed to the published version of the manuscript.

**Funding:** This research was funded by the Science and Technology Program of State Grid Corporation, grant number 521996220005, and the Huxiang Young Talents Science and Technology Innovation Program, grant number 2020RC3015.

**Institutional Review Board Statement:** Not applicable.

**Informed Consent Statement:** Not applicable.

**Data Availability Statement:** Data is unavailable due to ethical restrictions.

**Conflicts of Interest:** The authors declare no conflict of interest.

## References

1. Wen, Y.; Zhan, J.; Chung, C.Y.; Li, W. Frequency Stability Enhancement of Integrated AC/VSC-MTDC Systems With Massive Infeed of Offshore Wind Generation. *IEEE Trans. Power Syst.* **2018**, *33*, 5135–5146. [CrossRef]
2. Bueno, P.G.; Hernández, J.C.; Ruiz-Rodriguez, F.J. Stability assessment for transmission systems with large utility-scale photovoltaic units. *IET Renew. Power Gener.* **2016**, *10*, 584–597. [CrossRef]
3. Liu, Y.; Wang, J.; Yue, Z. Improved Multi-point estimation method based probabilistic transient stability assessment for power system with wind power. *Int. J. Electr. Power Energy Syst.* **2022**, *142*, 108283. [CrossRef]
4. Kundur, P. *Power System Stability and Control*; McGraw-Hill, Inc.: New York, NY, USA, 1994; ISBN 978-0070-35958-1.
5. Rahimi, F.A.; Lauby, M.G.; Wrubel, J.N.; Lee, K.L. Evaluation of the transient energy function method for on-line dynamic security analysis. *IEEE Trans. Power Syst.* **1993**, *8*, 497–507. [CrossRef]
6. Xue, Y.; Van Custem, T.; Ribbens-Pavella, M. Extended equal area criterion justifications, generalizations, applications. *IEEE Trans. Power Syst.* **1989**, *4*, 44–52. [CrossRef]
7. Tang, L.; Sun, W. An Automated Transient Stability Constrained Optimal Power Flow Based on Trajectory Sensitivity Analysis. *IEEE Trans. Power Syst.* **2017**, *32*, 590–599. [CrossRef]
8. Xu, Y.; Dong, Z.Y.; Zhang, R.; Xue, Y.; Hill, D.J. A Decomposition-Based Practical Approach to Transient Stability-Constrained Unit Commitment. *IEEE Trans. Power Syst.* **2015**, *30*, 1455–1464. [CrossRef]
9. Gurusinghe, D.R.; Rajapakse, A.D. Post-Disturbance Transient Stability Status Prediction Using Synchrophasor Measurements. *IEEE Trans. Power Syst.* **2016**, *31*, 3656–3664. [CrossRef]
10. Yu, J.J.Q.; Hill, D.J.; Lam, A.Y.S.; Gu, J.; Li, V.O.K. Intelligent Time-Adaptive Transient Stability Assessment System. *IEEE Trans. Power Syst.* **2018**, *33*, 1049–1058. [CrossRef]
11. Xu, Y.; Dong, Z.; Meng, K.; Zhang, R.; Wong, K. Real-time transient stability assessment model using extreme learning machine. *IET Gener. Transm. Distrib.* **2011**, *5*, 314–322. [CrossRef]
12. Yan, R.; Geng, G.; Jiang, Q.; Li, Y. Fast Transient Stability Batch Assessment Using Cascaded Convolutional Neural Networks. In Proceedings of the 2020 IEEE Power & Energy Society General Meeting (PESGM), Montreal, QC, Canada, 2–6 August 2020; IEEE: Montreal, QC, Canada, 2020; pp. 2802–2813.
13. Zhu, L.; Hill, D.J.; Lu, C. Hierarchical Deep Learning Machine for Power System Online Transient Stability Prediction. *IEEE Trans. Power Syst.* **2020**, *35*, 2399–2411. [CrossRef]
14. He, M.; Vittal, V.; Zhang, J. Online dynamic security assessment with missing pmu measurements: A data mining approach. *IEEE Trans. Power Syst.* **2013**, *28*, 1969–1977. [CrossRef]
15. Zhang, Y.; Xu, Y.; Dong, Z.Y. Robust Ensemble Data Analytics for Incomplete PMU Measurements-Based Power System Stability Assessment. *IEEE Trans. Power Syst.* **2018**, *33*, 1124–1126. [CrossRef]
16. Wang, H.; Hu, L.; Zhang, Y. SVM based imbalanced correction method for Power Systems Transient stability evaluation. *ISA Trans.* **2022**. [CrossRef] [PubMed]
17. Wang, Q.; Pang, C.; Qian, C. Sparse Dictionary Learning for Transient Stability Assessment. *Front. Energy Res.* **2022**, *10*, 932770. [CrossRef]
18. Zhang, R.; Yao, W.; Shi, Z.; Zeng, L.; Tang, Y.; Wen, J. A graph attention networks-based model to distinguish the transient rotor angle instability and short-term voltage instability in power systems. *Int. J. Electr. Power Energy Syst.* **2022**, *137*, 107783. [CrossRef]
19. Zhou, Y.; Zhang, P. Noise-Resilient Quantum Machine Learning for Stability Assessment of Power Systems. *IEEE Trans. Power Syst.* **2023**, *38*, 475–487. [CrossRef]
20. He, X.; Zhao, K.; Chu, X. AutoML: A survey of the state-of-the-art. *Knowl.-Based Syst.* **2021**, *212*, 106622. [CrossRef]
21. Li, Z.; Guo, H.; Wang, W.M.; Guan, Y.; Barenji, A.V.; Huang, G.Q.; McFall, K.S.; Chen, X. A Blockchain and AutoML Approach for Open and Automated Customer Service. *IEEE Trans. Ind. Inform.* **2019**, *15*, 3642–3651. [CrossRef]
22. Tuggener, L.; Amirian, M.; Rombach, K.; Lörwald, S.; Varlet, A.; Westermann, C.; Stadelmann, T. Automated Machine Learning in Practice: State of the Art and Recent Results. In Proceedings of the 2019 6th Swiss Conference on Data Science (SDS), Bern, Switzerland, 14 June 2019; pp. 31–36.
23. Lundberg, S.M.; Lee, S.-I. A Unified Approach to Interpreting Model Predictions. In Proceedings of the Advances in Neural Information Processing Systems, Long Beach, CA, USA, 4–9 December 2017; Guyon, I., Luxburg, U.V., Bengio, S., Wallach, H., Fergus, R., Vishwanathan, S., Garnett, R., Eds.; Curran Associates, Inc.: Red Hook, NY, USA, 2017; Volume 30.
24. Feature Importance. Available online: https://catboost.ai/en/docs/concepts/fstr (accessed on 16 March 2022).

25. Anuradha, P.; David, V.K. Feature Selection and Prediction of Heart Diseases Using Gradient Boosting Algorithms. In Proceedings of the 2021 International Conference on Artificial Intelligence and Smart Systems (ICAIS), Coimbatore, India, 25–27 March 2021; pp. 711–717.
26. Prokhorenkova, L.; Gusev, G.; Vorobev, A.; Dorogush, A.V.; Gulin, A. CatBoost: Unbiased Boosting with Categorical Features. In Proceedings of the Advances in Neural Information Processing Systems, Montreal, QC, Canada, 3–8 December 2018; Bengio, S., Wallach, H., Larochelle, H., Grauman, K., Cesa-Bianchi, N., Garnett, R., Eds.; Curran Associates, Inc.: Red Hook, NY, USA, 2018; Volume 31.
27. Punmiya, R.; Choe, S. Energy Theft Detection Using Gradient Boosting Theft Detector With Feature Engineering-Based Preprocessing. *IEEE Trans. Smart Grid* **2019**, *10*, 2326–2329. [CrossRef]
28. Deng, K.; Zhang, X.; Cheng, Y.; Zheng, Z.; Jiang, F.; Liu, W.; Peng, J. A remaining useful life prediction method with long-short term feature processing for aircraft engines. *Appl. Soft Comput.* **2020**, *93*, 106344. [CrossRef]
29. Shahriari, B.; Swersky, K.; Wang, Z.; Adams, R.P.; de Freitas, N. Taking the Human Out of the Loop: A Review of Bayesian Optimization. *Proc. IEEE* **2016**, *104*, 148–175. [CrossRef]
30. van Hoof, J.; Vanschoren, J. Hyperboost: Hyperparameter Optimization by Gradient Boosting Surrogate Models 2021. *arXiv* **2021**, arXiv:2101.02289.
31. Wang, R.; Liu, Y.; Ye, X.; Tang, Q.; Gou, J.; Huang, M.; Wen, Y. Power System Transient Stability Assessment Based on Bayesian Optimized LightGBM. In Proceedings of the 2019 IEEE 3rd Conference on Energy Internet and Energy System Integration (EI2), Changsha, China, 8–10 November 2019; IEEE: Changsha, China, 2019; pp. 263–268.
32. Lyu, W.; Xue, P.; Yang, F.; Yan, C.; Hong, Z.; Zeng, X.; Zhou, D. An Efficient Bayesian Optimization Approach for Automated Optimization of Analog Circuits. *IEEE Trans. Circuits Syst. I Regul. Pap.* **2018**, *65*, 1954–1967. [CrossRef]
33. Li, X.; Liu, C.; Guo, P.; Liu, S.; Ning, J. Deep learning-based transient stability assessment framework for large-scale modern power system. *Int. J. Electr. Power Energy Syst.* **2022**, *139*, 108010. [CrossRef]
34. Bradley, A.P. The use of the area under the ROC curve in the evaluation of machine learning algorithms. *Pattern Recognit.* **1997**, *30*, 1145–1159. [CrossRef]
35. Shap PyPI. Available online: https://pypi.org/project/shap/ (accessed on 22 May 2022).

*energies*

*Article*

# Inertia Identification and Analysis for High-Power-Electronic-Penetrated Power System Based on Measurement Data

**Zhentao Xu [1], Junjie Ma [1,2,*], Yousong Gao [1], Yong Li [1], Haifeng Yu [3] and Lu Wang [3]**

[1] College of Electrical and Information Engineering, Hunan University, Changsha 410082, China; xuzhentao@hnu.edu.cn (Z.X.); gaoyousong@hnu.edu.cn (Y.G.); yongli@hnu.edu.cn (Y.L.)
[2] College of Computer Science, Hunan First Normal University, Changsha 410221, China
[3] Economic & Technical Research Institute, State Grid Hunan Electric Power Company Limited, Changsha 410004, China; yuhf@hn.sgcc.com.cn (H.Y.); m13307472598_1@163.com (L.W.)
* Correspondence: majunjie1989@hnu.edu.cn

**Abstract:** With the gradual increases in the use of wind power and photovoltaic generation, the penetration rate of power electronics has increased in recent years. The inertia characteristics of power-electronic-based power sources are different from those of synchronous generators, making the evaluation of inertia difficult. In this paper, the inertia characteristics of power-electronic-based power sources are analyzed. A measurement-based inertia identification method for power-electronic-based power sources, as well as for high-power-electronic-penetrated power systems, is proposed by fitting the frequency and power data. The inertia characteristics of different control strategies and corresponding control parameters are discussed in a case study. It was proven that the inertia provided by power-electronic-based power sources can be much higher than that provided by a synchronous generator of the same capacity. It was also proven that the inertia provided by power-electronic-based power sources is not a constant value, but changes along with the output power of the sources.

**Keywords:** power-electronic-based power source; virtual inertia; inertia identification

**Citation:** Xu, Z.; Ma, J.; Gao, Y.; Li, Y.; Yu, H.; Wang, L. Inertia Identification and Analysis for High-Power-Electronic-Penetrated Power System Based on Measurement Data. *Energies* **2023**, *16*, 4101. https://doi.org/10.3390/en16104101

Academic Editor: José Gabriel Oliveira Pinto

Received: 27 March 2023
Revised: 9 May 2023
Accepted: 11 May 2023
Published: 15 May 2023



## 1. Introduction

The replacement of traditional fossil power generation by renewable power generation is the key to dealing with environmental concerns. In recent years, the capacity of renewable energy sources (RESs), such as photovoltaics and wind power, has gradually increased [1]. For instance, the photovoltaic capacity of China increased from 3.4 GW to 393 GW during the past decade. RESs integrate with power grids through power electronic converters. Meanwhile, power-electronic-based devices, such as battery energy storage systems (BESSs) and high-voltage direct current (HVDC) transmission systems, are applied to promote renewable energy consumption. The abovementioned facts have resulted in a high penetration of power electronics in modern power systems. For a receiving-end power grid, RESs, HVDC systems, and BESSs can be considered power-electronic-based power sources (PEPSs).

In traditional power systems, synchronous generators (SGs) can release the rotational kinetic energy of the rotating shafts to impede frequency changes under power unbalances caused by faults or large load switching [2]. This kind of energy is also known as inertia. However, in high-power-electronic-penetrated modern power systems, PEPSs have no shaft system to release inertia (such as in photovoltaics, BESSs, and HVDC systems), or the shaft system is decoupled by converters (such as in wind power generators) [3]. These PEPSs cannot automatically provide inertia to the system and are regarded as "zero-inertia" power sources. High penetrations of "zero-inertia" power sources reduce the system inertia levels, and this weakens the frequency stability [4]. The South Australia power outage accident in 2016 is a typical example of such a situation. In this case, the penetration of

RESs accounted for as high as 48.36% of the total capacity, leading to an insufficiency of system inertia. The power frequency dropped at a rate of 6.25 Hz/s in this accident [5].

To deal with the challenge of frequency instability caused by the integration of "zero-inertia" power sources, control techniques such as droop control, virtual inertia (VI) control, and virtual synchronous generator (VSG) control have been proposed [6,7]. Electronic converters can be controlled in two modes, known as the grid-forming mode and the grid-following mode [8,9]. The grid-following control converter operates in the form of current sources, and its output is controlled by the outer loop current reference. The grid-following source can provide frequency support to the system if frequency regulation control instructions are added [7]. Unlike the widely accepted and applied grid-following control, grid-forming control, particularly VSG control, has gained more attention in recent years and is still under discussion [10]. In grid-forming control, converters act as voltage sources such that the converter can respond instantaneously to system changes. The main control method for grid-forming sources is VSG control, which mimic the inertia and damping characteristic of generators. Thus, VSG units behave as a virtual inertia emulation when system frequency changes. Meanwhile, VSG control suffers the same issue of power fluctuations as do the SGs [11]. In summary, PEPSs with appropriate control strategies can provide inertia support for gird. In this paper, the PEPSs with additional inertia control are called virtual inertia power sources, and the term 'virtual inertia' is used to represent the energy released by virtual inertia power sources in inertia response.

Given the significant role of virtual inertia, it is essential to analyze the inertia characteristics of PEPSs under different control strategies, and to quantitatively evaluate the inertia level of the power-electronic-penetrated power system. At present, there is no mature theoretical method for studying the inertia characteristics of PEPSs. The work in [12] studied the dynamic performance of BESSs with different convertor controls and compared their frequency containment capabilities using evaluation indicators. However, Ref. [12] ignored the inertia characteristics analysis for BESSs and did not quantitatively evaluate their inertia support capabilities. In Ref. [13], an equivalent inertia estimation method for wind turbines was proposed on the basis of frequency dynamic response. Yet the method was not verified in a realistic system. Ref. [14] analyzed the inertia characteristics of photovoltaic converters based on generalized droop control by using the electrical torque analysis method, and the influences of control parameters on inertia characteristics were also analyzed in the study.

In addition, due to the application of wide-area measurement systems (WAMSs), the inertia levels of the grid or generating units can be estimated using actual system measurement data [15,16]. There has been some research on inertia estimation for power-electronic-penetrated power systems. In Ref. [17], the influence of HVDC systems on the inertia of power systems was considered. Refs. [18,19] considered the impact of wind power on inertia estimation. However, the above studies did not consider the actual inertia support of PEPSs under different control strategies and parameters.

Considering the aforementioned works, this paper analyzes the inertia characteristics of PEPSs by identifying their virtual inertia. Drawing from the inertia response mechanism, a system inertia identification method based on measurement data is proposed. The method is verified in a BESS-connected IEEE 39 bus system in which the inertia support provided by PEPSs has also been assessed.

The main contributions of this study are as follows:

1. It reveals the nature of the virtual inertia of PEPSs and provides a defined expression for the equivalent inertia coefficient to reflect the actual inertia response of PEPSs.
2. The inertia characteristics of PEPSs under different control strategies and control parameters are analyzed by the identification of equivalent inertia coefficients.
3. It quantitatively assesses the inertia support provided by PEPS based on the proposed system inertia identification method.

The rest of the paper is organized as follows. Section 2 illustrates the similarities and differences between the virtual inertia of PEPSs and the inertia of SGs, and proposes the inertia calculation methods for high-power-electronic-penetrated power systems. Section 3 proposes the inertia identification method based on the polynomial fitting of frequency and power data curves. Section 4 subscribes the commonly used control strategies for PEPS converters. In Section 5, the validation of the proposed method is verified, and the inertia contribution of PEPSs is discussed. Conclusions are drawn in Section 6.

## 2. Inertia in High-Power-Electronic-Penetrated Power Systems

### *2.1. Inertia of a Synchronous Generator*

In traditional power systems, inertia mainly comes from the rotational kinetic energy of synchronous generators. The rotational kinetic energy ($E_G$) of an SG is provided by the following equation [20]:

$$E_G = \frac{1}{2} J_G {\omega_G}^2 = \frac{1}{2} J_G (2\pi f_G)^2 \tag{1}$$

where $J_G$ is the moment of inertia of the SG, $\omega_G$ is the rotor speed, and $f_G$ is the rotor frequency.

The inertia time constant, also known as the inertia coefficient, is defined as the ratio of the rotational kinetic energy at rated conditions to its rated apparent power. The inertia time constant ($H_G$) is expressed as follows:

$$H_G = \frac{E_{G,n}}{S_G} = \frac{J_G {\omega_n}^2}{2S_G} \tag{2}$$

where $E_{G,n}$ is the rotational kinetic energy at rated conditions, $S_G$ is the rated apparent power, and $\omega_n$ is the rated rotor speed.

When the mechanical power and electrical power of a generator are unbalanced, the generator's rotor speed will change. Due to the effect of inertia, the kinetic energy stored in the generator rotor is released, thus resisting the frequency change. Neglecting the influence of damping torque, the dynamic response of an synchronous generator can be expressed thus:

$$\dot{E}_G = J_G \omega_G \cdot \dot{\omega}_G = \frac{2H_G S_G}{\omega_G} \dot{\omega}_G = \frac{J_G {\omega_n}^2}{2S_G} \dot{f}_G = P_m - P_e \tag{3}$$

where $P_m$ is the mechanical power of the synchronous generator and $P_e$ is the electrical power. Typically, because frequency deviation is small, $f_G$ can be replaced by rated frequency $f_n$:

$$\frac{2H_G S_G}{f_G} \dot{f}_G = \frac{2H_G S_G}{f_G} \frac{df_G}{dt} = P_m - P_e \tag{4}$$

Equation (4) is the swing equation, neglecting damping terms, which reflects the inertia response of SGs. From Equation (4), the inertia coefficient ($H_G$) can be derived from its unbalanced power and RoCoF:

$$H_G = \frac{f_n}{2S_G} \frac{\Delta P}{\frac{df_G}{dt}} \tag{5}$$

where $\Delta P$ is the unbalanced power of the SG.

Although the generator rotor stores a large amount of rotational kinetic energy, only a small portion of the stored rotational kinetic energy is released or absorbed during the inertia response due to the frequency deviation limitation. The energy absorbed or injected by the rotor of the generator into the system after a power disturbance ($E_{av}$) can be calculated by the following equation [21]:

$$E_{av} = E_{G,n} - E_{G,t} = \frac{1}{2} J_G \left( {\omega_n}^2 - {\omega_t}^2 \right) \tag{6}$$

where $E_{G,n}$ and $E_{G,t}$ represent the rotational kinetic energies of the SG under rated conditions and at a certain time $t$ during the inertia response, respectively.

According to Equations (2) and (6), the expression for the energy released or absorbed by the generator rotor into the power system can be expressed thus:

$$E_{av} = \frac{{f_n}^2 - {f_t}^2}{{f_n}^2} H_G S_G \tag{7}$$

From Equation (7), it can be seen that the inertia released by the SG after a large disturbance is not only determined by the inertia coefficient and rated capacity of the SG but also affected by the actual frequency deviation.

### 2.2. Virtual Inertia of PEPSs

PEPSs do not have rotating shafts, and so they cannot provide physical inertia for the power grid to which they are connected. However, PEPSs can provide frequency support when frequency control strategies are adopted for their converters. The energy provided by a PEPS does not come from the inertia of the actual rotor, so it is called virtual inertia. Therefore, in a high-power-electronic-penetrated power system, not only can SGs provide inertia, but PEPSs with additional inertia control can also provide inertia support for the grid.

The equivalent inertia coefficient ($H_{eq}$) of a PEPS is defined to quantitatively characterize the suppression effect of the active output on frequency changes. Referring to the measurement method of the SG's inertia coefficient mentioned above, the equivalent inertia coefficient ($H_{eq}$) can be calculated using the following formula (8):

$$H_{eq} = \frac{f_n}{2S_G} \frac{\Delta P_{es}}{\frac{df_{es}}{dt}} \tag{8}$$

where $H_{eq}$ is the equivalent inertia coefficient of the PEPS (measured in seconds), $S_{es}$ is the rated power of the PEPS, $\Delta P_{es}$ is the unbalanced power of the PEPS, and $f_{es}$ is the virtual electrical frequency of the PEPS, usually equal to the frequency at the connection bus of the PEPS.

Analogous to Equations (2) and (7), the stored inertia and post-disturbance virtual inertia output of the PEPS can be expressed thus:

$$E_{es} = H_{eq} S_{es} \tag{9}$$

$$E_{av} = E_{es,n} - E_{es,t} = \frac{{f_n}^2 - {f_t}^2}{{f_n}^2} H_{eq} S_{es} \tag{10}$$

where $E_{es}$ is the stored virtual inertia of the PEPS, $E_{es,t}$ is the virtual inertia of the PEPS at time $t$, $H_{eq}$ is the equivalent inertia coefficient of the PEPS, $S_{es}$ is the rated apparent power of the PEPS, and $f_t$ is the frequency of the PEPS at time $t$.

The PEPS equipped with virtual inertia needs to output an additional amount of power to impede frequency changes during disturbances. The energy output by the PEPS to achieve inertia support can be obtained by integrating the active power, as shown below:

$$\Delta E_{es} = \int_{t_c}^{t} (P_{es} - P_{ref}) dt = \int_{t_c}^{t} \Delta P_{es} dt \tag{11}$$

where $\Delta E_{es}$ represents the energy output by the PEPS and $\Delta P_{es}$ represents the post-disturbance unbalanced power.

The equivalent inertia coefficient of a PEPS reflects the suppressive effect of its active power output on RoCoF during the inertia response. The equivalent inertia coefficients of PEPS are determined by the control strategies, control parameters, and circuit component parameters of the converter and are subject to the maximum output power of the converter. The equivalent inertia coefficient of a PEPS can be considered as the inertia coefficient of an SG with the same rated power. Additionally, the output energy of the PEPS should be equal to its virtual inertia. In other words, the results of Equations (10) and (11) should be consistent for the same time period.

### 2.3. Total Inertia of High-Power-Electronic-Penetrated Power Systems

The Center of Inertia (CoI) theory is mainly used for the transient stability analysis of entire power systems. According to the CoI theory, all generators in such a system can be represented as a large equivalent generator to describe the dynamic characteristics of the entire system. The system equivalent inertia coefficient $H_{sys}$ is commonly used to measure the total inertia of the entire power system. In traditional power systems, inertia is mainly provided by SGs. The system inertia coefficient $H_{sys}$ of traditional power systems is defined thus [22]:

$$H_{sys} = \frac{\sum_{i=1}^{N} S_{G,i} H_{G,i}}{\sum_{i=1}^{N} S_{G,i}} \tag{12}$$

where $N$ is the number of SGs in the system, $H_{G,i}$ is the inertia constant of the $i$-th generator, and $S_{G,i}$ is the rated apparent power of the $i$-th generator.

The CoI frequency ($f_{coi}$) is defined as the weighted average of the frequencies of all generators in the system, with the inertia time constant as the weighting factor:

$$f_{coi} = \frac{\sum_{i=1}^{N} f_{G,i} H_{G,i}}{\sum_{i=1}^{N} H_{G,i}} \tag{13}$$

where $f_{G,i}$ and $H_{G,i}$ are the frequency and inertia time constant of the $i$-th SG, respectively.

When Equation (4) represents the swing equation of the equivalent generator, the frequency dynamic behavior of the power system can be expressed as follows:

$$\frac{2H_{sys}S}{f_n}\frac{df_{coi}}{dt} = \sum_{i=1}^{N}(P_{m,i} - P_{e,i}) = \sum_{i=1}^{N} \Delta P_{G,i} \tag{14}$$

where $S$ is the total rated apparent power of the system's generator, and $P_{m,i}$, $P_{e,i}$ and $\Delta P_{G,i}$ are the mechanical power, electrical power, and unbalanced power of the $i$-th SG, respectively.

The large-scale integration of PEPSs has changed the dynamic response of power systems. On the one hand, the integration of zero-inertia power sources will cause a decrease in system inertia, leading to frequency instability. On the other hand, control strategies such as VSG control make the converter output have inertia characteristics, and inject virtual inertia into the system, so that the system inertia has various forms such as rotational inertia and virtual inertia. Considering the impact of PEPSs, the calculation expression of the system equivalent inertia coefficient is modified. The equivalent inertia coefficient of a power system with PEPSs can be expressed thus:

$$H_{sys} = \frac{\sum_{i=1}^{N} S_{G,i} H_{G,i} + \sum_{j=1}^{M} S_{es,j} H_{eq,j}}{\sum_{i=1}^{N} S_{G,i} + \sum_{j=1}^{M} S_{es,j} + \sum_{k=1}^{R} P_k} \tag{15}$$

where $N$ represents the number of SGs, $M$ represents the number of virtual inertia power sources, and $R$ represents the number of zero-inertia power sources. $H_{G,i}$ and $S_{G,i}$ represent the inertia coefficient and rated apparent power of the $i$-th SG, respectively, $H_{eq,j}$ and $S_{es,j}$ represent the inertia coefficient and rated apparent power of the $j$-th virtual inertia power sources, respectively, and $P_k$ represents the active power of $k$-th zero-inertia power sources.

Based on Equation (15) and the CoI theory, the relationship between system inertia and CoI frequency can be expressed thus:

$$\frac{2H_{sys}S}{f_n}\frac{df_{coi}}{dt} = \sum_{i=1}^{N} \Delta P_{G,i} + \sum_{j=1}^{M} \Delta P_{es,j} \tag{16}$$

where $\Delta P_{G,i}$ and $\Delta P_{es,j}$ represent the power unbalances of the $i$-th SG and the $j$-th virtual inertia power source, respectively. $S$ represents the total rated power of the system's generating equipment, as shown below:

$$S = \sum_{i=1}^{N} S_{G,i} + \sum_{j=1}^{M} S_{es,j} + \sum_{k=1}^{R} P_k \tag{17}$$

The CoI frequency of the high-power-electronic-penetrated power system is calculated by weighting the frequency of all generating equipment with inertia coefficients (or equivalent inertia coefficients):

$$f_{coi} = \frac{\sum_{i=1}^{N} f_{G,i} H_{G,i} + \sum_{j=1}^{M} f_{es,j} H_{eq,j}}{\sum_{i=1}^{N} H_{G,i} + \sum_{j=1}^{M} H_{eq,j}} \tag{18}$$

where $f_{G,i}$ and $f_{es,j}$ represent the frequencies of SGs and the electric frequencies of PEPSs in the power system, respectively.

According to the Equation (16), the system inertia coefficient of high-power-electronic-penetrated power systems can be calculated by applying the total power unbalance of all generating equipment and the CoI frequency:

$$H_{sys} = \frac{f_n}{2S} \frac{\sum_{i=1}^{N} \Delta P_{G,i} + \sum_{j=1}^{M} \Delta P_{es,j}}{\frac{df_{coi}}{dt}} \tag{19}$$

## 3. Inertia Identification Method Based on Polynomial Fitting of Measurement Data

Polynomial fitting is a simple and practical fitting method, and it helps to mitigate the impact of measurement-data noise and oscillation [20]. In this paper, the polynomial fitting is used to fit the active power and frequency measurement data, so as to identify the equivalent inertia coefficient of the PEPS or the system inertia coefficient of the power system. This study assumes that the required measurement data are available from the phase measurement unit (PMU).

Before the fitting carried out, the onset of the grid disturbance is identified by examining whether the absolute value of the RoCoF exceeds a preset threshold (for example, the threshold has been set to 0.05 Hz/s in [23]). This step is crucial in determining the starting point of the polynomial fitting.

This study uses the fixed-order polynomial fitting method to identify the equivalent inertia coefficients of PEPSs. The post-disturbance frequency measurement data is subjected to $\mathrm{n}_1$-th-order polynomial fitting, and the frequency fitting polynomial $f_{es}(t)$ can be expressed thus:

$$f_{es}(t) = a_{\mathrm{n}_1} t^{\mathrm{n}_1} + \ldots + a_1 t + a_0 \tag{20}$$

where $t$ is the time ($t \geq 0$, assuming that $t_0$ = 0) and $a_0$, $a_1$, ... , $a_{\mathrm{n}1}$ are the fitted polynomial coefficients of the frequency data.

The power unbalance data of the PEPS is fitted with an $n_2$-th-order polynomial to obtain the power fitting polynomial $\Delta P_{es}$, as shown in Equation (21).

$$\Delta P_{es}(t) = b_{\mathrm{n}_2} t^{\mathrm{n}_2} + \ldots + b_1 t + b_0 \tag{21}$$

where $b_0$, $b_1$, ... , $b_{\mathrm{n}2}$ are the fitted polynomial coefficients of PEPS power.

Substituting the obtained fitting polynomial into Equation (8) yields the equivalent inertia coefficient of the PEPS:

$$H_{eq}(t) = \frac{f_n}{2S_{es}} \frac{\Delta P_{es}(t)}{\frac{df_{es}(t)}{dt}} \tag{22}$$

It is worth noting that the power-frequency dynamic characteristics of PEPSs are influenced by the control and parameters of the converter. Therefore, the equivalent inertia coefficient $H_{eq}(t)$ of the PEPS is a function that varies with time.

To improve the identification accuracy of $H_{sys}$, this study refers to the variable-order polynomial fitting method proposed in [23]. Figure 1 shows the flowchart of the system inertia identification with the variable-order polynomial fitting method.

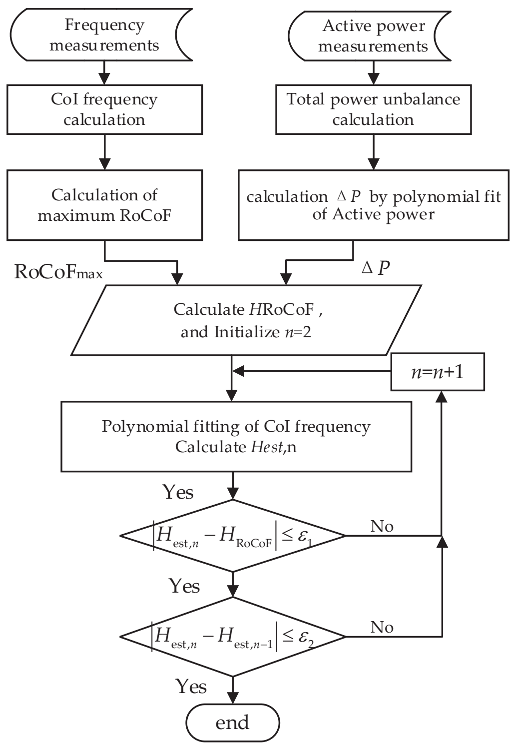


**Figure 1.** Flow chart of inertia identification based on variable-order polynomial fitting.

Firstly, the CoI frequency and the total power unbalance of the generating units are calculated by processing the frequency and power measurements. The total active power unbalance fitting polynomial $\Delta P(t)$ is obtained by $n_3$-th-order polynomial fitting:

$$\Delta P(t) = B_{n_3} t^{n_3} + \cdots + B_1 t + B_0 \tag{23}$$

where $B_0$, $B_1$, . . . , $B_{n3}$ are the coefficients of the power data fitting polynomial.

Typically, the instant of the disturbance (i.e., $t$ = 0) is taken as the identification time. Set $t$ = 0 to obtain the identified value of total active power unbalance $\Delta P$ at the instant of the disturbance. The maximum RoCoF is available from the measured frequency data. After obtaining $\text{RoCoF}_{\text{max}}$ and $\Delta P$, a rough estimate of the system inertia coefficient $H_{\text{RoCoF}}$ can be calculated using Equation (19). In case of low noise and low oscillation levels, $H_{\text{RoCoF}}$ is close to the actual system inertia coefficient. Therefore, $H_{\text{RoCoF}}$ is used as the benchmark value for the iterative convergence of the algorithms.

The next step is to initialize the starting order of the polynomial to $n$ = 2. Then, a variable-order polynomial is fitted to the CoI frequency data from the 2-th-order, and the CoI frequency n-th-order polynomial can be expressed thus:

$$f_{coi}(t) = A_n t^n + \cdots + A_1 t + A_0 \tag{24}$$

where $A_0, A_1, \ldots, A_n$ are the fitted polynomial coefficients of CoI frequency.

Based on the fitting curve, the post-disturbance RoCoF and active power unbalance are identified. The system inertia coefficient can be calculated thus:

$$H_{sys} = \frac{f_n}{2S} \frac{\Delta P|_{t=0}}{\left.\frac{df_{coi}}{dt}\right|_{t=0}} = \frac{f_n B_0}{2SA_1} \tag{25}$$

Then, the calculated value ($H_{est,n}$) is compared with the rough estimated value ($H_{\mathrm{RoCoF}}$) and the estimated value in the last literation ($H_{est,n\text{-}1}$) to ensure that the estimate is within a reasonable limit. If the errors are smaller than their corresponding predefined tolerance values $\varepsilon_1$ and $\varepsilon_2$, then the loop terminates. If not, the loop continues with an increment in the order of the polynomial until convergence is met.

The order of polynomial fitting has a significant impact on the identification results. If the order is too small, the curve-fitting effect is poor. If the order is too large, it may cause overfitting, which also leads to poor identification results. Therefore, an upper limit $n_{max}$ needs to be set. If the loop reaches the upper limit of the order and the error still cannot meet the requirements, the loop is terminated. The tolerance value can be increased until the loop converges. In Refs. [24,25], fifth-order and seventh-order polynomials are used to suppress the oscillatory components of frequency data, respectively. In this study, the upper limit of the order $n_{max}$ was set at 12, and the tolerance values $\varepsilon_1$ and $\varepsilon_2$ were set at 0.3 s and 0.01 s, respectively.

The specific steps of the proposed inertia identification method are as follows:

Step 1: Collect the frequency data and active power data of all generating units and determine the onset of the large disturbance.

Step 2: Perform polynomial fitting on the frequency data and active power data of the PEPS, and identify the PEPS equivalent inertia coefficient according to Equation (22).

Step 3: According to the data collected from each generating unit, the CoI frequency is calculated using Equation (18), and the total active power unbalance is also calculated.

Step 4: The total active power unbalance and the CoI frequency are fitted by a variable-order polynomial iterative process to identify the system inertia coefficient.

## 4. Common Control Strategies for PEPSs

The power output of PEPS is primarily determined by control strategies and control parameters. This section introduces four typical converter control strategies and analyzes the active-frequency dynamic characteristics of different control strategies. Given the primary objective of this paper is to analyze the frequency characteristics of converters, the active-frequency control loop in each control strategy is described in detail.

Grid-connected converter control is mainly classified into two types: grid-following control and grid-forming control. In grid-following mode, the converter's reference current is controlled by a phase-locked loop (PLL) to ensure synchronization between the grid-following source and the grid. The grid-following control method involves decoupling the control of active and reactive power in the outer loop [26]. Grid-following sources without additional frequency regulation control, such as in PQ control, can be approximated as constant power sources. If frequency regulation control instructions are added to an outer loop's current reference, the concerned grid-following source can provide frequency support to the system. The active power-frequency droop control realizes frequency regulation by adding a frequency-deviation control instruction [7,8]. The VI control realizes inertia support by adding an inertia gain control instruction [7,8]. As is shown in Table 1, $K_f$ represents the droop coefficient of droop control, and $T_j$ represents the virtual inertia coefficient of VI control.

**Table 1.** Comparison of common control strategies for PEPSs.

| Strategy | Reference | Control Block Diagram | Frequency Characteristics |
|---|---|---|---|
| PQ control | [26] | 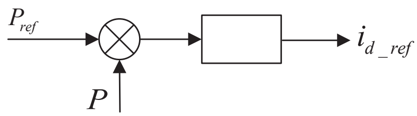 | No frequency support capability |
| Droop control | [7,8] | 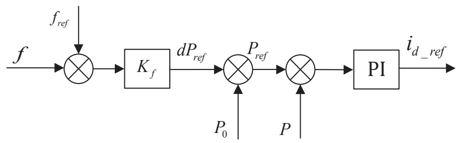 | Equipped with primary frequency regulation feature |
| VI control | [7,8] | 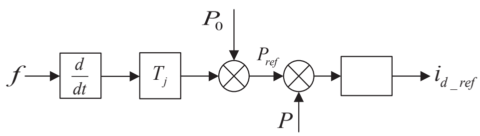 | Equipped with inertia emulation feature |
| VSG control | [27] | 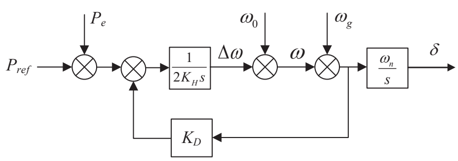 | Equipped with inertia and damping emulation feature of an SG |

VSG control is a type of grid-forming control mode that introduces the swing equation of an SG in the control algorithm. The dynamic behavior of a VSG control converter is similar to that of an SG, involving inertia response and active power regulation. Meanwhile, VSG control has power oscillation issues in transient processes. The outer loop of VSG control consists of active and reactive power control modules, which generate the frequency (power angle) reference and voltage reference for the converter [27]. The inertia control parameter $K_H$ and the damping control parameter $K_D$ correspond to the inertia characteristics and damping characteristics of VSGs, respectively.

## 5. Case Study

The test system used in the study was the IEEE 39-bus power system, which is shown in Figure 2, where "G" represents synchronous generator, and 1 to 39 represents different buses. The system includes generators G1–G10. G2–G5 are equipped with IEEE G3 hydroturbine governor models, each with a governor gain of 2 and a deadband of 0.03 Hz; G6–G9 are equipped with IEEE G3 hydroturbine governor models and have no primary frequency control; G10 is equipped with the IEEE G1 steam-turbine governor model with a governor gain of 2. The relevant parameters for each generator in the system are shown in Table 2.

In this study, BESSs were used as representations for additional frequency control PEPSs. A BESS with a rated capacity of 80 MW/100.2 MWh was connected in bus29. The battery model used in the case study is provided in DIgSILENT/PowerFactory, and the battery model's description can be seen in [28]. The wind turbine generator (WTG) adopts the Type 4 WTG generic model [29], which operates in a constant-power-output mode. A large disturbance fault was set at time 1 s, where the active power of load21 suddenly increased by 226 MW from 274 MW to 500 MW. This sudden active power increase caused a power unbalance and resulted in a system frequency drop.

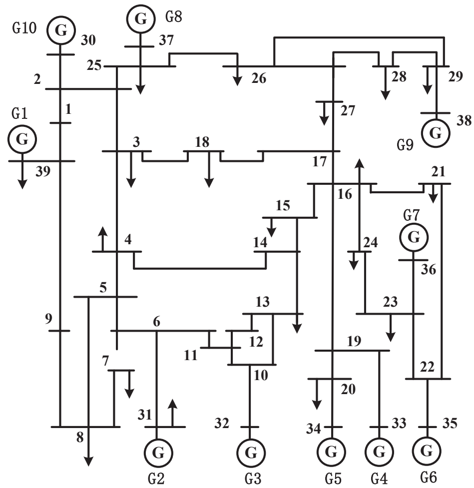


**Figure 2.** Topology diagram of the 39-bus power system.

**Table 2.** Parameters of the generators of the 39-bus power system.

| Generator | 1 | 2 | 3 | 4 | 5 | 6 | 7 | 8 | 9 | 10 | Total |
|---|---|---|---|---|---|---|---|---|---|---|---|
| $P$/MW | 1000 | 520.8 | 650 | 632 | 508 | 650 | 560 | 540 | 830 | 250 | 6140.8 |
| $S$/MVA | 10,000 | 700 | 800 | 800 | 600 | 800 | 700 | 700 | 1000 | 1000 | 17,100 |
| $H$/s | 5.000 | 4.329 | 4.475 | 3.575 | 4.333 | 4.350 | 3.771 | 3.471 | 3.450 | 4.200 | - |

### 5.1. Virtual Inertia Identification of PEPSs

#### 5.1.1. Verification of the Accuracy of Virtual Inertia Identification

For an individual PEPS, Equations (20)–(22) form the theoretical basis for the virtual inertia identification of the PEPS. Therefore, the accuracy of the virtual inertia identification method can be reflected by the fitting degree of frequency and power data. To verify the accuracy and applicability of the virtual inertia identification method, taking the VSG-controlled BESS as an example, the fitting frequency and active power were compared with the corresponding measurements. The frequency-fitting curve and the power-fitting curve are shown in Figure 3.

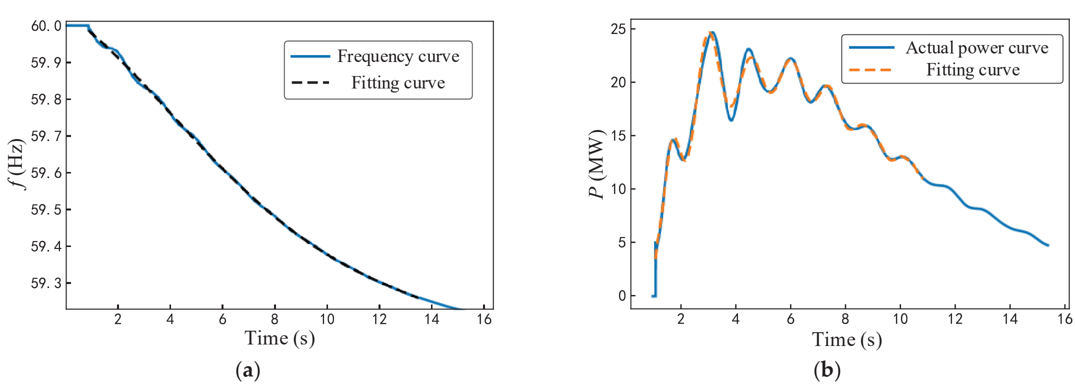


**Figure 3.** Curve fitting of measured frequency and active power. (**a**) Frequency fitting; (**b**) Active power fitting.

From Figure 3, it can be seen that the deviation between the actual frequency and the fitting frequency is within 0.001 Hz. Additionally, the deviation of the power data is within 0.05 MW. The fitting effect indicates that the method is able to accurately fit the measurement data for the identification of the equivalent inertia coefficient.

#### 5.1.2. Inertia under Different VSG Control Parameters

The identified equivalent inertia coefficient $H_{eq}(t)$ can be derived from fitting frequency and fitting power. Figure 4 shows the curve of the VSG control equivalent inertia coefficient over time. The $H_{eq}(t)$ exhibits oscillation characteristics similar to those of the output power, fluctuating to some extent as the output power fluctuates but tending to stabilize as the output power stabilizes. $H_{eq}(t)$ reaches the first peak after approximately 1 s following a large disturbance and subsequently oscillates around the value of the inertia control parameter $K_H$ = 100. Due to the effects of converter control delay, $H_{eq}(0)$ cannot accurately reflect the inertia support capability of VSG control. Based on this reason, the obtained $H_{eq}(t)$ is sampled every 0.01 s from the first peak to the last valley point, discarding the part where the fault just occurred. The average value is taken as the identification value $H_{eq}$ of the equivalent inertia coefficient to characterize the inertia support capability of the VSG-controlled BESS. The identification value $H_{eq}$ of the VSG equivalent inertia coefficient is 101.33 s, which is slightly larger than the set value of the inertia control parameter $K_H$ = 100, with a deviation percentage of 1.33%. The main reasons for the error are the influence of power oscillation and errors in the fitting process. In addition, the frequency data of the BESS connection bus is used instead of the virtual frequency of the BESS to calculate the inertia identification value. In fact, the virtual frequency of the BESS and the connection bus frequency may not be completely consistent, and this affects the identification result of the equivalent inertia coefficient $H_{eq}(t)$.

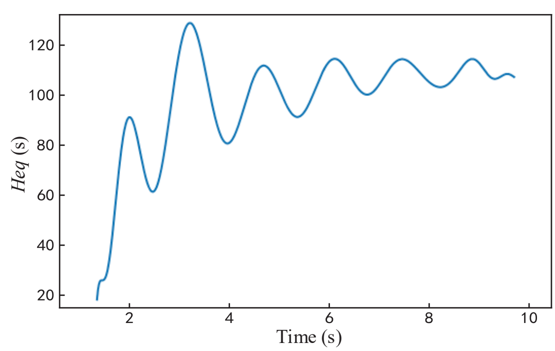


**Figure 4.** $H_{eq}(t)$ curve of VSG control.

To investigate the impact of the control parameter on VSG inertia support, two cases are set as follows:

Case 1: Set $K_D$ to 1000 and $K_H$ to 50, 100, and 150;
Case 2: Set $K_H$ to 100 and $K_D$ to 200, 600, and 1000.

It can be seen from Figure 5 that $H_{eq}(t)$ increases as $K_H$ increases, indicating that $K_H$ plays a significant role in the converter's inertia support. The VSG damping control parameter $K_D$ has little influence on the equivalent inertia coefficient value, but increasing $K_D$ can reduce the oscillation amplitude of $H_{eq}(t)$, because the damping control parameter $K_D$ has a direct impact on the suppression of the active output oscillation.

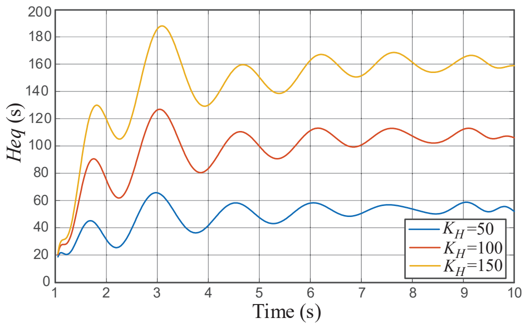


(**a**)

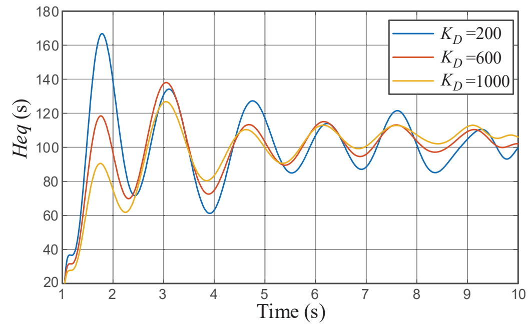


(**b**)

**Figure 5.** $H_{eq}(t)$ under different VSG control parameters: (**a**) changing $K_H$ and (**b**) changing $K_D$.

The equivalent inertia coefficient identification value $H_{eq}$, under different VSG control parameter combinations, is obtained according to the above average calculation method. The results are shown in Figure 6. It can be seen that $K_H$ plays a decisive role in inertia support, while $K_D$ has a relatively small impact in inertia support.

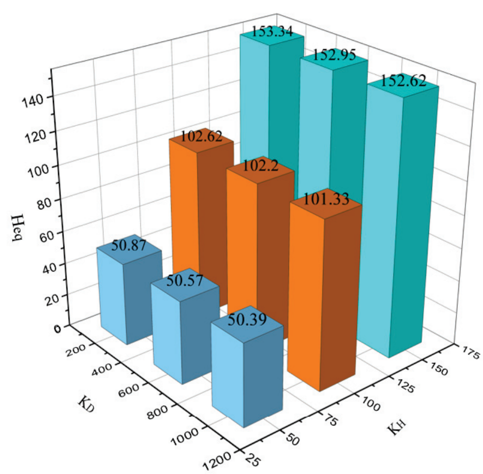


**Figure 6.** The identification results of $H_{eq}$ under different VSG control parameters.

### 5.1.3. Inertia under Different Control Strategies

In order to analyze the inertia characteristics under different control strategies, the equivalent inertia coefficients of the BESS under different controls are identified in this section. Considering the constraints of BESS size [30], the control parameters are shown in Table 3.

**Table 3.** Control parameters of various control.

| Control Parameters | Value |
|---|---|
| Inertia control parameter $K_H$ | 100 |
| Virtual inertia coefficient $T_j$ | 200 |
| Droop coefficient $K_f$ | 40 |
| Droop control deadband | 0.3 Hz |

The equivalent inertia coefficients of the various control strategies are identified by the proposed method, and the equivalent inertia coefficient $H_{eq}(t)$ curves of the corresponding control parameters are obtained as shown in Figure 7.

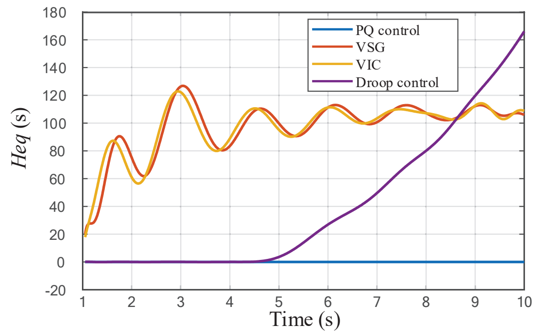


**Figure 7.** $H_{eq}(t)$ under different control strategies.

From Figure 7, it can be seen that the output of PQ control is not affected by frequency changes. Thus, the $H_{eq}(t)$ of PQ control remains at zero. The $H_{eq}(t)$ of VI control responds similarly to that of the VSG control when there is no deadband or delay-time loop and the virtual inertia coefficient $T_j$ is set to twice the inertia control coefficient $K_H$. Droop control does not provide power output within the frequency deadband. However, once the frequency exceeds the deadband, it generates active power according to the frequency deviation, leading to a continuous increase in $H_{eq}(t)$. Therefore, it is difficult to quantitatively characterize the inertial effect of droop control with a constant. This proves that the $H_{eq}(t)$ of a PEPS is related to its control strategies. Even if the PEPS emulates the characteristics of a synchronous generator by using VSG control, its $H_{eq}(t)$ may not be constant due to its control period or control time-delay effect.

### *5.2. Inertia Identification of PEPS-Integrated Power Systems*

#### 5.2.1. Inertia under Different PEPS Compositions

When zero-inertia RESs are integrated with a power system, the inertia level of the system will be reduced, posing a threat to system frequency stability. However, on the grid side, a large-capacity VSG-controlled BESS can be directly connected to regulate the system frequency and improve the system's inertia level.

To verify the effectiveness of the proposed method and quantitatively analyze the impact of PEPSs on system inertia, this section identifies the system inertia coefficients under different PEPS compositions. The specific scenario settings are as follows:

The inertia coefficient of G9 is set to 15 s.

Scenario 1: All generating units are synchronous generators;
Scenario 2: Replace G9 with 166 WTGs with a rated power of 5 MW per unit;
Scenario 3: Replace G9 with 166 WTGs with a rated power of 5 MW per unit and configure the VSG-controlled BESS with the inertia control parameter $K_H$ set to 187.

Figure 8 shows the system frequency response curves for the three scenarios. The inertia identification results under different PEPS compositions are shown in Table 4.

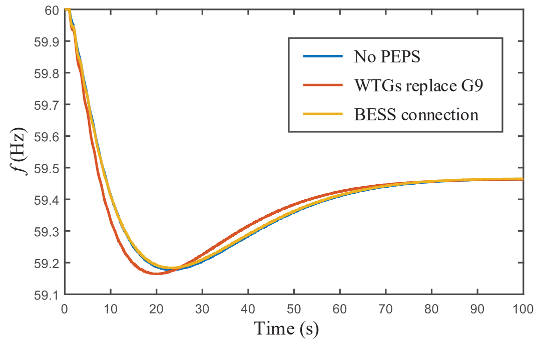


**Figure 8.** Frequency response before and after BESS is connected in a wind-power-integrated system.

**Table 4.** Inertia identification under different PEPS compositions.

| Scenario | $RoCoF_{max}$(Hz/s) | $f_{min}$ (Hz) | $H_{sys}$(s) |
|---|---|---|---|
| 1 | 0.094 | 59.183 | 5.187 |
| 2 | 0.156 | 59.164 | 4.467 |
| 3 | 0.102 | 59.183 | 5.291 |

According to the results in Figure 8 and Table 4, it can be seen that after WTGs are integrated into the system, the $H_{sys}$ of the system decreases by about 0.7 s, and the $RoCoF_{max}$ increases. The integration of WTGs leads to a decrease in frequency stability. However, after the configuration of the VSG-controlled BESS, the system inertia is effectively supplemented. At this point, the system inertia coefficient is similar to that of the traditional system, and the inertia level is restored to that of a system without WTGs. Therefore, VSG-controlled BESSs has significant application value in power systems with high penetrations of RESs. The frequency response curves in Figure 8 and the inertia identification results in Table 4 verify the effectiveness of the proposed system-inertia-identification method.

### 5.2.2. Inertia under Different VSG Control Parameters of BESSs

As mentioned earlier, the inertia control parameter $K_H$ is directly related to the inertia support capability of the VSG-controlled BESS. Figure 9 displays the post-disturbance frequency dynamic response of the power system with BESSs configured with different inertia control parameters.

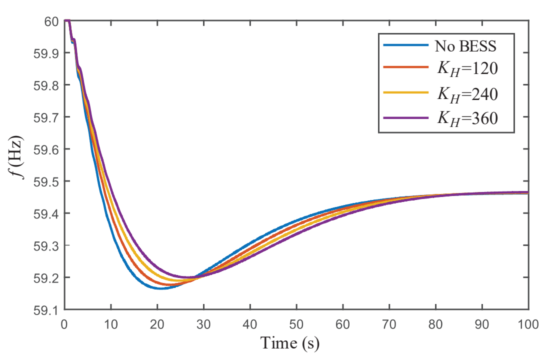


**Figure 9.** Frequency response curves under different VSG control parameters $K_H$.

From Figure 9, it can be seen that increasing the inertia control parameter can improve the system's inertia support capability and thus improve the frequency stability of the system.

In order to quantitatively assess the inertia support capability of BESSs with different inertia control parameters, the power system inertia was identified by the proposed method in this paper. The identification and evaluation results are shown in Table 5.

**Table 5.** Inertia identification under different VSG parameters.

| $K_H$ | $H_{eq}$(s) | Stored Virtual Inertia Provided by BESS(MW·s) | $H_{sys}$(s) |
|---|---|---|---|
| - | 0 | 0 | 4.596 |
| 120 | 121.74 | 9739.2 | 5.193 |
| 240 | 244.57 | 19,565.6 | 5.876 |
| 360 | 369.91 | 29,592.8 | 6.603 |

In Table 5, the third column displays the "stored virtual inertia" provided by the BESS, and this is calculated by multiplying the equivalent inertia coefficient $H_{eq}$ by the rated apparent power of the BESS, according to Equation (11). From the perspective of system planning, the stored virtual inertia represents the inertia stored by the BESS if it is viewed as an equivalent generator. The stored virtual inertia of the VSG-controlled BESS is mainly determined by the control parameters rather than by the BESS' capacity. This proves that the inertia provided by a BESS can be much higher than that of a synchronous generator of the same capacity.

From the perspective of an individual generating unit, it is observed that a larger $K_H$ results in a larger $H_{eq}$. This indicates that if the BESS is viewed as an equivalent SG, its inertia coefficient is larger and its inertia support capability is better. From the perspective of the entire system, it can be seen from the results of $H_{sys}$ identification that increasing the $K_H$ can improve the overall system inertia level. The inertia identification results can provide guidance for configuring control parameters according to system inertia requirements.

### 5.3. Energy Analysis of BESSs

In a VSG-controlled BESS-connected power system, both the generator and BESS can absorb or inject energy into the system to provide inertia support when the system frequency changes. In order to verify the equivalence of virtual inertia, the inertia coefficient $H_9$ of G9 is set to 15 s and 5 s to represent high-inertia and low-inertia systems, respectively. In the low-inertia system, the VSG-controlled BESS was connected with certain parameter configurations to make the frequency response curve as similar as possible to that of the high-inertia system's frequency response curve.

Figure 10 shows the frequency response of the 39-bus system before and after a VSG-controlled BESS is configured. The inertia control parameter $K_H$ of the BESS is 125. It can be seen that the low-inertia system has a greater RoCoF and a lower-frequency nadir in the inertia response than the high-inertia system does. The yellow line shows that configuring the VSG-controlled BESS can significantly improve the inertia level of the system. After the VSG-controlled BESS is configured in the low-inertia system, the frequency response curve of the system is basically consistent with that of the high-inertia system, and the frequency nadir is very close: approximately 59.18 Hz for both systems.

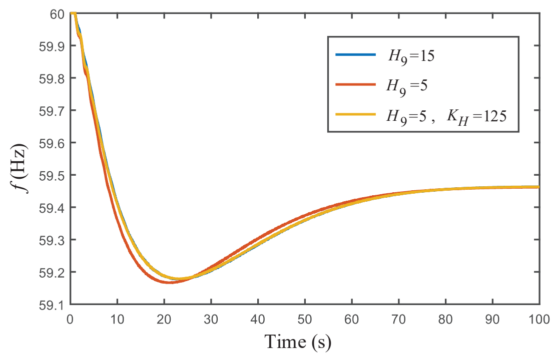


**Figure 10.** Frequency curve of the system with or without a VSG-controlled BESS.

Figure 11 shows that after the disturbance fault occurs, the VSG-controlled BESS immediately issues instructions to release active power to contain the frequency drop. Almost at the moment of disturbance, the active output of BESS reaches its maximum, and then decreases until the inertia response basically ends. By integrating the active power during the inertia response, the energy provided by the BESS can be obtained as follows:

$$E_{es} = \int_{1}^{23.58} P(t)dt = 273.7634 \text{ MW} \cdot \text{s}$$

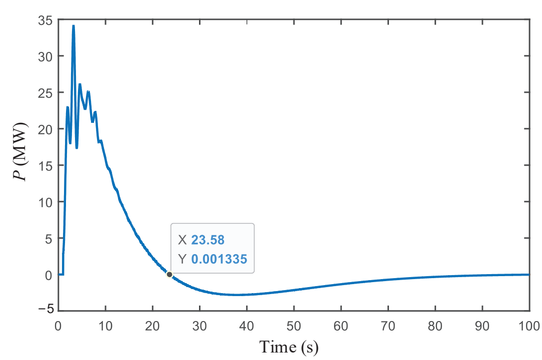


**Figure 11.** Active power curve of a VSG-controlled BESS.

According to Equation (7), the rotational kinetic energy provided by SGs in a high-inertia system and a low-inertia system can be calculated separately. $E_{G,av1}$ and $E_{G,av2}$ represent the rotational kinetic energy released by the generator in a high-inertia and low-inertia system, respectively. The reduction in rotational kinetic energy released by the generators is calculated as follows:

$$\Delta E_{G,av} = E_{G,av1} - E_{G,av2} = \frac{{f_n}^2 - {f_t}^2}{{f_n}^2} \Delta H_G S_G = 273.7634 \text{ MW} \cdot \text{s}$$

The reduction in rotational kinetic energy released by the synchronous generator ($\Delta E_{G,av}$) is approximately equal to the energy released by the BESS ($E_{es}$); i.e., the virtual inertia provided by the BESS just makes up for the reduction in the synchronous generator inertia, so that the frequency response curve of the low-inertia system is basically the same as the frequency response curve of the high-inertia system.

By utilizing the polynomial fitting method to identify the equivalent inertia coefficient of a BESS, the $H_{eq}$ is obtained as 128.04 s. According to Equation (10), the virtual inertia provided by a BESS in the inertia response is:

$$E_{BESS,av} = \frac{{f_n}^2 - {f_t}^2}{{f_n}^2} H_{eq} S_{es} = \frac{60^2 - 59.18^2}{60^2} \times 128.04 \times 80 = 276.5664\ \text{MVA} \cdot \text{s}$$

It can be seen that $E_{es}$ is approximately equal to $E_{BESS,av}$. The above analysis and calculations verify that VSG-controlled BESSs can provide inertia support like generators during the inertia response. A VSG-controlled BESS can be regarded as an SG with an inertia coefficient of $H_{eq}$ and a rated apparent power of $S_{es}$. The energy output from a BESS can be considered as the rotational kinetic energy released by the virtual rotor.

In addition, it is observed that the energy released to the system during the inertia response accounts for a small proportion of the actual capacity of a BESS. Therefore, the impact of the changes in the state of charge (SOC) need not be considered during the inertia response.

## 6. Conclusions

This paper starts from the physical viewpoint that power system inertia is the energy for impeding frequency changes and defines the concepts of virtual inertia and the equivalent inertia coefficient. Based on the theoretical analysis of inertia, an inertia identification method for high-power-electronic-penetrated power systems is proposed. The inertia characteristics of PEPSs under different strategies and parameters have been analyzed by using the proposed inertia identification method. The following conclusions are drawn based on the analyses in this paper.

Differing from what one might find in a synchronous generator, the virtual inertia provided by a PEPS is primarily affected by its control strategies and parameters. Thus, the inertia response effect of a PEPSs is time-varying. Even if the PEPS simulates the output characteristics of synchronous generators under VSG control, its equivalent inertia coefficient may not be a constant due to the impact of control periods or control time-delay effects.

The equivalent inertia coefficient of VSG control has certain fluctuations during output power fluctuations but tends to stabilize as output power stabilizes. Therefore, the inertia response effect of VSG control can be characterized by a constant that is close to the inertia control parameter. Additionally, the inertia control parameter $K_H$ plays a decisive role in inertia support.

The virtual inertia provided by VSG-controlled BESSs is equivalent to the inertia provided by synchronous generators. In high-power-electronic-penetrated power systems, the integration of zero-inertia RESs reduces system inertia levels, while VSG-controlled BESSs can compensate for the reduced inertia caused by integrating zero-inertia RESs.

The inertia identification method proposed in this paper can quantitatively assess the impact of PEPSs on power system inertia. The conclusions drawn in this paper can provide references for configuring power electronic equipment and its control parameters according to system inertia requirements.

**Author Contributions:** Conceptualization, J.M. and Y.L.; methodology, Z.X. and Y.G.; software, H.Y.; validation, Z.X.; formal analysis, L.W.; investigation, Z.X.; resources, H.Y.; data curation, H.Y.; writing—original draft preparation, Z.X.; writing—review and editing, J.M. and Y.L; visualization, Y.G.; supervision, Y.L.; project administration, J.M. and L.W.; funding acquisition, Y.L. and J.M.; All authors have read and agreed to the published version of the manuscript.

**Funding:** This research was funded by Youth Foundation of National Natural Science Foundation of China (NSFC), granted number 52007057, and Key Science and Technology Special Projects of Hunan Province, grant number 2020GK1011.

**Data Availability Statement:** The model data presented in this study are available in [IEEE Std C37.20.4-2001], where the modification. Parameters and simulation conditions that used in this study is given in manuscript.

**Conflicts of Interest:** The authors declare no conflict of interest.

## References

1. Alam, M.S.; Chowdhury, T.A.; Dhar, A.; Al-Ismail, F.S.; Choudhury, M.S.H.; Shafiullah, M.; Hossain, M.I.; Hossain, M.A.; Ullah, A.; Rahman, S.M. Solar and wind energy integrated system frequency control: A critical review on recent developments. *Energies* **2023**, *16*, 812. [CrossRef]
2. Bevrani, H.; Golpira, H.; Messina, A.R.; Hatziargyriou, N.; Milano, F.; Ise, T. Power system frequency control: An updated review of current solutions and new challenges. *Electr. Power Syst. Res.* **2021**, *194*, 107114. [CrossRef]
3. Qiang, L.; Bixing, R.; Weijia, T.; Dajiang, W.; Chenggen, W.; Zhenhua, L. Analyzing the inertia of power grid systems comprising diverse conventional and renewable energy sources. *Energy Rep.* **2022**, *8*, 15095–15105.
4. Ulbig, A.; Borsche, T.S.; Andersson, G. Impact of low rotational inertia on power system stability and operation. *IFAC Proc. Vol.* **2014**, *47*, 7290–7297. [CrossRef]
5. AEMO. Update Report—Black System Event in South Australia on 28 September 2016. *Technical Report*. 2016. Available online: https://apo.org.au/sites/default/files/resource-files/2016-10/apo-nid68095.pdf (accessed on 23 March 2023).
6. Tamrakar, U.; Shrestha, D.; Maharjan, M.; Bhattarai, B.P.; Hansen, T.M.; Tonkoski, R. Virtual inertia: Current trends and future directions. *Appl. Sci.* **2017**, *7*, 654. [CrossRef]
7. Abuagreb, M.; Allehyani, M.F.; Johnson, B.K. Overview of Virtual Synchronous Generators: Existing Projects, Challenges, and Future Trends. *Electronics* **2022**, *11*, 2843. [CrossRef]
8. Rocabert, J.; Luna, A.; Blaabjerg, F.; Rodriguez, P. Control of power converters in AC microgrids. *IEEE Trans. Power Electron.* **2012**, *27*, 4734–4749. [CrossRef]
9. Paolone, M.; Gaunt, T.; Guillaud, X.; Liserre, M.; Vournas, C. Fundamentals of power systems modelling in the presence of converter-interfaced generation. *Electr. Power Syst. Res.* **2020**, *189*, 106811. [CrossRef]
10. Unruh, P.; Nuschke, M.; Strauß, P.; Welck, F. Overview on Grid-Forming Inverter Control Methods. *Energies* **2020**, *13*, 2589. [CrossRef]
11. Suvorov, A.; Askarov, A.; Kievets, A.; Rudnik, V. A comprehensive assessment of the state-of-the-art virtual synchronous generator models. *Electr. Power Syst. Res.* **2022**, *209*, 108054. [CrossRef]
12. Zuo, Y.; Yuan, Z.; Sossan, F.; Zecchino, A.; Cherkaoui, R.; Paolone, M. Performance assessment of grid-forming and grid-following converter-interfaced battery energy storage systems on frequency regulation in low-inertia power grids. *Sustain. Energy Grids Netw.* **2021**, *27*, 100496. [CrossRef]
13. Zhang, N.; Zhu, X.; Wang, D.; Wu, X.; Bu, J. Estimation and Influencing Factors Analysis for Equivalent Inertia of Wind Turbines with Active Inertia Support. In Proceedings of the 2022 7th Asia Conference on Power and Electrical Engineering (ACPEE), Hangzhou, China, 15–17 April 2022.
14. Zha, Y.; Lin, J.; Li, G.; Wang, Y.; Zhang, Y. Analysis of Inertia Characteristics of Photovoltaic Power Generation System Based on Generalized Droop Control. *IEEE Access* **2021**, *9*, 37834–37839. [CrossRef]
15. Rossetto Moraes, G.; Ilea, V.; Berizzi, A.; Pisani, C.; Giannuzzi, G.; Zaottini, R. A Perturbation-based methodology to estimate the equivalent inertia of an area monitored by PMUs. *Energies* **2021**, *14*, 8477. [CrossRef]
16. Nozal, L.; Kontis, E.O.; Mauricio, J.M.; Demoulias, C.S. Provision of inertial response as ancillary service from active distribution networks to the transmission system. *IET Gener. Transm. Distrib.* **2020**, *14*, 5123–5134. [CrossRef]
17. Hu, L.; Li, Y.; Wang, W.; Tan, Y.; Cao, Y.; Lee, K. Inertia estimation of power grid with VSC-MTDC system. *IFAC-PapersOnLine* **2018**, *51*, 197–202. [CrossRef]
18. Sun, F.; Sun, J.; Zhang, X.; Yang, H.; Qian, X.; Peng, Y. Measurement method of inertia constant of power system based on large-scale wind power grid connection. *Energy Rep.* **2022**, *8*, 200–209. [CrossRef]
19. Beltran, O.; Pea, R.; Segundo, J.; Esparza, A.; Muljadi, E.; Wenzhong, D. Inertia estimation of wind power plants based on the swing equation and phasor measurement units. *Appl. Sci.* **2018**, *8*, 12. [CrossRef]
20. Dimoulias, S.C.; Kontis, E.O.; Papagiannis, G.K. Inertia estimation of synchronous devices: Review of available techniques and comparative assessment of conventional measurement-based approaches. *Energies* **2022**, *15*, 7767. [CrossRef]
21. Spahic, E.; Varma, D.; Beck, G.; Kuhn, G.; Hild, V. Impact of reduced system inertia on stable power system operation and an overview of possible solutions. In Proceedings of the 2016 IEEE Power and Energy Society General Meeting (PESGM), Boston, MA, USA, 17–21 July 2016.
22. Carlini, E.M.; Pizzo, F.D.; Giannuzzi, G.M.; Lauria, D.; Pisani, C. Online analysis and prediction of the inertia in power systems with renewable power generation based on a minimum variance harmonic finite impulse response filter. *Int. J. Electr. Power Energy Syst.* **2021**, *131*, 107042. [CrossRef]
23. Phurailatpam, C.; Rather, Z.H.; Bahrani, B.; Doolla, S. Measurement based estimation of inertia in AC microgrids. *IEEE Trans. Sustain. Energy* **2019**, *11*, 1975–1984. [CrossRef]

24. Ashton, P.M.; Taylor, G.A.; Carter, A.M.; Bradley, M.E.; Hung, W. Application of phasor measurement units to estimate power system inertial frequency response. In Proceedings of the 2013 IEEE Power & Energy Society General Meeting, Vancouver, BC, Canada, 21–25 July 2013.
25. Wang, B.; Sun, H.; Li, W.; Yang, C.; Wei, W.; Zhao, B.; Xu, S. Power system inertia estimation method based on maximum frequency deviation. *IET Renew. Power Gener.* **2022**, *16*, 622–633. [CrossRef]
26. Wang, D.; Yan, Y.; Shen, Y.; Hu, Z. Active and Reactive Power Coupling Characteristics Based Inertial and Primary Frequency Control Strategy of Battery Energy Storage Station. In Proceedings of the 2020 12th IEEE PES Asia-Pacific Power and Energy Engineering Conference (APPEEC), Nanjing, China, 20–23 September 2020.
27. Mallemaci, V.; Mandrile, F.; Rubino, S.; Mazza, A.; Carpaneto, E.; Bojoi, R. A comprehensive comparison of Virtual Synchronous Generators with focus on virtual inertia and frequency regulation. *Electr. Power Syst. Res.* **2021**, *201*, 107516. [CrossRef]
28. Adrees, A.; Milanovic, J.V. Study of frequency response in power system with renewable generation and energy storage. In Proceedings of the 2016 Power Systems Computation Conference (PSCC), Genoa, Italy, 20–24 June 2016.
29. Srensen, P.; Andresen, B.; Fortmann, J.; Pourbeik, P. Modular structure of wind turbine models in IEC 61400-27-1. In Proceedings of the 2013 IEEE Power & Energy Society General Meeting, Vancouver, BC, Canada, 21–25 July 2013.
30. Abuagreb, M.; Abuhussein, A.; Alzahir, S. Sizing of Energy Storage System for Virtual Inertia Emulation. In Proceedings of the 2022 IEEE 31st International Symposium on Industrial Electronics (ISIE), Anchorage, AK, USA, 1–3 June 2022.

*energies*

*Article*

# Fault Handling and Localization Strategy Based on Waveform Characteristics Recognition with Coordination of Peterson Coil and Resistance Grounding Method

**Zhengyang Li, Yijia Cao *, Chun Chen, Yansha Li and Jinglu Li**

School of Electrical & Information Engineering, Changsha University of Science and Technology, Changsha 410114, China; 18684810261@163.com (Z.L.); 13787104968@163.com (J.L.)
* Correspondence: yjcao@csust.edu.cn

**Abstract:** To address challenges in locating high-impedance grounding faults (HIGFs) and isolating fault areas in resonant grounding systems, this paper proposes a novel fault identification method based on coordinating a Peterson coil and a resistance grounding system. This method ensures power supply reliability by extinguishing the fault arc during transient faults with the Peterson coil. When a fault is determined to be permanent, the neutral point switches to a resistance grounding mode, ensuring regular distribution of zero-sequence currents in the network, thereby addressing the challenges of HIGF localization and fault area isolation. Fault calibration and nature determination rely on recognizing neutral point displacement voltage waveforms and dynamic characteristics, eliminating interference from asymmetric phase voltage variations. Fault area identification involves assessing the polarity of zero-sequence current waveforms attenuation during grounding mode switching, preventing misjudgments in grounding protection due to random initial fault angles and Peterson coil compensation states. Field experiments validate the feasibility of this fault location method and its control strategy.

**Keywords:** high-impedance grounding fault; fault area isolation; waveform characteristics; polarity difference

**Citation:** Li, Z.; Cao, Y.; Chen, C.; Li, Y.; Li, J. Fault Handling and Localization Strategy Based on Waveform Characteristics Recognition with Coordination of Peterson Coil and Resistance Grounding Method. *Energies* **2024**, *17*, 3510. https://doi.org/10.3390/en17143510

Academic Editor: Salvatore Celozzi

Received: 18 June 2024
Revised: 9 July 2024
Accepted: 16 July 2024
Published: 17 July 2024



## 1. Introduction

With the advancement of digital distribution systems, economically efficient and self-healing distribution networks are widely recognized as primary development goals for power systems. [1] Accurately detecting and isolating single-line-to-ground (SLG) represents a critical research challenge that needs to be addressed in self-healing distribution systems [2–4].

Traditional fault handling strategies often struggle to achieve fault isolation in resonant grounded systems. Automatic Peterson coils, equipped with series-connected damping resistors, can operate in various compensation states, including over-compensation, under-compensation, or full compensation. Moreover, the tuning of automatic Peterson coils is random, leading to unpredictable levels of output compensation current. These factors result in the zero-sequence current distribution in the network becoming irregular under fault conditions. Consequently, this irregularity complicates fault line selection and fault area location [5]. Furthermore, due to the complex operating conditions of distribution networks, traditional methods often employ broader fault detection thresholds to ensure selectivity, leading to potential misidentification of HIGFs [6].

In small-resistance grounded systems, identifying HIGFs poses a critical challenge in fault zone identification. During HIGF events, significant fault transition resistances are connected in series within the fault zero-sequence circuit. This results in minimal changes in zero-sequence current amplitude, which may not be sufficient to activate zero-sequence current protection. Even when fault handling procedures are initiated, these subtle variations in zero-sequence current amplitude typically do not offer adequate support for precise fault zone identification. Moreover, in cases involving small-resistance or metallic grounding faults, ground protection devices often lack the capability to determine if fault point insulation can self-recover, thereby significantly affecting power supply continuity [7]. In summary, small-resistance grounded systems face challenges in meeting the power supply reliability and fault identification accuracy requirements of distribution networks.

Although the single neutral point grounding method has unique advantages, it cannot meet the multidimensional requirements related to the safety and reliability of distribution networks. Both academia and industry are investigating fault handling approaches that integrate various neutral point grounding methods, including 'multi-mode grounding' and 'flexible grounding', with the aim of addressing safety and reliability concerns within power distribution systems [8,9].

Wan et al. proposed a fault line identification method for flexible grounding systems where Peterson coils are connected in parallel with small-resistance grounding. This method aims to mitigate the chaotic disturbances caused by the randomness of Peterson coil compensation states by analyzing the trajectory of changes in the zero-sequence currents of feeders and zero-sequence voltages of buses after the parallel resistors are engaged [10,11]. Zeng proposed a delay switching strategy utilizing Peterson coils and resistor grounding to amplify fault electrical quantities for the identification of faulted feeders. The objective was to ensure power supply reliability while simultaneously considering grid safety [12]. Wang proposed an identification method for single-phase grounding faults using Neutral Point-to-Ground Complex Impedance (EHPC) adaptive control based on Peterson coils. This method ensures the amplification of zero-sequence parameters while preventing ground arc reignition, thus achieving fault point identification [13,14]. However, due to changes in the operation mode of distribution networks or the influence of unstable grounding factors (such as tree obstructions and flashovers), previous methods generally lack the capability to accurately identify grounding faults. This results in insufficient criteria for determining whether the insulation at the grounding fault point can correctly recover and for accurately identifying the faulted feeder.

Voltage and current waveform characteristics contain a wealth of fault information, making the application of waveform features in fault identification and localization both practical and feasible. Y. Xue et al. developed several methods, including the transient zero-sequence current projection coefficient method, the transient energy method, and the wavelet coefficient energy analysis method, to identify single-phase grounding faults under complex conditions based on the resonance frequency proportion coefficient during the fault process [15–18]. B. Wang et al. applied the dynamic trajectory of the volt-ampere characteristics of zero-mode voltage and current to the identification of HIGFs [19,20]. M.A. Barik et al. utilized the polarity characteristics of transient electrical quantities during ground faults to quantitatively or qualitatively calculate fault location information [21–26].

While the above-mentioned methods have demonstrated the capability to identify faulted feeders or fault regions and have shown satisfactory performance in handling HIGFs under ideal conditions, complex factors including special fault phase angles and the randomness of Peterson coil compensation states may lead to waveform characteristic disturbances. Particularly under conditions of HIGFs, threshold-based methods relying on waveform characteristics exhibit significant deficiencies due to the difficulty in capturing characteristic quantities.

This paper proposes a collaborative control method involving Peterson coils and resistor grounding to identify single-phase grounding fault regions. By establishing zero-sequence circuit models for various grounding modes, the evolving mechanisms of fault features during fault perception and segment identification with the concurrent application of different grounding methods are revealed. The waveform characteristics of neutral point displacement voltage during fault inception and zero-sequence current at node switching when grounding methods change are extracted using empirical wavelet transform (EWT).

The DC attenuation component in voltage waveform characteristics is utilized to detect fault occurrence and eliminate interference from asymmetrical phase voltage changes, while the current waveform characteristics are used to derive attenuation coefficients and identify fault regions based on their polarity differences. The proposed method combines waveform and frequency domain features for fault identification, enabling the identification of HIGFs under any fault initial phase angle. Moreover, the method utilizes the polarity changes in zero-sequence current attenuation at the fault node when a Peterson coil is disconnected, thereby indicating the fault region independently of the Peterson coil compensation state.

## 2. Analysis of Challenges in Ground Fault Identification under Complex Operating Conditions

There are difficulties in identifying SLGs in Peterson coil grounded systems, and issues with unreliable power supply and HIGF identification in small-resistance grounded systems. Although the combined application of both can leverage strengths and mitigate weaknesses to some extent, the asymmetric voltage changes in the grid environment and the complex operating conditions at fault points constrain their seamless integration. Consequently, this paper establishes a fault zero-sequence circuit model to elucidate the evolving mechanism of fault characteristic quantities during the collaborative processing of single-phase ground faults. Figure 1 illustrates the equivalent model of the fault zero-sequence circuit during the transition of neutral point grounding methods.

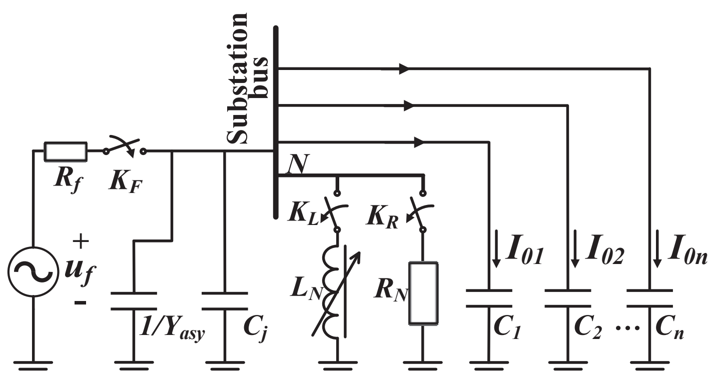


**Figure 1.** Fault Zero-Sequence Circuit during Cooperative Control of Neutral Point Grounding Methods.

Due to the relatively small unit inductance and resistance of distribution lines, the primary component of impedance in the zero-sequence circuit is the distributed capacitance to ground of the lines. To analyze the zero-sequence fault characteristics of SLG, we have neglected the line's inductance and resistance values, focusing solely on the effect of the distributed capacitance to ground of the lines. In Figure 1, $u_f$ represents the virtual power source at the fault point; switches $K_L$ and $K_R$ are, respectively, used to connect/disconnect the Peterson coil $L_N$ and grounding resistor $R_N$ at the neutral point $N$; $C_1, C_2, \ldots, C_j, \ldots, C_n$ represent the ground capacitance of each feeder line. The closure of switch $K_F$ indicates the occurrence of a ground fault; $Y_{asy}$ denotes the virtual asymmetrical admittance.

The mathematical expression for the virtual asymmetrical admittance $Y_{asy}$ is given by Equation (1) [27],

$$Y_{asy} = G_A + j\omega C_A + a^2(G_B + j\omega C_B) + a(G_C + j\omega C_C) \tag{1}$$

where $a = e^{j120}$ is the rotation factor; $G_A$, $G_B$, $G_C$ represent the leakage conductance to ground of the three phases; and $C_A$, $C_B$, $C_C$ denote the capacitance to ground of the three phases.

By using Equation (1), the asymmetrical voltages in the system can be expressed as Equation (2),

$$\dot{U}_{NN'} = -U_{ph}\frac{Y_{asy}}{G_{\Sigma} + j\omega C_{\Sigma}} \tag{2}$$

where $\dot{U}_{NN'}$ represents the virtual asymmetric voltage of the distribution system; $G_{\Sigma} = G_A + G_B + G_C$ represents the total system ground leakage conductance; $C_{\Sigma} = C_A + C_B + C_C$ denotes the total system ground capacitance; $U_{ph}$ stands for the amplitude of phase source voltage. The detailed derivation of Equation (2) can be found in Appendix A, Equations (A1) and (A2).

Using Equation (2), the expression for the neutral point displacement voltage $\dot{U}_{N0}$ can be derived as shown in Equation (3),

$$\dot{U}_{N0} = \frac{Y_C}{Y_C + Y_N}\dot{U}_{NN'} \tag{3}$$

where $Y_C$ represents the system's ground capacitance admittance; $Y_N = 1/j\omega L_N$ for resonant grounded systems; $Y_N = 1/R_N$ for resistance grounded systems. The detailed derivation of Equation (3) can be found in Appendix A, Equation (A3).

*2.1. Voltage Asymmetry Leading to Misidentification of SLGs*

When the neutral point is initially grounded through Peterson coils, the neutral point displacement voltage $\dot{U}_{N0}$ of the unbalanced power grid can be represented by Equation (4),

$$\dot{U}_{N0} = -\frac{Y_C j\omega L}{Y_C j\omega L + 1}U_{ph}\sum_{1}^{n}\frac{Y_{asy}}{G_{\Sigma} + j\omega C_{\Sigma}} \tag{4}$$

where $U_{ph}$ represents the system phase voltage.

Analysis of Equation (4) reveals that the inductive current provided by Peterson coils differs in direction from the current vector provided by the virtual asymmetrical admittance in the unbalanced power grid. This leads to variations in the trend of $\dot{U}_{N0}$. Considering the ground resistance $R_S$ and the damping resistance $R_Z$ of the Peterson coil, the zero-sequence circuit of the asymmetrical network and the voltage-current phasor diagram can be depicted based on Equation (4), as illustrated in Figure 2.

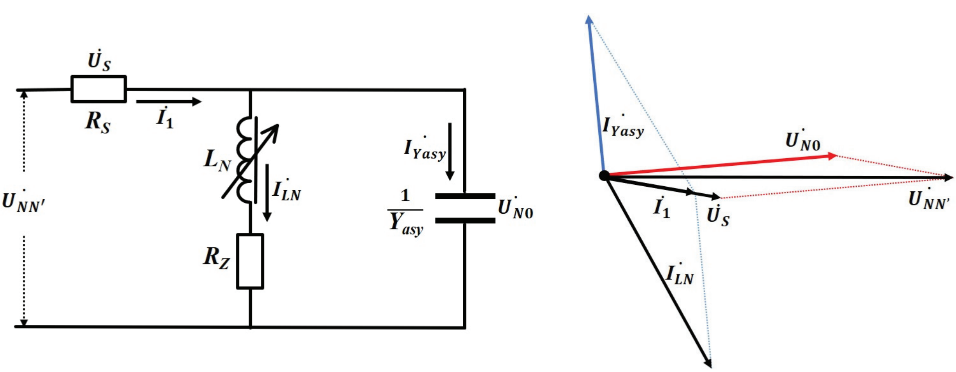


(**a**) (**b**)

**Figure 2.** (**a**) Zero-sequence circuit of the asymmetrical network with Peterson coil grounding system; (**b**) Voltage-current vector model.

From the vector diagram, it is evident that the inductance and damping resistance of the Peterson coil branch jointly cause the branch current to lag behind $\dot{U}_{N0}$ and deviate.

By synthesizing the current in the Peterson coil branch with the current in the virtual admittance branch, the current in the loss resistance branch can be derived to determine the voltage direction. Subsequently, the vector model of the asymmetrical voltage $\dot{U}_{NN'}$ is synthesized.

Combining the above characteristics leads to the conclusion that the direction and magnitude of $\dot{U}_{N0}$ vary under the influence of the Peterson coil branch and the virtual asymmetrical admittance. However, during HIGFs, the only observed change is in the capacitive current leading $\dot{U}_{N0}$, which overlaps with the range of $\dot{U}_{N0}$ variation during non-fault periods. The dispersion in the tuning range of the Peterson coil and the magnitude of the asymmetrical admittance leads to irregularities in the deviation direction of the asymmetrical voltage. Consequently, it is not possible to utilize effective waveform characteristic changes of $\dot{U}_{N0}$ to judge the occurrence of faults.

### 2.2. Special Fault Initial Phase Causes Disappearance of Fault Characteristics

When a ground fault occurs, the waveform of $\dot{U}_{N0}$ in the resistor grounding system exhibits a significant DC attenuation component. Utilizing this waveform characteristic can partly address the issue of asymmetric interference. However, the randomness of the fault initial phase angle may lead to the disappearance of the voltage waveform attenuation feature. In this paper, we establish differential Equation (5) at the moment of a single-phase ground fault occurrence in the resistor grounding system to analyze this problem,

$$u_f = u_{N0} + R_f\left(C_\Sigma \frac{du_{N0}}{dt} + \frac{u_{N0}}{R_N}\right) \tag{5}$$

where $R_N$ represents the neutral point grounding resistance; $R_f$ denotes the fault point transition resistance; $u_f$ represents the fault virtual voltage source $u_f = U_{ph}\cos(\omega t + \varphi)$; and $u_{N0}$ represents the transient neutral point displacement voltage.

Solving the first-order differential Equation (5) yields Equation (6).

$$\begin{aligned} u_{N0}(t) = {} & \frac{U_{ph}}{\sqrt{{R_f}^2{C_\Sigma}^2\omega^2 + (R_f + R_N)/R_N}}\cos(\omega t + \varphi \\ & - \tan^{-1} R_f C_\Sigma \omega) + Ke^{-(R_f/R_N + \frac{t}{R_f C_\Sigma})} \end{aligned} \tag{6}$$

Under the assumption of ideal conditions with three-phase symmetry, the overall response equation of the circuit can be derived as Equation (7).

$$\begin{cases} u_{N0}(t) = (U_{N0ph}\cos\theta_1 - \frac{U_{ph}\cos(\varphi - \tan^{-1} R_f C_\Sigma \omega)}{\sqrt{{R_f}^2{C_\Sigma}^2\omega^2 + (R_f + R_N)/R_N}})k \\ \quad + \frac{U_{ph}\cos(\omega t + \varphi - \tan^{-1} R_f C_\Sigma \omega)}{\sqrt{{R_f}^2{C_\Sigma}^2\omega^2 + (R_f + R_N)/R_N}} \\ k = e^{-(\frac{R_f}{R_N} + \frac{t}{R_f C_\Sigma})} \end{cases} \tag{7}$$

From Equation (7), it is evident that during a ground fault, the alternating component of the $\dot{U}_{N0}$ increases, while a decaying direct current component also emerges. As the transition resistance increases, the peak value of the DC offset decreases, and the decay time increases, as illustrated in Figure 3a. Figure 3 shows the neutral point displacement voltage waveforms under balanced phase voltage conditions for different transition resistances and different initial fault angles.

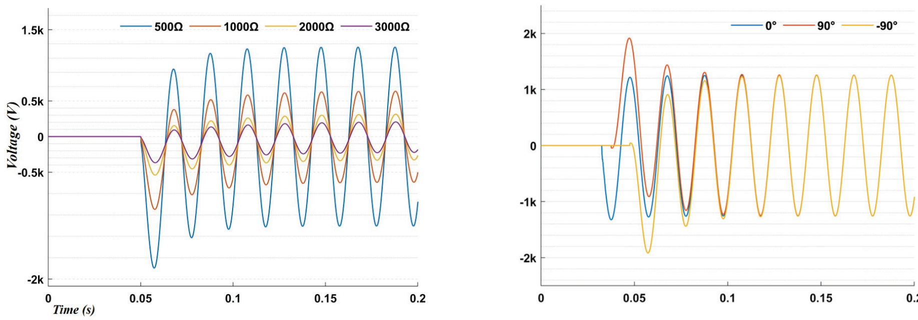


(**a**) (**b**)

**Figure 3.** (**a**) $U_{N0}$ under Different Transition Resistances; (**b**) $U_{N0}$ under Different Initial Fault Angles.

Assuming the equilibrium value of the initial fault angle is $\theta_2$, the expression for $\theta_2$ can be derived from Equation (7) as shown in Equation (8).

$$\begin{aligned}\theta_2 = {} & \cos^{-1}(U_{ph}{}^{-1}(U_{N0ph}\cos\theta_1\sqrt{R_f{}^2C_\Sigma{}^2\omega^2+(R_f+R_N)/R_N} \\ & -\tan^{-1}R_fC_\Sigma\omega))\end{aligned} \quad (8)$$

Considering the influence of the fault initial phase angle $\varphi$, the DC offset component decay process indicates the following trends: when $\varphi = \theta_2$, the DC decay vanishes. As $\varphi$ moves away from $\theta_2$, the peaks of the DC decay rise, reaching their maximum at $\varphi = \theta_2 + \pi/2$, as depicted in Figure 3b.

In summary, the random distribution characteristics of the initial fault angle can result in the disappearance of the attenuation features in the neutral point displacement voltage waveform. Therefore, when using waveform characteristics for fault identification, it is not sufficient to rely solely on the attenuation component as an indicator of fault occurrence.

## 3. Coordinated Fault Identification Strategy Using Peterson Coil and Resistor

### *3.1. Structure and Principles of the Proposed Fault Identification Method*

The structure of the Peterson coil-resistor collaborative fault handling device is shown in Figure 4.

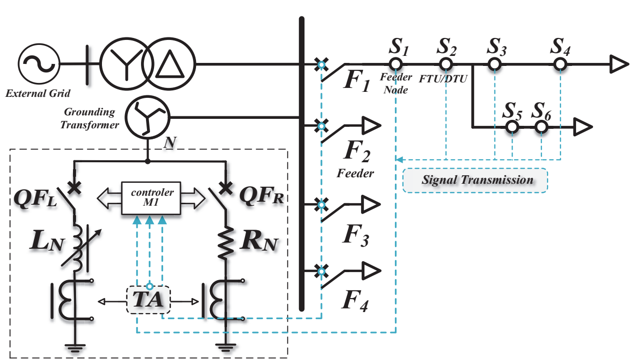


**Figure 4.** Structure of the Peterson Coil-Resistor Collaborative Fault Handling Device.

In the figure, $L_N$ represents the inductance of the Peterson coil, and $R_N$ represents the neutral point grounding resistor. To distinguish from the theoretical analysis in Figure 1, $Q_{FL}$ is used here to represent the switch of the Peterson coil branch of the device and $Q_{FR}$ represents the switch of the resistance branch.

In normal operation, the distribution network utilizes resistance grounding at the neutral point. The criterion for detecting single-phase ground faults is based on the voltage variation characteristics of the neutral point displacement. Peterson coil branches are activated upon detection of a single-phase ground fault to suppress capacitive fault currents.

After a specific delay $\Delta T_X$ (the delay time corresponds to the duration for the fault arc to extinguish, as detailed in reference [28]), the Peterson coil is deactivated. Then, the resistance branch is reconnected. Since the time allocated for the fault arc to extinguish is generally 2–3 s, the response speed of the switches can be neglected. Subsequently, the nature of the faults is determined based on changes in $U_{N0}$ and zero-sequence current amplitude. If, upon switching back to the resistance grounding branch, differences in characteristic quantities persist compared to the normal state, the faults are classified as permanent. The fault line and section can then be determined through the zero-sequence current fault characteristics when the Peterson coil branch switch is engaged.

Manual switching of the Peterson coil grounding mode is necessary to ensure the reliability of the Peterson coil operation when there is a change in the operating mode of the grid. After completing measurements of grid capacitance currents and performing automatic tuning, the Peterson coil switches back to the resistance grounding mode to dampen overvoltage in the grid.

### *3.2. Application of Electrical Quantity Waveform Feature Recognition in Coordinated Fault Handling*

In the fault identification strategy proposed in this paper, waveform feature extraction and attenuation component processing techniques are utilized to identify the occurrence of ground faults and the fault regions. To address the challenge of difficult fault perception caused by high-resistance grounding faults in asymmetric power systems, this paper introduces a method for identifying the attenuation characteristics of neutral point displacement voltage waveforms. By combining this approach with mode frequency differences, the proposed method achieves accurate detection of grounding faults. Furthermore, to enhance precise fault area identification, the paper extracts attenuation coefficients from zero-sequence current waveforms and utilizes polarity differences in these coefficients to identify fault regions.

#### 3.2.1. Analysis of Fault Attenuation Process in Neutral Point Displacement Voltage

The transient process of grounding faults occurring in resistance-grounded systems has been analyzed through the zero-sequence circuitry in the preceding sections. Due to the sinusoidal trajectory of $U_{N0}$ during normal operation, $\theta_2$ varies with factors such as the faulted phase and fault inception angle, leading to ineffective detection of DC attenuation components.

However, higher transition resistances exert a more pronounced damping effect on the oscillation process during fault occurrences, presenting a significant contrast to the voltage asymmetry changes during normal grid operation.

This paper utilizes the Variational Mode Decomposition (VMD) method to decompose the neutral point displacement waveforms under typical special fault phase angles during HIGF and voltage asymmetry conditions. The VMD method was proposed by Dragomiretskiy et al. This method assumes that any signal is composed of a series of sub-signals with specific center frequencies and finite bandwidths. By constructing and solving a variational problem, it determines the center frequencies and bandwidth constraints and identifies effective components corresponding to each center frequency in the frequency domain. The decomposition steps of the VMD method are referenced from [29].

Figures 5 and 6 depict the decomposed modes for two different scenarios. By analyzing the frequency characteristics of these decomposition modes using Fast Fourier Transform (FFT), the resonant frequency bands of the original waveforms can be identified.

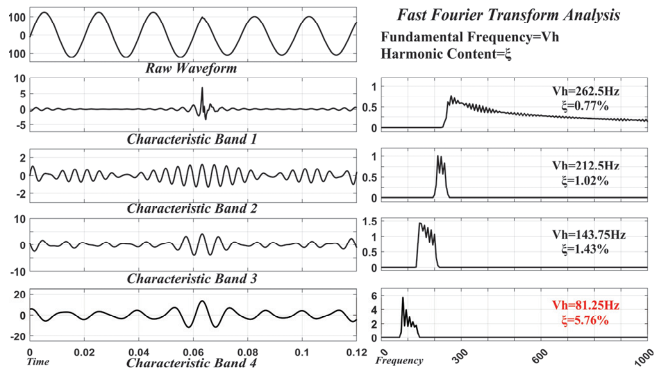


**Figure 5.** Decomposition and FFT Analysis of Voltage Waveform under High-Resistance Grounding Fault.

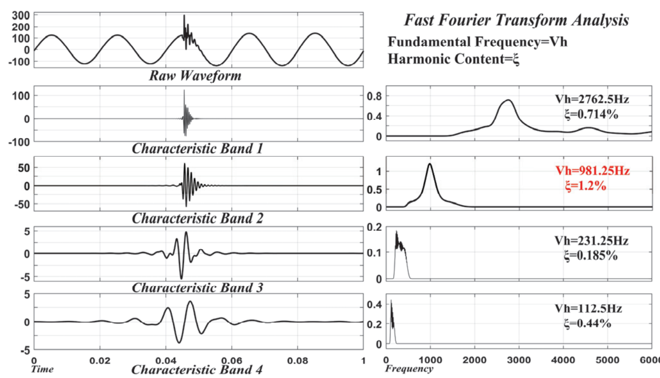


**Figure 6.** Decomposition and FFT Analysis of Voltage Waveform with Phase Voltage Asymmetric Variations.

In the above figure, $V_h$ represents the modal center frequency, and $\xi$ denotes the proportion of the center frequency within the fundamental wave.

A comparison between Figures 5 and 6 allows us to draw the following conclusion: due to the damping effect of the transition resistance, the harmonic frequencies during high-resistance grounding faults are concentrated near the fundamental frequency, with minimal high-frequency harmonic content. In contrast, during dynamic changes in phase voltage asymmetry, there is a distribution of both low-frequency and high-frequency harmonics. The harmonic content during asymmetric voltage changes is related to the closing angle. When the closing angle is 0°, the harmonic frequency content is minimal, reaching its peak at 90°, as shown in Tables 1 and 2.

**Table 1.** The frequency band of the $U_{N0}$ in HIGF.

| **HIGF C Phase $\varphi = \theta_2$** | **1 kΩ** | **2 kΩ** | **3 kΩ** | **4 kΩ** | **5 kΩ** |
|---|---|---|---|---|---|
| $V_h$: | 125 Hz | 112 Hz | 87.5 Hz | 83.8 Hz | 65 Hz |
| $\xi$: | 5.66% | 4.67% | 4.02% | 3.58% | 1.99% |

**Table 2.** The frequency band of the $U_{N0}$ in asymmetric voltage variation.

| $U_{N0}$ Initial Value: 86.6 V | | Change Value 80.83 V | 75.06 V | 69.28 V | 63.51 V | 57.74 V |
|---|---|---|---|---|---|---|
| 0° | $V_h$: | 2805 Hz | 2743 Hz | 2657 Hz | 2682 Hz | 2732 Hz |
| | $\xi$: | 0.11% | 0.12% | 0.11% | 0.10% | 0.11% |
| 90° | $V_h$: | 996 Hz | 1001 Hz | 1042 Hz | 1050 Hz | 987 Hz |
| | $\xi$: | 0.55% | 0.45% | 0.36% | 0.44% | 0.42% |

A comparison between Tables 1 and 2 leads to the conclusion that when there is an asymmetric variation, the resonant frequency of $U_{N0}$ is higher, typically distributed within the high-order modal frequency band. However, during high-resistance grounding faults, the resonant frequency of $U_{N0}$ is lower, situated within the lowest frequency band mode of the decomposed modal frequencies.

During HIGF, the accurate detection of ground faults can be achieved utilizing the aforementioned characteristics. When $\varphi \neq \theta_2$, HIGF can be identified using the direct current offset component. When $\varphi = \theta_2$, differentiation between HIGF and dynamic changes in phase voltage asymmetry can be made based on the difference in high-frequency harmonic content.

#### 3.2.2. Analysis of Zero-Sequence Current Attenuation Process during Grounding Method Switching

When the fault is permanent, switch $Q_{FL}$ is opened at time $T_1$, and the Peterson coil circuit exits operation. At this moment, the ground capacitance loses the compensating effect of inductive current, regardless of whether the Peterson coil was in an under-compensation or over-compensation state. This process can be equivalent to the closure of capacitor $C$ in an $RC$ series-parallel circuit at time $T_1$, as shown in Figure 7.

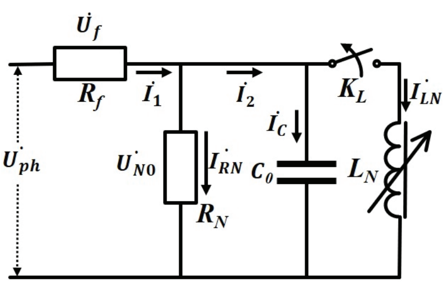


(**a**)

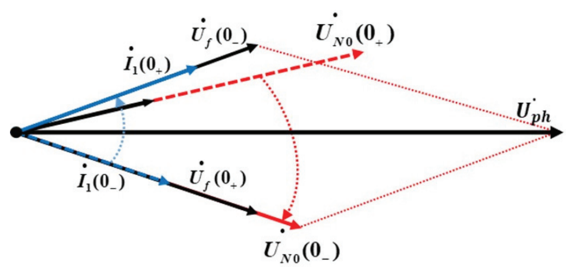


(**b**)

**Figure 7.** (**a**) Zero-Sequence Equivalent Circuit During Fault Coordination Process; (**b**) Voltage-Current Vector Model.

Before the switching operation, $U_{N0}(0-) = R_N I_{RN}$; $u_C(0-) = U_{N0}(0-)$. According to the switching rule, after the switching operation, we obtain $u_C(0_-) = u_C(0_+)$. According to the KVL and KCL, the relationship between the voltages and currents of each component after the switch is closed, as illustrated in Equation (9).

$$\begin{cases} \dot{U}_{ph} = R_f(C\frac{du_C}{dt} + \frac{u_C}{R_N}) + u_C \\ i_C = \frac{\dot{U}_{ph} - u_C}{R_f} - \frac{u_C}{R_N} \end{cases} \quad (9)$$

Assuming the time constant of the capacitor circuit is $\tau$, $\tau = R_N C_0$. The voltage total response equation of the capacitor circuit during this stage can be represented by Equation (10).

$$u_c = \frac{R_N U_{ph}}{R_N + R_f} + (R_N I_{RN} - \frac{R_N U_{ph}}{R_N + R_f})e^{-\frac{t}{\tau}} \tag{10}$$

In Equation (10), the first half on the right-hand side represents the steady-state component, while the second half represents the decaying free component. The decay component is directly related to the transition resistance at the fault point and the neutral point resistance. As the transition resistance increases, the peak value of the offset component decreases, and the decay time increases. The decay process of the zero-sequence current after capacitor closure is given by Equation (11).

$$\dot{I}_C = C_0 \frac{du_c}{dt} = (-I_{RN} + \frac{U_{ph}}{R_N + R_f})e^{-\frac{t}{\tau}} \tag{11}$$

In a resistance-grounded system, significant differences exist in the amplitude and direction of zero-sequence currents between the upstream node (near the substation) and the downstream node (far from the substation) at the fault point. Due to the shunting effect of line-to-ground capacitance, the zero-sequence current gradually increases from the substation feeder to the fault point, reaching its maximum value at the node just before the fault point. Subsequently, the zero-sequence current gradually decreases at nodes downstream of the fault point, as illustrated in Figure 8.

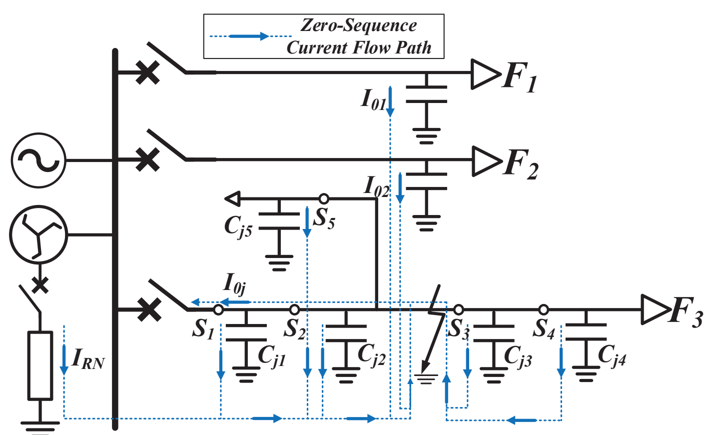


**Figure 8.** Zero-Sequence Current Network Distribution Structure.

Let $C_{j1}$, $C_{j2}$, …, $C_{jn}$ denote the line-to-ground capacitances of the fault feeder sections, and $G_{j1}$, $G_{j2}$, …, $G_{jn}$ denote the line-to-ground conductance of the fault feeder sections. The fault occurs at node $i$. Based on Kirchhoff's Current Law (KCL), the relationship for zero-sequence currents upstream and downstream of the fault point can be derived as Equation (12),

$$\begin{cases} \dot{I_o}^{Power} = \dot{U}_{N0} j\omega (C_\Sigma - \sum\limits_{i=1}^{k} C_{ji}) - \dfrac{\dot{U}_f}{R_f + \sum\limits_{i=1}^{k} G_{ji}} + \dfrac{\dot{U}_{N0}}{R_N} \\ \dot{I_o}^{Load} = \dfrac{\dot{U}_f}{R_f + G_{jn}} - \dot{U}_{N0} j\omega C_{jn} \end{cases} \tag{12}$$

where $I_0^{power}$ represents the zero-sequence current at the upstream node of the fault point, while $I_0^{Load}$ represents the zero-sequence current at the downstream node of the fault point.

The analysis above indicates that accurate localization of small-resistance grounding faults can be achieved through the magnitude of zero-sequence currents at nodes. However, due to the current-limiting effect of high-resistance grounding resistors, differentiating the fault characteristics of zero-sequence currents at various nodes becomes challenging, making it difficult to precisely locate HIGF areas using traditional methods. The zero-sequence currents in the resistance-grounding system exhibit directional distribution within the network. After the Peterson coil is removed from operation, the attenuation components of zero-sequence currents at upstream and downstream nodes exhibit different attenuation directions. Therefore, this paper proposes utilizing the disparity in the attenuation directions of zero-sequence currents as a supplementary method for detecting HIGFs. Figure 9 depicts the waveform differences between the upstream and downstream nodes upon the removal of the Peterson coil.

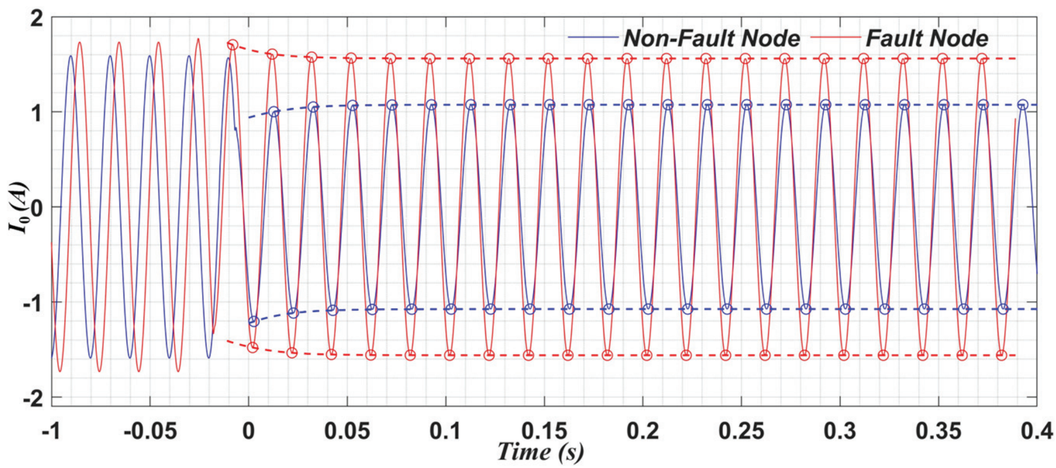


**Figure 9.** Differences in Zero-Sequence Current Waveforms between Upstream and Downstream Nodes during Faults.

### 3.3. *Extracting and Analyzing Waveform Characteristics*

Given the time-frequency characteristics of neutral point displacement voltage and zero-sequence current in fault coordination processes, this paper employs EWT [30] to decompose the feature quantities and construct modal components for each frequency band. The EWT combines the adaptive capability of Empirical Mode Decomposition (EMD) with the orthogonality of wavelet methods. It provides better physical interpretability while avoiding the issues of mode mixing and over-decomposition [31]. The modal signals obtained from this method exhibit good stability and robustness. The decomposition process is described in detail in the literature [32].

#### 3.3.1. Fault Detection Based on Voltage Attenuation Components and Modal Frequencies

We can detect ground faults based on the direct current modal component in the modal components obtained through EWT decomposition of neutral point displacement voltage. Figure 10 illustrates the modal components obtained through the EWT method when a permanent HIGF occurs.

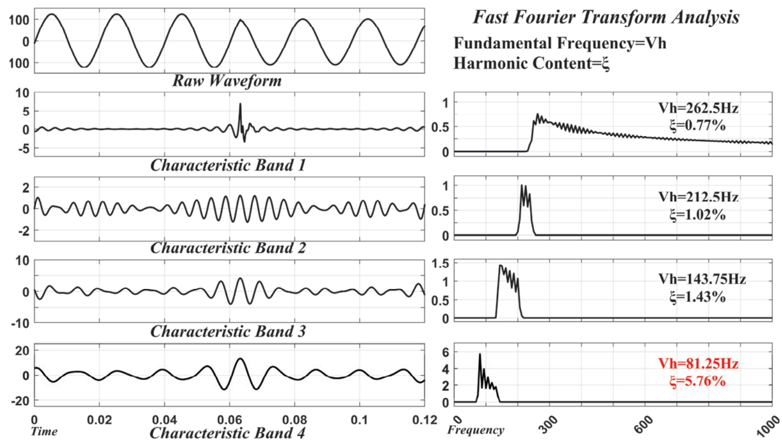


**Figure 10.** Decomposition of Neutral Point Displacement Voltage Waveform in HIGF.

When a specific fault phase angle causes the disappearance of the DC component, the resonance band distribution characteristics obtained from the previous analysis can distinguish between HIGF and voltage asymmetry changes. The variance contribution ratio can intuitively reflect the energy provided by the decomposition modes to the signal fluctuation in the original waveform. The process of calculating the mode variance contribution rate is as follows: after calculating the variance for each mode, the proportion in the original signal variance is computed, as shown in Equation (13).

$$PCR = \frac{{s_i}^2}{{\sigma_o}^2} = \frac{\int [{e_i}^2(t) - \overline{e_i}]^2 dt}{\int [Y^2(t) - \overline{y}]^2 dt} \tag{13}$$

The harmonic main frequencies $V_X$ of each mode are obtained through FFT. Weighted averaging of the harmonic main frequencies is performed using *PCR* as the weighting factor to calculate the maximum frequency value $V_g$ in the energy spectrum, as shown in Equation (14). The value $V_g$ describes the harmonic frequency in the decomposition mode that has the greatest impact on signal fluctuations.

$$V_g = \frac{\sum\limits_{i=1}^{N} V_X^i PCR_i}{\sum\limits_{i=1}^{N} PCR_i} \tag{14}$$

The directional nature of $V_g$ in the decomposition mode frequency bands can distinguish between HIGF and voltage asymmetry changes. If $V_g$ points to the high-frequency modal component, it is judged that a voltage asymmetry change has occurred; if $V_g$ points to the low-frequency modal component, it is considered that an HIGF has occurred. Figure 11 visually illustrates the frequency characteristics of the neutral point displacement voltage under different conditions.

As shown in Figure 11, under the condition of a specific initial fault angle, $V_g$ successfully indicated the frequency band characteristics in both HIGF and voltage asymmetry changes. During high-resistance grounding faults, $V_g$ pointed to the low-frequency modal component, while in voltage asymmetry changes, $V_g$ pointed to the high-frequency modal component.

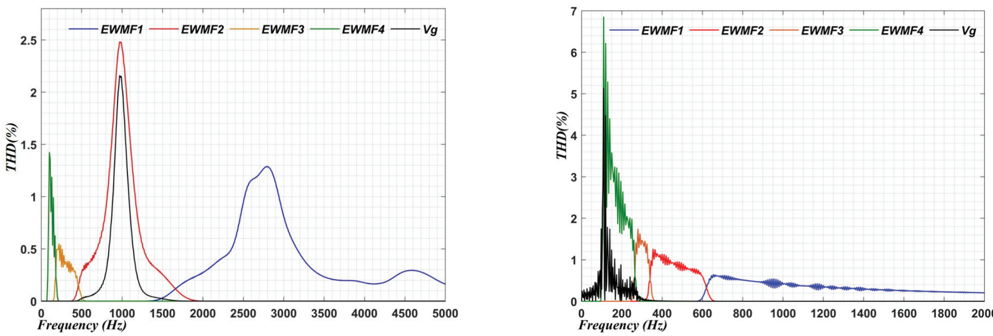


(**a**) (**b**)

**Figure 11.** (**a**) Modal Frequency Band Distribution During Voltage Asymmetry Changes; (**b**) Modal Frequency Band Distribution During HIGF.

3.3.2. Fault Zone Localization Based on Zero-Sequence Current Attenuation Coefficient

Based on the analysis above, the fault zone can be determined using the attenuation polarity of the zero-sequence current at feeder nodes when the Peterson coil is removed. Firstly, EWT is applied to decompose the zero-sequence current waveforms at the beginning of each feeder. The decomposed DC attenuation component characterizes the direction of zero-sequence current attenuation. Then, the fault zone is identified based on the polarity characteristics of zero-sequence current attenuation at the nodes of the faulted feeder.

The method for extracting the polarity characteristics of zero-sequence current attenuation is as follows. First, the EWT is used to decompose the zero-sequence current at each feeder and node, resulting in the nonlinear attenuation mode $E_{res}(t)$. Then, the Nonlinear Least Squares (NLS) method is applied to fit the attenuation term and obtain a nonlinear attenuation model. The objective function is shown in Equation (15).

$$E(t) = \delta_f e^{-\lambda_f t} + \alpha \tag{15}$$

The fitting process includes minimizing the sum of squared residuals (Equation (16)) and iteratively solving for the optimal parameters using the Levenberg–Marquardt method.

$$S(\theta) = \sum_{i=1}^{n} \left[e_{res} - \left(\delta_f e^{-\lambda_f t} + \alpha\right)\right]^2 \tag{16}$$

The above process yields two variables: the attenuation coefficient $\lambda_f$ and the attenuation zero-point $\delta_f$. The sign of the attenuation coefficient indicates the direction of zero-sequence current attenuation, while the attenuation zero point represents the time when attenuation terminates.

The identification of fault sections can be achieved by leveraging the opposite polarity of the attenuation coefficients of zero-sequence currents at upstream and downstream fault nodes. Specifically, the fault area can be located by examining the sign of the zero-sequence current attenuation coefficient $\lambda_f$ at each node before the attenuation zero-point $\delta_f$.

*3.4. Process Flow of Neutral Point Coordination Control Method for SLG*

The fault characteristic identification stage of the neutral point grounding SLG coordination control method consists of five time sequences ($T_0$–$T_4$), as shown in Figure 12.

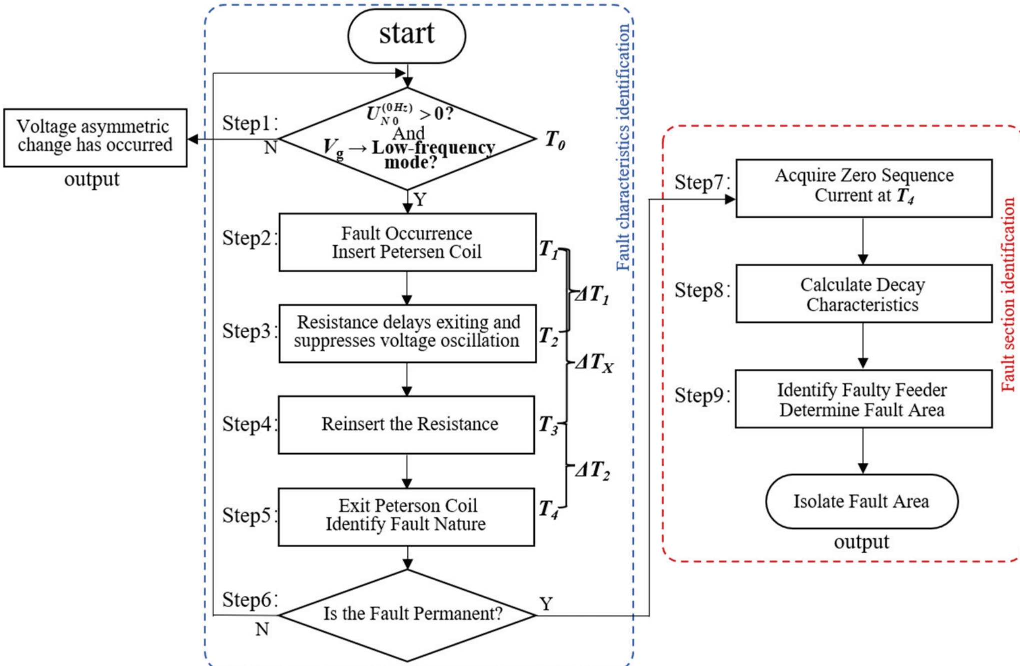


**Figure 12.** Flowchart of Neutral Point Coordinated Fault Handling Strategy.

Step 1: Upon detection of a fluctuation in $U_{N0}$, grounding faults are diagnosed by analyzing the decay of the direct current component of the neutral point displacement voltage to identify HIGF while excluding asymmetrical disturbances in grid operation. The calculation method is shown in Equations (13) and (14). Mark the occurrence of the fault as $T_0$.

Step 2: At time $T_1$, the Peterson coil is activated to suppress fault currents. During the delay $\Delta T_1$, both the Peterson coil branch and the resistance branch operate simultaneously in the grounding circuit, with the resistance branch rapidly suppressing the attenuation component in the Peterson coil.

Step 3: At time $T_2$, the resistance grounding branch is deactivated, allowing the Peterson coil to extinguish the fault arc within the delay $\Delta T_X$.

Step 4: At time $T_3$, the resistance branch is reactivated to suppress the electrical quantity free oscillation process caused by disconnecting the Peterson coil.

Step 5: After a delay of $\Delta T_2$, the Peterson coil is disconnected. The fault nature is determined by assessing whether the $U_{N0}$ and zero-sequence current amplitudes of each feeder have returned to normal.

Step 6: If all characteristics return to normal, the fault is classified as transient, and the resistance branch continues to operate. If the fault characteristics do not return to normal, the fault is deemed permanent.

Step 7: At time $T_4$, the fault feeder is determined by analyzing the attenuation of the zero-sequence current free component of each feeder, thereby completing the identification of the fault region.

Step 8: At time $T_4$, the calculation of the zero-sequence current attenuation coefficients at the starting end of the faulted line and at the line node is implemented using Equations (15) and (16).

Step 9: By comparing the polarity of the zero-sequence current attenuation coefficients between upstream and downstream nodes at the fault point, the identification of the fault region is achieved.

## 4. Experimental Analysis

### 4.1. Detection Experiment of HIGF and Voltage Asymmetry

To validate the accuracy of the proposed method for fault detection, we constructed a typical 10 kV distribution system in the PSCAD 5.0 simulation environment, as illustrated in Figure 13.

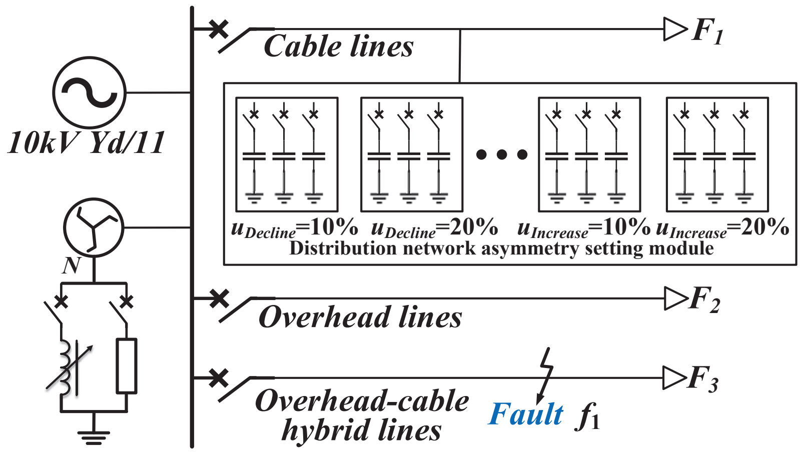


**Figure 13.** Simulation Experiment Distribution Network Structure.

Three lines ($F_1$~$F_3$) in the distribution network are set up using lumped parameter line models. Specifically, $F_1$ represents a cable line, $F_2$ represents an overhead line, and $F_3$ represents a hybrid overhead-cable line. Line $F_1$ is equipped with a three-phase voltage asymmetry offset testing module, which operates by adjusting the asymmetrical state of the three-phase voltages through varying the capacitance to ground of each phase, and the degree of asymmetry is defined by the displacement of the neutral point voltage $u_{00}$(%). The parameters of the cable and overhead lines are listed in Table 3. Line $F_3$ is equipped with a single-phase ground fault module, simulating a high-resistance ground fault by varying the fault resistance value and the fault occurrence time.

**Table 3.** Cable and overhead line simulation parameters.

| Line Impedance (Ω/km) | Positive Sequence Parameter | | | Zero Sequence Parameters | | |
|---|---|---|---|---|---|---|
| | $R^{(1)}$ | $X_L{}^{(1)}$ | $X_C{}^{(1)}$ | $R^{(0)}$ | $X_L{}^{(0)}$ | $X_C{}^{(0)}$ |
| Cable line | 0.27 | 0.08 | 8469.9 | 2.7 | 0.3488 | 11,538.8 |
| Overhead line | 0.17 | 0.38 | 318,471.3 | 0.25 | 1.72 | 398,289.2 |

During normal operation, the effective value of $U_{N0}$ is 86.6 V, with phase A having the highest voltage and phase C having the lowest voltage. In line $F_1$, the capacitance parameters to ground of the three phases are adjusted to induce variations in $U_{N0}$ within the range of 1.0% to 2.0%. The value $\Delta u$ represents the difference in these variations, simulating changes in the asymmetry of the three-phase voltages in the distribution network. Under the influence of the three-phase asymmetry, the behavior of the neutral point displacement voltage during ground faults and normal operation is illustrated in Figure 14.

From Figure 14, it can be observed that when the HIGF occurs precisely at a specific initial phase angle of the fault, the decay component of the $U_{N0}$ disappears. Moreover, the variation in the magnitude of $U_{N0}$ is similar to that observed when voltage asymmetry occurs. The results of applying the method proposed in this paper and the traditional steady-state magnitude judgment method are shown in Tables 4 and 5, respectively.

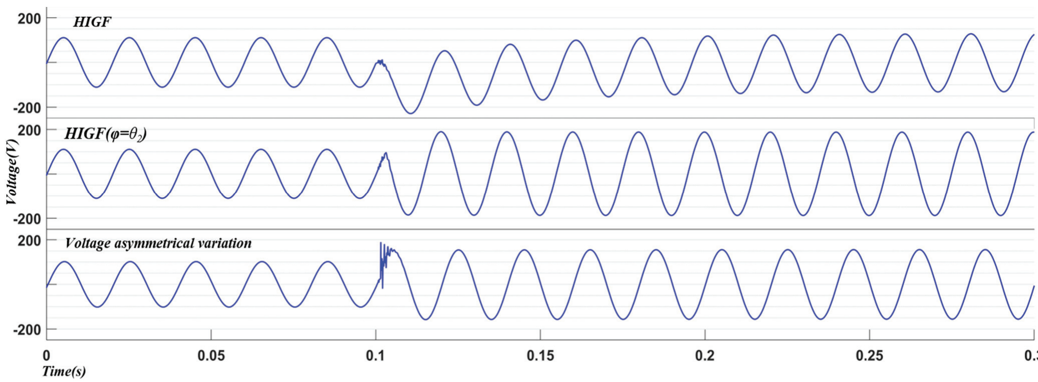


**Figure 14.** Variations in Neutral Point Displacement Voltage Waveform.

**Table 4.** $U_{N0}$ on HIGF ($\varphi = \theta_2$).

| $R_f$ (Ω) | Modal Frequency Band (Hz) | $V_g$ (Hz) | Method in This Paper | Steady-State Method |
|---|---|---|---|---|
| 1 kΩ | [2250~15,587, 1293~2662, 781~1637, 181~568] | 226 | Fault | Fault |
| 2 kΩ | [2200~13,712, 1293~2100, 781~1637, 103~577] | 171 | Fault | / |
| 3 kΩ | [1656~8675, 1056~1618, 856~1000, 91~603] | 138 | Fault | / |
| 4 kΩ | [1068~5925, 1006~1093, 968~1018, 88~581] | 116 | Fault | / |
| 5 kΩ | [756~5300, 581~748, 443~593, 68~426] | 97 | Fault | / |

**Table 5.** $U_{N0}$ on voltage asymmetrical variations.

| $\Delta u$ (V) | Modal Frequency Band (Hz) | $V_g$ (Hz) | Method in This Paper | Steady-State Method |
|---|---|---|---|---|
| −28.87 | [3456~12,150, 1512~4031, 556~1818, 118~793] | 1975 | Non-fault | / |
| −23.096 | [3568~10,381, 1537~4068, 493~1818, 106~693] | 2238 | Non-fault | / |
| −17.322 | [4893~12,268, 3556~5675, 1656~3593, 218~1731] | 2713 | Non-fault | / |
| −11.548 | [3668~10,193, 1631~4081, 493~1806, 106~681] | 3077 | Non-fault | / |
| −5.774 | [3637~11,831, 1937~4062, 493~1756, 106~668] | 4166 | Non-fault | / |
| 5.774 | [4131~16,156, 3306~4600, 1675~3225, 231~1700] | 3972 | Non-fault | / |
| 11.548 | [4075~16,068, 3187~4506, 1700~3306, 231~1675] | 3656 | Non-fault | / |
| 17.322 | [4931~15,993, 2931~5418, 1768~3368, 218~1633] | 2713 | Non-fault | / |
| 23.096 | [4843~15,400, 2912~5431, 1743~3381, 234~1455] | 2659 | Non-fault | / |
| 28.87 | [4781~14,518, 2918~5437, 1756~3393, 248~1662] | 2021 | Non-fault | Fault |

Analyzing the data from the charts, we can conclude that the average frequency based on the energy spectrum shows excellent directionality across different modal frequency bands, allowing for clear differentiation between faults and voltage asymmetry changes even when the DC decay component disappears. Compared to other methods, the approach presented in this paper accurately identifies ground faults for transition resistances below 5 kΩ and does not produce false positives during voltage asymmetry changes.

*4.2. Fault Zone Localization Experiment*

We used centralized capacitors to simulate the line-to-ground capacitance. The distribution test network was constructed using transformers, circuit breakers, primary and secondary integrated intelligent circuit breakers, and oscillographs. To validate the observability of the attenuation component by the zero-sequence current transformer, we utilized primary and secondary integrated intelligent switches as nodes to measure the zero-sequence current variations according to the proposed method. Figure 15 shows the architecture of the experimental network. The fault point is simulated using several groups of heat-dissipating resistors and a fast switch. The simulation method for the fault point and the line is shown in Figure 16.

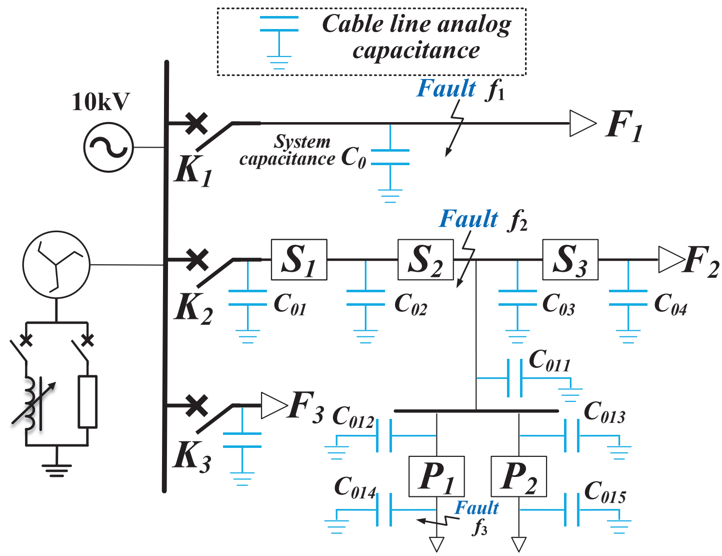


**Figure 15.** Architecture of the Distribution Experimental Network.

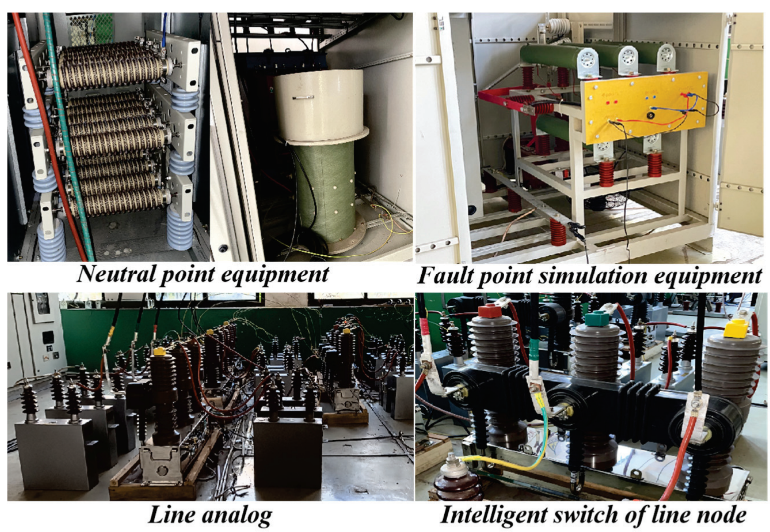


**Figure 16.** Layout of the Distribution Experimental Network.

The identification of fault areas was validated through comparative experiments by setting fault points $f_2$ and $f_3$. Figure 17 shows the recorded zero-sequence currents at nodes $S_2$ and $S_3$ when a 3000 Ω transition resistance ground fault occurs at fault point $f_2$.

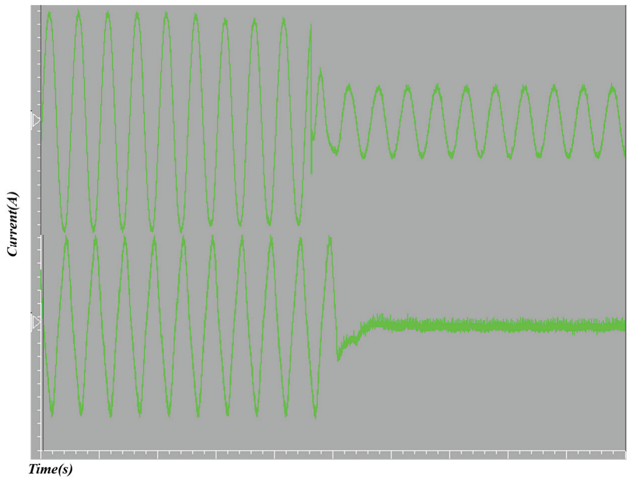


**Figure 17.** Experimental Network Waveform Data.

After extracting the recorded data, filtering was performed using a FIR filter. It was observed that during the process of Peterson coil disconnection, each node correctly observed the direction of zero-sequence current attenuation and the variation in its magnitude. Figure 18 illustrates the variation of zero-sequence currents at nodes in the distribution experimental network for fault points $f_2$ and $f_3$. Dashed lines in the figure indicate the trend of waveform changes.

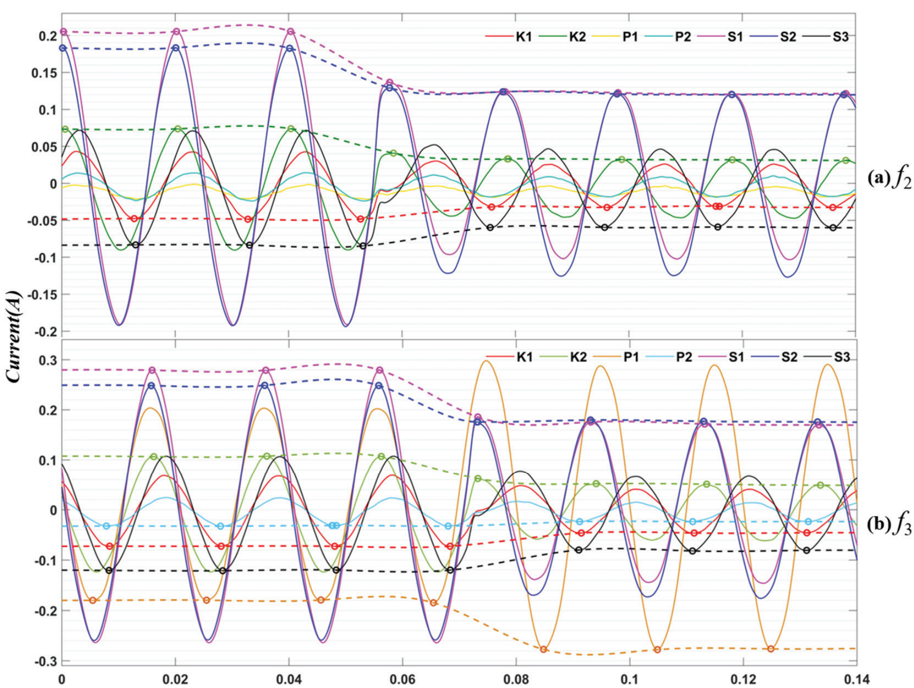


**Figure 18.** Zero-Sequence Current Waveform Analysis Chart.

Comparing Figure 18a,b, it is evident that the nodes exhibit opposite directions of zero-sequence current attenuation before and after the fault. Moreover, when branch line node $P_1$ is included as the upstream node of the fault, its zero-sequence current magnitude notably increases, indicating the same waveform attenuation direction as the upstream fault node.

After validating the observability of the zero-sequence current attenuation process, we proceeded with ground fault experiments at fault points with transition resistances ranging from 1 kΩ to 5 kΩ. The attenuation coefficients $\lambda_f$ obtained from some experiments are illustrated in Figure 19. Table 6 compares the judgment accuracy between our proposed method and the transient fault current polarity comparison method [19].

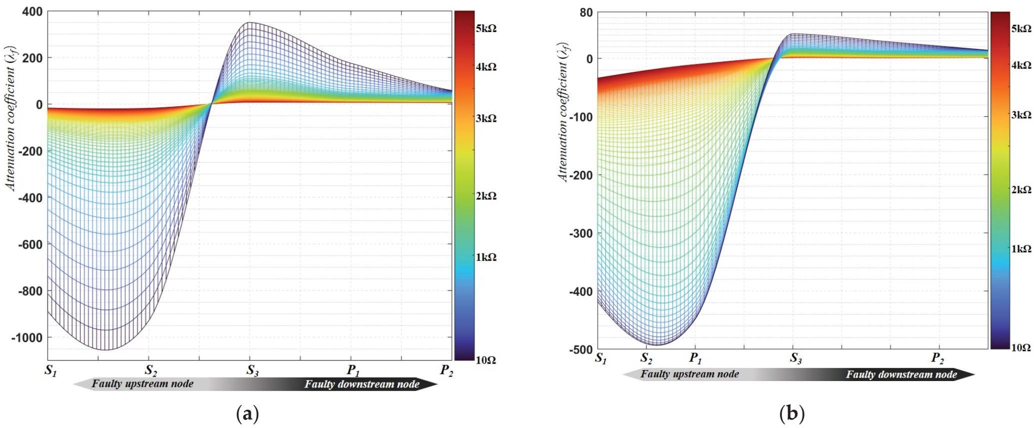


**Figure 19.** (**a**) Fault Point $f_2$; (**b**) Fault Point $f_3$.

**Table 6.** Comparison of Fault Zone Criteria and Methods.

| $R_f$ (Ω) | Fault Point | Attenuation Coefficient ($\lambda_f$) | | | | | Method in This Paper | Comparison Method |
|---|---|---|---|---|---|---|---|---|
| | | $S_1$ | $S_2$ | $S_3$ | $P_1$ | $P_2$ | | |
| 1 k | $f_2$ | −308.23 | −297.18 | 64.03 | 10.58 | 18.22 | $S_2$~$S_3$ | $S_2$~$S_3$ |
| | $f_3$ | −311.05 | −303.24 | 65.23 | −323.30 | 12.24 | $P_1$~ | $S_2$~$S_3$ |
| 3 k | $f_2$ | −56.40 | −49.29 | 12.11 | 4.22 | 6.02 | $S_2$~$S_3$ | $S_2$~$S_3$ |
| | $f_3$ | −56.40 | −49.29 | 10.33 | −52.50 | 5.29 | $P_1$~ | / |
| 5 k | $f_2$ | −30.23 | −26.58 | 5.14 | 2.12 | 1.88 | $S_2$~$S_3$ | / |
| | $f_3$ | −28.39 | −23.10 | 3.32 | −30.21 | 1.21 | $P_1$~ | / |

The analysis of experimental results reveals the following: in the experiments conducted at fault point $f_2$, the attenuation coefficients of nodes $S_1$ and $S_2$ upstream of the fault are negative, while those of nodes $S_3$, $P_1$, and $P_2$ downstream of the fault are positive. Consequently, the fault area is determined to be between nodes $S_2$ and $S_3$. Similarly, in the experiments at fault point $f_3$, the attenuation coefficients of nodes $S_1$, $S_2$, and $P_1$ upstream of the fault on the feeder are negative, whereas those of nodes $P_2$ and $S_3$ downstream of the fault are positive, indicating that the fault area is at branch line $P_1$.

In Table 6, the node criteria intuitively display the polarity differences of the attenuation coefficients at fault nodes. The comparative method, influenced by the fault initial phase angle and resonant compensation angle, resulted in misjudgments of the fault area for high-resistance ground faults. The method proposed in this paper determines the fault area based on the characteristic of the attenuation direction of the zero-sequence current at each node when disconnecting the Peterson coil. It is not affected by the fault initial phase angle or resonant compensation angle. In 10 fault area determination experiments, the accuracy rate of the comparative method was 30%, while the method proposed in this paper achieved 100% accurate fault determination.

### *4.3. Engineering Application Validation*

The methodology proposed in this paper has been applied in several distribution networks in central China, yielding favorable outcomes in fault handling. Field experiments were conducted on a distribution feeder located in Hubei Province, China, to assess fault handling and fault area determination. Figure 20 illustrates the topological structure of the feeder line. Under normal conditions, the grid is powered by transformer $T_1$ with switch B506 in the open position. When a fault is detected, switches on both sides of the fault location (such as switches B309 and B022 on either side of fault location $f_2$) can be opened, and switch B506 can be closed to restore power to the affected area via transformer $T_2$.

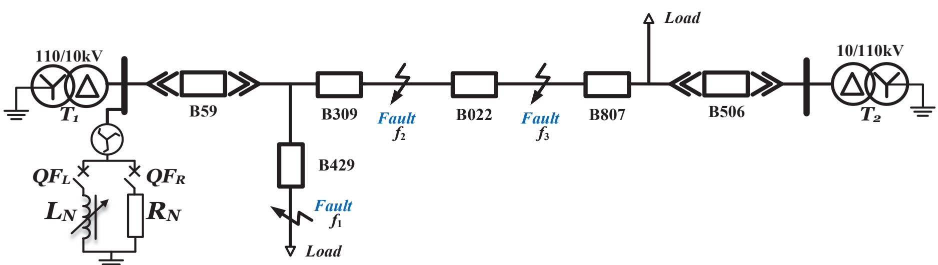


**Figure 20.** Experimental Feeder Line Topological Structure.

The experiments were conducted at fault points $f_1$, $f_2$, and $f_3$ with increasing fault resistance. The experimental data are shown in Table 7.

**Table 7.** Comparison of Fault Zone Criteria and Methods.

| Point of Failure | Fault Point Resistance (Ω) | Fault Area Judgment Result |
|---|---|---|
| fault point 1 | 0 | After B429 switch |
| | 1000 | After B429 switch |
| | 4000 | After B429 switch |
| fault point 2 | 0 | B309–B022 |
| | 1000 | B309–B022 |
| | 4000 | B309–B022 |
| fault point 3 | 0 | B022–B807 |
| | 1000 | B022–B807 |
| | 4000 | B022–B807 |

The data indicate that in testing environments with fault transition resistances below 4 kΩ, the proposed method accurately identifies the fault region and demonstrates good engineering practicality.

## 5. Conclusions

This paper proposes a novel fault identification method based on coordinated control of a Peterson coil and resistance grounding, aimed at enhancing the safety of distribution systems while ensuring power supply reliability. Furthermore, fault perception and fault region identification methods based on waveform characteristics are introduced, effectively improving the accuracy and sensitivity of identifying ground faults. The following conclusions can be drawn:

(1) The approach proposed in this paper utilizes the Peterson coil to eliminate transient faults and switches to resistance grounding during permanent faults. This method alters the distribution pattern of zero-sequence currents between faulty and non-faulty

feeders, addressing challenges in ground selection and fault region identification associated with Peterson coil grounding. Moreover, it resolves issues concerning the lack of power supply reliability associated with small-resistance grounding.

(2) Time-frequency variations in neutral displacement voltage waveforms accurately detect ground faults. The temporal decay components of the voltage waveform can discern HIGFs, while differences in harmonic frequency bands in the frequency domain can precisely differentiate voltage asymmetry changes from HIGFs. This paper combines the time-frequency characteristics of voltage waveforms to achieve accurate fault detection while eliminating interference from voltage asymmetry changes and specific fault initial phase angles.

(3) Waveform characteristics of zero-sequence currents during the transition of neutral grounding modes can identify fault regions. When disconnecting the Peterson coil, the zero-sequence current waveforms exhibit opposite attenuation directions at the upstream and downstream regions of the fault feeder, as well as at the head ends of the fault feeder and the healthy feeder. The polarity difference in the attenuation coefficients of zero-sequence currents can be utilized to identify the fault area, unaffected by the compensation status of the Peterson coil. Compared to quantitative methods based on threshold judgment, the qualitative analysis approach proposed in this paper enhances the accuracy of identifying high-resistance ground faults.

Experimental data demonstrate that our proposed method can accurately identify the fault area under a fault transition resistance of 5 kΩ. In practical engineering validation, the method accurately identifies the fault area under conditions where the fault transition resistance ($R_f$) is less than or equal to 4 kΩ.

**Author Contributions:** Conceptualization, Z.L. and Y.C.; methodology, C.C.; software, Z.L.; validation, Z.L., Y.L., and J.L.; formal analysis, Z.L.; investigation, Y.L.; resources, J.L.; data curation, Z.L.; writing—original draft preparation, Z.L.; writing—review and editing, Z.L.; visualization, Z.L. and C.C.; supervision, Y.C.; project administration, Y.C.; funding acquisition, Y.C. All authors have read and agreed to the published version of the manuscript.

**Funding:** This research was funded by the JOINT FUNDS OF THE NATIONAL NATURAL SCIENCE FOUNDATION OF CHINA, grant number U23B20128 and THE NATIONAL NATURAL SCIENCE FOUNDATION OF CHINA, grant number 52007009.

**Data Availability Statement:** The original contributions presented in the study are included in the article; further inquiries can be directed to the corresponding authors.

**Conflicts of Interest:** The authors declare no conflicts of interest.

## Appendix A

In ungrounded systems, the three-phase voltages satisfy Kirchhoff's law. Therefore, Equation (A1) can be derived,

$$\dot{U}_A Y_A + \dot{U}_B Y_B + \dot{U}_C Y_C = 0 \tag{A1}$$

where $Y_A$, $Y_B$, and $Y_C$ represent the admittances of the three phases of the power grid to ground.

Due to inevitable operational differences among the three phases, these differences are reflected in the virtual asymmetric admittance and ultimately manifest in the degree of offset in the three-phase voltages. The voltage offset among the three phases adheres to the principles of trigonometry. Thus, Equation (A2) can be derived.

$$\dot{U}_{NN'} = -\frac{\dot{U}_A(G_A + j\omega C_A) + \dot{U}_B(G_B + j\omega C_B) + \dot{U}_C(G_C + j\omega C_C)}{G_A + G_B + G_C + j\omega C_A + j\omega C_B + j\omega C_C} \tag{A2}$$

Combining Equation (1) enables the rewriting of the asymmetric voltage $\dot{U}_{NN'}$ as expressed by Equation (2) in the paper.

Using the equivalent zero-sequence circuit shown in Figure 1, the relationship between the neutral point displacement voltage $\dot{U}_{N0}$ under non-fault conditions and the asymmetric voltage $\dot{U}_{NN'}$ can be expressed as Equation (A3),

$$\dot{U}_{N0} = -\frac{j\omega(C_A + a^2 C_B + aC_C)}{j\omega C_\Sigma + Y_N + 1/R_S} U_{ph} \tag{A3}$$

where $R_S$ represents the resistive losses, which must be accounted for when the neutral point is grounded through the Peterson coil.

Equation (3) in the paper can be derived from Equation (A3).

## References


1. Leite, J.B.; Mantovani, J.R.S. Development of a Self-Healing Strategy with Multiagent Systems for Distribution Networks. *IEEE Trans. Smart Grid* **2017**, *8*, 2198–2206. [CrossRef]
2. Torres, B.S.; Ferreira, L.R.; Aoki, A.R. Distributed Intelligent System for Self-Healing in Smart Grids. *IEEE Trans. Power Deliv.* **2018**, *33*, 2394–2403. [CrossRef]
3. Reiz, C.; Pereira, C.E.M.; Leite, J.B. A Self-Healing Strategy for Modern Distribution Networks. *Energies* **2023**, *16*, 5890. [CrossRef]
4. Kezunovic, M. Smart Fault Location for Smart Grids. *IEEE Trans. Smart Grid* **2011**, *2*, 11–22. [CrossRef]
5. Wang, X.; Gao, J.; Wei, X.; Guo, L.; Song, G.; Wang, P. Faulty Feeder Detection Under High Impedance Faults for Resonant Grounding Distribution Systems. *IEEE Trans. Smart Grid* **2023**, *14*, 1880–1895. [CrossRef]
6. Deng, F.; Xu, F.; Feng, S.X.; Zeng, X.J.; Huang, Y.F.; Zeng, Z.; Zhang, Z. Research on High Impedance Fault Detection Method Based on Energy Distribution Characteristics of Traveling Wave Full Waveform. *Proc. CSEE* **2022**, *42*, 8177–8190.
7. Li, Z.; Li, J. Intelligent Resistance Grounding Method of Neutral Point Based on Single-phase Grounding Fault Zone of Distribution Network. *Power Syst. Autom.* **2019**, *43*, 145–150.
8. Wang, Y.; Yin, X.; Xu, W.; Yin, X.; Wen, M.; Jiang, L. Fault Line Selection in Cooperation with Multi-Mode Grounding Control for Updates the Floating Nuclear Power Plant Grid. *Prot. Control. Mod. Power Syst.* **2020**, *5*, 1–10. [CrossRef]
9. Chen, X.J.; Yao, Y.; Han, Y.F.; Pei, Z.X.; Pan, M.M.; Shao, W.Q.; Zhang, Y.; Zhang, S. Fault Line Selection Method Based on Model Identification for Flexible Grounded Distribution System. In Proceedings of the 2023 4th International Conference on Advanced Electrical and Energy Systems (AEES), Shanghai, China, 1–3 December 2023; pp. 190–194.
10. Wang, X.Q.; Shao, W.Q.; Zhao, Y.F.; Li, Z.M. A Method of Faulty Line Selection for the Flexible Grounding System Based on the Parallel Resistance Identification. In Proceedings of the 2023 IEEE International Conference on Power Science and Technology (ICPST), Kunming, China, 5–7 May 2023; pp. 103–107.
11. Liu, K.; Zhang, S.; Zhao, J.; Zhang, C.; Liu, B. Reliability-Enhanced Hybrid Grounding System Based on Active Neutral-Point Voltage Regulator and Low-Resistance. *IEEE Trans. Power Deliv.* **2021**, *36*, 3270–3273. [CrossRef]
12. Zeng, H.; Yang, P.; Cheng, H.; Xin, J.; Lin, W.; Hu, W.; Wan, M.; Li, Y.; Wu, H. Research on Single-Phase to Ground Fault Simulation Base on a New Type Neutral Point Flexible Grounding Mode. *IEEE Access* **2019**, *7*, 82563–82570. [CrossRef]
13. Wang, P.; Chen, B.; Zhou, H.; Cuihua, T.; Sun, B. Fault Location in Resonant Grounded Network by Adaptive Control of Neutral-to-Earth Complex Impedance. *IEEE Trans. Power Deliv.* **2018**, *33*, 689–698. [CrossRef]
14. Wang, P.; Chen, B.; Tian, C.; Sun, B.; Zhou, M.; Yuan, J. A Novel Neutral Electromagnetic Hybrid Flexible Grounding Method in Distribution Networks. *IEEE Trans. Power Deliv.* **2017**, *32*, 1350–1358.
15. Xue, Y.; Chen, X.; Song, H.; Xu, B. Resonance Analysis and Faulty Feeder Identification of High-Impedance Faults in a Resonant Grounding System. *IEEE Trans. Power Deliv.* **2017**, *32*, 1545–1555. [CrossRef]
16. Fang, Y.; Xue, Y.D.; Song, H.M. Transient energy analysis and faulty feeder identification method of high impedance fault in the resonant grounding system. *Proc. CSEE* **2018**, *38*, 5636–5645.
17. Costa, F.B.; Souza, B.A.; Brito, N.S.D.; Silva, J.A.C.B.; Santos, W.C. Real-Time Detection of Transients Induced by High-Impedance Faults Based on the Boundary Wavelet Transform. *IEEE Trans. Ind. Appl.* **2015**, *51*, 5312–5323. [CrossRef]
18. Zhang, C.; Liu, K.; Zhang, S.; Liu, B.; Zhao, J. Discrete Fréchet Distance Algorithm-Based Faulty Feeder Selection Method for Flexible Grounding System in Distribution Networks. In Proceedings of the 2021 IEEE Texas Power and Energy Conference (TPEC), College Station, TX, USA, 2–5 February 2021; pp. 1–6.
19. Wang, B.; Cui, X. Nonlinear Modeling Analysis and Arc High-Impedance Faults Detection in Active Distribution Networks with Neutral Grounding via Petersen Coil. *IEEE Trans. Smart Grid* **2022**, *13*, 1888–1898. [CrossRef]
20. Wang, B.; Cui, X. Detection Method of Arc High Resistance Grounding Fault in Resonant Grounding System Based on Dynamic Trajectory of Volt-ampere Characteristic. *Proc. CSEE* **2021**, *41*, 6959–6968.
21. Wei, X.; Wang, X.; Gao, J.; Yang, D.; Wei, K.; Guo, L.; Wei, Y. Faulty Feeder Identification Method Considering Inverter Transformer Effects in Converter Dominated Distribution Network. *IEEE Trans. Smart Grid* **2023**, *14*, 939–953. [CrossRef]

22. Zhou, Y.; Zhang, J.; Ba, Y.; Ma, H.; Wu, L.; Zhu, J. A Fault Line Selection Method for Small Current Grounding Systems Based on Zero-Mode Transient Information. In Proceedings of the 2022 China International Conference on Electricity Distribution (CICED), Changsha, China, 7–8 September 2022; pp. 1414–1418.
23. Zheng, Q.; Xinyi, Z.; Matloob, B. Fault Location Method of Single-phase to Earth Fault in Distribution Network Based on The Variance of Three-phase Asymmetrical Current Fault Component. In Proceedings of the 2020 7th International Forum on Electrical Engineering and Automation (IFEEA), Hefei, China, 25–27 September 2020; pp. 305–311.
24. Liu, P.; Du, S.; Sun, K.; Zhu, J.; Xie, D.; Liu, Y. Single-Line-to-Ground Fault Feeder Selection Considering Device Polarity Reverse Installation in Resonant Grounding System. *IEEE Trans. Power Deliv.* **2021**, *36*, 2204–2212. [CrossRef]
25. Pang, Q.; Liu, Y.; Li, X. Current polarity comparison-based fault location for active distribution network. *Power Syst. Prot. Control.* **2018**, *46*, 101–108.
26. Barik, M.A.; Gargoom, A.; Mahmud, M.A.; Haque, M.E.; Al-Khalidi, H.; Oo, A.M.T. A Decentralized Fault Detection Technique for Detecting Single Phase to Ground Faults in Power Distribution Systems with Resonant Grounding. *IEEE Trans. Power Deliv.* **2018**, *33*, 2462–2473. [CrossRef]
27. Liu, B.W.; Zeng, X.J.; Ma, H.Z.; Wang, C.Y.; Wan, Z.X. Equivalent Model and Grounding Fault Detection Method for Distribution Lines with Asymmetry Parameters. *Autom. Electr. Power Syst.* **2022**, *46*, 159–167.
28. Zhao, J. Research on the Application of Dynamic Grounding Device for Neutral Point of Distribution Network. Master's Thesis, Changsha University of Science & Technology, Changsha, China, April 2016.
29. Dragomiretskiy, K.; Zosso, D. Variational Mode Decomposition. *IEEE Trans. Signal Process.* **2014**, *62*, 531–544. [CrossRef]
30. Gilles, J. Empirical wavelet transform. *IEEE Trans. Signal Process.* **2013**, *61*, 3999–4010. [CrossRef]
31. Thirumala, K.; Umarikar, A.C.; Jain, T. Estimation of single-phase and three-phase power-quality indices using empirical wavelet transform. *IEEE Trans. Power Deliv.* **2014**, *30*, 445–454. [CrossRef]
32. Wu, S.; Ji, S.; Zhu, L.; Dai, S.; Gao, L.; Dang, Y.; Zheng, L.; Sun, J.; Liang, N. Comprehensive Prediction Method of Converter Transformer Vibration State Parameters Based on Multiple Information Decomposition and Time-varying Weight Combination. *Proc. CSEE* **2020**, *40*, 7792–7805.

*energies*

*Article*

# Decentralized Robust Power System Stabilization Using Ellipsoid-Based Sliding Mode Control

**Ehab H. E. Bayoumi [1,*], Hisham M. Soliman [2] and Farag A. El-Sheikhi [3]**

1 Department of Electrical Engineering, Faculty of Engineering and Technology, University of Botswana, Gaborone UB0022, Botswana
2 Department of Electrical Power Engineering, Faculty of Engineering, Cairo University, Giza 12613, Egypt; mohammedhisham@eng.cu.edu.eg
3 Department of Electrical and Electronics Engineering, Istanbul Esenyurt University, Istanbul 34517, Turkey; farag.elsheikhi@gmail.com
* Correspondence: ehab.bayoumi@gmail.com

**Abstract:** Power systems are naturally prone to numerous uncertainties. Power system functioning is inherently unpredictable, which makes the networks susceptible to instability. Rotor-angle instability is a critical problem that, if not effectively resolved, may result in a series of failures and perhaps cause blackouts (collapse). The issue of state feedback sliding mode control (SMC) for the excitation system is addressed in this work. Control is decentralized by splitting the global system into several subsystems. The effect of the rest of the system on a particular subsystem is considered a disturbance. The next step is to build the state feedback controller with the disturbance attenuation level in mind to guarantee the asymptotic stability of the closed-loop system. The algorithm for SMC design is introduced. It is predicated on choosing the sliding surface correctly using the invariant ellipsoid approach. According to the control architecture, the system motion in the sliding mode is guaranteed to only be minorly affected by mismatched disturbances in power systems. Furthermore, the proposed controllers are expressed in terms of Linear Matrix Inequalities (LMIs) using the Lyapunov theory. Lastly, an IEEE test system is used to illustrate how successful the suggested approach is.

**Keywords:** excitation control; sliding mode control; linear matrix inequalities optimization; invariant-ellipsoid method; unmatched uncertainties

**Citation:** Bayoumi, E.H.E.; Soliman, H.M.; El-Sheikhi, F.A. Decentralized Robust Power System Stabilization Using Ellipsoid-Based Sliding Mode Control. *Energies* **2024**, *17*, 4249. https://doi.org/10.3390/en17174249

Academic Editor: Ahmed Abu-Siada

Received: 18 July 2024
Revised: 19 August 2024
Accepted: 21 August 2024
Published: 25 August 2024



## 1. Introduction

### 1.1. Survey of the Related Publications

One of the most challenging difficulties with interconnected power networks is ensuring the power system's security and reliability [1]. Voltage instability, rotor-angle instability and frequency instability are three types of instability that may occur when a power system is in operation [1]. The load frequency control under magnitude and generation rate constraints imposed in practice are given in [2]. Rotor-angle instability occurs when the angle difference between the rotors of distinct generators in a system exceeds a particular limit owing to an unexpected transient occurrence (uncertainties), which may cause power oscillations to rise and perhaps lead to a complete system failure [3]. Rotor-angle stability is of paramount importance to power engineers to keep synchronous generators in synchronism. The uncertainties can be internal (plant changes due to, e.g., load changes) or external, represented by deterministic or stochastic models. The stochastic uncertainty can result from, e.g., random wind speed (or temperature) changes which lead to changes in phase conductors' spacing and consequently random changes in the line reactance (resistance) of a transmission line. There are generally four types of power system oscillations, the most common of which is local-machine oscillation. This oscillation type happens when one or more synchronous generators in a particular power station swing jointly against the entire power system or load center, typically at a frequency of 0.7–3 Hz. Moreover, an inter-area oscillation takes place when a group of generators in one area swing against another group of generators in a different area, typically at a frequency of 0.1–0.7 Hz [1–3].

Disruptions to both large and small signal stability may have a substantial impact on the power system. Synchronous generators are supplied with an Automatic Voltage Regulator (AVR) to regulate the terminal voltage of the generator [1,3]. Increasing the gain in the loop of the excitation channel reduces the steady-state error while potentially introducing instability. When the AVR is properly calibrated, it can reduce system oscillation. An additional stabilizing signal (generated by a power system stabilizer PSS [1,3]) can also be added to the excitation channel to dampen systems' oscillations. Several studies have investigated the degree to which the Automatic Voltage Regulator (AVR) and Power System Stabilizer (PSS) may significantly impact the stability of a power system. In essence, the AVR and PSS have an inversely related relationship. The AVR's high gain and quick reaction harm power system stability while enhancing transient stability, and vice versa. On the other hand, the Power System Stabilizer (PSS) decreases the capacity of the system to maintain stability by over-riding the voltage signal to the exciter and increasing the stability of oscillations [4]. Nevertheless, the coordination of AVR and PSS design may be used to provide optimum power stability for the investigation of both transient and oscillation stability [4]. Furthermore, the operations of both devices are intricately linked.

Power systems are by nature subject to low-frequency oscillations that may increase to cause system separation which causes a great loss of the national economy if not properly quenched. The system's uncertainty can be deterministic or stochastic. There are many methods to design the PSS/AVR systems for deterministic uncertainties: (1) The conventional PSS, which is commonly used in industry. Its structure can be single or double-stage lead-lag with one or two inputs, proportional–integral–derivative (PID) [5], or multi-band [6]. (2) Robust methods: Kharitonov's theorem [7], Qualitative Feedback Theorem (QFT) [8], Sliding Mode Control (SMC) [9], $H\infty$ for disturbance attenuation [10], (3) adaptive PSS [11], (4) intelligent-based PSS, in which many evolutionary techniques exist, Genetic Algorithm (GA), Tabu search, particle swarm optimization (PSO), simulated annealing [12], neural networks [13] and Fuzzy Logic for damping interarea oscillations [14]. Adaptive fuzzy SMC is given in [15]. Among many of the above techniques, SMC is a nonlinear control and one of the most effective control methodologies for nonlinear power system stabilization due to its outstanding robustness against uncertainties. The control action of the SMC is discontinuous. On the other hand, the SMC is a well established control method for applications in nonlinear plants because of its low sensitivity to parameter variations and external disturbances. The SMC is applied in stabilizing a single machine connected to an infinite bus as well as for multi-machine systems. Recently, the integral SMC methodology is proposed for power systems stabilization. Note that the conventional SMC is robust with respect to matched perturbation only while in practice, and power systems can be affected by unmatched perturbations. The SMC against mismatched uncertainties will be tackled in this paper.

The above discussion deals with power systems subject to deterministic uncertainties. Stochastic uncertainties in power systems prevent the modeling of stochastic stability using ordinary differential equations (ODEs) because of the rapid and abrupt changes in slope at the corners of the external stochastic disturbance. This might lead to an indeterminate derivative of the ODE. Stochastic differential or difference equations are used to explain the behavior of system dynamics when subjected to random variations. There is a lack of research on stochastic stability for power systems, as shown by the limited number of studies conducted [16–18]. A Markov jump can be used to model the stochastic changes in the topology (e.g., a power system's transmission line hit by lightning strikes, associated with the opening and closing of circuit breakers. The line reactance, which is influenced by the distance between phase conductors, varies as a result of random variations in wind speed). These fluctuations are considered to be a stochastic external disturbance. The observer-based output feedback excitation control using the invariant ellipsoid method is given in [19]. Ref. [20] considers the stochastic stability in power systems with time delay.

Although controlling large power systems using one hub computer (centralized control) provides a firm control grip, it has the following limitations: (1) if the hub fails, complete loss of control occurs, (2) it requires an expensive communication network to transmit the states to the hub, and (3) it is affected by the data packet loss and time delay, which degrades system performance or even cause instability. To avoid these limitations, this paper adds the following challenges in the introduction of decentralized stabilization of a multi-machine power system.

### *1.2. Contributions*

- Control decentralization is achieved by splitting the multi-machine system into subsystems. For each machine, a controller is installed using only the local states. For a specific machine, the influence of the rest of the system is seen as an external disturbance that must be minimized.
- The SMC design for power system excitation control is based on the methodology described in [9]. It is predicated on choosing the sliding surface correctly using the invariant ellipsoid approach. Unlike the conventional SMC, which cannot eliminate the effects of unmatched disturbances, the proposed SMC ensures minimizing the effects of the unmatched disturbances on system state trajectories in a sliding mode.
- The ellipsoidal SMC method in [9] is extended to a decentralized excitation stabilization design. The proposed decentralized design is unlike the conventional centralized control, which requires a costly communication network associated with its time-delay that might cause system instability.
- The proposed design can be applied to large power systems because of its decentralized structure. This is accomplished by decomposing the large system into small size subsystems for which a controller can be easily obtained for each.
- A simple design process that does not call for costly computational techniques.
- Using the features of Lyapunov functions, the closed-loop stability is ensured.
- The theoretical conclusions are validated by the simulation results on a multi-machine IEEE test system.

### *1.3. Notations*

Standard notations are used. $(.)'$ indicates the transpose of a vector or matrix. A symmetric positive (negative) definite matrix is denoted by $p > 0$ $(< 0)$. $(M + N + *)$ is the notation for $(M + N + M' + N')$. Furthermore, the symbol (*) in a matrix denotes the symmetric portion, i.e., $\begin{bmatrix} \boldsymbol{M} & \boldsymbol{N} \\ * & \boldsymbol{Z} \end{bmatrix}$ **means** $\begin{bmatrix} \boldsymbol{M} & \boldsymbol{N} \\ \boldsymbol{N\prime} & \boldsymbol{Z} \end{bmatrix}$. The symbols 0 and I stand for the zero matrix and the identity matrix, respectively. The time derivative of $x$ is denoted by $\dot{x}$.

The order of the paper is as follows. The earlier research on power system stabilization is presented in Section 1. The system modeling and problem are formulated in Section 2. The ellipsoid approach of state feedback sliding mode control design is shown in Section 3. Results of a benchmark example simulation are provided in Section 4. Section 5 contains the conclusions.

## 2. Power System Model and Problem Formulation

For small perturbations, the dynamics of an N+1 machine system (with machine#N+1 taken as a reference) can be linearized around an operating point. The dynamics of the rest N machines can be modeled by the state equation

$$\dot{\hat{\boldsymbol{x}}} = \hat{\boldsymbol{A}}\hat{\boldsymbol{x}} + \hat{\boldsymbol{B}}\hat{\boldsymbol{u}} \tag{1}$$

The selected test system is the four-machine, 11-bus two-area IEEE test power system, Figure 1. The test system has two completely symmetrical areas connected by two 230 kV transmission lines spanning 220 km. Every region is furnished with two identical round rotor generators, each having a rating of 20 KV/900 MVA. The synchronous machines possess similar characteristics, with the exception of their inertia. In Area 1, the inertia is H = 6.5 s, whereas in Area 2 it is H = 6.175 s. The loads are shown as constant impedances and distributed across the two sections, as seen in Figure 1. The complete parameters are provided in [1].

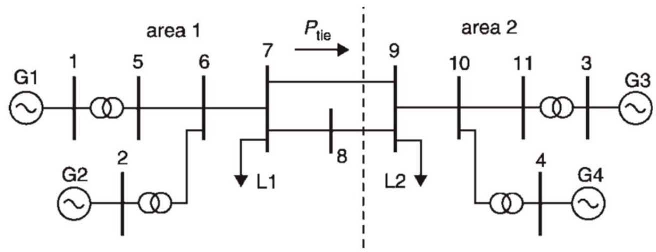


**Figure 1.** IEEE Two-areas four-machines, 11-bus test power system.

For the benchmark system *N* + 1 = 4, with machine # 4 taken as the reference, the dynamics of the three rest machines, Equation (1) becomes $\hat{x} = \begin{bmatrix} x_1' & x_2' & x_3' \end{bmatrix}'$, **similarly for** $\hat{u} = \begin{bmatrix} u_1 & u_2 & u_3 \end{bmatrix}'$. The state vector and the control input of each machine is $\begin{bmatrix} \Delta\delta & \Delta w & \Delta E_q' \end{bmatrix}$ and $E_f$, **respectively**. Where Δδ: rotor-angle deviation, rad, Δω: speed deviation, pu, $\Delta Eq'_{,}$: deviation in the quadrature axis transient voltage, pu, $\Delta E_f$: deviations in the field voltage, pu.

The matrices $\hat{A} = \begin{bmatrix} A_1 & A_{12} & A_{13} \\ A_{21} & A_2 & A_{23} \\ A_{31} & A_{32} & A_3 \end{bmatrix}$, $\hat{B} = \textbf{block diag}\begin{bmatrix} B_1 & B_2 & B_3 \end{bmatrix}$ The numerical values of the above matrices are given in Appendix A. To achieve control decentralization, system (1) is split into three subsystems, and the dynamics for each are as follows:

$$\dot{x} = Ax + Bu + Dw, x(0) = x_0, w = \hat{x}, \tag{2}$$

Note that, for a particular subsystem, the impact of the rest on it is considered an external disturbance whose effect has to be attenuated. For machine# i, i = 1, 2, ...N, (N = three machines in our case)

$$A = A_i, B = B_i, D = D_i = \begin{bmatrix} A_{i1} & A_{i2} & \ldots 0_{ii} & \ldots .A_{iN} \end{bmatrix}, w = \hat{x}$$

where for each machine $x(t)$, $u(t)$, $w(t)$ are the state, control input, and the external disturbance vectors of dimension n, m, and k (k = n. N) respectively. The pairs (***A***, ***B***), and (***A***, ***C***) are assumed to be controllable and observable respectively. The disturbance is unknown but bounded as follows:

$$w' Q_w w \le w_0 + x' Q_x x \tag{3}$$

where the positive definite matrices $Q_w$, $Q_x$, and positive scalar $w_0$ are given.

Note that the external disturbance for power systems is unmatched (the matrix D does not lie in the range (***B***, i.e., $D \neq B.\Phi$, $\Phi$ = any matrix).

The decentralized state feedback control for each machine using its local states is

$$u = Kx \tag{4}$$

The controller gain ***K*** must be designed to stabilize the benchmark system subject to the constraint (3). SMC is selected for the controller (4) because of its paramount robustness against system uncertainties.

## 3. SMC by the Invariant Ellipsoid Method

The invariant ellipsoid method is a recently developed robust control method [9]. The method stabilizes linear and a class of nonlinear systems against plant uncertainties and attenuates the external disturbance effects. It has many applications, e.g., microgrids control [21] and synchronous motor position control [22].

The structure of SMC to stabilize perturbed systems is [23]

$$\boldsymbol{u}(\boldsymbol{t}) = -\left(\widetilde{\boldsymbol{C}}\boldsymbol{B}\right)^{-\mathbf{1}}\widetilde{\boldsymbol{C}}\boldsymbol{A}\boldsymbol{x}(\boldsymbol{t}) - \boldsymbol{M}(\boldsymbol{x}(\boldsymbol{t})).\mathbf{sign}\left[\widetilde{\boldsymbol{C}}\boldsymbol{x}(\boldsymbol{t})\right], \boldsymbol{M}(\boldsymbol{x}(\boldsymbol{t})) > \mathbf{0} \tag{5}$$

Here, the matrix $\widetilde{\boldsymbol{C}} \in \mathrm{R}^{\mathrm{m}\times\mathrm{n}}$ is a sliding surface such that $\det(\widetilde{\boldsymbol{C}}\boldsymbol{B}) \neq 0$ and the positive control gain function $\boldsymbol{M}(\boldsymbol{x})$ has the form

$$\boldsymbol{M}(\boldsymbol{x}) = \sqrt{(\boldsymbol{\alpha} + \boldsymbol{x}'\boldsymbol{R}\boldsymbol{x})}, \tag{6}$$

where the scalar $\alpha$ and the positive definite matrix R are bounded control parameters as $\boldsymbol{\alpha} < \boldsymbol{\alpha}_{max}$, $\|\boldsymbol{R}\| \leq \boldsymbol{\beta}$, $\boldsymbol{\alpha}$, $\boldsymbol{\beta}$ are scalars > 0. Such control can eliminate the disturbance if it lies in the range (B) and the is termed matched disturbance.

In power systems, the matching condition is not satisfied. In this scenario, the system (2) may have mismatched disturbances which cannot be suppressed using the traditional sliding mode control method. So, the primary challenge is creating a sliding mode control that uses the invariant ellipsoid approach to reduce (in a sense) the impacts of the unmatched disturbance [9].

### *3.1. Invariant Ellipsoid Method [9]*

**Definition 1.** *The ellipsoid*

$$\boldsymbol{E}(\boldsymbol{P}) = \left\{\boldsymbol{x} \in \boldsymbol{R}^{\boldsymbol{n}} : \boldsymbol{x}'\boldsymbol{P}^{-1}\boldsymbol{x} < \mathbf{1}\right\}, \boldsymbol{P} > \mathbf{0} \tag{7}$$

If any state trajectory of the system initialed inside the ellipsoid remains inside it for all time instants $t > 0$, then the ellipsoid centered at the origin with a configuration matrix $P$ is said to be state-invariant for the system (2) with the disturbances (3); however, a trajectory starting outside the ellipsoid is attracted to this ellipsoid as time evolves (so the term attracting ellipsoid). Note that the Lyapunov function in (7) is so selected to allow for obtaining the ellipsoidal design of the proposed control, as will be seen later.

One way to think about the invariant ellipsoid is as a feature of how unmatched perturbations (3) affect the system (2). The smallest (in a sense) invariant ellipsoid (7) in the SMC application offers a "minimum deviation of any possible trajectory from the origin in a sliding mode". The primary issue under consideration is creating a control that will allow any system (2) trajectory to converge into the previously established "minimum invariant ellipsoid". For these kinds of optimization problems, the standard criterion is minimal $\mathrm{tr}(\mathrm{P}^{-1})$. The sum of the squares of the semi-axes of the ellipsoid is described by the trace of the matrix $\mathrm{P}^{-1}$.

The invariant ellipsoid for the linear disturbed control system (using the Linear Matrix Inequalities optimization) is used to obtain an appropriate sliding surface $\widetilde{\boldsymbol{C}}\boldsymbol{x} = \mathbf{0}$, [9].

### *3.2. System Decomposition and Main Result*

Since rank($\boldsymbol{B}$) = m, the matrix $\boldsymbol{B}$ can be decomposed as follows:

$$\boldsymbol{B} = \begin{bmatrix} \boldsymbol{B_1} \\ \boldsymbol{B_2} \end{bmatrix}$$

where the dimensions of $B_1$, $B_2$ are (n−m).m, and m. m, respectively, with det($B_2$) $\neq \mathbf{0}$. In this case, there exists the nonsingular transformation [24]

$$\begin{bmatrix} x_1 \\ x_2 \end{bmatrix} = Gx, \textbf{where } G = \begin{bmatrix} I_{n-m} & -B_1B_2^{-1} \\ 0 & B_2^{-1} \end{bmatrix}$$

That reduces system (2) to the form

$$\left.\begin{aligned} \dot{x}_1 &= A_{11}x_1 + A_{12}x_2 + D_1 w \\ \dot{x}_2 &= A_{21}x_2 + A_{22}x_2 + u + D_2 w \end{aligned}\right] \tag{8}$$

where the dimensions of $x_1$, $x_2$, are n−m, and m respectively. The matrices $A_{11}..A_{22}$ are of appropriate dimensions, and there should be no confusion with those given in the Appendix. Hence

$$\begin{bmatrix} A_{11} & A_{12} \\ A_{21} & A_{22} \end{bmatrix} = GAG^{-1} \textbf{and} \begin{bmatrix} D_1 \\ D_2 \end{bmatrix} = GD$$

where the dimensions of $D_1$, and $D_2$ are (n−m).k, and m.k respectively. Note that if the system (2) is controllable, then $\{A_{11}, A_{12}\}$ is also controllable [24]. The following theorem is derived in [9]

**Theorem 1.** *The solution* $(\alpha,\ \tau,\ \delta,\ L,\ Y,\ X,\ Z)$ *of the minimization problem*

$$\textit{minimize trace}(Z)$$

Subject to the following inequality constraints

$$\begin{bmatrix} \beta^2 I_n & * \\ R & I_n \end{bmatrix} \geq 0, R \geq \frac{\alpha}{w_0} Q_x,$$
$$0 < \alpha \leq \alpha_{max},$$

$$\begin{bmatrix} (A_{11}X - A_{12}Y + {}^*) + \tau X & * & * \\ D_1' & -\frac{\tau}{w_0}Q_w & * \\ \begin{bmatrix} X \\ -Y \end{bmatrix} & 0 & -\frac{w_0}{\tau}Q_x^{-1} \end{bmatrix} < 0,$$

$$\begin{bmatrix} X & * \\ \begin{bmatrix} X \\ -Y \end{bmatrix} & GZG' \end{bmatrix} \geq 0,$$

$$\begin{bmatrix} \frac{\alpha}{w_0}Q_w & * \\ GD & \begin{bmatrix} \delta.X & * \\ 0 & L \end{bmatrix} \end{bmatrix} > 0,$$

$$\begin{bmatrix} \frac{1}{\delta}X & * \\ Y & I_m - L \end{bmatrix} \geq 0$$

The solution of the above theorem provides the system's minimum invariant ellipsoid (7). Moreover, the SMC is given by (5), (6), where the sliding surface is $\overset{\sim}{C} = \left(YX^{-1}, I_m\right)G$. The above minimization problem can be solved using any gradient-free algorithm, e.g., the particle swarm optimization.

The above theorem is solved using the MATLAB LMI toolbox, yalmip interface, and sedumi solvers [25–27] (assuming $\alpha_{max} = 100, \beta_{max} = 7, Q_{w0} = I, Q_x = I, w_0 = 0.1$) to obtain the decentralized excitation control with the sliding surfaces in Table 1. The MATLAB LMI toolbox is selected for solving the above optimization because it is the easiest and most productive software environment for engineers and scientists. For each machine, u(t) is the scalar sliding mode controller of the form (5).

**Table 1.** Proposed design.

| Machine # | $\alpha$ | $R$ | Sliding surface $\tilde{C}$ |
|---|---|---|---|
| 1 | 0.6592 | [6.8119, $-1.0325 \times 10^{-13}$, $6.6887 \times 10^{-13}$<br>$-1.0325 \times 10^{-13}$, 6.8119, $-7.6312 \times 10^{-13}$<br>$6.6887 \times 10^{-13}$, $-7.6312 \times 10^{-13}$, 6.8119] | [−0.98782 −99.5610 8] |
| 2 | 0.58687 | [6.4499, $6.4696 \times 10^{-13}$, $8.0441 \times 10^{-13}$<br>$6.4696 \times 10^{-13}$, 6.4499, $-4.0267 \times 10^{-13}$<br>$8.0441 \times 10^{-13}$, $-4.0267 \times 10^{-13}$, 6.4499] | [−24.71 −42.9985 8] |
| 3 | 0.63266 | [6.6725, $2.7361 \times 10^{-12}$, $-7.2498 \times 10^{-12}$<br>$2.7361 \times 10^{-12}$, 6.6725, $-3.1488 \times 10^{-12}$<br>$-7.2498 \times 10^{-12}$, $-3.1488 \times 10^{-12}$, 6.6725] | [−72.22 −109.310 8] |

Note that the merits of the proposed decentralized control are not without a price. The severity of decentralization constraint may result in an infeasible solution to the above LMI optimization problem. However, this does not imply system instability because the theorem's condition is only sufficient.

## 4. Simulation Validation

The simulation results are provided to verify the effectiveness and resilience of the suggested technique in a comparison analysis conducted utilizing a conventional sliding mode excitation control. All simulation results were performed in MATLAB using the ode23 solver with a relative tolerance of $10^{-3}$. To avoid the chattering effect, the sign function in (5) is substituted by a saturation function [24].

### 4.1. Simulation of Multi-Machine Power System

To verify the improvement in stability resulting from the suggested stabilizer, a cleared three-phase fault test is conducted which results in rotor-angle deviation $x_0$ = [0.87, 0, 0,0.6, 0, 0, 0.07, 0, 0]′.

The following three scenarios of operation were examined: the condition of a normal load, a light load, and a heavy load. Once the fault is cleared, the controller efficiently facilitates the system in rapidly attaining a stable operational state.

At nominal load, Figure 2 shows that the suggested approach provides superior control performance than conventional SMC in terms of settling time and damping effect. The proposed SMC also provides oscillations of fewer magnitudes and frequencies than the conventional SMC. This results in less fatigue and longer life for the generators' rotors. Note that the control signal of the proposed design does not violate the permissible range, ±5 p.u, whereas the conventional signal does.

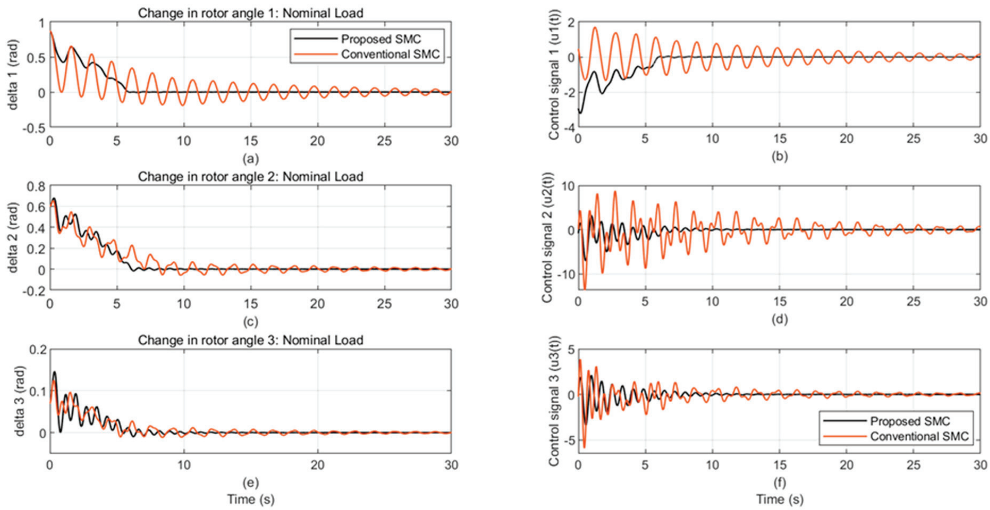


**Figure 2.** Rotor-angle deviations and control input in nominal load case. (**a**,**b**) rotor angle and control signal of machine 1 respectively, (**c**,**d**) rotor angle and control signal of machine 2 respectively, (**e**,**f**) rotor angle and control signal of machine 3 respectively.

### *4.2. Robustness Assessment*

To assess the robustness of the suggested stabilizer, the power system is tested during heavy load operation (Figure 3) and light load operation (Figure 4). These tests demonstrate the improved performance of the proposed controller in a multi-machine power system compared to the traditional SMC controller.

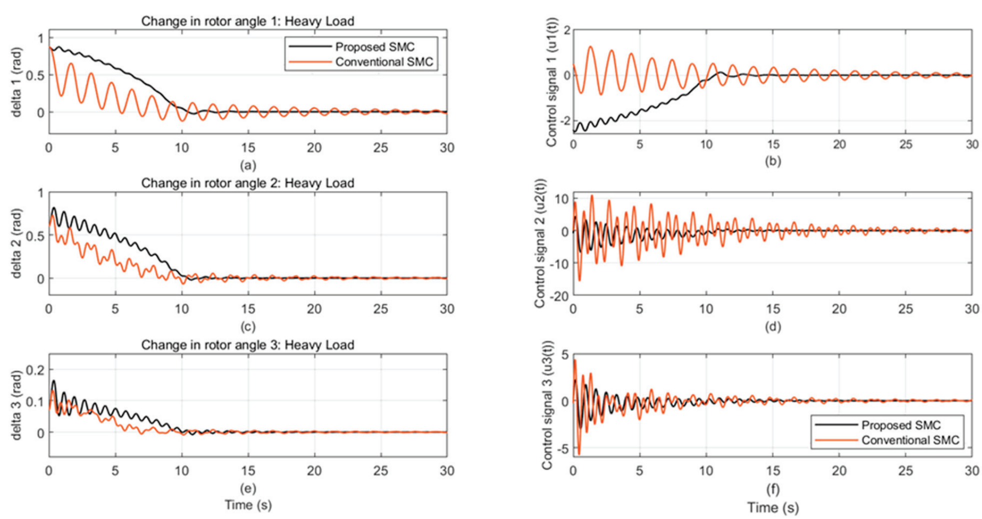


**Figure 3.** Rotor-angle deviations and control input in heavy load case. (**a**,**b**) rotor angle and control signal of machine 1 respectively, (**c**,**d**) rotor angle and control signal of machine 2 respectively, (**e**,**f**) rotor angle and control signal of machine 3 respectively.

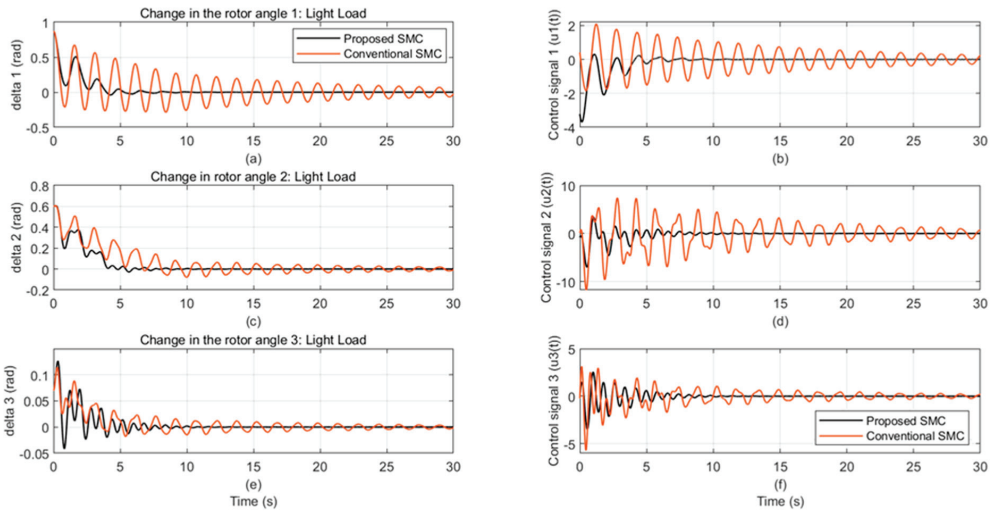


**Figure 4.** Rotor-angle deviations and control input in light load case. (**a**,**b**) rotor angle and control signal of machine 1 respectively, (**c**,**d**) rotor angle and control signal of machine 2 respectively, (**e**,**f**) rotor angle and control signal of machine 3 respectively.

This article utilizes several operating points to showcase the efficacy of the suggested control method in mitigating oscillations after a significant disturbance on a power system. The proposed control method offers improved transient response and enhanced resilience compared to traditional sliding mode control (SMC).

Note that the above simulations show the superiority of the proposed SMC stabilization against unmatched disturbances over the conventional one. The idea of the ellipsoidal SMC is to force the state trajectory $x(t)$ to be attracted to a very small region (min ellipsoid volume) around the origin and for $x(t)$ to remain despite the existence of the external disturbance.

## 5. Conclusions

This paper presents an innovative control approach for a decentralized power system excitation control. Control decentralization is carried out by splitting the global system into subsystems; for each subsystem, a controller is installed which uses its local states. The effect of the rest of the system on a particular machine is considered as an external disturbance, the effect of which must be minimized. The design is based on the SMC with the invariant-ellipsoid method to attenuate the effects of unmatched external disturbances. The effectiveness of the proposed control method is illustrated with simulations of the IEEE test power system. Different loading conditions are utilized to evaluate the proposed decentralized excitation SMC efficiency, demonstrating superior performance to conventional SMC.

For future work, the applicability of the proposed method to handle unbalanced conditions and dampen oscillations in decentralized power systems is under investigation. Note that the stabilization of distributed generators under unbalanced conditions is given in [28].

**Author Contributions:** Methodology, H.M.S. and E.H.E.B.; software, H.M.S. and E.H.E.B.; validation, H.M.S. and F.A.E.-S.; data curation, E.H.E.B. and F.A.E.-S.; writing—review and editing, H.M.S., E.H.E.B. and F.A.E.-S.; visualization, F.A.E.-S.; supervision, H.M.S. and E.H.E.B. All authors have read and agreed to the published version of the manuscript.

**Funding:** This research received no external funding.

**Data Availability Statement:** The original contributions presented in the study are included in the article, further inquiries can be directed to the corresponding author.

**Conflicts of Interest:** The authors declare no conflicts of interest.

## Appendix A. The Multi-Machine Model

The benchmark state equations at nominal load (tie-line power = 415 MW) is

(i) Machine # 1

$$A_1 = \begin{bmatrix} 0 & 377 & 0 \\ -0.045693 & 0 & -0.089833 \\ -0.14728 & 0 & -0.32082 \end{bmatrix}, B_1 = \begin{bmatrix} 0 & 0 & 0.125 \end{bmatrix}'$$

$$D_1 = \begin{bmatrix} 0 & A_{12} & A_{13} \end{bmatrix}$$

$$\text{where, } A_{12} = \begin{bmatrix} 0 & 0 & 0 \\ 0.045365 & 0 & -0.0031733 \\ 0.11398 & 0 & 0.10123 \end{bmatrix}, A_{13} = \begin{bmatrix} 0 & 0 & 0 \\ -0.0026 & 0 & -0.0126 \\ 0.0082 & 0 & -0.0085 \end{bmatrix}$$

(ii) Machine # 2

$$A_2 = \begin{bmatrix} 0 & 377 & 0 \\ -0.0626 & 0 & -0.1129 \\ -0.1597 & 0 & -0.3632 \end{bmatrix}, B_2 = \begin{bmatrix} 0 & 0 & 0.125 \end{bmatrix}'$$

$$D_2 = \begin{bmatrix} A_{21} & 0 & A_{23} \end{bmatrix}$$

$$\text{where, } A_{21} = \begin{bmatrix} 0 & 0 & 0 \\ 0.0566 & 0 & 0.0237 \\ 0.1024 & 0 & 0.1304 \end{bmatrix}, A_{23} = \begin{bmatrix} 0 & 0 & 0 \\ -0.001 & 0 & -0.0129 \\ 0.0169 & 0 & -0.0017 \end{bmatrix}$$

(iii) Machine # 3

$$A_3 = \begin{bmatrix} 0 & 377 & 0 \\ -0.094 & 0 & -0.1194 \\ -0.2056 & 0 & -0.4063 \end{bmatrix}, B_3 = \begin{bmatrix} 0 & 0 & 0.125 \end{bmatrix}'$$

$$D_3 = \begin{bmatrix} A_{31} & A_{32} & 0 \end{bmatrix}$$

$$\text{where, } A_{31} = \begin{bmatrix} 0 & 0 & 0 \\ 0.0107 & 0 & 0.0028 \\ 0.0183 & 0 & 0.0171 \end{bmatrix}, A_{32} = \begin{bmatrix} 0 & 0 & 0 \\ 0.0106 & 0 & -.0002 \\ 0.024 & 0 & 0.0212 \end{bmatrix}.$$

## References

1. Kundur, P.; Balu, N.J.; Lauby, M.G. *Power System Stability and Control*; McGraw-Hill Education: New York, NY, USA, 1994; Volume 7.
2. Soliman, H.M.; Benzaouia, A.; El-Sheikhi, F.A.; Buyukatak, K. Grid Frequency Stabilization under Magnitude and Generation Rate Constraints. *Int. J. Model. Identif. Control.* **2024**, *44*, 174–180. [CrossRef]
3. Sauer, P.W.; Pai, M.A.; Chow, J.H. *Power System Dynamics and Stability: With Synchro phasor Measurement and Power System Toolbox*; Wiley: Hoboken, NJ, USA, 2017.
4. Dudgeon, G.J.W.; Leithead, W.E.; Dysko, A.; O'Reilly, J.; McDonald, J.R. The effective role of AVR and PSS in power systems: Frequency response analysis. *Power Syst. IEEE Trans.* **2007**, *22*, 1986–1994. [CrossRef]
5. Mrad, F.; Karaki, S.; Copti, B. An adaptive fuzzy-synchronous machine stabilize. *IEEE Trans. Syst. Man Cybern. Part C Appl. Rev.* **2000**, *30*, 131–137. [CrossRef]
6. Sarkar, D.U.; Prakash, T. A Recent Review on Approaches to Design Power System Stabilizers: Status, Challenges and Future Scope. *IEEE Access* **2023**, *11*, 34044–34061. [CrossRef]
7. Rigatos, G.; Siano, P. Design of robust electric power system stabilizers using Kharitonov's theorem. *Math. Comput. Simul.* **2011**, *82*, 181–191. [CrossRef]
8. Garcia-Sanz, M.; Houpis, C.H. *Wind Energy Systems: Control Engineering Design*; CRC Press: Boca Raton, FL, USA, 2012.
9. Poznyak, A.; Polyakov, A.; Azhmyakov, V. *Attractive Ellipsoids in Robust Control*; Springer: Cham, Switzerland, 2014.
10. Boukas, E.; AL-Sunni, F.M. *Mechatronic Systems Analysis, Design and Implementation*; Springer: Berlin/Heidelberg, Germany, 2011.

11. Yaghooti, A.; Buygi, M.O.; Shanechi, M.H.M. Designing coordinated power system stabilizers: A reference model based controller design. *IEEE Trans Power Syst.* **2016**, *31*, 1–11. [CrossRef]
12. Abido, M.A.; Abdel-Magid, Y.L. Optimal design of power system stabilizers using evolutionary programming. *IEEE Trans. Energy Con.* **2002**, *17*, 429–436. [CrossRef]
13. Sarkar, D.U.; Prakash, T. A Neural Network Approach to Design Power System Stabilizer for Damping Power Oscillations. In Proceedings of the 22nd National Power Systems Conference (NPSC), New Delhi, India, 17–19 December 2022.
14. Hussein, T.; Saad, M.S.; Elshafei, A.L.; Bahgat, A. Damping inter-area modes of oscillation using an adaptive fuzzy power system stabilizer. *Electr. Power Syst. Res. Dec.* **2010**, *80*, 1428–1436. [CrossRef]
15. Saoudi, K.; Harmas, M.N. Enhanced design of an indirect adaptive fuzzy sliding mode power system stabilizer for multi-machine power systems. *I.J. Electr. Power Energy Syst.* **2014**, *54*, 425–443. [CrossRef]
16. Ju, P. *Stochastic Dynamics of Power Systems*; Springer: Berlin/Heidelberg, Germany, 2019.
17. Ye, K.; Zhao, J.; Duan, N.; Maldonado, D.A. Stochastic Power System Dynamic Simulation and Stability Assessment Considering Dynamics from Correlated Loads and PVs. *IEEE Trans. Ind. Appl.* **2022**, *58*, 7764–7775. [CrossRef]
18. Lu, Z.; Lu, S.; Xu, M.; Cui, B. A robust stochastic stability analysis approach for power system considering wind speed prediction error based on Markov model. *Comput. Stand. Interfaces* **2021**, *75*, 103503. [CrossRef]
19. Poznyak, A.S.; Alazki, H.; Soliman, H.M. Invariant-set Design of Observer-based Robust Control for Power Systems Under Stochastic Topology and Parameters Changes. *I. J. Electr. Power Energy Syst.* **2021**, *131*, 107112. [CrossRef]
20. Poznyak, A.; Alazk, H.; Soliman, H. Attractive ellipsoidal design for robust stabilization of time-delay stochastic power systems under a series of lightning surges. *Comput. Electr. Eng.* **2024**, *116*, 109228. [CrossRef]
21. Poznyak, A.S.; Soliman, H.M.; Alazki, H.; Bayoumi, E.H.E.; De Santis, M. Decentralized passivity-based voltage tracker for islanded DC-microgrids: Attracting ellipsoid approach. *Energies* **2024**, *17*, 1529. [CrossRef]
22. Bayoumi, E.H.E. Sliding Mode Position Control of Synchronous Motor with Parameters and Load Uncertainties. *Electromotion Sci. J.* **2010**, *17*, 99–106.
23. Edwards, C.; Spergeon, S. *Sliding Mode Control: Theory and Applications*; Taylor and Francis: Abingdon, UK, 1998.
24. Utkin, V.I.; Guldner, J.; Shi, J. *Sliding Modes in Electromechanical Systems*; Taylor and Francis: London, UK, 1999.
25. The MathWorks Inc. *MATLAB, Version: 9.13.0 (R2023b)*; The MathWorks Inc.: Natick, Massachusetts, 2023; Available online: https://www.mathworks.com (accessed on 2 August 2024).
26. Available online: https://yalmip.github.io/ (accessed on 19 August 2024).
27. Available online: https://sedumi.ie.lehigh.edu/?page_id=58 (accessed on 19 August 2024).
28. Jin, P.; Li, Y.; Li, G.; Chen, Z.; Zhai, X. Optimized hierarchical power oscillations control for distributed generation under unbalanced conditions. *Appl. Energy* **2017**, *194*, 343–352. [CrossRef]

*energies*

*Article*

# Research on Self-Recovery Ignition Protection Circuit for High-Voltage Power Supply System Based on Improved Gray Wolf Algorithm

**Jingyi Zhu †, Wanlu Zhu *,†, Haifeng Wei and Yi Zhang**

Department of Automation, Jiangsu University of Science and Technology, Zhenjiang 212000, China; 221210301105@stu.just.edu.cn (J.Z.); whf21@126.com (H.W.); zyi82@126.com (Y.Z.)
* Correspondence: zhuwanlu@just.edu.cn
† These authors contributed equally to this work.

**Abstract:** In order to solve the problems of traditional high-voltage power supply ignition protection circuits, such as non-essential start–stop power supply, a slow response speed, the system needing to be restarted manually, and so on, a high-voltage power supply system self-recovery ignition protection circuit was designed using an IGWO (improved grey wolf optimization) and PID control strategy designed to speed up the response speed, and improve the reliability and stability of the system. In high-voltage power supply operation, the firing discharge phenomenon occurs. Current transformers fire signal into a current signal through the firing voltage value and Zener diode voltage comparison to set the safety threshold; when the threshold is exceeded, the fire protection mechanism is activated, reducing the power supply voltage output to protect the high-voltage power supply system. When the ignition signal disappears, based on the IGWO-PID control of the ignition self-recovery circuit according to the feedback voltage, the DC supply voltage of the high-voltage power supply is adjusted, inhibiting the ignition discharge and, according to the ignition signal, "segmented" to restore the output of the initial voltage. MATLAB/Simulink was used to establish a system simulation model and physical platform test. The results show that the protection effect of the designed scheme is an improvement, in line with the needs of practical work.

**Keywords:** ignition protection circuit; self-recovery; high-voltage power supply; IGWO-PID control

**Citation:** Zhu, J.; Zhu, W.; Wei, H.; Zhang, Y. Research on Self-Recovery Ignition Protection Circuit for High-Voltage Power Supply System Based on Improved Gray Wolf Algorithm. *Energies* **2024**, *17*, 6332. https://doi.org/10.3390/en17246332

Academic Editor: Kumars Rouzbehi

Received: 4 November 2024
Revised: 3 December 2024
Accepted: 5 December 2024
Published: 16 December 2024



## 1. Introduction

With the progress of science and technology and industrial upgrading, the requirements of industrial equipment in power supply systems continue to increase. With the rapid development of power electronics technology, the traditional low-efficiency and large volume of DC power supplies have been unable to meet the high standards of modern industry. High-voltage DC power supplies have gradually become the core of modern industrial equipment due to their advantages of high efficiency, high reliability, and high stability [1–3]. High-voltage DC power supplies adopt new power electronic devices to optimize the design and improve the overall system performance, showing great potential for application in the field of new energy and smart grids, improving energy efficiency, reducing energy loss, and promoting the transformation of the global energy structure. Ensuring efficient energy conversion at the same time as stability and safety in high-voltage DC power supplies has become a key research area. In practical applications, as a high-voltage power supply is generally in a high-voltage loading work state, the operation process will produce surge voltage, sudden current changes, and firing discharge phenomena, affecting the performance of power switching devices, and even burning out the control system, thus triggering a series of safety hazards. In view of this, the design of a set of efficient protection circuits is essential to enhance the reliability of high-voltage power supply systems [4–9].

In traditional high-voltage power supply systems, the design of the ignition protection circuit usually uses a voltage comparator to sample and compare ignition events. When an ignition discharge phenomenon is detected, the circuit immediately cuts off the power supply and triggers an error report from the host computer, and the system needs to restart the power supply to return to the normal operating state, which has obvious limitations in practical applications [10,11]. On the one hand, conventional firing protection circuits tend to unconditionally cut off the power supply when a firing event is detected. This practice may lead to frequent power supply shutdown in the case of frequent occurrence of minor ignition discharges, which not only shortens the life of the switching devices, but also seriously affects the work efficiency. In many engineering applications, minor firing discharges are considered part of normal system operation and do not always require immediate power shutdown. On the other hand, the response speed and bandwidth of voltage comparators limit their ability to quickly detect high-frequency firing events. In high-frequency switching power supplies, firing events may occur very rapidly, and the voltage comparator may not be able to capture these rapidly changing voltage variations in time, resulting in the protection circuitry being unable to respond in a timely manner, leading to insufficiently rapid handling of the firing event and increasing the risk of system damage. In addition, once a firing event occurs, the high-voltage power supply firing protection circuit should have self-recovery capability and be able to automatically return to normal operation after the fault is cleared, which increases the maintenance cost and reduces the reliability and automation of the system [12,13]. It can be said that there are obvious limitations in the response speed, self-recovery ability, and handling of minor ignition events in ignition protection circuits in traditional high-voltage power supply systems.

Ref. [14], on the basis of the design of a traditional high-voltage power supply ignition protection circuit, proposes a relay group and operational amplifier circuit based on the realization of the instantaneous cut-off and delayed recovery of the voltage input in the case of ignition. In addition, the voltage output is regulated by a high-voltage PID circuit to realize the control of the high-voltage power supply. The PID algorithm is widely used in the industrial field for its simple and efficient advantages, but when applied to special systems such as high-voltage power supplies, the overshooting and stability problems are more prominent. Ref. [15] studied a medical X-ray machine power supply system based on an improved BP algorithm; the traditional BP algorithm has the problem of easily falling into local optima during the training process, and an optimization strategy is proposed, aiming to improve the global search ability and convergence speed of the algorithm. By introducing a momentum term and an adaptive learning rate adjustment mechanism, the complex nonlinear problem is effectively dealt with, so as to regulate the high-voltage power supply and reduce the system ripple and voltage rise time. The generalization ability and computational resource consumption of the algorithms in the study still need to be further explored and optimized. Ref. [16] explores the type III loop compensation optimization method for voltage-mode Buck circuits. An optimization strategy based on zero-pole theory is proposed for the stability and dynamic response problems that Buck circuits may encounter in practical applications. Through comparative experiments with traditional compensation methods, the output voltage overshoot of the circuit during sudden load changes is reduced, and the stabilization time of the system is shortened, thus improving the overall performance. The parameter adjustment in the study is inflexible and only holds under specific conditions, and is not universal. Ref. [17] is titled 'Study on the Improvement and Application of Grey Wolf Optimization Algorithm' by Xing Li. Aiming at the problems of accuracy, convergence speed, and the tendency to fall into local optimality, this paper proposes two improvement strategies, which significantly enhance the performance of the algorithm. The article proposes an improved GWO algorithm based on the hunting behavior of spiral bubble nets, which enhances the global and local search ability of the algorithm and improves the convergence speed and accuracy by means of a nonlinearly decreasing convergence factor and the hunting behavior of spiral bubble nets. In addition, for the constrained optimization problem, this paper uses the augmented Lagrange multiplier method to transform the constrained problem into an unconstrained problem and applies the improved GWO algorithm to solve it, verifying the effectiveness of the algorithm. These improvements not only promote the development of the GWO algorithm but also provide new solutions for engineering design, parameter optimization, and other fields.

The IGWO algorithm is a group intelligence-based optimization algorithm that finds optimal solutions by simulating the social hierarchy and hunting behavior of gray wolves. Compared with modern optimization algorithms such as the musical chairs algorithm, spider bee optimization algorithm, and gold panning optimization algorithm, the IGWO algorithm has its unique advantages and limitations. The IGWO algorithm performs well on multimodal and high-dimensional optimization problems, thanks to its ability to simulate the global and local search of gray wolf hunting behavior. In contrast, for the musical chairs algorithm, while it may perform well on some specific problems, its performance is often limited by the spatial structure of the problem and parameter settings. The spider bee optimization algorithm, on the other hand, performs better on continuous space optimization problems, especially when the solution space is smoother. The gold panning optimization algorithm, on the other hand, is known for its simulation of the search behavior during gold panning and is particularly effective for optimization problems with implicit patterns. In terms of efficiency, the IGWO algorithm is able to quickly converge to the global optimal solution by dynamically adjusting the search strategy. The musical chairs algorithm, on the other hand, may require more iterations to achieve the same result, which may be a disadvantage in high-voltage power supply application scenarios. The speed of convergence of the spider bee optimization algorithm and the gold rush optimization algorithm, on the other hand, depends on the specific characteristics of the problem and the tuning of the algorithm parameters. In terms of adaptability, the IGWO algorithm is capable of adapting to different search environments and constraints, making it applicable to a wide range of engineering and scientific problems. In contrast, the musical chairs algorithm and the spider bee optimization algorithm may require algorithmic adaptation for specific problems. The Gold Rush optimization algorithm may not be as widely adaptable as the IGWO algorithm, although it performs well on some problems. However, the IGWO algorithm is relatively complex in terms of parameter tuning and algorithm implementation, which may increase the difficulty of using the algorithm in practical applications. The musical chairs algorithm and the spider bee optimization algorithm usually have simpler parameter structures that are easy to implement and tune. Although the Gold Rush optimization algorithm also has simple parameter settings, its performance may be limited by the problem characteristics. In conclusion, the musical chairs algorithm, the spider bee optimization algorithm, and the gold panning optimization algorithm may provide simpler solutions to particular problems, but they may not be as adaptable and efficient as the IGWO algorithm.

The innovative and academic value of the high-voltage power supply firing device developed in this paper compared with existing devices can be summarized as follows: (1) In this paper, we design more intelligent protection strategies to distinguish between minor firing and abnormal firing events in normal operation to avoid non-essential power interruptions [18–22], in order to solve the non-essential shutdown of high-voltage power supply by the traditional high-voltage power supply firing protection circuit. (2) In this paper, we develop a more accurate and fast ignition detection technology to adapt to the protection needs of high-frequency switching power supplies, and solve the problems of slow and unresponsive response in ignition protection detection of high-frequency high-voltage power supplies. (3) In this paper, we enhance the self-recovery function of the protection circuit to ensure that after the firing fault is cleared, the normal operation of the system can be quickly and automatically restored when the firing event protection circuit shuts down the power supply, enabling the system to return to normal operating conditions in a timely manner.

The protection circuit can accurately identify the ignition phenomenon and achieve uninterrupted operation under the safety threshold. When the safety threshold is exceeded, the DC-side switching element of the front auxiliary power supply is quickly cut off to protect the high-voltage power supply, and then, through the 'segmented' voltage start, it is expected to achieve the effect that the output voltage ripple of the self-recovery circuit of the ignition is less than 1%, and the accuracy of the output voltage and current is as high as 99%.

The remainder of the paper is split into four sections. The first section outlines the general design framework for the self-recovering firing protection circuit, describes the design flow in detail, and highlights key considerations during the design of the IGWO-PID PWM controller. The second section further delves into the subdivided design of the self-recovery lightering protection circuit, including detailed design options for the safety threshold judgment circuit and the control circuit. Meanwhile, this section focuses on the design principles and implementation methods of the IGWO-PID PWM controller. The third section simulates and analyzes the high-voltage power supply self-recovery circuit. Based on the optimized controller parameters, this section demonstrates the voltage output curves and evaluates the application effect and optimization performance of the IGWO optimization algorithm in the high-voltage power supply system to verify its effectiveness in practical engineering. The fourth section describes the process of building an experimental platform on an 80 kV high-voltage power supply product to simulate the actual firing environment and test the firing response and self-recovery performance. The experimental results in this section provide empirical support for the practical application of the self-recovery ignition protection circuit. Overall, the research work in this paper is not only innovative in theory but also has important guiding significance in practical application.

## 2. High-Voltage Power Supply Self-Recovery Ignition Protection Circuit Overall Design

The self-recovering ignition protection circuit overall design block diagram is shown in Figure 1. The DC voltage input by the full-bridge inverter for the AC voltage output flows into the corresponding turns ratio of the high-frequency transformer to obtain a higher AC voltage, and then through the doubling circuit to obtain a high DC voltage; at the same time, in the doubling rectifier module sampling the resistor sampling voltage, current is sampled and transmitted to the MCU; the MCU compares the sampling value with the set value of the feedback adjustment to control the PWM signal drive circuit. The MCU compares the sampling value with the set value for feedback adjustment and controls the PWM signal driving circuit, forming a closed-loop system to stabilize the output of the high-voltage power supply. When the firing phenomenon occurs and the sampling signal is within the normal voltage range, the high-voltage power supply works normally; once the sampling signal exceeds the normal voltage value, the MCU accepts the signal to turn off the high-voltage power supply, and when the firing discharge disappears, the hybrid control circuit of IGWO and PID is turned on [23–25], and the output voltage of the system is restored to the initial set value.

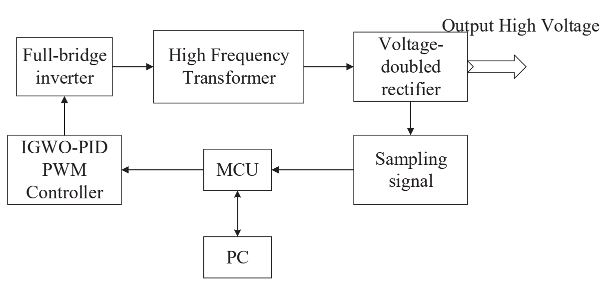


**Figure 1.** Block diagram of the overall design flow of the high-voltage power supply.

To ensure the stability of the output voltage, this paper proposes a PID controller design based on the IGWO of the lighter self-recovery circuit, which is combined with the MCU to perform a "segmented" ramp output voltage [26–30] to achieve the lighter self-recovery circuit of the regulated voltage regulation. This circuit is shown in Figure 2. The circuit design covers several key aspects such as feedback gain, compensation amplification, and PWM. The feedback gain module is responsible for establishing the proportionality between the set voltage and the actual output voltage. By using a resistor divider, the module can realize an accurate mapping between the set voltage and the output voltage, and the position of the feedback point does not change with the output voltage Vout, ensuring that the current in the lower resistor of the feedback module remains constant. Considering the instability that the high-voltage power supply system may exhibit when the frequency exceeds the output filter cut-off frequency, this paper introduces the IGWO-PID controller as the compensation amplification module. Through frequency-domain analysis, this controller not only realizes accurate voltage regulation but also ensures that the total phase shift of the system is always less than 360° within the full operating frequency range, which meets the dynamic response requirements, thus effectively meeting the performance requirements of the system. In the pulse-width modulation link, the proportionality between the duty cycle and the amplitude of the modulated sawtooth wave voltage is precisely controlled. By setting the input and the amplitude of the sawtooth wave voltage, the gain of the link is set to a fixed constant value, ensuring the stability and accuracy of the PWM signal. Through precise feedback gain control, dynamic compensation amplification, and stable pulse-width modulation, the stability and self-recovery capability of the high-voltage power supply system in the face of fluctuations in the input power supply are effectively enhanced.

The program also has some limitations. The gray wolf algorithm is able to adapt to systems with different complexity and nonlinear characteristics by simulating the social hierarchy and hunting behavior of wolves and optimizing the parameters of the PID controller. However, the grey wolf optimization algorithm is a heuristic optimization algorithm that produces an optimal solution that is only close to the original optimal solution, which means that in PWM control, the PID parameters that are rectified using the GWO may not be optimal, but are usually close enough to achieve good control.

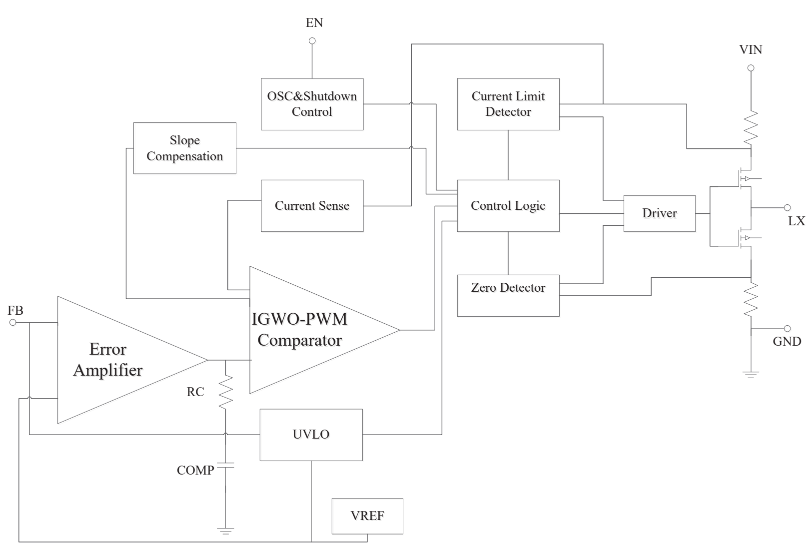


**Figure 2.** Sketch of IGWO-PID PWM controller design.

## 3. Self-Recovery Lightering Protection Circuit Design

### *3.1. Ignition Safety Threshold Judgment Circuit Design*

To avoid non-essential shutdown, starting and stopping the power supply, the self-recovery lightering protection circuit is divided into a lightering threshold judgment circuit and a lightering self-recovery circuit. As shown in Figure 3, the ignition threshold judgment circuit uses a current transformer to monitor the induced current in the circuit as an indication of the ignition phenomenon. When the current detected by the current transformer exceeds the set safety threshold, the voltage value on the sampling resistor $R1$ reaches or exceeds the rated breakdown voltage of the Zener diode $Z1$. At this point, $Z1$ reverses breakdown and conducts, resulting in current flowing through $Z1$. This change triggers the base potential of the NPN-type transistor $Q1$ to rise to a high level, causing $Q1$ to conduct and output a clear firing signal. If no ignition phenomenon is detected, the circuit remains in a non-activated state with no signal output. The design is simple in structure, stable in performance, and economically efficient.

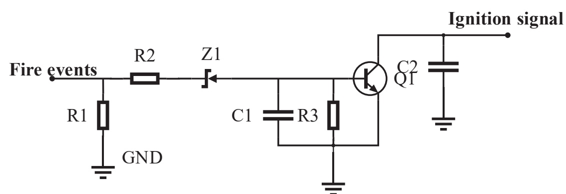


**Figure 3.** Threshold judgment circuit.

The selected current transformer model is the ZMCT103C, which, according to its supplied datasheet, has an operating temperature range of −40 °C to +85 °C. This means that the device can operate stably within the specified operating temperature range. In addition, it has an isolation withstand voltage of 4500 V, indicating that it has good electrical isolation performance, which reduces the risk of damage due to voltage shocks. The selected diode, SZMMSZ5231BT1G, manufactured by ON Semiconductor, Phoenix City, AZ, USA has an operating temperature range of −55 °C to +150 °C and complies with the automotive-grade standard AEC-Q101, meaning that it is designed to operate stably for long periods of time in harsh environments, where the life expectancy of this type of device is typically years or even decades depending on its operating conditions and environmental factors.

### *3.2. Control Circuit Design*

In the study of the self-recovery lightering protection mechanism of the high-voltage power supply system, the design of the control circuit is crucial. In this paper, a self-recovery strategy is designed to perform an instantaneous cut-off of the power output through the MCU when an abnormal signal is detected by the ignition safety threshold judgment circuit. Subsequently, the MCU restarts the high-voltage power supply after a preset delay period to ensure a smooth transition of the system to the normal operating state. For the output voltage instability caused by input power fluctuations, this paper designs a PID controller based on the improved grey wolf optimization (IGWO) algorithm, combined with the MCU to perform a "segmented" ramp output voltage. For larger firing events, the "three-stage" ramp output voltage is adopted, while for general firing events, the self-recovery circuit adopts the "two-stage" ramp output voltage to realize voltage regulation of the firing self-recovery circuit [31,32].

As shown in Figure 4, the feedback block diagram of the self-recovery circuit demonstrates the realization process of this control strategy. The design not only improves the dynamic response capability of the system but also ensures that the system can quickly recover to the predetermined rated output voltage in the face of changes in the input power supply through precise feedback control, effectively solving the voltage oscillation problem that may occur in traditional high-voltage power supply systems when the input power supply fluctuates.

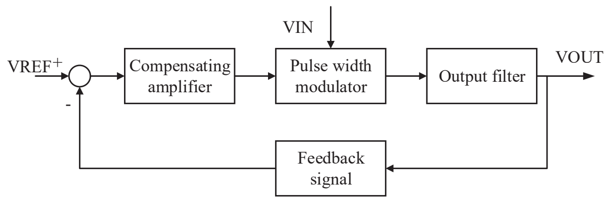


**Figure 4.** Block diagram of regulated voltage regulation feedback based on IGWO-PID controller.

High-voltage power supply designs use more type II and type III controllers for loop compensation, introducing additional high-frequency poles to attenuate high-frequency noise, variants of the PID controller. In order to make the loop more stable, the phase margin of the switching power supply is more than 45°, the gain margin of the switching power supply is more than 10 dB, and the bandwidth of the switching power supply after compensation reaches 1/5–1/10 of the switching frequency, which is used to keep away from the switching noise of the switching power supply. In our design we selected a type III controller. Figure 5 shows the circuit topology of the PID controller, first analyzed from the frequency-domain point of view. The circuit composed of $R_1$, $R_3$, and $C_3$ is regarded as an impedance $Z_1$; the circuit composed of $R_2$ , $C_2$, and $C_1$ is regarded as another impedance $Z_2$. The two impedances can be calculated as follows:

$$\begin{cases} Z_1 = R_1 // \frac{1}{jwC_1} \\ Z_2 = \left(R_2 + \frac{1}{jwC_2}\right) // \frac{1}{jwC_3} \end{cases} \tag{1}$$

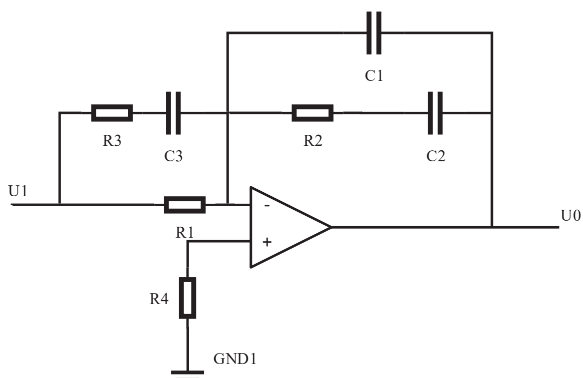


**Figure 5.** PID controller.

According to the integrated op amp circuit false short and false break characteristics, it can be obtained that

$$\frac{U_1 - 0}{Z_1} = \frac{0 - U_0}{Z_2} \tag{2}$$

Then, the transfer function is

$$H(s) = \frac{R_1 + R_3}{R_1 R_3 C_1} \times \frac{\left(S + \frac{1}{R_2 C_2}\right)\left(S + \frac{1}{(R_1+R_3)C_3}\right)}{S\left(S + \frac{C_1+C_2}{R_2 C_1 C_2}\right)\left(S + \frac{1}{R_3 C_3}\right)} \tag{3}$$

where $S = jw$.

Analyzing it from the time-domain perspective, $R_1$ and $C_1$ form the proportional part, $R_2$ and $C_2$ form the integral part, and $R_3$ and $C_3$ form the differential part; they can be obtained as follows:

$$\begin{cases} U_P = \frac{U_1 \cdot R_1}{R_1 + R_2} \\ U_I = \frac{1}{R_2 C_2} \int U_1 dt \\ U_D = \frac{1}{R_3 C_3} \cdot \frac{dU_1}{dt} \end{cases} \tag{4}$$

The output $U_0$ of the operational amplifier is connected to the proportional portion $U_P$ through the feedback network $R_4$ to obtain the relationship between the output voltage and the input voltage:

$$U_0 = U_P - U_I - U_D \tag{5}$$

That is

$$U_0 = \frac{R_1}{R_1 + R_2} \cdot U_1 - \frac{1}{R_2 C_2} \int U_1 dt - \frac{1}{R_3 C_3} \cdot \frac{dU_1}{dt} \tag{6}$$

From Equation (6), set the proportional, integral and differential coefficients:

$$\begin{cases} K_P = \frac{R_1}{R_1 + R_2} \\ K_I = -\frac{1}{R_2 C_2} \\ K_D = -\frac{1}{R_3 C_3} \end{cases} \tag{7}$$

In order to accurately regulate the type III controller, the IGWO algorithm is introduced to determine the proportional, integral, and differential coefficients of the PID controller, to avoid local optimization, to speed up the response speed, and to enhance the stability of the system, and the main workflow is shown in Figure 6.

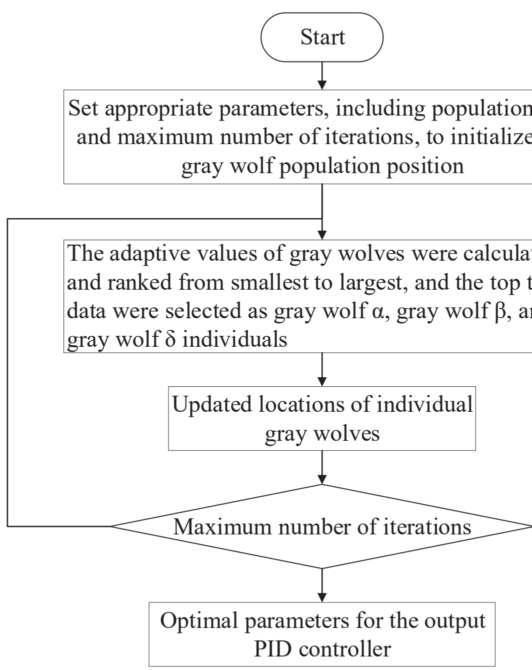


**Figure 6.** Flow chart of the improved grey wolf optimization algorithm.

The main workflow is divided into four steps: Step 1: Set appropriate parameters, such as the population size, the maximum number of iterations, and the location of the initialized generated gray wolf population; then use the chaotic initialization method to generate the initial gray wolf population and set the number of iterations to 1. Step 2: For each iteration, calculate the fitness value of each individual gray wolf, sort the resulting fitness values from smallest to largest, select the location of the first three gray wolves with the smallest fitness values and note them as gray wolf $\alpha$, gray wolf $\beta$, and gray wolf $\delta$, respectively. Step 3: Update the gray wolf positions based on the adaptation values of the current intelligent gray wolf individuals. Step 4: If the end condition of the algorithm is satisfied (reaching the specified accuracy or the maximum number of iterations), the algorithm stops iterating and outputs the optimal solution; otherwise, go to step 2.

*3.3. IGWO Algorithm Based on the Self-Recovery of High-Voltage Power Supply Firing*

The IGWO algorithm mainly focuses on two aspects: on the one hand, it improves the algorithm update iteration mechanism; on the other hand, it uses the optimization of inter-algorithm complementary combinations of other algorithms. This paper optimizes the gray wolf algorithm by the former, and uses the size of $|\overrightarrow{A}|$ and 1 to separate the gray wolf and the prey, and to find the better prey. When applying the grey wolf optimization algorithm, it is not difficult to find that the results are perfect when the optimal solution position is close to the origin. Explaining the flow of the algorithm, the behavior in the gray wolf algorithm is symmetric, with the head wolf as the center, and there is no anomaly in the movement of individual gray wolves; but as a whole, it produces a weak tendency to move closer to the origin.

With an increase in iteration number $t$, the value of $A$ converges linearly from 2 to 0. In the whole iteration process of the grey wolf optimization algorithm, the probability of $A$ randomly falling in the interval of $[-1,1]$ is larger, which leads to the over-representation of the local search, thus causing the algorithm to fall into a local optimum and affecting the solution of the global optimum. Based on this finding, this paper proposes the following scheme: in the pre-iteration $A > 1$, the individual gray wolves are mainly global search, and in the late iteration, local search is carried out, i.e., controlling the position of $A$ randomly falling in the interval $[-2,2]$, so that the group first spreads to the whole solution space, and then converges to the center of the group. An improvement of the tracking–hunting phase formula is shown in Equations (8) and (9):

$$\begin{cases} \overrightarrow{D} = \left|\overrightarrow{C} \cdot \overrightarrow{X_i}(t) - \overrightarrow{X}(t)\right| \\ \overrightarrow{X}(t+1) = \overrightarrow{X_i}(t) - \overrightarrow{A} \cdot \overrightarrow{D} \\ a = 2 - 2t/Max_t \\ \overrightarrow{A} = 2a \cdot \overrightarrow{r}_1 - a \\ \overrightarrow{C} = 2a\overrightarrow{r_2} \end{cases} \tag{8}$$

$$A = \begin{cases} ar_1 + \frac{t}{Max_t}(2r_1+1) - 2, r_1 \leq 0.5; \\ ar_1 + \frac{t}{Max_t}(2r_1-1),\ r_1 > 0.5. \end{cases} \tag{9}$$

where $\overrightarrow{D}$ denotes the distance between the individual gray wolf and the prey, and $\overrightarrow{X_i}(t)$, $\overrightarrow{X}(t)$, and $\overrightarrow{X}(t+1)$ are the prey position, the gray wolf position, and the updated position of the gray wolf, respectively. $\overrightarrow{A}$ and $\overrightarrow{C}$ denote the coefficient vectors; the size of $C$ is positively correlated with the stochastic weights of the gray wolf's position on the prey's influence. $t$ denotes the number of iterations, $a$ denotes the convergence factor, $Max_t$ denotes the maximum number of iterations, and $\overrightarrow{r_1}$ and $\overrightarrow{r_2}$ denote the stochastic vectors in the interval $[0,1]$.

In the improved algorithm, the probability that the value of $A$ is in the interval $[-1,1]$ increases gradually from 0 to 1, i.e., the global search accounts for a smaller and smaller proportion and the local search accounts for a larger and larger proportion to avoid falling into a local optimum, helping to quickly converge to the global optimum solution or the approximate global optimum solution; and because *C* is nonlinearly decreasing, stochastic, and provides the decision space for the global search in the iterative process, the algorithm does not easily fall into a local optimum, the accuracy of the global optimal solution is greatly improved, and the algorithm can be optimized theoretically.

## 4. Simulation

### 4.1. Simulink Simulation of Voltage Rise to 80 kV

Simulating the high-voltage power supply environment in MATLAB2021A with all the devices in an ideal environment may not be able to fully simulate all the non-ideal factors that may occur in the actual hardware, such as temperature variations, power supply fluctuations, component aging, etc., which leads to the test results being more favorable than the actual situation. Second, in the simulation process, we approximate certain component characteristics and system dynamics to simplify the problem. While this simplification helps to improve the simulation efficiency, it may also overlook some subtle but important system behaviors. We assume that the IGWO-PID-based high-voltage power supply circuit is built in an ideal environment to test its performance. As shown in Figure 7, a high-voltage power supply circuit is built based on IGWO-PID, including an inverter circuit, high-frequency transformer, and voltage doubler circuit, and its main device parameters are shown in Table 1.

**Table 1.** Important parameters of the simulation model.

| Parameter | Value |
|---|---|
| Input voltage | 100 V |
| Output voltage | 80 kV |
| Coil turns ratio | 8:800 |
| Capacitance, C | $2.2 \times 10^{-6}$ F |

In the MOSFET, the coil is the ideal device environment. The ignition-triggered high-voltage power supply shutdown is simulated, and the power supply is re-boosted to restore it to the initial voltage, and once again work normally. For setting 80 kV as the target voltage value, running the M file, and then running the model, the output voltage response graph is shown in Figure 8. The output voltage reaches the target voltage value in about 2 ms, the system response speed is fast, and the stability of the output voltage rising waveform is strong, which meets the requirements of the high-voltage power supply design.

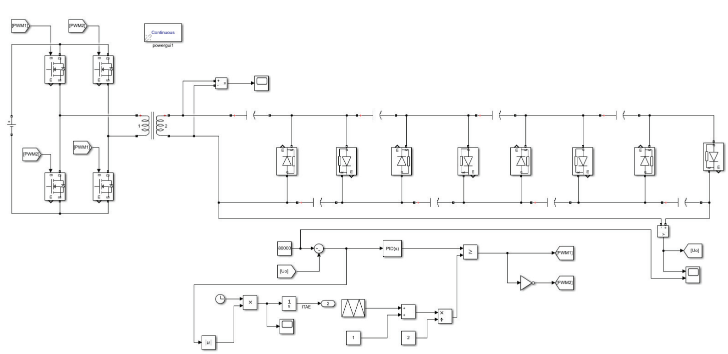


**Figure 7.** Simulink simulation model of high-voltage power supply based on IGWO-PID.

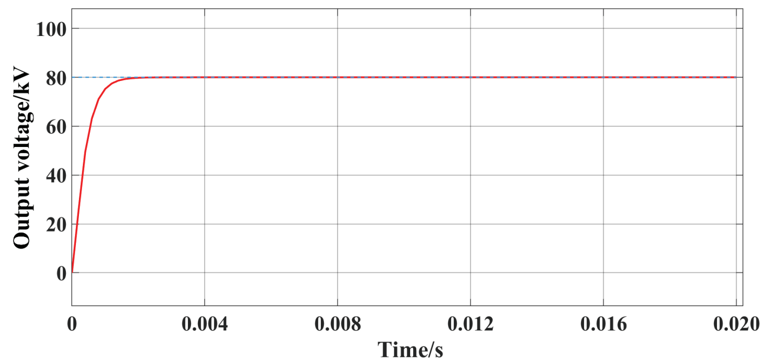


**Figure 8.** Output voltage response of high-voltage power supply system based on IGWO-PID.

### *4.2. PID Controller Parameter Adjustment*

Parameter adjustment has always been a difficult problem for PID controllers; the three coefficients of the PID controller parameters are independent of each other, affecting the response speed of the system, steady-state error, and overshooting. However, in practice, the three coefficients produce coupling between the three coefficients, and the use of a trial-and-error method makes it difficult to obtain a more optimized value. It is common in academia to use a stool, a design tool for system compensators in MATLAB, to add zeros and poles to adjust the system performance, visualize the time- and frequency-domain performance metrics, and update the root trajectory, obtaining a Bode plot and response curve in real time.

As shown in Figure 9, according to the simulation model-related parameters in Table 2, the MATLAB Bode plot compensation tool sisotool is utilized to add the zero-pole point for direct compensation, and the parameters are derived, showing that a better compensation effect can be obtained.

Where the transfer function is

$$G(s) = \frac{V_g}{V_m(1-D)^2} \cdot \frac{1 - \frac{Ls}{R(1-D)^2}}{1 + \frac{Ls}{R(1-D)^2} + \frac{LCs^2}{(1-D)^2}} \tag{10}$$

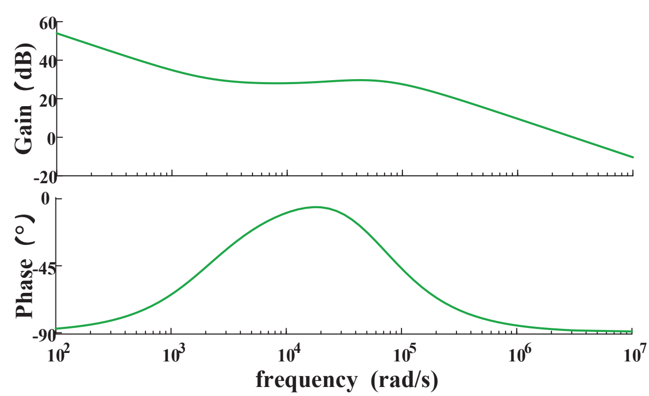


**Figure 9.** Bode plot of transfer function after sisotool adjustment.

**Table 2.** Important parameters of the simulation model.

| Parameter | Value |
|---|---|
| Input voltage, $Vg$ | 100 V |
| Output voltage, $V0$ | 300 V |
| Triangular wave carrier amplitude | 200 V |
| Capacitance, $C$ | $33 \times 10^{-6}$ F |
| Inductor, $L$ | $470 \times 10^{-6}$ H |
| Load | 30 R |
| Duty cycle, $D$ | $2/3$ |

In practical engineering applications, the control system often presents nonlinear and time-varying characteristics. sisotool tuning of PID controller parameters is suitable for single-input single-output systems, and there are limitations in its applicability and effectiveness when dealing with multiple-input multiple-output or complex systems with highly nonlinear and time-varying characteristics. Therefore, the PID controller parameters are regulated and optimized according to IGWO, and the global search of the parameter space is carried out by simulating the social behavior and hunting strategy of gray wolves, with a view to finding the optimal PID parameter configurations. In practical engineering applications such as high-voltage power supply systems, the IGWO-optimized PID controller shows significant performance improvement. The Bird's plot of the optimized system is shown in Figure 10, and its gain margins and phase margins are in line with the engineering requirements, and the system meets the expected design criteria in terms of stability and performance.

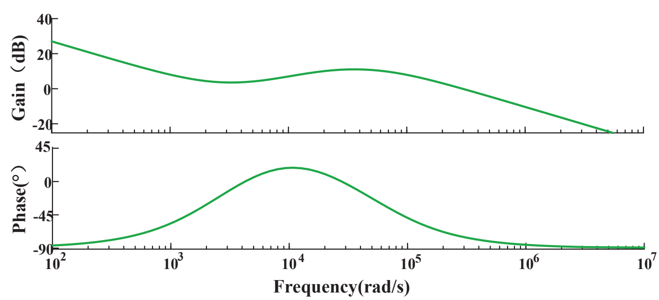


**Figure 10.** PID Bode plot after optimization of IGWO regulation.

### *4.3. Comparative Analysis of the Mustiness of Improved Gray Wolf Algorithms*

#### 4.3.1. Comparison of PSO, IGWO, and SWO Performance

To verify the feasibility of the improved GWO algorithm, one each of the unimodal, multimodal, and composite benchmark functions, F4, F11, and F20, was randomly selected and compared with the PSO algorithm and the Spider Wasp Optimization (SWO) algorithm. To ensure the accuracy of the comparison results and the persuasiveness of the data, we set the same parameters for all the algorithms: the population size was 30, the number of iterations was 500, and each algorithm was run independently 20 times to calculate the average performance. The randomly selected CEC test functions and the comparison of the best values of the objective functions of the different algorithms are shown in Tables 3 and 4.

**Table 3.** Randomly selected CEC test functions.

| Function | Dimensionality | Range | Theoretical Minimum |
|---|---|---|---|
| $f_4(x)$ | 30 | $R_1$ | 0 |
| $f_{11}(x)$ | 30 | $R_2$ | 0 |
| $f_{20}(x)$ | 6 | $R_3$ | $-3$ |

**Table 4.** Comparison of the optimal values of the objective functions of different algorithms.

| | F4 | F11 | F20 |
|---|---|---|---|
| GWO | $5.92 \times 10^{-7}$ | 0 | −3.311 |
| SWO | $5.5238 \times 10^{-7}$ | 0 | −3.312 |
| IGWO | $1.7434 \times 10^{-16}$ | 0 | −3.1624 |

The corresponding functional equations in the table are as follows:

$$\begin{cases} f_4(x) = \max_i\{|x_i|, 1 \le i \le n\} \\ f_{11}(x) = \frac{1}{4000}\sum\limits_{i=1}^{n} {x_i}^2 - \prod\limits_{i=1}^{n}\cos\left(\frac{x_i}{\sqrt{i}}\right) + 1 \\ f_{20}(x) = -\sum_{i=1}^{4} c_i \exp\left(-\sum_{j=1}^{6} a_{ij}\left(x_j - p_{ij}\right)^2\right) \end{cases} \tag{11}$$

Convergence through analysis Figure 11, we can clearly observe the superior performance of the improved grey wolf optimization (GWO) algorithm. The number of iterations required by the improved GWO algorithm is significantly lower than that of other algorithms when the optimal solutions of the objective function are close; and when the number of iterations is similar, the optimal solution obtained by the improved GWO algorithm is closer to the theoretical optimal value. Therefore, it can be confirmed that the improved GWO algorithm is not only feasible but also has significant improvement in convergence speed and solution accuracy. Applying this algorithm to real engineering cases can effectively solve a variety of problems, thus improving the effectiveness of the work and the quality of the results.

#### 4.3.2. Comparison of GWO, IGWO, and PSO Performance

A PID engine involving the desired research algorithm was created using M-files, and a model of the PID regulation transfer function was built in Simulink to verify the feasibility of the algorithm. The transfer function $Gs = -\frac{10}{s+10}$ was selected as the test function to evaluate the tracking performance of the PID controller parameters optimized by the genetic algorithm on the step response of the system. The experimental setup was as follows: the population size of the genetic algorithm was set to 100, the number of iterations was set to 200, the number of repetitive tests was set to 30, and the traditional GWO and PSO regulate the effect of the PID controller in the IGWO regulation effect comparison experiment.

Figure 12 shows the step function response graphs of the three algorithms to regulate PID, focusing on the steady-state value, rise time, and overshoot amount of the three indicators. The results show that although the GWO regulation PID has a faster response speed, it is accompanied by a larger amount of overshooting; the PSO regulation PID does not produce an overshoot, but the response speed is relatively slower, compared to the IGWO regulation PID, which demonstrates superiority in the response speed and the steady-state performance, and has a greater potential to improve the system control performance.

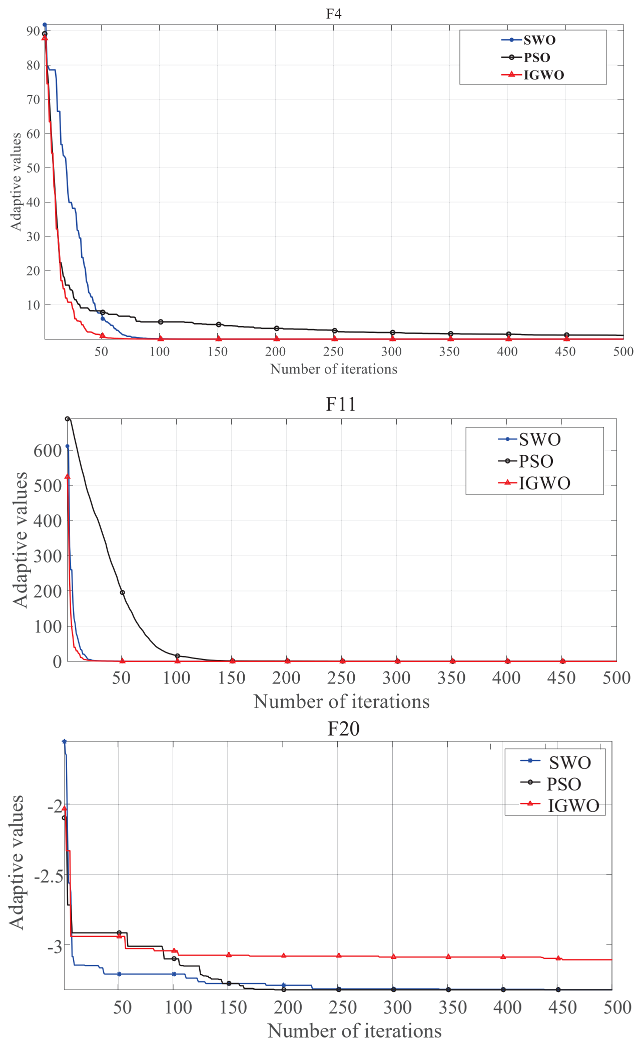


**Figure 11.** Convergence curves of the 3 comparison algorithms on the F4, F11, and F20 test functions.

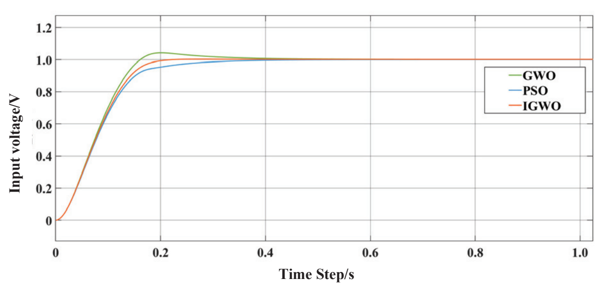


**Figure 12.** Comparison of step response curves.

## 5. Setting Up the Experimental Platform

As shown in Figure 13, the experimental platform based on the 80 kV high-voltage power supply developed by Xintlong Technology (Wuxi) Co., Ltd. (Wuxi, China) was set up, and the test prototype was subjected to a firing test and self-recovery test, and the relevant parameters of the test prototype are shown in Table 5.

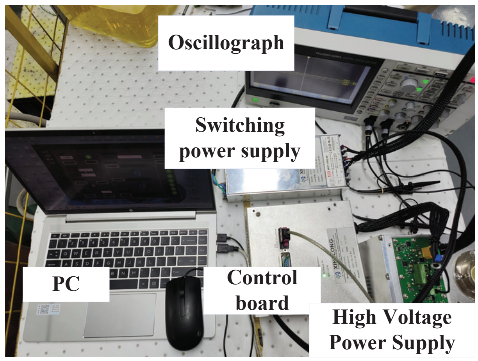


**Figure 13.** Experimental platform for high-voltage power supply firing test.

**Table 5.** Test power supply parameters and PID controller optimization parameter values.

| Parameter | Value | Parameter | Value |
|---|---|---|---|
| Load | 10 M | $R_1$ | 20 kΩ |
| Output current | 8 mA | $R_2$ | 4.7 kΩ |
| Output voltage | 80 kV | $R_3$ | 1 kΩ |
| Coil turns ratio | 8:800 | $C_1$ | 3.3 nF |
| Power | 640 W | $C_2$ | 100 nF |
| Voltage doubler capacitor, $C$ | $2.2 \times 10^{-6}$ F | $C_3$ | 10 nF |

Figure 14 shows the flow chart of the high-voltage power supply ignition test experimental platform. Using a 48 V/1000 W switching power supply to supply power to the control board, the control board drives the high-voltage power supply and receives the high-voltage power supply output voltage, output current, and the signal of the ignition, and then connects to the PC through the RS232 serial line, and interacts with the upper computer signals. A Tektronix TBS2074B, Biverton, OR, USA oscilloscope is used to measure the signals, and the electrode spacing is controlled to simulate the ignition environment under the 80 kV/8 mA working condition of the high-voltage power supply, and the load is placed in insulating oil to draw out the high voltage, which ensures the security of the test environment and maintains professionalism. Experimental method tests, micro-firing tests, firing discharge tests, and firing self-recovery tests are performed.

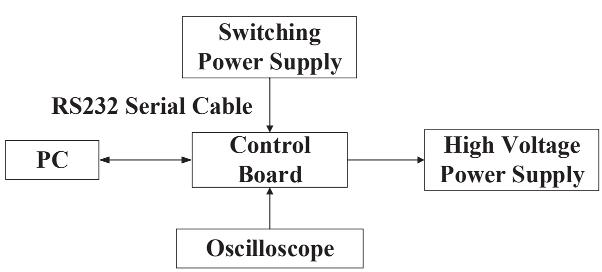


**Figure 14.** Flow chart of the high-voltage power supply firing test experiment platform.

### *5.1. Experimental Method Validation*

An experimental method of approaching and then distancing the electrodes was used to test the feasibility of the method of controlling the electrode spacing to simulate the lighting environment. The two electrodes were gradually brought together until a firing signal was detected, after which the displacement system was immediately operated to pull the electrodes further apart. As shown in Figure 15, the current waveform showed multiple spikes during the electrode proximity process, which belonged to the micro-firing discharge phenomenon. When the electrode spacing was reduced to a certain degree, the electric field strength increased, causing the breakdown voltage of the air or other medium to decrease, resulting in a discharge and a steep rise in current. At this time, the distance between the electrodes, power supply normal operation, and micro-fire discharge phenomenon also slowly disappear. Obviously, the electrode spacing has a close influence on the power supply current signal and the weak firing discharge can be detected, meaning the test method is feasible.

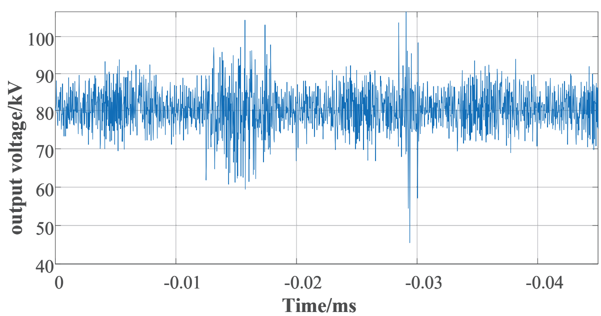


**Figure 15.** Feasibility verification of high-voltage power supply ignition program.

### *5.2. Ignition Test*

In performing the current signal measurement of the high-voltage power supply system, a Tektronix TBS2074B oscilloscope was used to measure the current response during firing, as shown in Figure 16a. In the case of slight firing, the current signal exhibited a rapid rise, peaked after about 3 microseconds, and quickly recovered to a level close to the initial state. The high-voltage power supply still operated normally. Although the high-voltage power supply system remained in normal operation during this process, the instantaneous peak value of the output current increased significantly, reaching more than three times the value of the normal operating current, and the firing produced greater damage to the high-voltage power supply system and internal devices. The slight ignition current did not exceed the set safety threshold, the system did not trigger the ignition signal, thus avoiding the non-essential start-stop cycle, which helped to maintain the stability of the system and extend the service life of the equipment. Figure 16b shows the waveform of the high-voltage power supply shutting down and stopping operation after a large firing discharge has occurred. When the high-voltage power supply system is subjected to a larger firing discharge event, the current signal shows an extreme rise, with a peak current of up to 48 mA, far exceeding the current level of the system during normal operation. This situation indicates that the larger firing event poses a serious threat to the system and requires immediate action to prevent further damage. The entire process from ignition to system shutdown lasts only 10 microseconds, and this rapid response mechanism is critical in protecting the high-voltage power system from catastrophic failure.

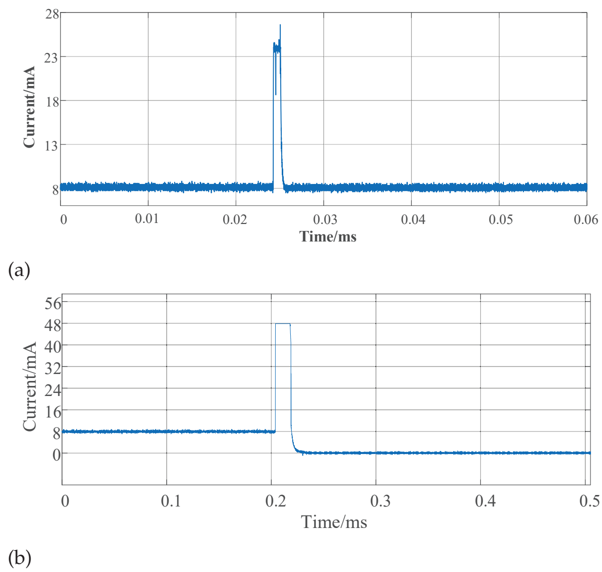


**Figure 16.** Current waveform of high-voltage power supply during ignition.

### 5.3. Ignition Self-Recovery Test

The ignition self-recovery circuit employs an intelligent MCU-based control method to optimize the power supply startup process and reduce the risk of an ignition event. The MCU executes a preset delay program after detecting the disappearance of the ignition signal to ensure a stable system environment for a smooth power supply startup.

The MCU selects an appropriate ramp startup strategy based on the spike current value detected during ignition. The peak current value serves as a benchmark for the selection of the startup strategy, ensuring that the current control during the power supply startup process is accurate and complies with safety standards. When the peak current value is less than or equal to 30 mA, a "two-stage" ramp output voltage strategy is adopted, involving two stages of voltage rise;

When the spike current value is greater than 30 mA, a "three-stage" ramp output voltage strategy is adopted, with an intermediate stage added to further refine the voltage rise process, in order to reduce the risk of firing under high current conditions. The "two-stage" ramp output voltage is shown in Figure 17: the voltage in the first 30 ms quickly rises to 20 kV, and then continues to rise to the normal operating voltage of the high-voltage power supply 80 kV, the whole process takes 170 ms, the waveform is stable, the segmented ramp output voltage can make the high-voltage power supply output steady. It is not prone to sparking discharge.

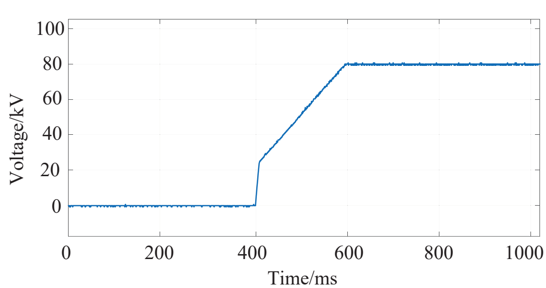


**Figure 17.** Flame-on recovery "two-stage" voltage start waveforms.

As shown in Figure 18, the "three-stage" voltage ramp is initiated when a large spike current is generated by the firing. The first stage of the voltage ramp takes 30 ms, increasing to 20 kV; in the second stage, the voltage continues to rise, but the rate has slowed down, from 20 kV to 50 kV; this process lasted 90 ms. Finally, the voltage enters the third stage, from 50 kV to 80 kV, a process that takes 80 ms. In this stage, the rate of rise of the voltage is further reduced until it reaches a steady state. During the whole process, there is no overshoot in the voltage rise curve, and the system control strategy effectively suppresses the overshoot and ensures the smooth transition and output of the voltage.

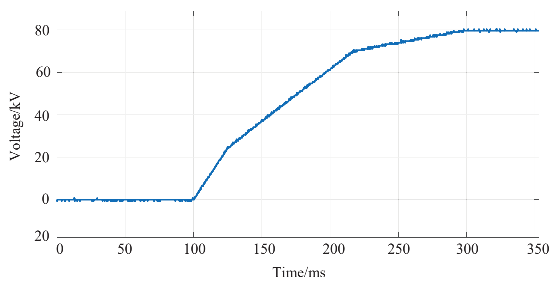


**Figure 18.** Flame-on recovery "three-stage" voltage start waveforms.

The high-voltage power supply system shows excellent performance in the process of self-recovery to the normal working state, the measured output value reaches 80.2 kV with the analog output set to 80 kV, and the accuracy of the output voltage is 99.875%. The high-voltage power supply system is stable, with good self-adaptive ability and anti-interference performance, and in the process effectively avoids the occurrence of firing discharge.

## 6. Conclusions

In this paper, a self-recovery firing protection circuit based on IGWO and PID control strategy for high-voltage power supply system is designed to protect the high-voltage power supply by quickly cutting off the switching elements on the DC side of the front-stage auxiliary power supply; it is suitable for high-voltage power supply with a wide voltage range of 60 kV–160 kV. After repeated experimental tests, we found that this protection circuit is able to detect the lightering event efficiently and to ensure that it continues to operate in a safe range. Once the set safety threshold is detected to be exceeded, the circuit automatically activates the firing protection function to protect the high-voltage power supply system from damage by reducing the voltage output of the power supply. This research methodology and solution are innovative. On the one hand, compared with the traditional PID parameter setting, the improved grey wolf algorithm can effectively avoid voltage overshoot, and the "segmented" voltage start effectively solves the voltage start fluctuation problem. On the other hand, the improved grey wolf algorithm has a faster system response, shorter regulation time, smaller fluctuations, and achieves a value closer to the reference value than other intelligent algorithms. Together with the example of a self-recovery ignition protection circuit of a high-voltage power supply system, it can effectively solve the ignition problem that causes non-essential starts and stops, and significantly improve the efficiency and quality of work. In short, the circuit has low static power consumption, stable operation, a rapid response time, and other characteristics to solve the problems that traditional high-voltage power supply ignition protection circuits have of non-essential starting and stopping of the power supply, slow response speeds, the system needing to be restarted manually, and other issues. It provides a reference for the relevant high-voltage power supply protection circuit design. In the future, there are still areas where the circuit can be improved, such as choosing switching tubes with higher precision. In the future, the design of the protection circuit will be further improved to make the design versatile and better improve the safety performance of the power supply.

**Author Contributions:** Conceptualization, J.Z. and W.Z.; methodology, J.Z.; software, J.Z.; validation, W.Z., H.W. and Y.Z.; formal analysis, J.Z.; investigation, W.Z.; resources, H.W.; data curation, Y.Z.; writing—original draft preparation, J.Z.; writing—review and editing, J.Z.; visualization, W.Z.; supervision, H.W.; project administration, Y.Z.; funding acquisition, W.Z. All authors have read and agreed to the published version of the manuscript.

**Funding:** This research was funded by the Natural Science Foundation of Jiangsu Province No. BK20221297, BK20231257, the National Natural Science Foundation of China under Grant No. 51977101, and the Zhenjiang City Industrial Prospective and Common Key Technology Research and Development Project under Grant No. GY2023003.

**Data Availability Statement:** Data are contained within the article.

**Conflicts of Interest:** The authors declare no conflicts of interest.

## References

1. Zhang, B. Development of 100 kV/25 mA low ripple high voltage DC power supply. *High Power Laser Part. Beams* **2023**, *35*, 135–139.
2. He, K.; Li, Q.; Xia, Y. Control strategy based on a 200 kV/15 A inverter-type DC high-voltage power supply. *High Power Laser Part. Beams* **2023**, *35*, 148–153.
3. Sahoo, B.; Panda, S. Improved grey wolf optimization technique for fuzzy aided PID controller design for power system frequency control. *Sustain. Energy Grids Netw.* **2018**, *16*, 278–299. [CrossRef]
4. Zheng, L.; Zhu, Y.; Ren, J.; Chang, C.; Ye, J. High-voltage DC–DC converter based on adaptive frequency conversion modulation. *J. Power Electron.* **2024**, *24*, 339–348. [CrossRef]
5. Schlatter, S.; Illenberger, P.; Rosset, S. Peta-pico-Voltron: An open-source high voltage power supply. *HardwareX* **2018**, *4*, e00039. [CrossRef]
6. Liu, J.; Zhong, S.; Zhang, J. Auxiliary power supply for medium-/high-voltage and high-power solid-state transformers. *IEEE Trans. Power Electron.* **2019**, *35*, 4791–4803. [CrossRef]
7. Zhang, L.; Ji, S.; Gu, S. Design considerations for high-voltage insulated gate drive power supply for 10-kV SiC MOSFET applied in medium-voltage converter. *IEEE Trans. Power Electron.* **2020**, *38*, 5712–5724. [CrossRef]
8. Bandeira, D.; Lazzarin, T.; Barbi, I. High voltage power supply using a T-type parallel resonant DC–DC converter. *IEEE Trans. Ind. Appl.* **2018**, *54*, 2459–2470. [CrossRef]
9. Liu, Y.; He, Z.; Hou, R. A Multi-Mode Wide Output Range High Voltage Power Supply for Magnetrons. *IEEE Trans. Ind. Electron.* **2022**, *70*, 11153–11162. [CrossRef]
10. Meng, Z.; Duan, J.; Sun, L. Voltage Drop Compensation Technology for High-Voltage and High-Power DC Energy Storage Power Supply System. *IEEE Trans. Ind. Electron.* **2023**, *71*, 549–559. [CrossRef]
11. Jafari, H.; Habibi, M. High-voltage charging power supply based on an LCC-type resonant converter operating at continuous conduction mode. *IEEE Trans. Power Appl.* **2019**, *35*, 5461–5478. [CrossRef]
12. Luo, Z.; Ker, M. A high-voltage-tolerant and power-efficient stimulator with adaptive power supply realized in low-voltage CMOS process for implantable biomedical applications. *IEEE J. Emerg. Sel. Top. Circuits Syst.* **2018**, *8*, 178–186. [CrossRef]
13. Takaki, K.; Hayashi, N.; Wang, D. High-voltage technologies for agriculture and food processing. *J. Phys. D Appl. Phys.* **2019**, *52*, 473001. [CrossRef]
14. Zhou, R. DC High Voltage Power Supply Protection Circuit Design. Master's Thesis, Shenyang Normal University, Shenyang, China, 2023.
15. Chen, Y.; Wang, Y.; Yu, Y. Research on power supply of medical X-ray machine based on improved BP algorithm. *Foreign Electron. Meas. Technol.* **2021**, *40*, 77–81.
16. Hong, Y.; Chen, B.; Wang, Q. Optimization method of Type III loop compensation in voltage-mode Buck circuits. *Power Supply Technol.* **2021**, *45*, 1209–1212+1226.
17. Li, X. Research on the Improvement and Application of Gray Wolf Optimization Algorithm. Ph.D. Thesis, Beijing Architecture University, Beijing, China, 2022.
18. Kang, P.; Jin, J.; Yan, W. Brushless DC motor control strategy based on improved GWO-PID. *Manuf. Autom.* **2023**, *45*, 147–152.
19. Bai, J.; Li, Z.; Ma, X. Application of PID controller optimized by Gray Wolf algorithm in temperature control of experimental coke oven. *Metall. Energy* **2023**, *42*, 55–59.
20. Neretti, G.; Ricco, M. Self-tuning high-voltage and high-frequency sinusoidal power supply for dielectric barrier discharge plasma generation. *Electronics* **2019**, *8*, 1137. [CrossRef]
21. Abood, L. Optimal modified PID controller for automatic voltage regulation system. *AIP Conf. Proc.* **2022**, *2415*, 030007.
22. Aziz, G.; Shneen, S.; Abdullah, F. Advanced optimal GWO-PID controller for DC motor. *Int. J. Adv. Appl. Sci.* **2022**, *11*, 263–276. [CrossRef]
23. Jagatheesan, K.; Boopathi, D.; Samanta, S. Grey wolf optimization algorithm-based PID controller for frequency stabilization of interconnected power generating system. *Soft Comput.* **2024**, *28*, 5057–5070. [CrossRef]

24. Padhy, S.; Panda, S. Application of a simplified Grey Wolf optimization technique for adaptive fuzzy PID controller design for frequency regulation of a distributed power generation system. *Prot. Control Mod. Power Syst.* **2021**, *6*, 1–16. [CrossRef]
25. Ghanamijaber, M. A hybrid fuzzy-PID controller based on gray wolf optimization algorithm in power system. *Evol. Syst.* **2019**, *10*, 273–284. [CrossRef]
26. Burkard, J.; Biela, J. Design of a protection concept for a 100-kVA hybrid transformer. *IEEE Trans. Power Electron.* **2019**, *35*, 3543–3557. [CrossRef]
27. Zhang, H. Modeling and loop compensation design of switching mode power supplies. *Linear Technol.* **2015**.
28. Bibian, S.; Jin, H. Time delay compensation of digital control for DC switchmode power supplies using prediction techniques. *IEEE Trans. Power Electron.* **2000**, *15*, 835–842. [CrossRef]
29. Ghosh, A.; Banerjee, S. Design and implementation of Type-II compensator in DC-DC switch-mode step-up power supply. In Proceedings of the 2015 Third International Conference on Computer, Communication, Control and Information Technology, West Bengal, India, 7–8 February 2015; pp. 1–5.
30. Ren, R.; Zhang, F.; Liu, B. A closed-loop modulation scheme for duty cycle compensation of PWM voltage distortion at high switching frequency inverter. *IEEE Trans. Ind. Electron.* **2019**, *67*, 1475–1486. [CrossRef]
31. Choi, H. Practical feedback loop design considerations for switched mode power supplies. *Fairchild Semicond. Power Semin.* **2010**, *2011*, 489–498.
32. Sheehan, R.; Diana, L. *Switch-Mode Power Converter Compensation Made Easy*; Texas Instruments: Dallas, TX, USA, 2016.

MDPI AG
Grosspeteranlage 5
4052 Basel
Switzerland
Tel.: +41 61 683 77 34

*Energies* Editorial Office
E-mail: energies@mdpi.com
www.mdpi.com/journal/energies

MDPI

Academic Open
Access Publishing

mdpi.com

ISBN 978-3-7258-3326-9